



**Investigation of Novel Partitioned Stator
Hybrid Excited Permanent Magnet Machines**

Hao HUA

A thesis submitted for the degree of Doctor of Philosophy

Department of Electronic and Electrical Engineering

The University of Sheffield

Mappin Building, Sheffield, S1 3JD, U.K.

February 2017

Abstract

Hybrid excited (HE) machines, which combine the high torque density of permanent magnet (PM) machines and the excellent flux controllability of electrical-excited (EE) machines, are of great interest in variable-speed electric drive systems. An additional degree of freedom, i.e. the ratio between the PM and field winding (FW) flux, is obtained. Among a variety of HE machine topologies, the stator-excited configurations employing both PMs and FWs on the stator are attracting increasing attention. This is thanks to the elimination of sliding contacts and complicated structures for three-dimensional (3-D) flux paths. Nevertheless, the stator-excited HE machines suffer from the sacrificed performance due to space conflict, with the stator accommodating PMs, FWs, and armature windings.

Partitioned stator (PS) machines were recently proposed to improve the space utilization of conventional stator-PM machines, in which two separate stators are employed to allocate armature windings and PMs respectively, with a salient iron-piece-rotor sandwiched between the two stators. As a result, more space is available for PM and/or copper, with which the torque density and efficiency are both remarkably boosted. In this thesis, based on the analysis on the existing PS machines and the inspiration from diverse rotor topologies in conventional rotor-PM synchronous machines, the new PM excitation stator topologies are proposed to extend the family of PS machines. Meanwhile, the ferrite PM is introduced to PS machines to take advantage of the enlarged available space whilst balancing performance and cost.

Moreover, the HE concept and the PS configuration can be integrated, providing the benefits of the stator-excited HE machines while relieving the space conflict. With tangentially magnetized PMs, the flexibility of PM and FW locations is identified by allocating the PMs to share the stator with either armature windings or FWs. The comparison between the proposed machines and the corresponding conventional HE machines reveals that the proposed machines can exhibit not only higher torque density, but also better flux controllability. Furthermore, a pair of PS-HE machines with radially magnetized PMs are investigated, based on which the series and parallel connections between the PMs and FWs are obtained respectively. It is found that the series PS-HE machines can exhibit higher torque while the parallel PS-HE machines benefit from better flux controllability. However, it should be noted that the mechanical weakness of the cup-rotor in the PS machines requires further work in the future.

Acknowledgements

I would like to express my gratitude to my supervisor, Prof. Z.Q. Zhu, for his continuous support, advice and encouragement throughout my Ph.D. study, which have been invaluable in the completion of this thesis. Great thanks are also due to all members of the Electrical Machines and Drives Research Group at the University of Sheffield, especially Mr. J.A. Wilkinson for his help in prototyping.

I also would like to thank IMRA U.K. Research Center for the sponsorship, particularly Mr. A. Pride, Dr. R. Deodhar, and Mr. T. Sasaki for their helpful comments and discussions.

Finally, I warmly thank my wife Xiaomei and my parents for their endless love, understanding and support.

Content

Abstract.....	2
Acknowledgements	3
Nomenclatures.....	9
Chapter 1. General Introduction	13
1.1 Introduction	13
1.2 HE Machines.....	13
1.2.1 Locations of PMs and FWs.....	15
1.2.2 Series or Parallel connection.....	21
1.3 Stator-PM Machines	26
1.3.1 Conventional single-stator PM machines	27
1.3.2 Partitioned-stator PM machines	31
1.4 Research Scope and Contributions.....	34
1.4.1 Scope of research	34
1.4.2 Contributions.....	40
Chapter 2. Partitioned Stator Permanent Magnet Machines with Different Magnet Topologies	41
2.1 Introduction	41
2.2 PS Machines Operating Principle and New PM Topologies	42
2.3 Influence of Key Parameters in Machines with New PM Excitation Stators	47
2.4 Comparison of PS Machines	52
2.4.1 Open-circuit back-EMF	54
2.4.2 Torque characteristics	55
2.4.3 Flux-weakening factor	58

2.5	Comparison of PS Machines Having Identical PM Usage Volume	59
2.5.1	Open-circuit back-EMF	60
2.5.2	Torque characteristics	61
2.5.3	Flux-weakening factor	63
2.6	Experimental Validation.....	63
2.7	Conclusion.....	71
Chapter 3.	Partitioned Stator Permanent Magnet Machines with Different Magnet Materials	72
3.1	Introduction	72
3.2	Machine Structure and Operating Principle	73
3.3	Performance Evaluation of Small PS Machines.....	76
3.3.1	Machine specifications.....	76
3.3.2	Electromagnetic performance	77
3.3.3	Economic issue	81
3.4	Performance Comparison of Prius2010 IPM-sized PS Machines	82
3.4.1	Machine specifications.....	83
3.4.2	Electromagnetic performance	85
3.4.3	Economic issue	93
3.4.4	Demagnetization of ferrite PS-SFPM machine.....	94
3.4.5	Mechanical analysis of the cup-rotor	100
3.5	Prototyping and Validation	103
3.6	Conclusion.....	109
Chapter 4.	Hybrid Excited Switched Flux Machine with Separate Field Winding Stator	111
4.1	Introduction	111
4.2	Machine Topology and Operating Principle	112
4.3	Electromagnetic Performance.....	117

4.3.1	Open-circuit back-EMF	120
4.3.2	Cogging torque.....	122
4.3.3	Flux regulation capability	124
4.3.4	On-load torque	125
4.3.5	Unbalanced magnetic force.....	128
4.4	Influence of Hybridization.....	130
4.5	Experimental Validation.....	132
4.6	Conclusion.....	135
Chapter 5. Partitioned Stator Hybrid Excited Switched Flux Machines		136
5.1	Introduction	136
5.2	Machine Topology and Operating Principle	137
5.3	Electromagnetic Performance.....	143
5.3.1	Open-circuit back-EMF	146
5.3.2	Cogging torque.....	148
5.3.3	Flux regulation capability	150
5.3.4	On-load torque	152
5.3.5	Unbalanced magnetic force.....	157
5.4	Influence of Hybridization.....	159
5.5	Experimental Validation.....	162
5.6	Conclusion.....	168
Chapter 6. Series Hybrid Excited Machines with Separate Excitation Stator.....		170
6.1	Introduction	170
6.2	Machine Topology and Operating Principle	172
6.3	Slot/Pole Number Combinations.....	177
6.4	Electromagnetic Performance.....	181
6.4.1	Open-circuit back-EMF	183

6.4.2	Cogging torque.....	185
6.4.3	Flux regulation capability	187
6.4.4	On-load torque	188
6.4.5	Torque-speed envelop.....	191
6.4.6	Unbalanced magnetic force.....	193
6.5	Experimental Validation.....	195
6.6	Conclusion.....	201
Chapter 7. Parallel Hybrid Excited Machine with Separate Excitation Stator		202
7.1	Introduction	202
7.2	Machine Topology and Operating Principle	204
7.3	Slot/Pole Number Combinations.....	211
7.4	Electromagnetic Performance.....	214
7.4.1	Open-circuit back-EMF	215
7.4.2	Cogging torque.....	217
7.4.3	Flux regulation capability	218
7.4.4	On-load torque	219
7.4.5	Unbalanced magnetic force.....	222
7.5	Experimental Validation.....	224
7.6	Conclusion.....	228
Chapter 8. General Conclusions		229
8.1	Summary	229
8.2	Machine Topologies.....	230
8.2.1	Developed sole PM PS machines	230
8.2.2	DS-HESF machines	230
8.2.3	PS-HESF machines.....	231
8.2.4	Series and Parallel PSHE machines.....	231

8.3	Performance Evaluation	233
8.3.1	Comparison of developed sole PM PS machines	233
8.3.2	DS-HESF machines	234
8.3.3	PS-HESF machines.....	235
8.3.4	Comparison of series and parallel PSHE machines.....	236
8.4	Future Work	240
8.4.1	Iron loss and efficiency	240
8.4.2	Control strategies with optimizing field and armature currents.....	242
8.4.3	Torque ripple suppression of the parallel PSHE machines.....	243
8.4.4	Investigations of noise, vibration and stiffness of the PS machines	243
	References.....	244
	Publications	260

Nomenclatures

B_r	Residual flux density	T
$C1, C2$	Casual integer	-
E_{FE}	Open-circuit back-EMF in flux-enhancing	V
E_{FW}	Open-circuit back-EMF in flux-weakening	V
E_{PM}	Open-circuit back-EMF with sole PM excitation	V
g	Air-gap length	m
H_c	Coercive force	A/m
h_{pm}	PM height	m
h_r	Rotor radial thickness	m
I_a	Armature current value	A
I_d	D-axis armature current	A
I_q	Q-axis armature current	A
J_s	Current density	A/m ²
k_1	Relative coil polarity	-
k_2	Relative PM polarity	-
K_{fw}	Flux-weakening factor	-
k_{pf}	Slot package factor	-
k_{PM}	PM length factor	-
K_h	Hysteresis loss coefficient of lamination	W/m ³
K_c	Classic eddy-current loss coefficient of lamination	W/m ³
K_e	Excess eddy-current loss coefficient of lamination	W/m ³
l_a	Machine active axial length	m
L_d	D-axis inductance	H
l_{ib}	Iron bridge thickness	m

N_{ac}	Number of turns in armature coil	-
N_{dc}	Number of turns in field coil	-
N_r	Rotor piece (rotor pole) number	-
N_s	Stator slot number	-
P_{cu}	Copper loss in armature windings	W
R_a	Armature winding resistance	Ω
R_{isi}	Inner stator inner radius of dual stator machine	m
R_{iso}	Inner stator outer radius of dual stator machine	m
R_{isy}	Inner stator yoke radius of dual stator machine	m
R_{osi}	Outer stator inner radius of dual stator machine	m
R_{oso}	Outer stator outer radius of dual stator machine	m
R_{osy}	Outer stator yoke radius of dual stator machine	m
R_{ri}	Rotor inner radius of single air-gap machine	m
R_{ro}	Rotor outer radius of single air-gap machine	m
R_{ry}	Rotor yoke radius of single air-gap machine	m
R_{si}	Stator inner radius of single air-gap machine	m
R_{so}	Stator outer radius of single air-gap machine	m
R_{sy}	Stator yoke radius of single air-gap machine	m
S_a	Slot area for each coil side	m ²
S_n	Number of spanned slots between the two coils for one phase	-
T_{ave}	Average torque	N·m
T_{max}	Maximum torque	N·m
T_{min}	Minimum torque	N·m
T_{ripple}	Torque ripple factor	-
w_{pm}	PM thickness	m
β_{ist}	Inner stator tooth arc of dual stator machine	rad

β_{ost}	Outer stator tooth arc of dual stator machine	rad
β_{pm}	PM pole arc	rad
β_{ri}	Rotor inner pole arc	rad
β_{ro}	Rotor outer pole arc	rad
β_{rt}	Rotor tooth pole arc of single air-gap machine	rad
β_{st}	Stator tooth pole arc of single air-gap machine	rad
β_{tip}	Outer stator tooth tip pole arc of dual stator machine	rad
γ	Split ratio	-
δ	Flux regulation capability	-
δ_{PM}	PM incline angle	rad
ε	PM usage efficiency	$\text{N}\cdot\text{m}/\text{m}^3$
θ_e	Rotor electrical position	rad
θ_m	Rotor mechanical position	rad
θ_v	Lag angle between Φ_{A2} and Φ_{A1}	rad
λ	Flux regulation ratio	-
ρ_{cu}	Electrical resistivity of copper	$\Omega\cdot\text{m}$
ν	Harmonic order	-
Φ_{A1}	Flux-linkage in coil A1	Wb
Φ_{A2}	Flux-linkage in coil A2	Wb
Φ_v	Amplitude for the ν^{th} harmonic flux linkage	Wb
φ_v	Phase for the ν^{th} harmonic flux linkage	rad
ψ_e	Flux-linkage generated by PMs combined with field windings	Wb
ψ_{PM}	PM flux-linkage	Wb
ω	Electrical angular speed	rad/s

Abbreviations

2-D	Two-dimensional
3-D	Three-dimensional
BLAC	Brushless AC
CPSR	Constant power speed range
DS	Dual stator
DSPM	Doubly salient permanent magnet
EMF	electro-motive force
FE	Finite element
FRPM	Flux reversal permanent magnet
FW	Field winding
HE	Hybrid excited
IPM	Interior permanent magnet
MTPA	Maximum torque per ampere
PM	Permanent magnet
PS	Partitioned stator
SF	Switched flux
SFPM	Switched flux permanent magnet
SPM	Surface-mounted permanent magnet
SRM	Switched reluctance machine
THD	Total harmonic distortion
UMF	Unbalanced magnetic force

Chapter 1. General Introduction

1.1 Introduction

Permanent magnet (PM) synchronous machines exhibit high torque density and high efficiency thanks to high energy-product PMs. A variety of PM machine topologies have thus been developed, and have attracted increasing interest. Nevertheless, amongst the variable-speed applications, which include electric vehicles [OKA11], [CHA08], [LIU10], more electric aircrafts [PAT08], and spindle drives [KOA10] etc., an excellent flux-weakening capability and a wide constant power speed range (CPSR) are critical. Unfortunately, PM machines suffer from relatively poor flux-weakening capability due to the dominant excitation of PMs.

Consequently, hybrid excited (HE) machines, which combine the merits of PM machines together with the flux controllability of electrical-excited (EE) machines, are being proposed and investigated [McC87], [AMA09], [WAN12c]. HE machines feature the coexistence of PMs and field windings (FWs), therefore inherently possessing flux-control capability. Among a multitude of HE machines, the topologies based on the stator-PM structures have great advantages, as they avoid sliding contacts and sophisticated three-dimensional (3-D) flux paths [FRE91], [LI95].

The stator-PM based HE machines, however, have PMs, FWs, as well as armature windings all on the stator, with redundant space on the rotor. Consequently, they suffer from a serious space conflict and thus sacrificed torque density. To address this, the partitioned stator (PS) technique with two stators to accommodate armature windings and excitations (PMs or/and FWs) individually, can be employed to enhance the performance of the stator-PM based HE machines. In this thesis, the PS technique is evaluated firstly, with particular reference to PM topologies and materials. Several novel HE machines based on the PS principle are then presented and investigated.

1.2 HE Machines

HE machines that employ both PM and FW excitations are proposed to combine the advantages of PM machines and EE machines. In the HE machine, FWs and PMs contribute to the air-gap field simultaneously, where the PM flux works as a constant component and the FW flux functions as the variable component, and thus the air-gap field is controllable.

Consequently, an additional degree of freedom, i.e. the ratio between the PM flux and the FW flux, is obtained in HE machines. During high speed operation, the negative DC field current can be applied in FWs to realize flux-weakening, which counters the PM flux and reduces the induced back electro-motive force (back-EMF), with which the constant power speed range (CPSR) is extended. Alternatively, during the low speed operation, the positive DC field current can be injected to boost the air-gap flux, and this is helpful to improve the torque output.

The topologies of HE machines are diverse, since the two excitation sources can be flexibly arranged. A variety of structures have been proposed and analyzed over the past two decades, [WAN15], [WAN16], and they can be classified as seen in Fig. 1.1.

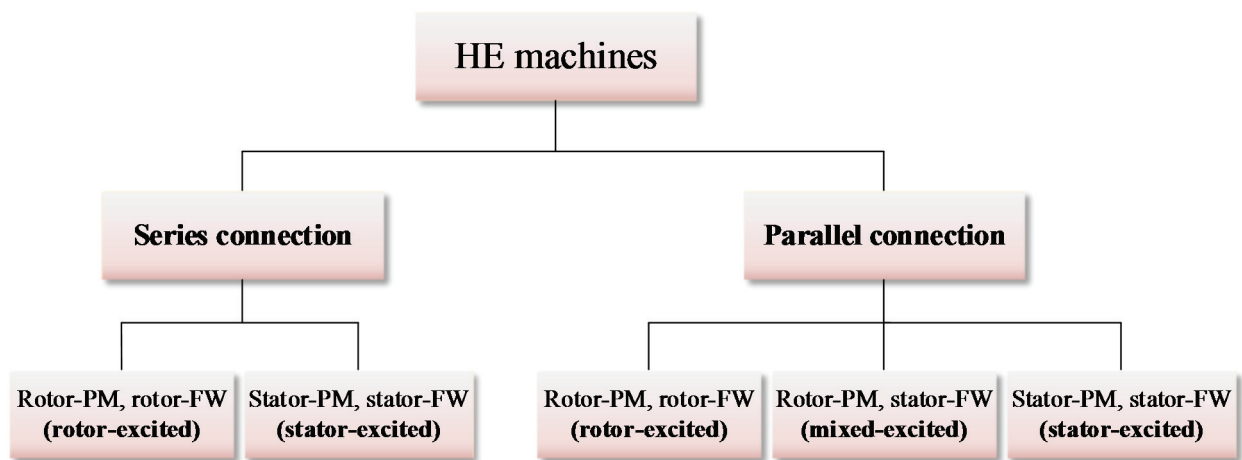


Fig. 1.1 Classification of HE machines.

In terms of the locations of the PMs and FWs, HE machines can be classified into several categories [OWE11], [AMA11], [ZHA14], as follows:

- PMs and FWs both placed on rotor. In this case, the flux controllability is attractive but the slip rings and brushes are required to conduct the field current.
- PMs on rotor while FWs on stator. In this case, the sliding contacts are avoided. However, the extra axial air-gap exists and the 3-D flux path is normally employed, which results in remarkable flux-leakage and sacrificed torque density.
- PMs and FWs both located on stator. In this case, the sliding contacts are absent and the structures are simplified. The robust rotor is free from PM or copper. Nevertheless, as the armature windings, FWs and PMs are all located on the stator, the space conflict is serious and torque density tends to be sacrificed.

On the other hand, according to the magnetic circuit configurations between the PM flux and the FW flux, HE machines can be categorized into two groups [AMA09], [OWE11], [WAN12b]:

- Series HE machines. In this case, the flux generated by the FWs goes through the PMs, i.e., they share the same path. The structures of these machines are relatively simple. However, as the relative permeability of the PM is low (close to the relative permeability of air), the FW flux has difficulty to effectively affect the air-gap field. Hence, the flux controllability is limited [AMA11]. Meanwhile, the field current has the potential to irreversibly demagnetize the PMs.
- Parallel HE machines. In this case, the PM flux and the FW flux have different trajectories. Therefore, the flux controllability is enhanced and the risk of irreversible demagnetization is alleviated. Nevertheless, the armature reaction tends to be significant and torque density may be sacrificed [KAM14].

1.2.1 Locations of PMs and FWs

A. Rotor-excited HE machines

Based on the classic rotor-PM synchronous machine, the rotor-excited HE machine was developed to enhance the flux controllability [HEN94]. As illustrated in Fig. 1.2, the FWs are wound around the rotor poles that have also been mounted with the PMs, whilst a conventional stator is employed. This topology is the integration of a PM synchronous machine and an EE synchronous machine. The air-gap flux density can be effectively enhanced or weakened by the field current [FOD07], [KAM12]. However, it can be noted that the slip rings and brushes are required to conduct the field current, since the FWs are located on the rotary component, which reduces robustness and increases machine maintenance cost.

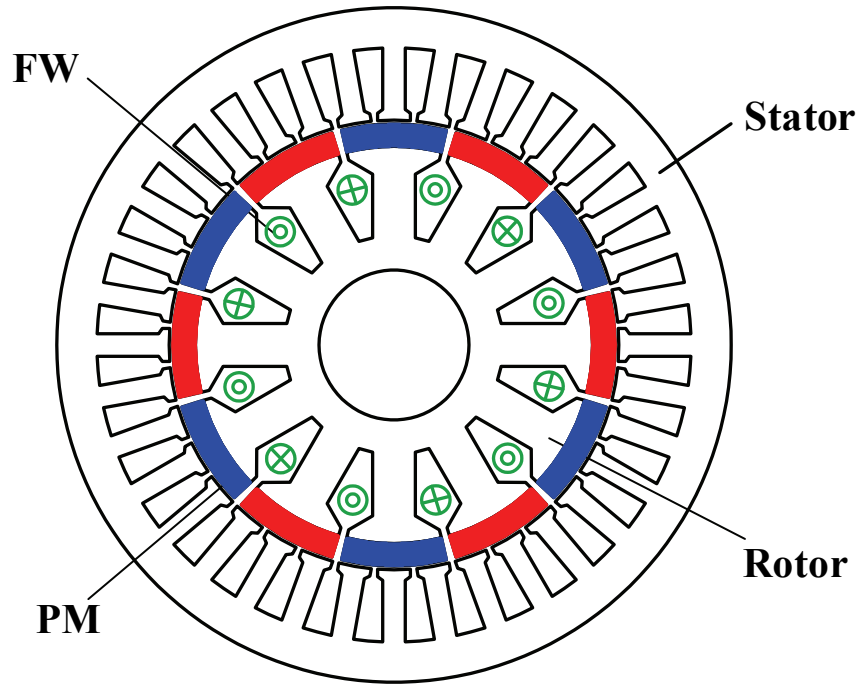


Fig. 1.2 Cross section of a series rotor-excited HE machine [HEN94].

B. Mixed-excited machines

In order to eliminate sliding contacts, the toroid FW is employed on the stationary component whilst the PMs are still on the rotor [McC87], [SPO89], i.e. the mixed-excited topology is presented. This structure has radial and axial fluxes at the same time, in which the PMs normally provide the radial flux as a constant component while the flux due to the toroid FW flows through the axial path. The 3-D flux is therefore employed. As illustrated in Fig. 1.3, a toroid FW is placed on the center of the stator yoke and the radially magnetized consequent-pole surface-mounted PM (SPM) is arranged on the rotor. To fit the center-based FW, the rotor is axially segmented into two parts and the consequent-pole is adopted to reduce the magnetic reluctance for the FW flux, which in turn enhances flux controllability. By injecting different field currents, the magnetization of iron poles on the rotor can be varied and the air-gap flux density is thus controllable [TAP02], [TAP03].

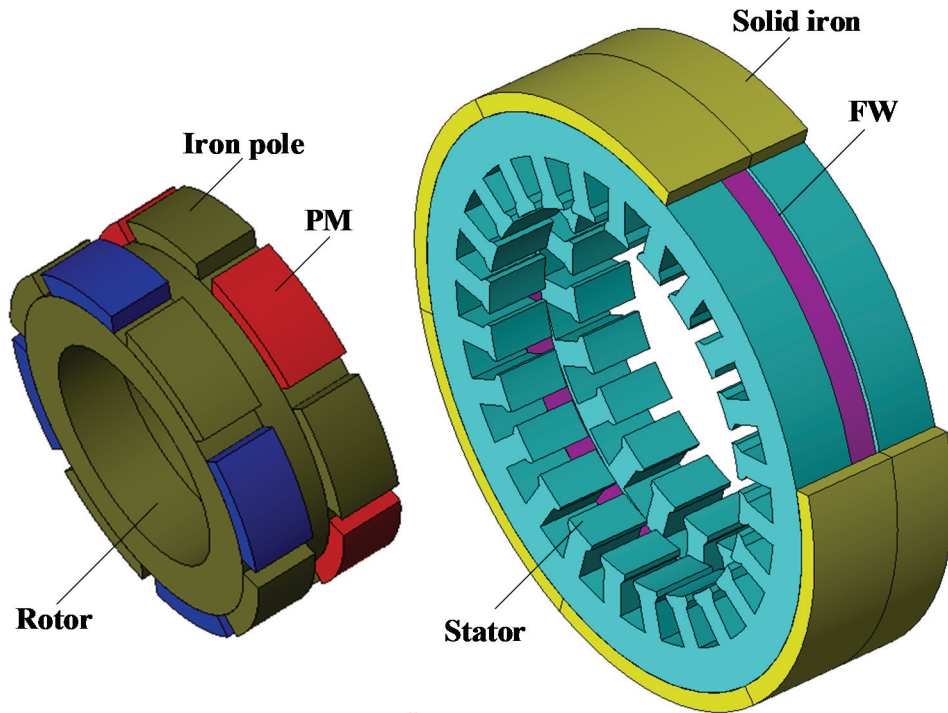
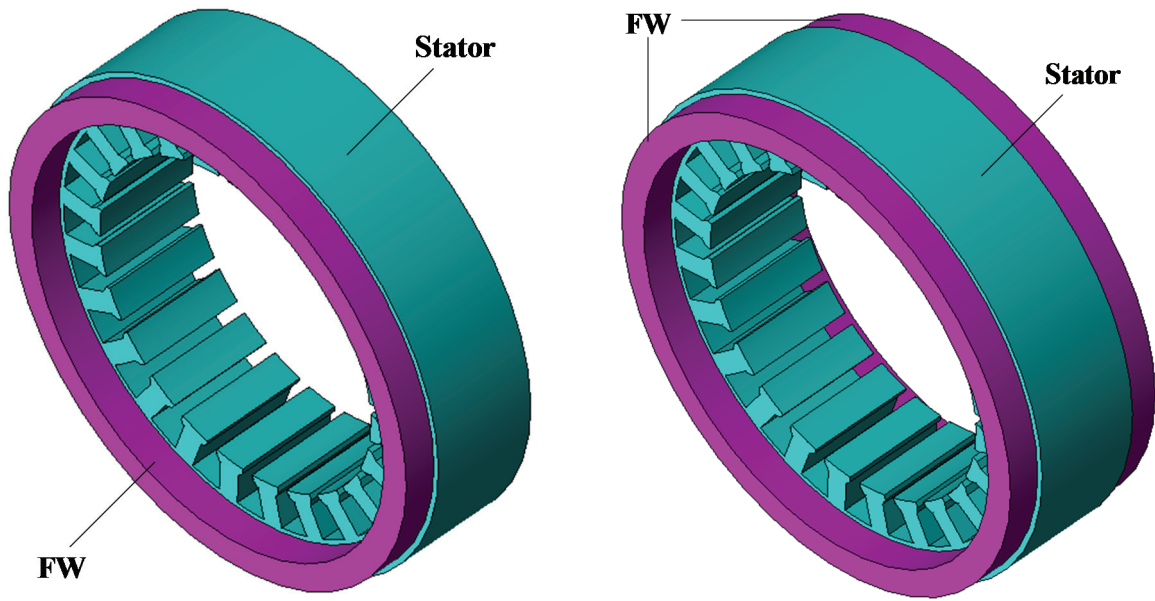


Fig. 1.3 Configuration of a mixed-excited HE machine with a toroid FW in stator yoke [TAP02].

In addition to the topologies with the center-based FW, more mixed-excited HE machines were developed. The FWs can also be accommodated on the machine axial extremities, on one side [ZHA08], [SHI11], [ZHA13], [ZHA14], Fig. 1.4(a) or on both sides [AMA09], [AMA11], [NED11], [HOA17], Fig. 1.4(b). More FW coils can thus be applied but additional stationary magnetic end-parts are required. Moreover, based on the end-based FW, the axially magnetized PM is employed on the rotor, which is sandwiched between the dual-stack half-pitch skewed salient rotor [KOS10], [OZA11], Fig. 1.5, or claw pole rotor [MEL11], [REB15], Fig. 1.6.



(a) FW on the stator one extremity

(b) FW on the stator both extremities

Fig. 1.4 Illustration of toroid FWs located on the stator extremities in mixed-excited HE machines.

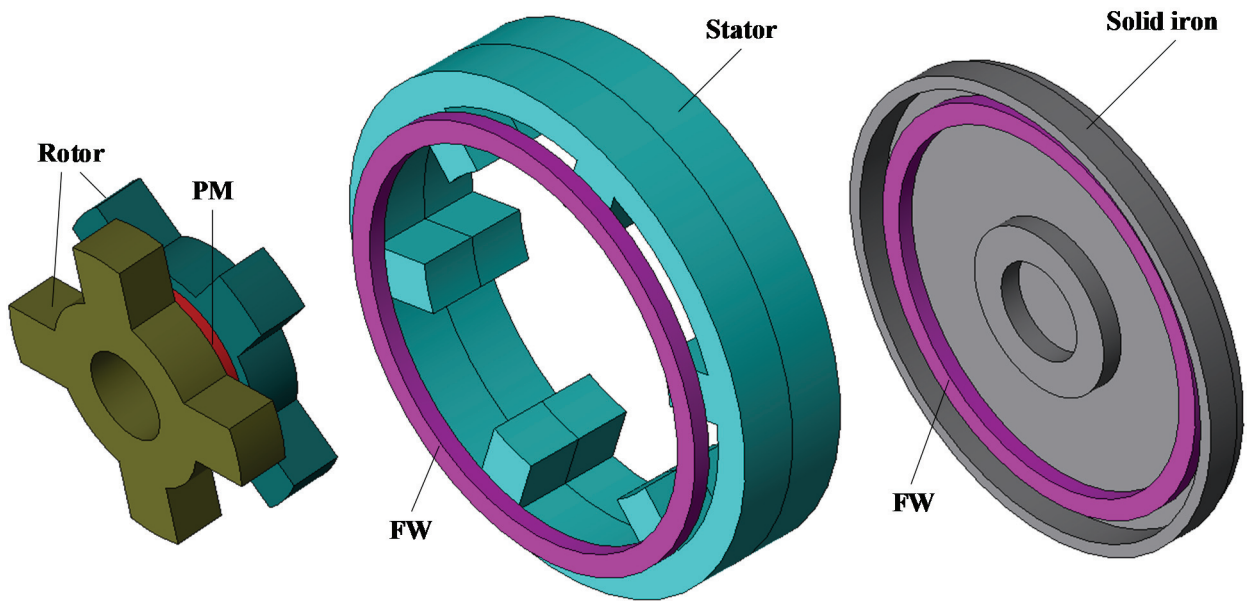


Fig. 1.5 Configuration of the mixed-excited HE machine with skewed dual-stack rotor [KOS10].

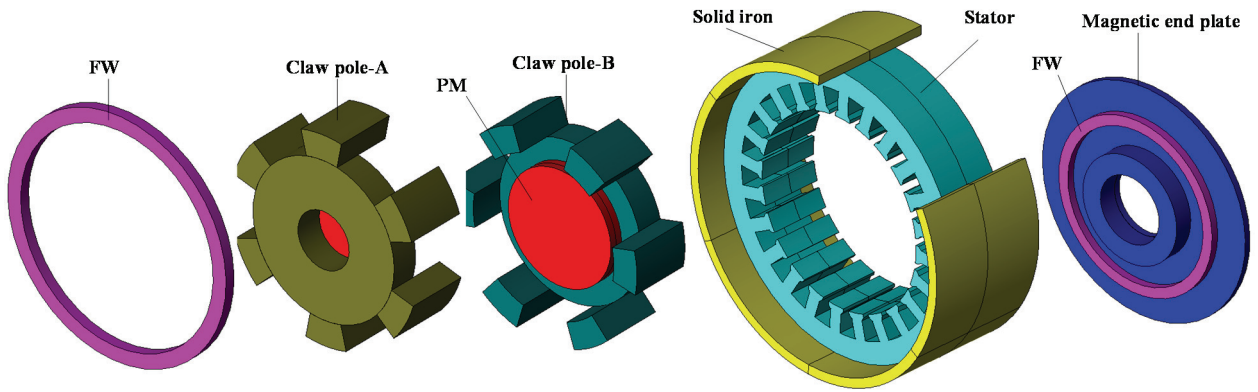


Fig. 1.6 Configuration of the mixed-excited HE machine with claw pole rotor [REB15].

In general, in the mixed-excited machine topologies, the extra axial air-gap always exists and the 3-D flux occurs, which corresponds to both sophisticated structures and significant flux-leakage that sacrifices torque density.

C. Stator-excited HE machines

Stator-excited HE machines can be obtained based on the stator-PM machines which locate PMs on the stator and employ the salient rotor free from excitations. The PMs and FWs, together with armature windings, are all placed on the stator [FRE91]. Therefore, the sliding contacts are avoided and the temperature rises of the PMs and coils are easily managed by forced cooling.

Originating from the very first stator-excited HE machine equipped with the low-cost ferrite PM [LI95], [LEO96], a typical three-phase 12-stator-slot/8-rotor-pole stator-excited HE machine with NdFeB PM is illustrated in Fig. 1.7 [ZHU07a]. Here, the tangentially magnetized PMs are inserted into the stator yoke. The FWs are also located on the stator, together with the three-phase concentrated non-overlapping armature windings. The number of the PMs is one-third of the number of armature coils for a three-phase machine. In this machine, the air-gap field is generated by the PMs and FWs at the same time. The flux linked by the armature coil can thus be enhanced or weakened with different field currents. It should be noted that the asymmetric flux path occurs to each armature coil while the phase flux-linkage is unipolar in this machine [CHA03], [CHA06a], which compromises torque density [HUA05].

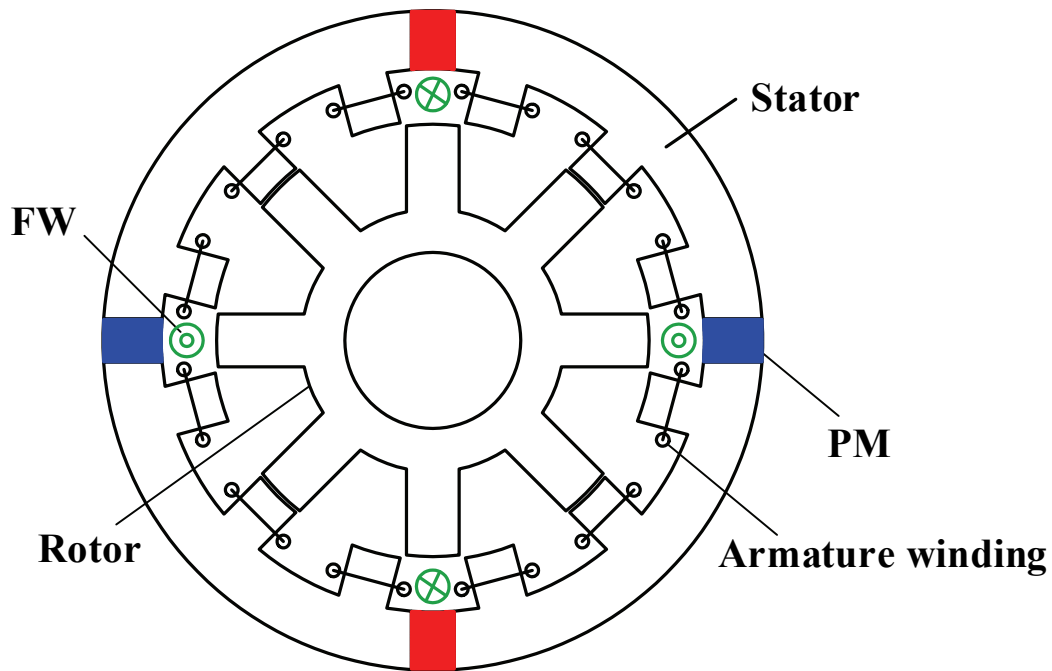


Fig. 1.7 Cross section of a series stator-excited HE machine with unipolar flux [ZHU07a].

Furthermore, the stator-excited HE machines with bipolar flux can be obtained by offering a symmetrical magnetic path for both the PM flux and FW flux, as illustrated in Fig. 1.8 [OWE10a], [HOA07]. The tangentially magnetized PMs are sandwiched in every stator tooth and the concentrated FW coils are also wound around every stator tooth, whereas the concentrated non-overlapping armature windings are inherited. As a result, each armature coil is excited by the PM and the FW together, while the PM flux and FW flux are both bipolar.

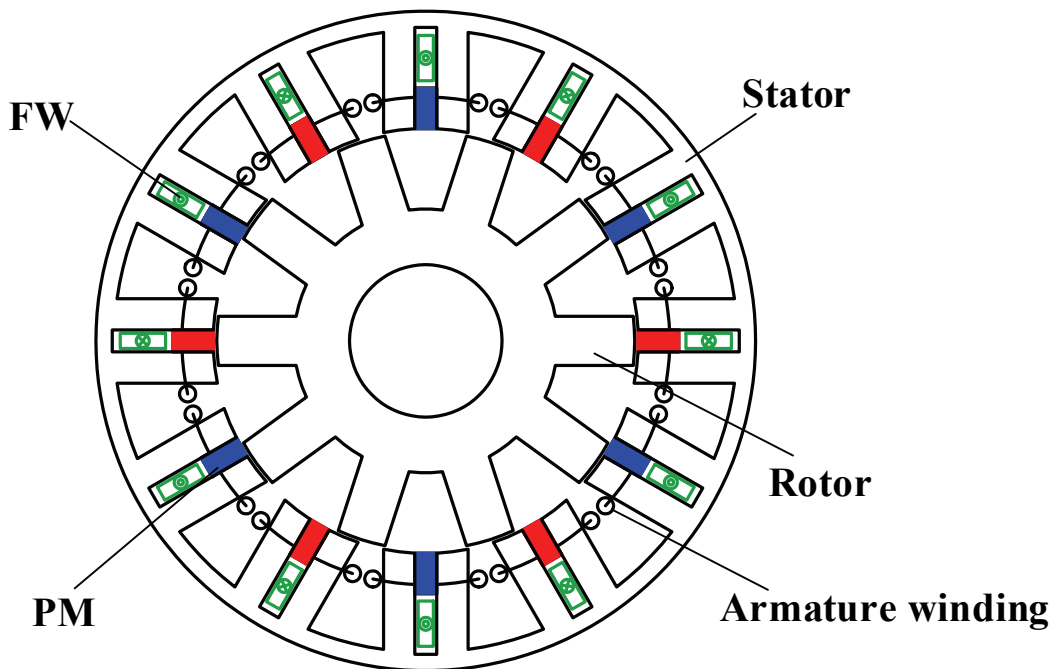


Fig. 1.8 Cross section of a parallel stator-excited HE machine with bipolar flux [OWE10a].

The stator-excited HE machines benefit from the relatively simple structures as well as from the absence of brushes and slips. It should be noted, however, that the major components including armature windings, PMs and FWs are all placed on the stator, which results in space conflict and therefore sacrifices the flux controllability as well as torque density.

1.2.2 Series or Parallel connection

Among the various topologies of HE machines, the connection configuration between the PM and FW fluxes features with either series or parallel connection.

A. Series HE machines

The series HE mode is easily obtained in the rotor-excited machines, Fig. 1.2, where the FW coils are wound around the PM poles. Thus, the flux due to the FWs flows through the PMs. Apart from the SPM structure, the spoke-type interior-PM (IPM) rotor is also applicable [BOU12], with which the flux-focusing of PM field is achieved and hence the torque density can be boosted. In addition, the consequent-pole rotor can be applied to reduce the PM usage volume and thus the cost. Meanwhile, the magnetic reluctance for the FW flux is decreased and flux controllability can be improved [KAM12], [KAM13], [KAM14].

The stator-excited HE machines can also be realized with series connections. In the machines with unipolar flux, Fig. 1.7, the FW flux loops through the PM and the series connection is hence presented. This is actually determined by the stator-slot/rotor-pole number combination and the relative location between PMs and FWs. Moreover, a series stator-excited HE machine with bipolar flux is shown in Fig. 1.9 [HUA09], [ZHA11], [HUA15], in which the FW flux must go through the PM in a loop. In fact, it can be found that the major difference between this series HE machine and the corresponding parallel HE machine, as shown in Fig. 1.8, is the elimination of the iron bridges which are adjacent to the FW slots. By eliminating these iron bridges, the bypass path for the FW flux is removed, which limits the flux controllability but also reduces the short-circuited PM flux and thus improves the torque output. The analysis of the iron bridge effects is included in [OWE10a], [ZHA16].

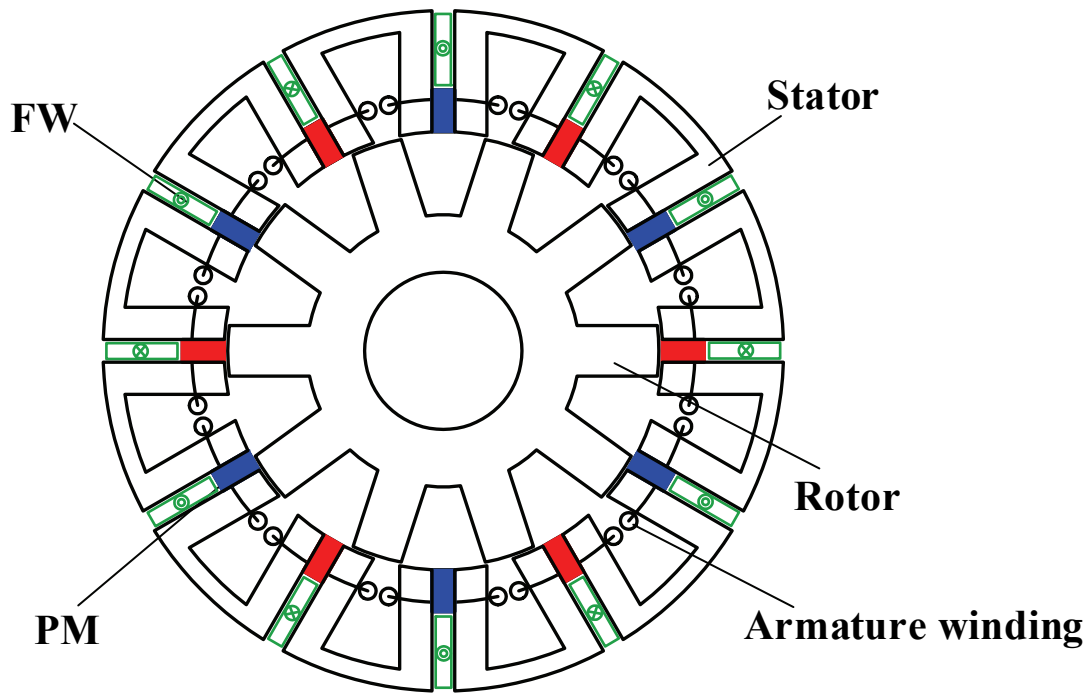


Fig. 1.9 Cross section of a series stator-excited HE machine with bipolar flux [HUA09].

B. Parallel HE machines

The parallel HE machine topology can be obtained in the rotor-excited machines by adjusting the rotor pole arrangement, with which the separate paths for the FW flux and PM flux are produced. A parallel HE machine is illustrated in Fig. 1.10 [LUO00], where the stator is identical to that in the corresponding series HE machine in Fig. 1.2, but a pair of FW poles coexist with the two pairs of PM poles in the rotor, and their fluxes can flow independently. As a result, the PM flux and the FW flux are connected in parallel and they contribute to the air-gap individually.

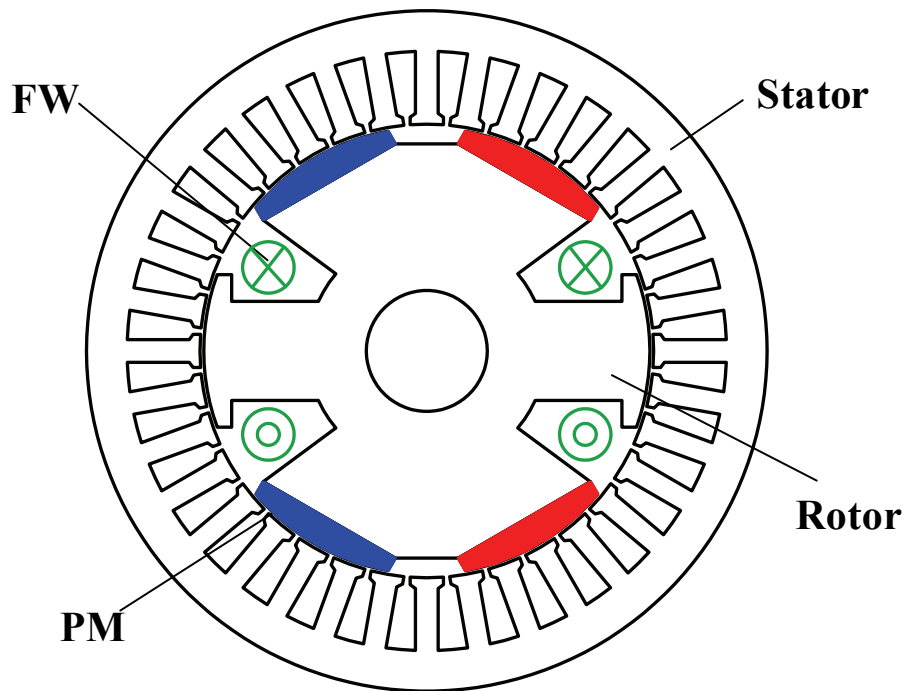


Fig. 1.10 Cross section of a parallel rotor-excited HE machine [LUO00].

The mixed-excited HE machines usually feature parallel connections [McC87], [SPO89], [TAP03], [AMA09], [ZHA08], where the PM flux only flows through the radial path whilst the FW flux has specific 3-D loops bypassing the PMs. In [KOS10], [MEL11], [OZA11], [REB15], the PM and FW fluxes both flow through the 3-D loops while having independent paths at the same time.

The parallel stator-excited HE machine with unipolar flux is obtained in Fig. 1.11 [CHE11a], which features an 18-stator-slot/12-rotor-pole structure. Compared with the series counterpart in Fig. 1.7, the major difference is the adjustment of stator-slot/rotor-pole combination and the PM piece number. With the stator-slot number increasing, the PM piece number is halved, with which the physical distance between the PMs is increased and the FW flux can loop without crossing the PMs. Several stator pole units are therefore obtained, excited by either PMs or FWs, and thus the parallel connection between the PM and FW fluxes is realized. Besides, the parallel stator-excited HE machine with bipolar flux has been illustrated in Fig. 1.8, where the FW flux can bypass the PMs through the iron bridges to produce a parallel connection.

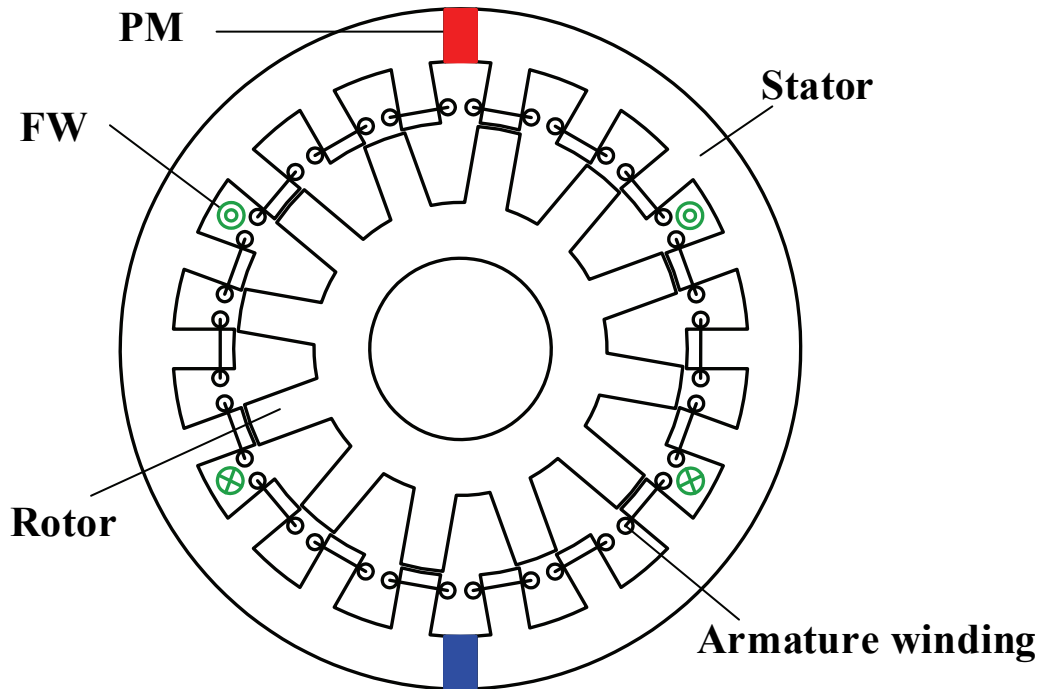


Fig. 1.11 Cross section of a parallel stator-excited HE machine with unipolar flux [CHE11a].

Moreover, the dual-stack technique has been used to realize the parallel connection in HE machines, which is applicable to both rotor-excited and stator-excited machines. In fact, the dual-stack HE machines are comprised of the axial integration of a PM synchronous machine and an EE synchronous machine, in which the PMs contribute to the air-gap field among one axial stack whilst the FWs work amongst the other stack. This technique is effective for the rotor-excited HE machines [SYV95], [SYV98], [NAO01], Fig. 1.12, where a surface-mounted PM machine and a conventional EE machine with FWs on rotor are combined together, whereas their stators are identical and they share the same armature windings. The dual-stack stator-excited HE machine can be obtained as well [WAN12], Fig. 1.13, which is based on the integration of a stator-PM machine and an EE machine with FWs on stator, in which they can share the same rotor, stator and armature windings. It should be noted, however, that the dual-stack machines suffer the additional gap between the two stacks to accommodate winding end-parts, which remarkably degrade the machine compactness and torque density.

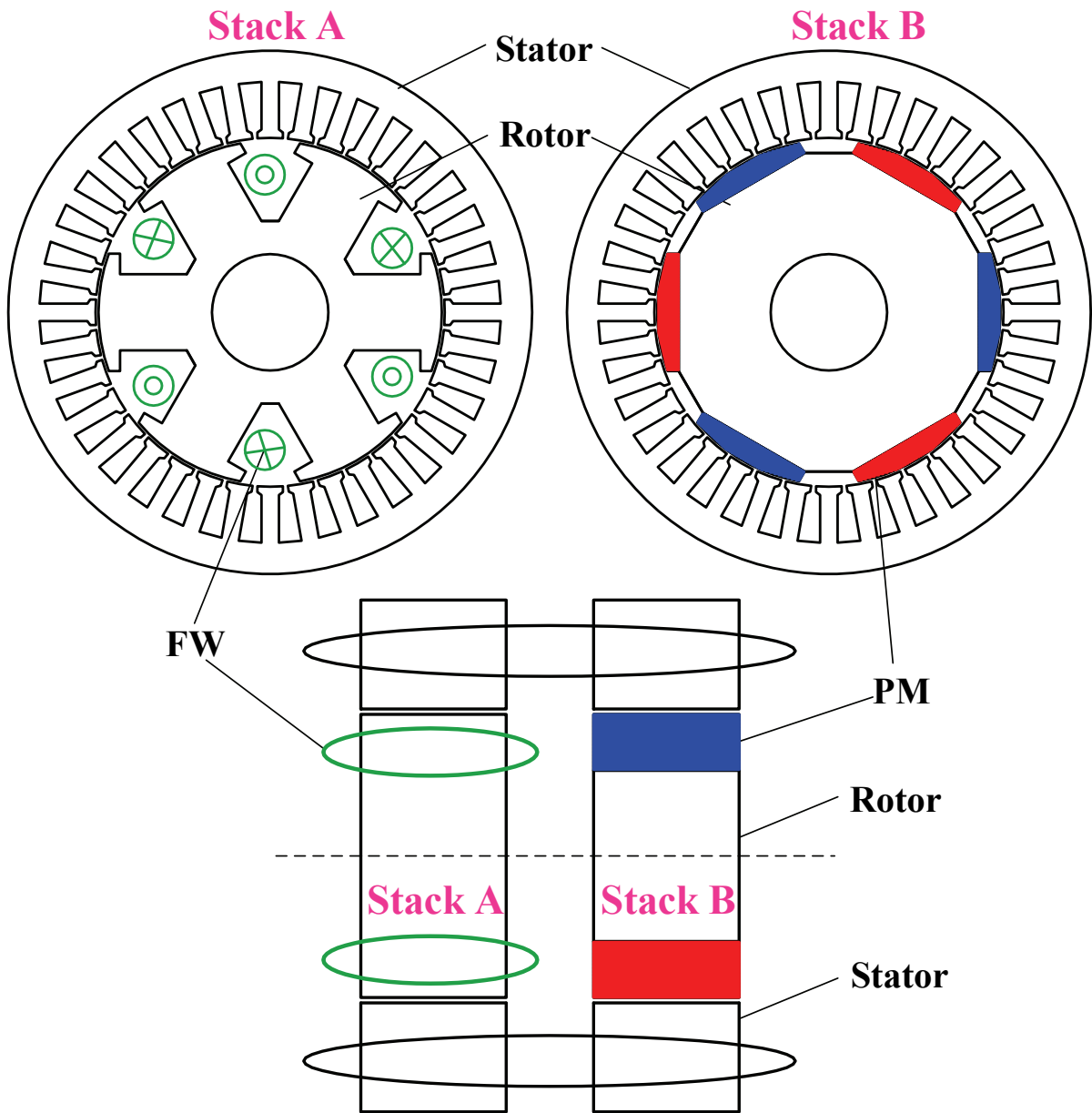


Fig. 1.12 Configuration of a dual-stack HE machine with EE rotor and PM rotor [SYV95].

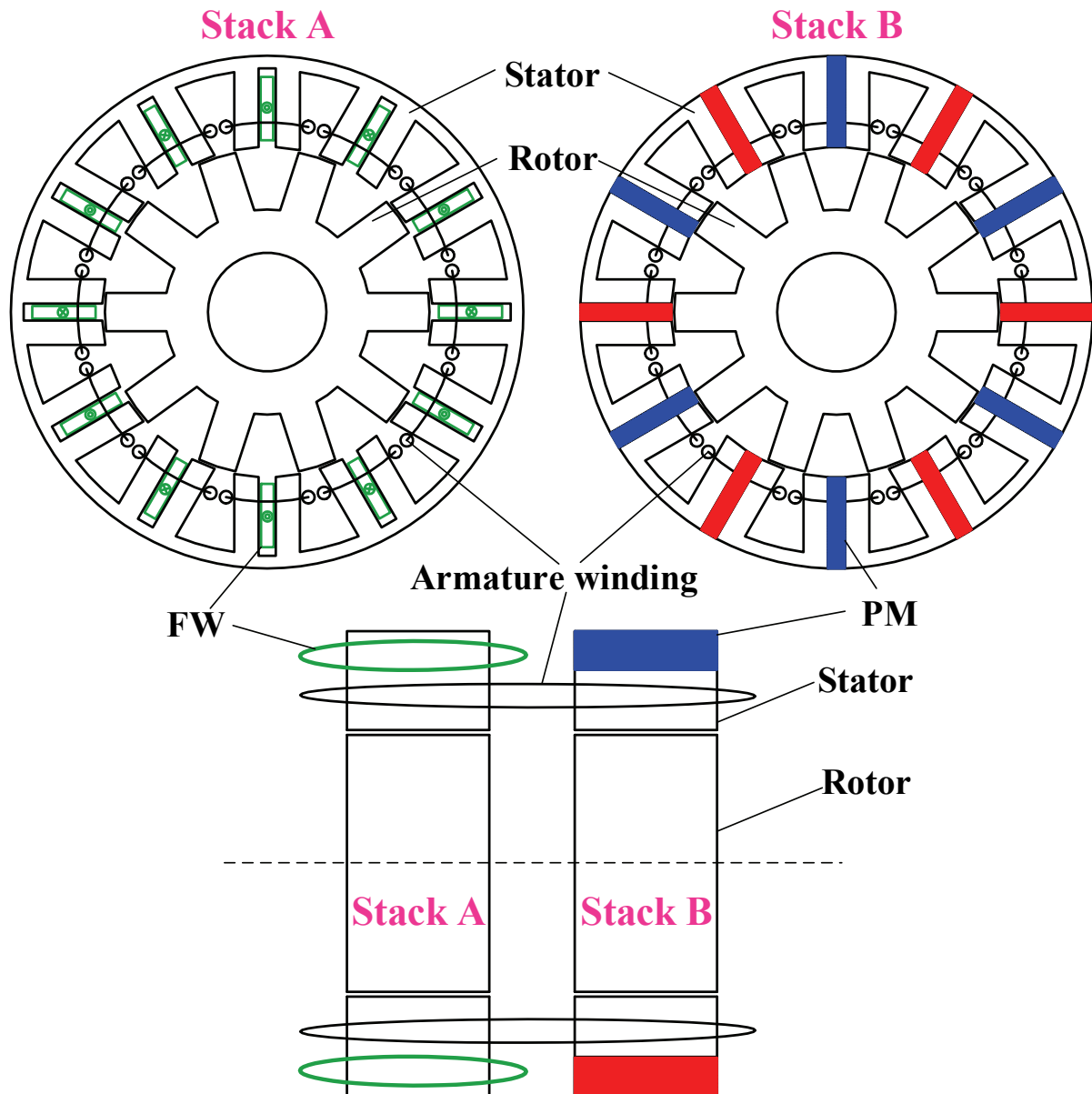


Fig. 1.13 Configuration of a dual-stack HE machine with EE stator and PM stator [WAN12].

1.3 Stator-PM Machines

Among the various HE machines introduced previously, the topologies based on the stator-PM machines characterized with the elimination of sliding contacts and the avoidance of complicated structures for 3-D flux, are excellent candidates for variable-speed applications. Therefore, the stator-PM based HE machines will be the focus of this thesis.

The stator-PM machines originate from the switched reluctance machine (SRM) that features a doubly salient structure, concentrated non-overlapping windings, robust rotor, and easy temperature management. The stator-PM machine was initially developed in [LAW52],

[RAU55], which features a single-phase configuration. By introducing the PMs into stator, the features of a SRM are inherited whilst the torque density and efficiency can be improved in the stator-PM machines. With the rotor rotating and the variation of magnetic permeance occurring, the flux linked by the armature windings due to the PM varies, although the PMs are physically stationary. Consequently, the back-electromotive force (back-EMF) is induced in the windings and the torque is generated with the current injected.

1.3.1 Conventional single-stator PM machines

The PM arrangement in the stator-PM machine is flexible, and thus various topologies have been proposed during past 20 years [ZHU11a], [CHE11c]. As the physical location between the armature coils and PMs is fixed, not only the bipolar flux but also the unipolar flux may occur in the armature coils, which is dependent on the PM arrangement. In general, the stator-PM machines can be classified into three groups as per PM positions:

- Doubly salient PM (DSPM) machines with PMs inserted in stator yokes (exhibiting unipolar flux)
- Flux reversal PM (FRPM) machines with PMs surface-mounted on stator teeth (exhibiting bipolar flux)
- Switched flux PM (SFPM) machines with PMs sandwiched in stator teeth (exhibiting bipolar flux)

A. DSPM machine

A stator-PM machine was presented in [LIA95], in which the PMs are inserted into the stator yokes of a SRM whilst all the other components of the SRM are inherited. This new machine topology is termed as a doubly salient PM (DSPM) machine. A developed three-phase 12-stator-slot/8-rotor-pole DSPM machine is illustrated in Fig. 1.14 [CHE00]. The four pieces of PMs are yoke-inserted, which span three stator teeth due to the three-phase configuration. Meanwhile, the concentrated non-overlapping armature windings are wound around each stator tooth and the salient rotor is free from copper and PM. Thanks to the stationary PMs and the rotation of the salient rotor, the flux linked by the armature coils varies periodically versus rotor position. However, it can be noted that each armature coil is excited by the PM asymmetrically, which results in unipolar coil and phase flux-linkages.

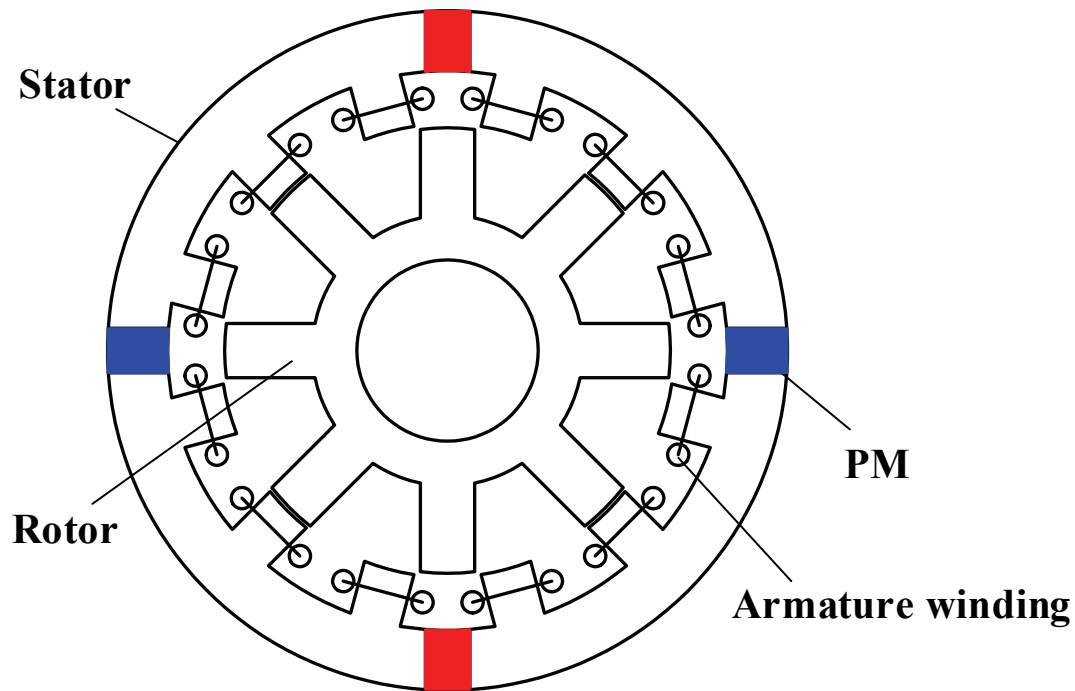


Fig. 1.14 Cross section of a 12-stator-slot/8-rotor-pole DSPM machine [CHE00].

B. FRPM machine

Another stator-PM structure, flux-reversal PM (FRPM) machine, was proposed in [DEO97], where a single-phase machine was firstly presented. In the FRPM machine, the radially magnetized PMs are surface-mounted on the stator teeth. Furthermore, the three-phase FRPM machines were developed and analysed in [WAN99], [WAN01]. A typical three-phase 12-stator-slot/10-rotor-pole FRPM machine is shown in Fig. 1.15, where the PMs that have opposite magnetization polarities are alternately surface-mounted on the stator teeth whilst the concentrated non-overlapping armature coils and a robust rotor are both inherited. As a pair of reversed PMs are mounted on each stator tooth and the symmetrical magnetic paths occur, the corresponding armature coil is excited by the PMs having opposite polarities periodically, which contributes to the bipolar coil and phase flux-linkages. The torque density can thus be improved [WAN99], [ZHA09], [CHE11c]. Moreover, thanks to the fact that the even order harmonics in coil flux-linkages can be cancelled [HUA08], the phase flux-linkage of the FRPM machine is more sinusoidal, which is beneficial to a smooth torque output. Besides, the stator-slot/rotor-pole combination of the FRPM machines is flexible [WAN99], [WAN01], [GAO16a], and the consequent-pole PM structure can be employed to save the PM usage volume and reduce the flux-leakage [GAO16b]. By introducing the concaves to the stator teeth or the flux barriers to the rotor poles, the flux-leakage can be further reduced [KIM04]. Both

the rotor shaping and the rotor paring technique with a pair of asymmetric rotor teeth are investigated to suppress the cogging torque [KIM05a], [KIM05b].

However, due to the surface-mounted PMs, the PM thickness contributes to the overall equivalent air-gap length. Therefore, the FRPM machine suffers a relatively high equivalent air-gap length and thus remarkable flux-leakages, which indicate the PM thickness should be designed carefully [BOL99]. In addition, the demagnetization withstand capability of the PMs is relatively poor in the FRPM machines, as the PM flux and the armature reaction flux are connected in series.

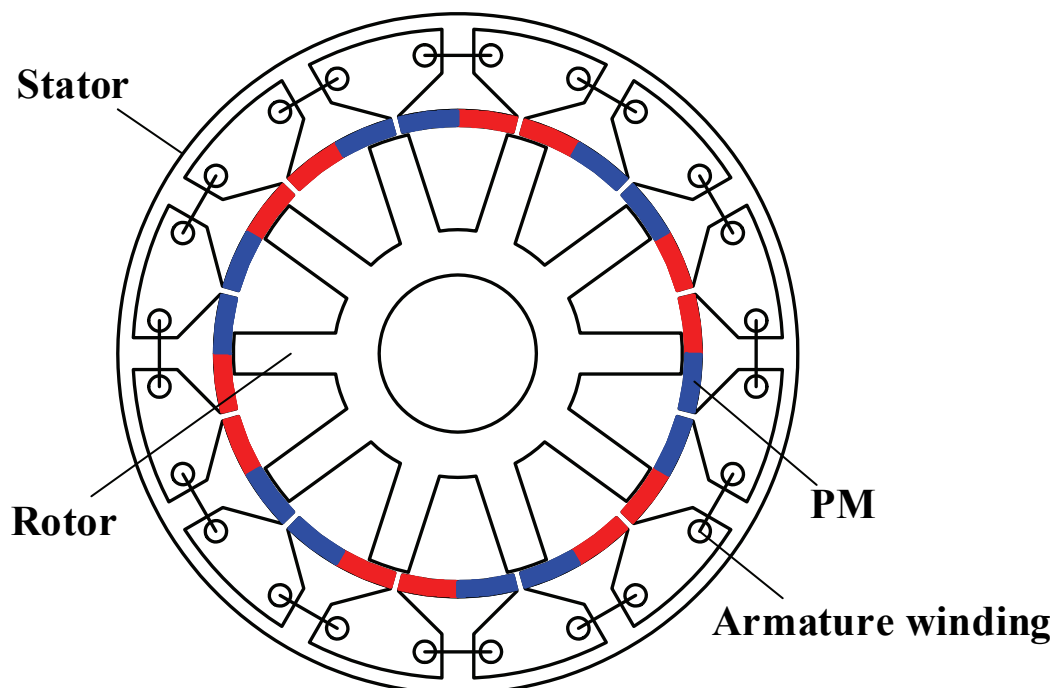


Fig. 1.15 Cross section of a 12-stator-slot/10-rotor-pole FRPM machine.

C. SFPM machine

A three-phase switched flux PM (SFPM) machine was proposed in [MAI87], [HOA97], in which the tangentially magnetized PMs are sandwiched in each stator tooth. A popular three-phase 12-stator-slot/10-rotor-pole SFPM machine is illustrated in Fig. 1.16 [HOA97], [ZHU05]. It can be seen here that the rotor is identical to that of the FRPM machine, and the concentrated non-overlapping armature windings are also inherited. The difference indicates that the PMs are tangentially magnetized and sandwiched inside the stator teeth, instead of the surface-mounted PMs in the FRPM machine. As with the FRPM machine, the SFPM machine features the symmetrical magnetic path for each armature coil and thus the bipolar coil and phase flux-linkages. The cancellation of the even order harmonics in coil flux-linkages is also

effective, which contributes to a sinusoidal phase flux-linkage [HUA08]. In addition, thanks to the tangentially magnetized PMs inserted into the center of the teeth, the PM usage volume can be boosted and the flux-focusing can be obtained. Therefore, the torque density of the SFPM machine is superior to its DSPM and FRPM counterparts [HUA05], [ZHA09], [ZHU11], [CHE11c]. Moreover, the demagnetization risk of the PMs is alleviated in the SFPM machines as the PM flux and the armature reaction flux are in parallel [ZHU05], [McF14]. Furthermore, the effects of the stator-slot/rotor-pole combination in the SFPM machines have been investigated [CHE10a], [CHE11d], which reveals that the 10-, 11-, 13-, 14-pole rotors are all feasible for the 12-stator-slot stator, and the different windings including the single-layer and double-layer configurations have been developed [CHE10b], [CHE10c], [OWE10b], [ZHU10]. Besides, the numbers of stator teeth and PMs can be halved in the SFPM machine to save the PM usage volume whilst maintaining torque output [ZHU10], [OWE10b], [CHE11d]. Meanwhile, the fault-tolerant teeth are introduced into the stator of SFPM machines to enhance the fault-tolerant capability [OWE10b], [CHE11e]. The modular stator technique can also be employed to further improve the fault-tolerant capability [HOA97], [TAR16]. The rotor shaping can be adopted to reduce the cogging torque in the SFPM machines as well [SIK15].

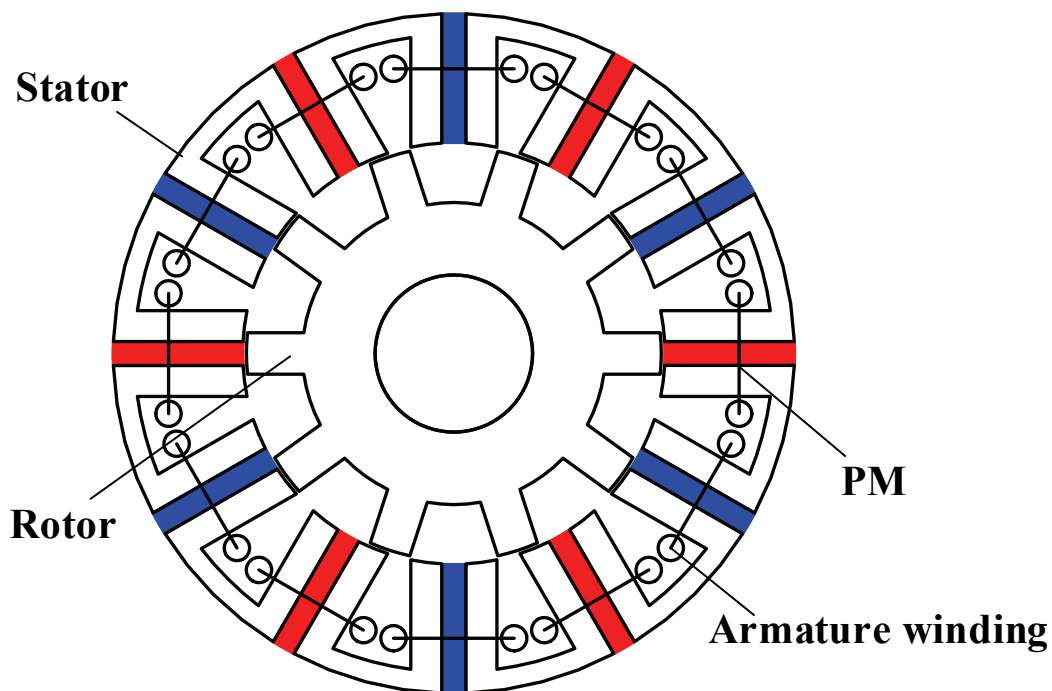


Fig. 1.16 Cross section of a 12-stator-slot/10-rotor-pole SFPM machine [ZHU05].

Although the SFPM machines are characterized with the sinusoidal flux-linkage and high torque density, they still suffer from a relatively large PM usage volume and severe magnetic

saturation in the stator [ZHU15a], as well as the space conflict between PMs, laminations, and armature windings [ZHU14a].

1.3.2 Partitioned-stator PM machines

To further improve the performance of the stator-PM machines, the partitioned stator (PS) technique was recently proposed [ZHU14a], [EVA15], in which the inner space of the conventional stator-PM machines is employed to relieve the crowded stator. In the PS machines, the two separate stators are adopted to accommodate the armature windings and excitation sources individually, while a rotor made of iron is sandwiched between the two stators. As a result, more space is available for PMs and/or coils, which is beneficial to torque density, whilst the PMs and windings are still stationary by inheriting the characteristics of the conventional stator-PM machines.

A. PS-DSPM machine

Based on the conventional DSPM machine illustrated in Fig. 1.14 and the PS principle, a three-phase 12-stator-slot/8-rotor-pole PS-DSPM machine is presented in Fig. 1.17 [WU15a]. The outer stator is equipped with 12 salient teeth, and wound with concentrated non-overlapping armature coils, whilst an inner stator is inserted with 4 pieces of tangentially magnetized PMs, and the PM center lines are aligned with the outer stator yokes. Meanwhile, a cup rotor consisting of iron pieces is sandwiched between the two stators. Compared with the conventional DSPM machine, the PS-DSPM machine inherits the identity of having yoke-inserted PMs with intervals of the phase number. However, their PMs are separated into the second stator and consequently the armature windings and PMs are partitioned. Therefore, the magnetic saturation is alleviated and space utilization is improved, which increases the torque density [WU15a]. Nevertheless, it should be noted that the PS-DSPM machine still presents the asymmetric magnetic paths and therefore the unipolar phase flux-linkages.

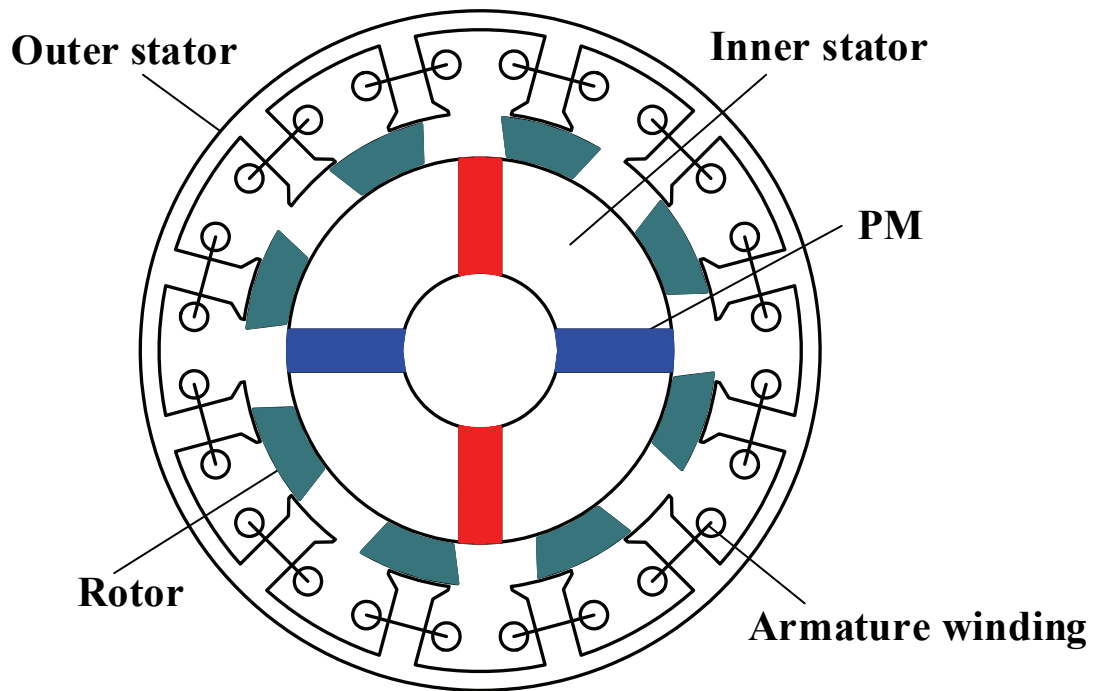


Fig. 1.17 Cross section of a 12-stator-slot/8-rotor-pole PS-DSPM machine [WU15a].

B. PS-FRPM machine

By applying the PS principle to the conventional FRPM machine in Fig. 1.15, the PS-FRPM machine is obtained. The cross section of a three-phase 12-stator-slot/10-rotor-pole PS-FRPM machine is presented in Fig. 1.18 [ZHU15b], where two stators accommodate concentrated non-overlapping armature windings and surface-mounted PMs respectively, whilst the cup-rotor is sandwiched between them. The PM number in the inner stator is equal to the tooth number in the outer stator, and the PM central lines are aligned with the outer stator yoke. Compared with the conventional machine, the space utilization is improved in the PS-FRPM machine, with which more PM and/or copper can be accommodated and magnetic saturation is reduced, both of which contribute to a higher torque density. Besides, the PM number is halved in the PS-FRPM machine as every two adjacent PMs having the identical polarity are unified as one single piece, which facilitates manufacturing. Moreover, features including the bipolar phase flux-linkages and the even order harmonics cancellation are inherited. It can be seen that the inner stator configuration in the PS-FRPM machine is identical to the rotor of a classic SPM machine [ZHU07b], which implies good manufacturability. More importantly, the armature reaction flux would not go through the PMs and thus the trade-off from PM thickness for torque output can be avoided [ZHU15b].

Different stator-slot/rotor-pole number combinations are investigated in [ZHU15b], and the 10-, 11-, 13- 14-pole rotors are all suitable for the 12-stator-slot outer stator. To reduce the PM usage volume, the consequent-pole inner stator can be adopted, in which the PM number is halved whilst the torque output is almost unchanged [WU15b], [WU16a]. Further, it is easy to find that the inner stator and outer stator are exchangeable, which is similar to the single air-gap machine. By exchanging the locations of armature windings and PMs, the torque density can be further improved in the PS-FRPM machine thanks to large PM usage volume, as well as the large diameter of air-gap [SHI17].

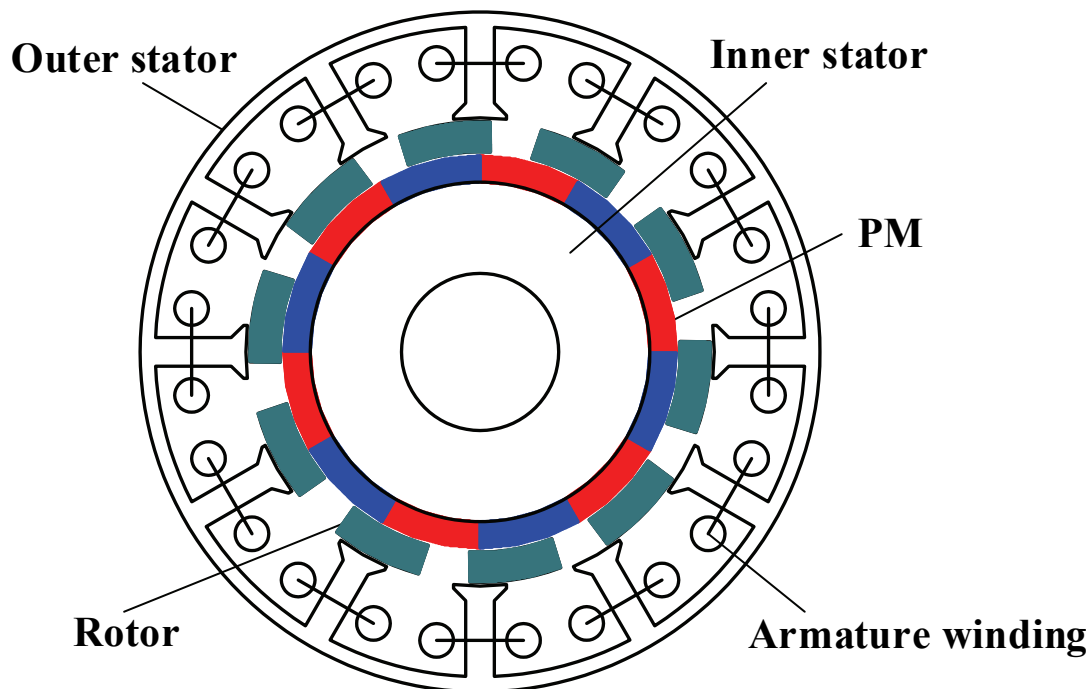


Fig. 1.18 Cross section of a 12-stator-slot/10-rotor-pole PS-FRPM machine [ZHU15b].

C. PS-SFPM machine

A three-phase 12-stator-slot/10-rotor-pole PS-SFPM machine combining the PS technique with the conventional SFPM machine, is illustrated in Fig. 1.19 [ZHU14a], [EVA15]. The concentrated non-overlapping armature windings are wound around the outer stator teeth and the tangentially magnetized PMs are located on the inner stator, with a cup-rotor sandwiched between the two stators. In this machine, the numbers of the stator teeth and the PMs are identical, and the PM center lines align to the outer stator teeth, i.e. the PM pole centers in the inner stator are aligned with the outer stator yokes. Compared with the conventional single air-gap SFPM machine, Fig. 1.16, the PMs are moved to a secondary stator, and thus separated from the windings. The phase flux-linkages in the PS-SFPM machine are also bipolar and free

from the even order harmonics. Meanwhile, thanks to the enlarged available space and the flux-focusing effect, the torque density is increased in the PS-SFPM machine. The stator-slot/rotor-pole combinations in the PS-SFPM machine are also flexible, and the 10-, 11-, 13-, 14-pole rotors are all feasible. In addition to the double-layer armature winding configurations, the single-layer armature windings are also available and they can exhibit slightly higher torque output as well as better fault-tolerance [EVA15]. Besides, it is revealed that the PM pieces number can be halved with the constant outer stator teeth number, in which the PM usage volume is greatly reduced and thus the torque per PM volume is boosted [AWA16].

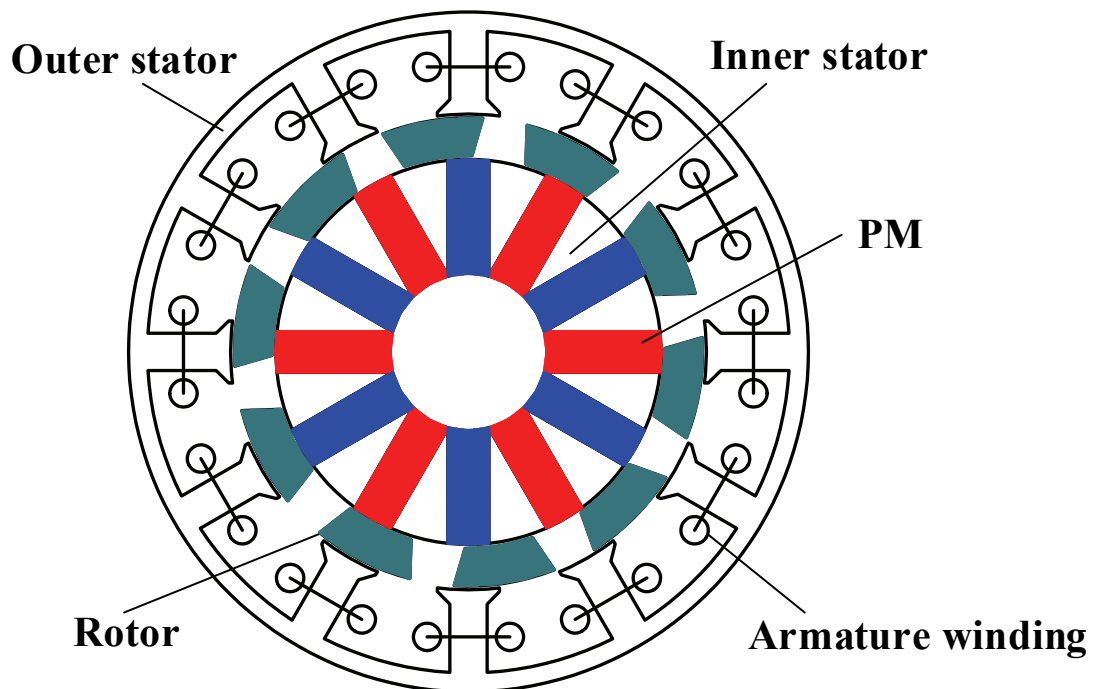


Fig. 1.19 Cross section of a 12-stator-slot/10-rotor-pole PS-SFPM machine [ZHU14a].

1.4 Research Scope and Contributions

1.4.1 Scope of research

The introduction is concerned mainly with HE machines, and the merits of the stator-PM based HE machines are identified. The development of the stator-PM machines is then reviewed and it is confirmed that the PS technique can alleviate the space conflict in the stator-PM machines and thus improve performance. Therefore, the PS-HE machines are proposed and investigated, which inherit the advantages of stator-PM based HE machines while also benefiting from enlarged available space.

The research reported in this thesis mainly focuses on the following aspects:

- 1) Firstly, the PS machines with different PM topologies on the inner stator (excitation stator) are investigated, and their characteristics are summarized.
- 2) Then, the PS machines with different PM materials are evaluated and compared.
- 3) Based on the conventional SFPM machine and the principle of PS machines, a HE machine employing an inner stator to accommodate FWs is evaluated. Meanwhile, a PS-HESF machine, based on the PS-SFPM machine but adopting FWs on the inner stator, is investigated. The difference between these two topologies is the PM locations.
- 4) A pair of PS-HE machines based on the PS-FRPM configuration are presented by allocating the FWs to the inner stator, which feature series and parallel connection between PMs and FWs, respectively.

The research structure and methodologies of the thesis are summarized in Fig. 1.20. The major PS-HE machine topologies proposed and investigated in the thesis are presented in Fig. 1.21.

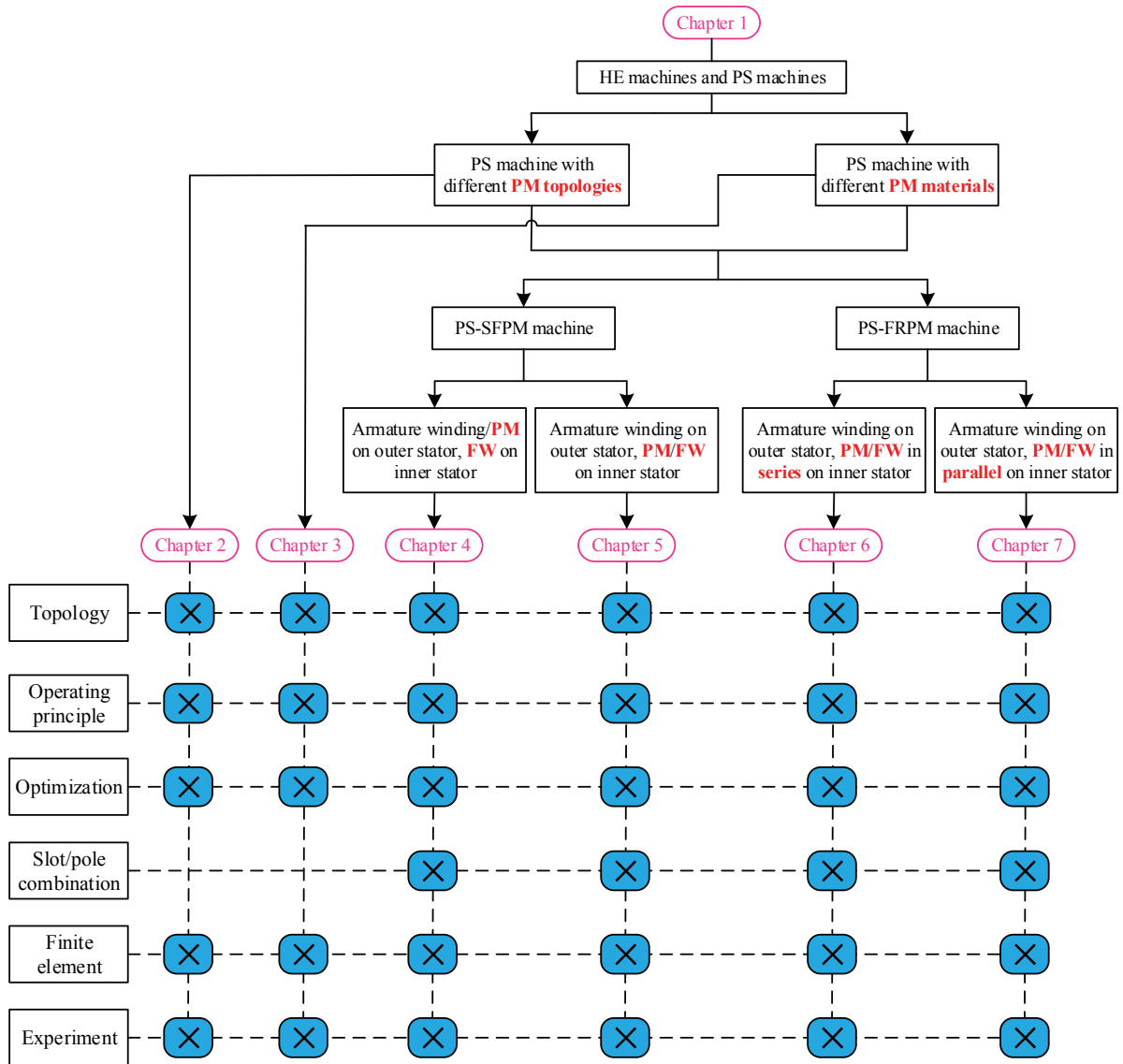
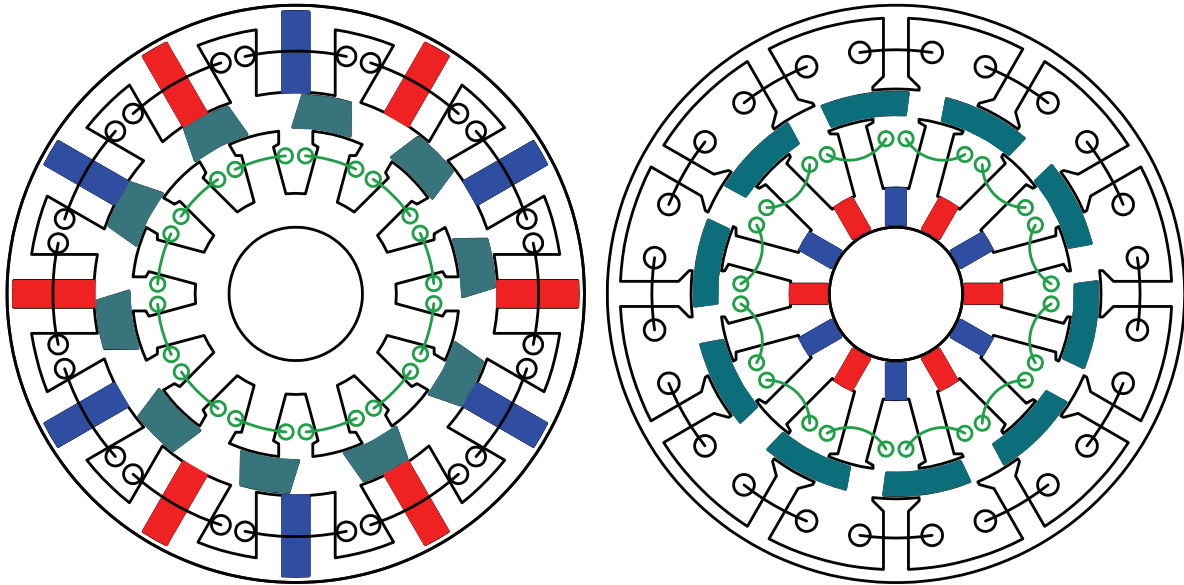
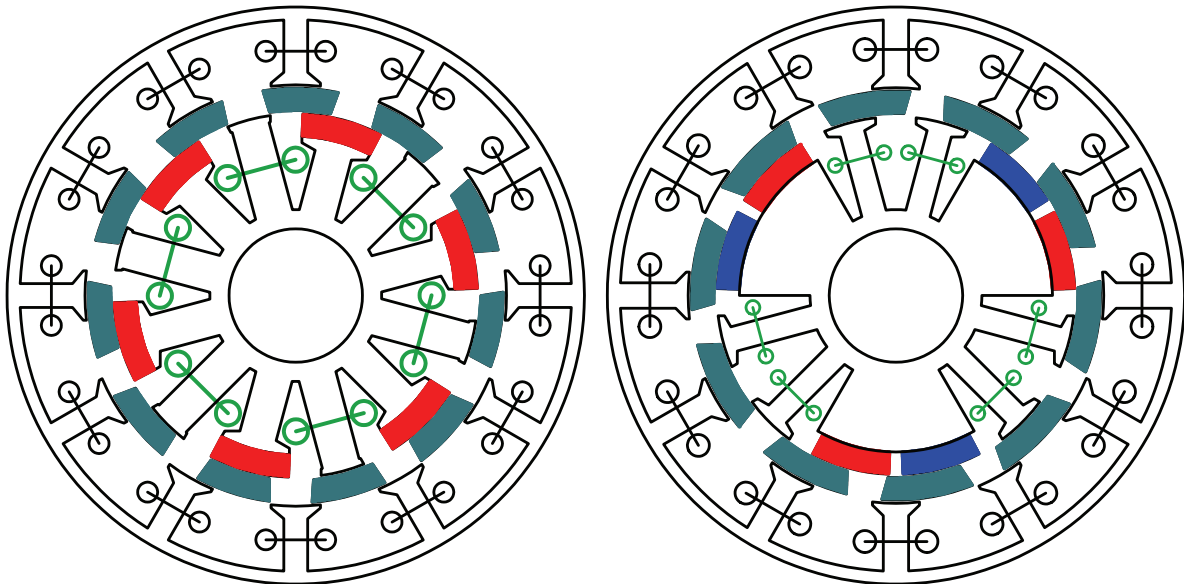


Fig. 1.20 Illustration of the scope and contributions of the thesis.



(a) DS-HESF, Chapter 4

(b) PS-HESF, Chapter 5



(c) Series PSHE, Chapter 6

(d) Parallel PSHE, Chapter 7

Fig. 1.21 Configurations of the proposed PS-HE machines in the thesis.

The contents of the subsequent chapters are summarised as follows:

Chapter 2

In this chapter, the existing PS-SFPM and PS-FRPM machines are proved to inherently share the same operating principle and similar machine topology as each other but with interior PM (IPM) and surface-mounted PM (SPM) stators, respectively. Then, two novel excitation stators with different PM configurations are proposed to extend the family of PS machines. Based on that, four globally optimized PS machines with different inner stator topologies are compared

in terms of back-EMF, cogging torque, electromagnetic torque, torque per PM volume and flux-weakening capability. The results reveal that the spoke-shaped IPM (IPM-spoke) inner stator exhibits the highest back-EMF and hence the highest average torque. The I-shaped IPM (IPM-I) inner stator has the best flux-weakening capability. The V-shaped IPM (IPM-V) produces the highest torque per PM volume. Furthermore, four machines are re-designed with the same PM usage volume, and the results show that the PS-SFPM machine still exhibits the highest back-EMF as well as the highest torque, although with sacrificed advantages.

Chapter 3

In this chapter, the potential of employing low-cost ferrite PMs in PS-SFPM machines is presented to address the problem of large PM usage volume and thus reduce material cost, which is attractive for the cost-sensitive applications. The ferrite PS-SFPM machine takes advantage of larger available space whilst balances the performance and cost. A pair of PS-SFPM machines equipped with NdFeB and ferrite PMs respectively are firstly evaluated and compared, where the ferrite one has much higher torque per cost. Furthermore, to better illustrate machine performance, the classic Toyota Prius2010 IPM machine is set as a baseline, and the corresponding NdFeB and ferrite PS-SFPM machines are optimized again. The results reveal that the NdFeB PS-SFPM machine has higher torque density than the Prius2010 IPM machine but it is more expensive, while the ferrite PS-SFPM machine can significantly reduce the cost and still exhibit good performance. The demagnetization behavior of the ferrite PS-SFPM machine is evaluated and a new method to improve the demagnetization withstand capability is proposed. Moreover, the mechanical analysis is conducted for the cup-rotor of the PS-SFPM machines.

Chapter 4

In this chapter, based on the conventional SFPM machine and the PS principle, a dual stator (DS) HE-SF (DS-HESF) machine is presented, which employs a secondary stator to specifically accommodate the FWs. The DS-HESF machine inherits the feature of the rotor that is free from PM and copper, and benefits from better space utilization. The topology and operating principle of the proposed machine are introduced in detail, and the effects of stator-slot/rotor-pole combinations are discussed. Based on two-dimensional (2-D) finite element (FE) analysis, the comparison between DS-HESF machines having different rotor-pole numbers is carried out, together with a conventional HESF machine as a baseline. The results show that

the DS-HESF machines exhibit not only higher torque density but also better flux regulation capability.

Chapter 5

In this chapter, the HE concept is applied to the PS-SFPM machine, and therefore a PS-HESF machine is obtained. The FWs and the tangentially magnetized PMs are both located in the inner stator, while the armature windings are placed on the outer stator, with the rotor sandwiched between the two stators. The operation principle of the PS-HESF machine is introduced and different stator-slot/rotor-pole combinations are included. The comparison results based on 2-D FE analysis reveal that the proposed PS-HESF machines can exhibit better flux controllability and higher torque density than the conventional counterpart. Moreover, the effects of the key design parameters on hybridization ratio are investigated, which indicates that the design of the PS-HESF machine is quite flexible and depends on the requirements for a specific application.

Chapter 6

In this chapter, a novel PSHE machine is proposed based on the existing PS-FRPM machine, in which the radially magnetized PMs and the FWs are alternately located in the inner stator poles. As a result, the consequent-pole is obtained in the inner stator whilst the PM flux and the FW flux are connected in series. The operation principle of the proposed series PSHE machine is introduced, with specific attention paid to explain the rules about the stator-slot/rotor-pole combinations for the symmetrical phase flux-linkages. It is revealed that the 12-stator-slot/11-rotor-pole and 12-stator-slot/13-rotor-pole machines can benefit from the phase flux-linkages free from even order harmonics while the 12-stator-slot/10-rotor-pole and 12-stator-slot/14-rotor-pole counterparts suffer significant harmonics in the phase flux-linkages. Moreover, thanks to the consequent-pole configuration, the PM usage volume in the proposed machines is reduced whilst the flux regulation capability is enhanced.

Chapter 7

In this chapter, a PSHE machine with parallel connection between the PM flux and the FW flux is presented by carefully adjusting the FWs and the PMs in the inner stator. The FW pole-pairs and the PM pole-pairs are alternately placed in the inner stator, and therefore the FW flux and the PM flux can loop individually. The electromagnetic performance of the proposed parallel PSHE machines with different stator-slot/rotor-pole combinations is evaluated. It is

found that the 12-stator-slot/10-rotor-pole and 12-stator-slot/14-rotor-pole machines have much lower harmonics in the phase flux-linkages. Moreover, the flux regulation capabilities are excellent in the parallel PSHE machines thanks to the parallel connections between the two kinks of fluxes.

Chapter 8

This chapter includes the general conclusions of the thesis and potential future work in this research area.

1.4.2 Contributions

The contributions of this thesis can be summarised as follows:

- The PS machines with different PM topologies on the inner stator are analyzed and compared to reveal their merits and demerits, which provides a guide to the design of PS machines.
- The PS machines with different PM materials are evaluated and compared, in which the machine with rare-earth free ferrite PM is presented, offering a solution to the cost-sensitive applications.
- Based on the PS principle, two HE machines having armature windings on the outer stator, FWs on the inner stator, and PMs either on the outer stator or inner stator, are proposed and investigated. The advantages of the stator-PM based HE machines are combined with the excellent space utilization of the PS machines.
- By investigating a pair of PS-HE machines originating from the PS-FRPM machine, which have series and parallel connections respectively, the key features of the two connections are demonstrated.

Chapter 2. Partitioned Stator Permanent Magnet Machines with Different Magnet Topologies

With the partitioned stator (PS) technique, the conventional stator-PM machines can be transformed to the PS machines to improve space utilization and electromagnetic performance. Recently, the PS-DSPM [WU15a], PS-FRPM [ZHU15b] and PS-SFPM [EVA15] machines were presented and analysed, and it is revealed that the PS-FRPM and PS-SFPM machines benefit from bipolar flux-linkage and higher torque densities. In this chapter, the PS-FRPM and PS-SFPM machines are investigated, and they are proved to naturally share the same operating principle and similar machine topology but with SPM and IPM configurations, respectively. Furthermore, the inner stator topologies of the PS machines are extended by employing new PM configurations. Moreover, four PS machines with different PM topologies including SPM, I-shaped IPM (IPM-I), V-shaped IPM (IPM-V) and spoke-shaped IPM (IPM-spoke) are evaluated and compared. The results reveal that the IPM-spoke inner stator exhibits the highest average torque due to the largest PM usage volume, while the IPM-I stator has the best flux-weakening capability and the IPM-V stator produces the highest torque per PM volume.

This part has been published in IEEE Transactions on Industry Applications.

2.1 Introduction

The conventional stator-PM machines benefit from robust structure, easy temperature management and excellent reliability etc. [ZHU11a], [CHE11c]. However, their stators are quite crowded with both windings and PMs, whilst the rotor inner space is not fully utilized [CAO12], [FAS14]. Therefore, the concept of PS is proposed [EVA15], in which two separate stators are employed to accommodate coils and PMs respectively, whilst a rotor consisting of iron-pieces is sandwiched between the stators. As a result, more space is available for armature windings to reduce the copper loss as well as for PMs to provide more freedom for PM usage and configurations, which are beneficial to the efficiency and torque density. Compared with the conventional dual stator PM machines presented in [NIU07], [LIU12], [LI14], the PS machines have simple and robust rotor that is free from PMs and windings, which still inherit the benefits of stator-PM machines. Besides, since armature windings and PMs are separately placed on the two stators, it is attractive for temperature management, which is superior to the

dual stator switched flux PM (SFPM) machine directly employing two identical stators [ZON14], [KIM16a].

Based on the conventional FRPM and SFPM machines, the PS-FRPM and PS-SFPM machines are proposed in [ZHU15b] and [EVA15] respectively. In this chapter, the operating principles of the PS-FRPM and PS-SFPM machines are identified, and they inherently belong to the same machine type whilst the differences are only on the PM excitation stator. Further, as the topology of PM excitation stator is similar to the rotor of classic rotor-PM synchronous machines, the rotor structure of rotor-PM synchronous machines can be applied into the PM excitation stator of PS machines. Consequently, two additional PS machines having different PM excitation stators are presented. With the same overall active dimensions and operating conditions, four globally optimized PS machines with distinct PM excitation stators are compared to identify their merits and drawbacks.

The purpose of this chapter is to establish the relation between the existing PS machines and further extend the machine topologies. In section 2.2, the operating principles of PS-FRPM and PS-SFPM machines are investigated, and the novel PS machines with I-shaped IPM (IPM-I) and V-shaped IPM (IPM-V) inner stators are introduced. The influences of key geometric parameters of PS-IPM-I and PS-IPM-V machines are specified in section 2.3. Then, in section 2.4, four globally optimized PS machines are comprehensively compared based on 2-D FE analysis. In section 2.5, four PS machines are re-designed to employ the identical PM usage volume, and the comparison is carried out to further illustrate their characteristics. Finally, four prototypes are fabricated and experimentally validated to confirm the analyses.

2.2 PS Machines Operating Principle and New PM Topologies

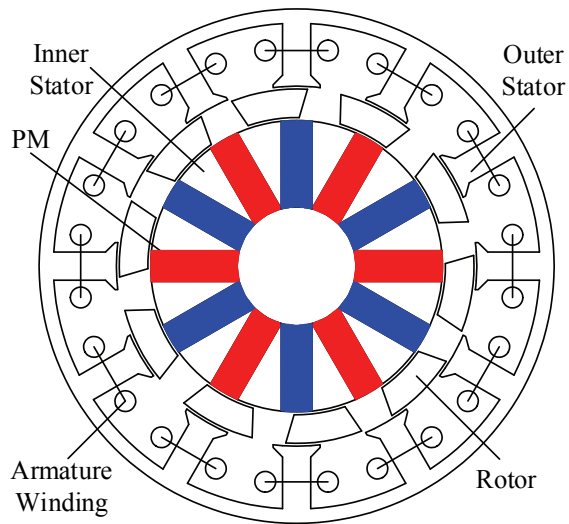
A three-phase 12/10 stator-slot/rotor-pole PS-SFPM machine is illustrated in Fig. 2.1(a), in which the tangentially magnetized PMs in stator teeth are moved to a secondary stator physically separated from the original one, while the concentrated non-overlapping armature windings are still located on the original stator [EVA15]. The pole number in the secondary stator is the same as the tooth number in the original stator. Meanwhile, the center lines of the PMs in the secondary stator are aligned to the original stator teeth. The original stator works as outer armature windings stator while the secondary stator works as inner PM excitation stator. The salient rotor only comprising laminations is sandwiched between the two stators to generate the change of magnetic permeance and hence the variation of flux-linkage. Although

the structure of PS-SFPM machine is more complicated compared with the conventional one, they still share the same operating principle, while the PMs are still stationary. Moreover, with this PS method, the space confliction between armature windings and PMs in the conventional SFPM machine is solved. Nevertheless, the PS-SFPM machines suffer dual air-gap and thus more complicated structure, in which the cup-rotor may degrade the mechanical strength. In addition, the heat dissipation of the cup-rotor would be challenging as it is surrounded by two layers of air-gaps although it consists of salient iron pole pieces only.

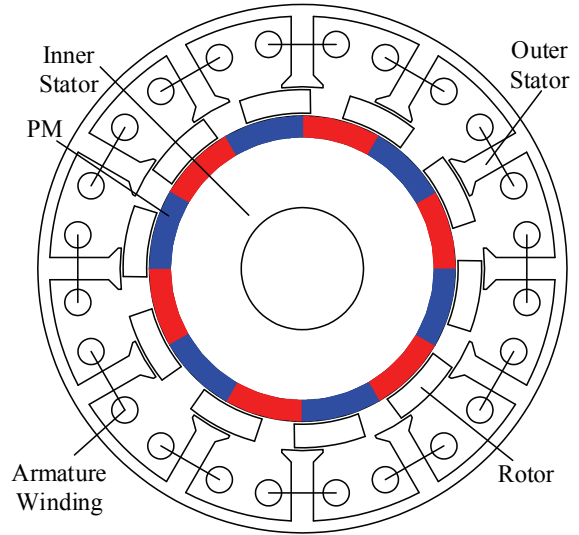
Fig. 2.1(b) illustrates a 12/10 PS-FRPM machine, in which the PMs mounted on the surface of stator teeth are moved to a secondary stator and the center lines of the PMs are aligned to the center lines of the original stator slots [ZHU15b]. In addition to the larger space for copper and PMs, the number of PMs is halved since the adjacent PMs having same polarity can be combined together as one, improving manufacturability.

It is evident that the PS-SFPM and PS-FRPM machines have same machine topologies except with IPM and SPM stators, respectively. As shown in the open-circuit field distributions, Fig. 2.2(a) and (b), the two machines have similar flux paths. Further, their open-circuit radial flux densities on the outer air-gap are shown in Fig. 2.3, in which the waveforms of the PS-SFPM and PS-FRPM machines are similar although the PS-SFPM machine has higher amplitude due to flux-focusing effect. As a consequence, the effects of inner PM excitation stator combined with the rotor on the armature windings are identical in the two machines, resulting in similar variations of flux-linkages generated by PMs.

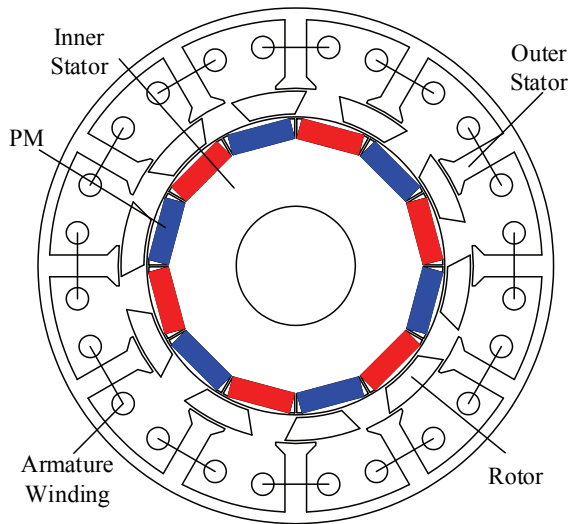
In fact, it is easy to note that the PM excitation stator of the PS-SFPM machine is similar to the spoke-shaped IPM (IPM-spoke) rotor of the conventional rotor-PM synchronous machine, whilst the PM excitation stator of the PS-FRPM machine is similar to the SPM rotor. The PS-SFPM and PS-FRPM machines can be intrinsically classified as one machine type, only with difference in PM configurations, i.e. IPM and SPM respectively, on the PM excitation stator.



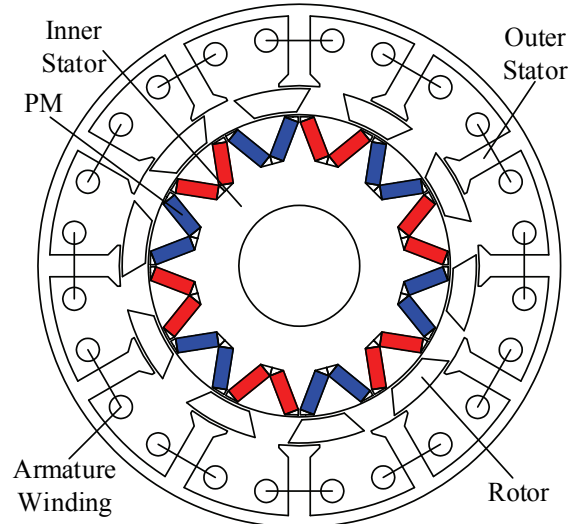
(a) PS-SFPM machine (PS-IPM-spoke)



(b) PS-FRPM machine (PS-SPM)

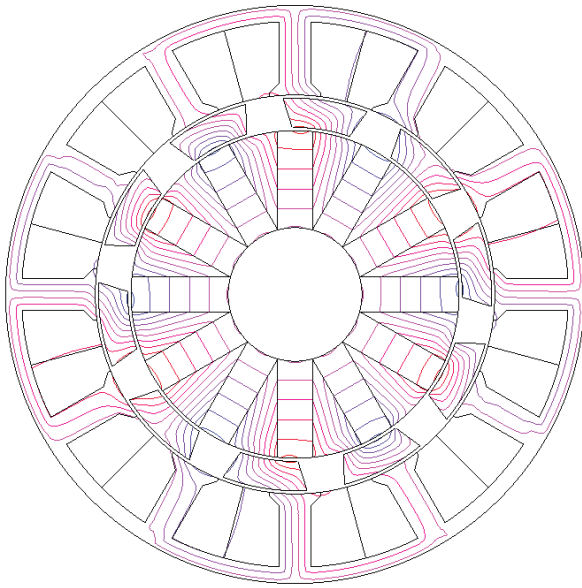


(c) PS-IPM-I machine

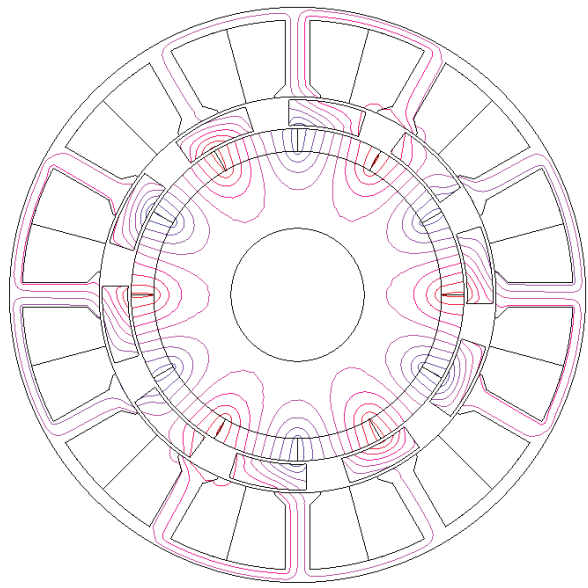


(d) PS-IPM-V machine

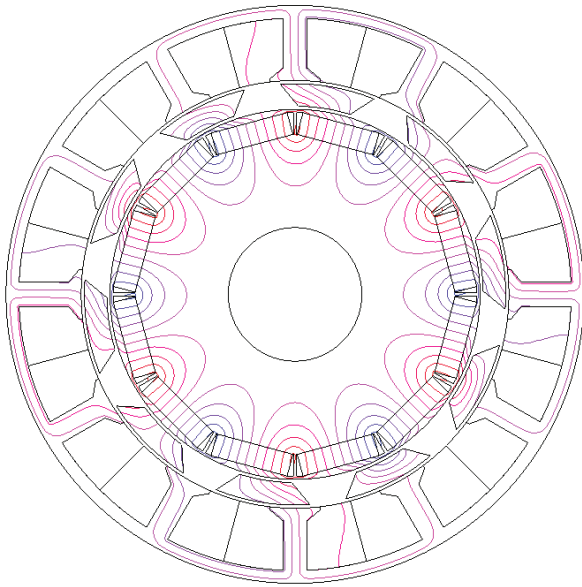
Fig. 2.1 Cross sections of different 12/10 PS machines



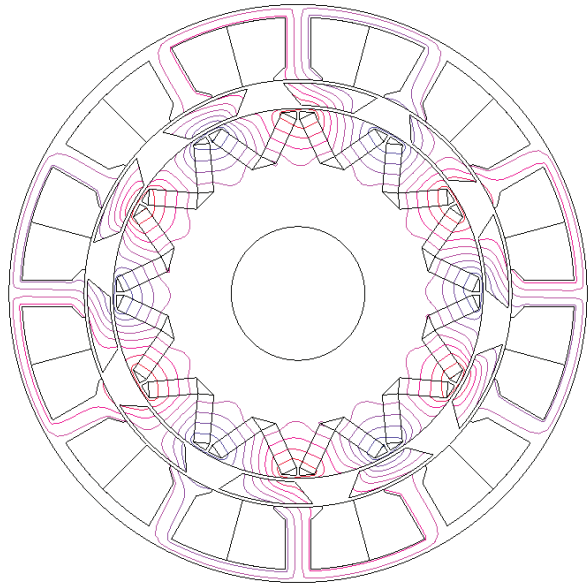
(a) PS-SFPM machine (PS-IPM-spoke)



(b) PS-FRPM machine (PS-SPM)

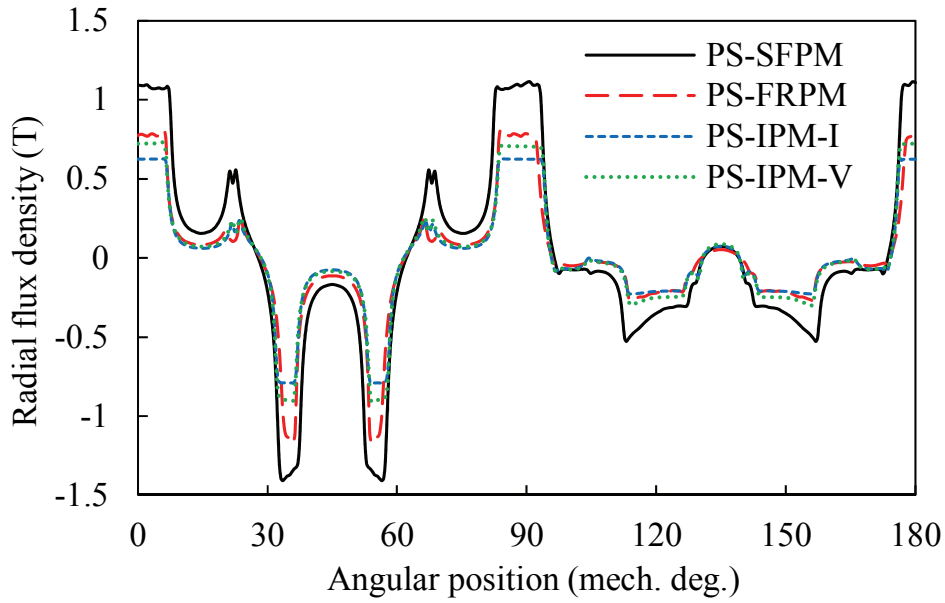


(c) PS-IPM-I machine

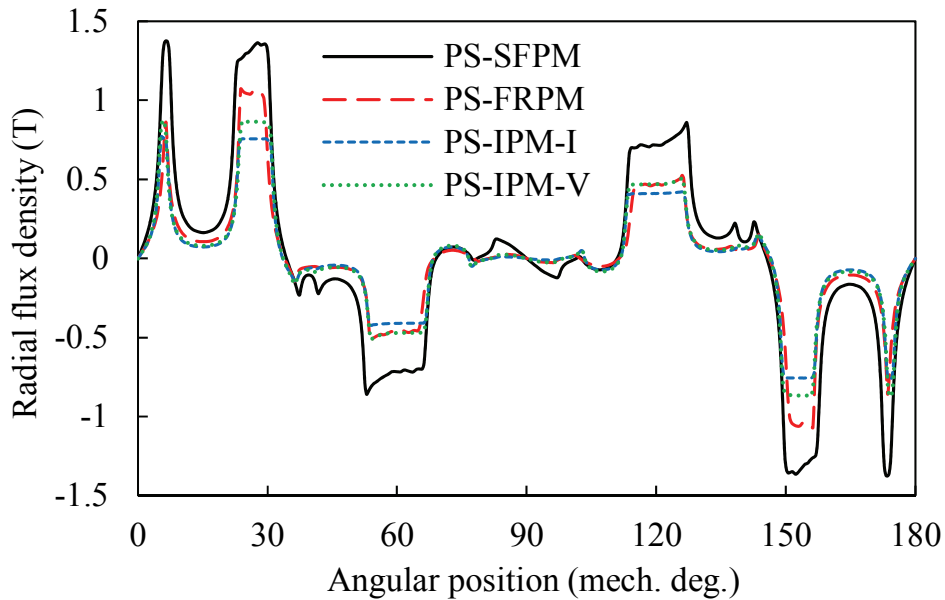


(d) PS-IPM-V machine

Fig. 2.2 Open-circuit field distributions of different 12/10 PS machines.



(a) At d -axis rotor position



(b) At q -axis rotor position

Fig. 2.3 Open-circuit radial flux density waveforms on the outer air-gap.

As the rotor structures in conventional rotor-PM synchronous machines are diverse with different PM arrangements, the topologies of PM excitation stator in PS machines can be extended as well. Applying the parallel magnetized I-shaped IPM on inner stator while keeping others the same, the PS-IPM-I machine can be obtained as in Fig. 2.1(c). The PMs are inserted inside the inner stator and surrounded by iron, which would contribute to better flux-weakening performance and demagnetization withstand capability [JAH86], [WEL03]. The open-circuit field distributions are illustrated in Fig. 2.2(c), which exhibit similar flux paths as the

aforementioned PS machines. The radial flux densities on the outer air-gap of the PS-IPM-I machine are shown in Fig. 2.3 as well, in which the similar waveforms but lower amplitude can be observed.

Furthermore, to achieve flux-focusing effect, the V-shaped IPM (IPM-V) structure is employed, as shown in Fig. 2.1(d), in which two pieces of parallel magnetized PMs are placed in one pole with a specific incline angle δ_{PM} . The rotor, outer stator and armature windings are all the same with the previous three machines. Its open-circuit field distributions shown in Fig. 2.2(d) and radial air-gap flux densities shown in Fig. 2.3 reveal that the PS-IPM-V machine has similar flux-linkage variation as others. In fact, the IPM-spoke structure is an extreme case of the IPM-V topology, if the PM incline angle is very large and two adjacent PM pieces belonged to different poles are combined together.

The four PS machines presented in Fig. 2.1 belong to one machine type since they have similar topologies, i.e. same outer stators, armature windings, rotors and pole number in inner stators, and follow the identical operating principle, i.e. the interaction between the field produced by the inner stator modulated by the rotor and that produced by the outer stator. In the following section, the advantages and disadvantages of each machine will be summarized.

2.3 Influence of Key Parameters in Machines with New PM Excitation Stators

The influences of several key design parameters of the PS-IPM-I and PS-IPM-V machines are investigated in this section, based on which the new machines can be optimized. The geometric parameters are analyzed with the identical conditions of 25mm axial length, 90mm outer diameter, and 20W copper losses in armature windings. The zero d -axis current control strategy is employed since the reluctance torque is negligible. The armature winding copper loss P_{cu} can be calculated as:

$$P_{cu} = 3I_a^2 \cdot R_a = \frac{2N_s \cdot I_a^2 \cdot \rho_{cu} \cdot N_{ac}^2 \cdot l_a}{S_a \cdot k_{pf}} \quad (2.1)$$

where I_a is the phase current, N_s , N_{ac} , l_a , S_a , k_{pf} , ρ_{cu} represent the stator slot number, the number of turns in armature coil, the active axial length, the slot area for coil side, the slot package factor and the electrical resistivity of copper, respectively. The slot package factor is always kept at 0.5 in the corresponding machines. In addition, it should be noted that the skin effect and proximity effect of the conductors on the armature winding copper loss are not taken into

account. This constraints on copper loss is more favorable in the design of machines for low speed applications since the iron loss, together with the skin effect and proximity effect, would not contribute to the major loss component.

The key design parameters of the PS-IPM-V machine are illustrated in Fig. 2.4 and those of the PS-IPM-I machine are similar but without PM incline angle δ_{PM} . The split ratio γ is defined as:

$$\gamma = \frac{R_{osi}}{R_{oso}} \quad (2.2)$$

where R_{osi} and R_{oso} are the inner and outer radius of outer stator respectively.

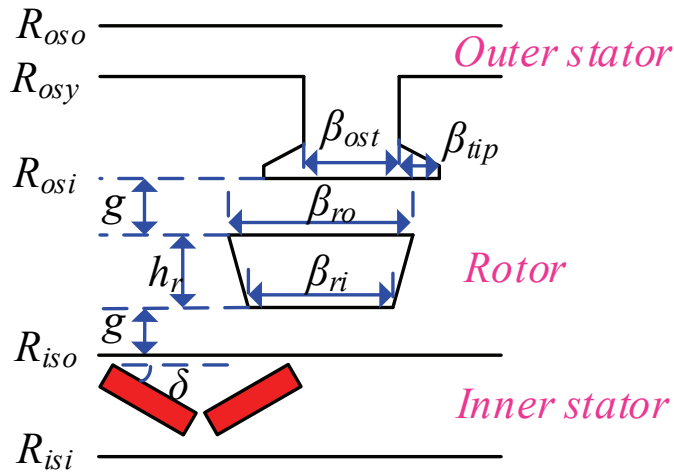


Fig. 2.4 Illustration of key geometric parameters of PS-IPM-V machine.

For a PS-IPM-V machine, the larger δ_{PM} would contribute to a higher torque due to better flux-focusing effect, but PM volume increases and the PM usage efficiency (ϵ , torque per PM volume) would decline [EVA10], [WU10], [ZHA15a]. Thus, the design of PS-IPM-V machine is flexible and PM incline angle should be investigated with the consideration of PM usage efficiency. Fig. 2.5 shows the average torque and torque per PM volume variations versus incline angle under different split ratios, in which torque increases continuously while ϵ reaches maximum value when δ_{PM} is around 40° and tends to drop dramatically after angle exceeds 50° . Consequently, by compromising the torque and ϵ performance, $\delta_{PM}=50^\circ$ is chosen as the preferred value for PS-IPM-V machine and further analyses are conducted.

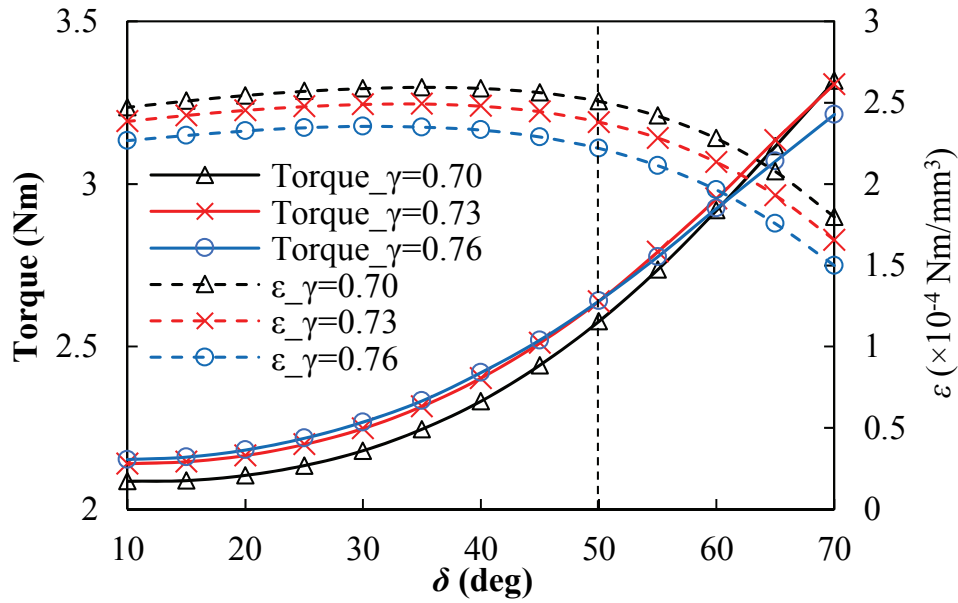


Fig. 2.5 Torque and PM usage efficiency variations with PM incline angle under different split ratios of PS-IPM-V machine.

Afterwards, the relations between average torque and a variety of geometric parameters of the PS-IPM-I and PS-IPM-V machines are investigated. The split ratio γ affects the balance between PM flux-linkage and electric loading, as higher γ provides larger available space for PMs as well as larger air-gap diameter while the lower γ offers larger slot area for armature windings. The average torques versus different γ of the PS-IPM-I and PS-IPM-V machines are shown in Fig. 2.6, in which the torque values both increase firstly but then descend when γ is very high. The optimal values for the two machines are both around 0.75.

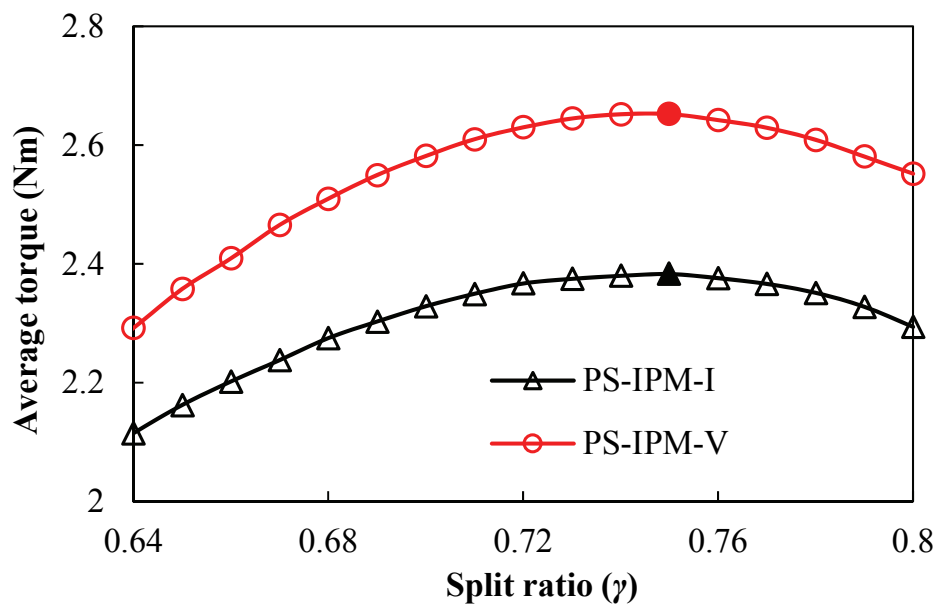


Fig. 2.6 Average torque versus different split ratios.

The average torque versus outer stator tooth pole arc β_{ost} is shown in Fig. 2.7, in which 6.5° is approximately the best values for both PS-IPM-I and PS-IPM-V machines since larger teeth would significantly reduce the available slot area and smaller teeth have to suffer severe saturations. Fig. 2.8 shows the relation between average torque and outer stator tip arc β_{tip} . The optimal values for the PS-IPM-I and PS-IPM-V machines are around 3° and 3.5° respectively.

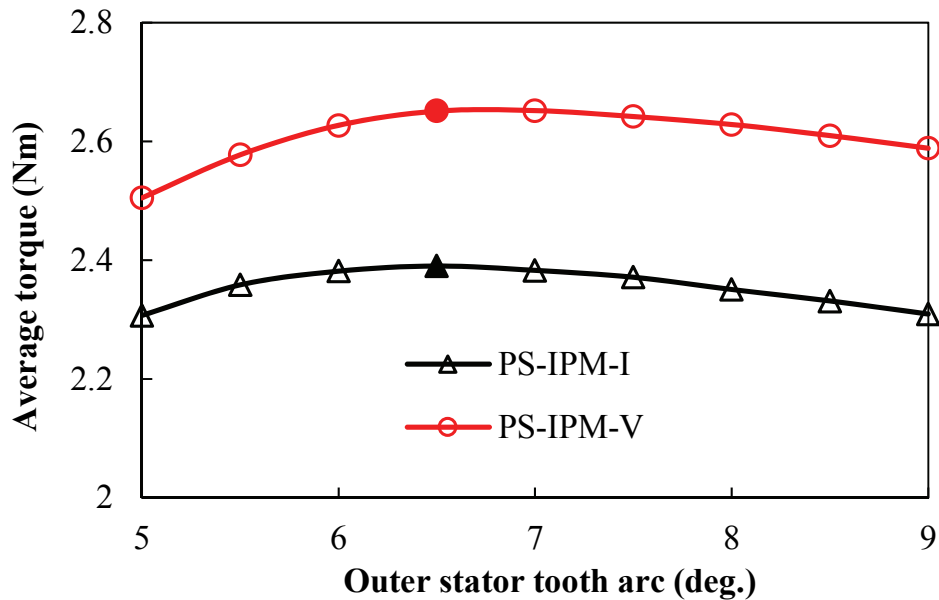


Fig. 2.7 Average torque versus different pole arcs of outer stator teeth.

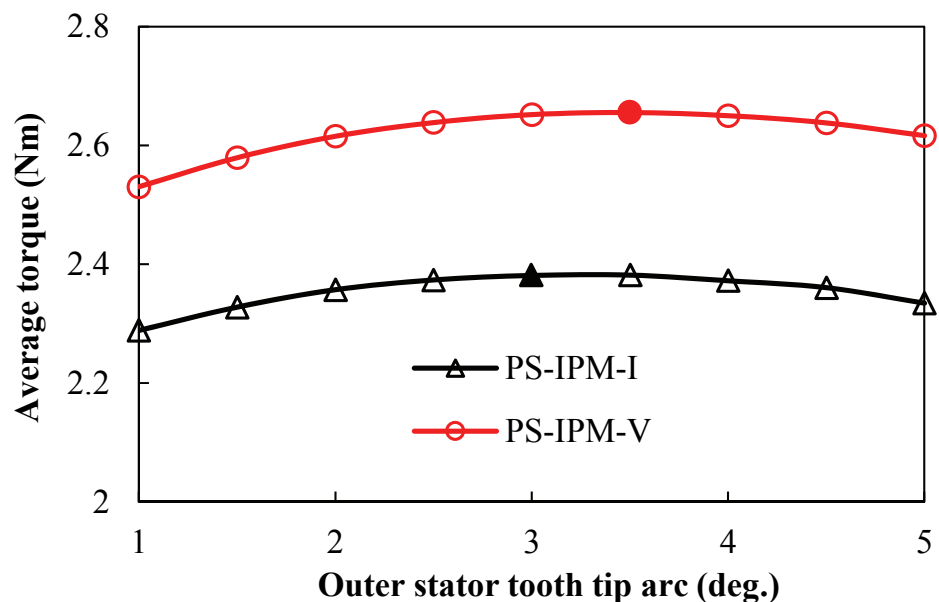


Fig. 2.8 Average torque versus different outer stator tooth tip arcs.

Then, the radial thicknesses h_r of rotor iron pieces of the PS-IPM-I and PS-IPM-V machines are analyzed as well and its effect on average torque is illustrated in Fig. 2.9. The optimal values for both machines locate at around 3.5 mm since a thicker rotor would reduce the space

for PMs as well as armature windings while a thinner rotor cannot maintain the necessary saliency ratio.

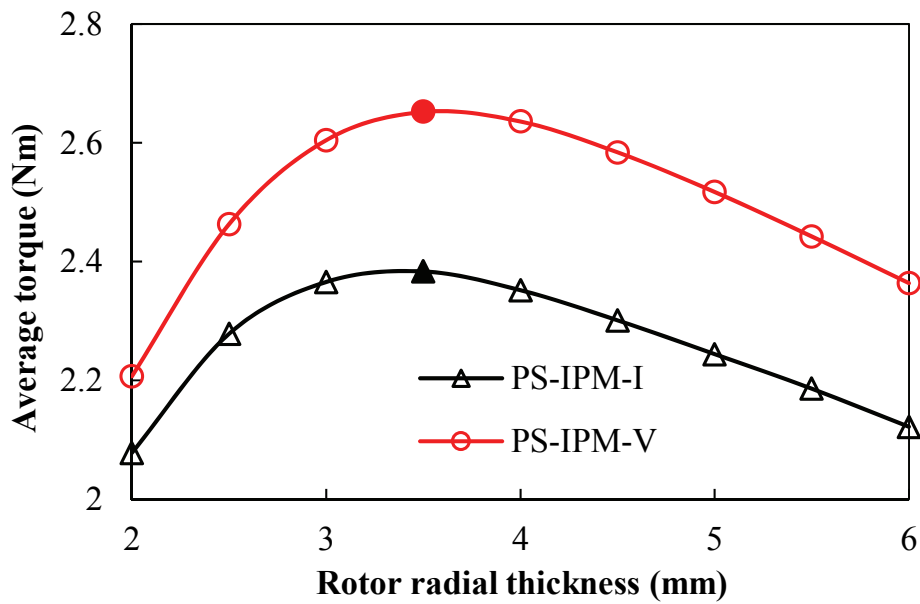


Fig. 2.9 Average torque versus different rotor radial thicknesses.

The influences of rotor inner pole arc β_{ri} and outer pole arc β_{ro} are shown in Fig. 2.10 and Fig. 2.11 respectively. The average torque would increase at first and then tend to decrease with inner and outer pole arcs increasing. This can be explained by the fact that the moderate values are able to avoid significant flux-leakage as well as magnetic saturation. Therefore, the optimal rotor inner and outer pole arc values for the two machines are 16° and 26° , respectively.

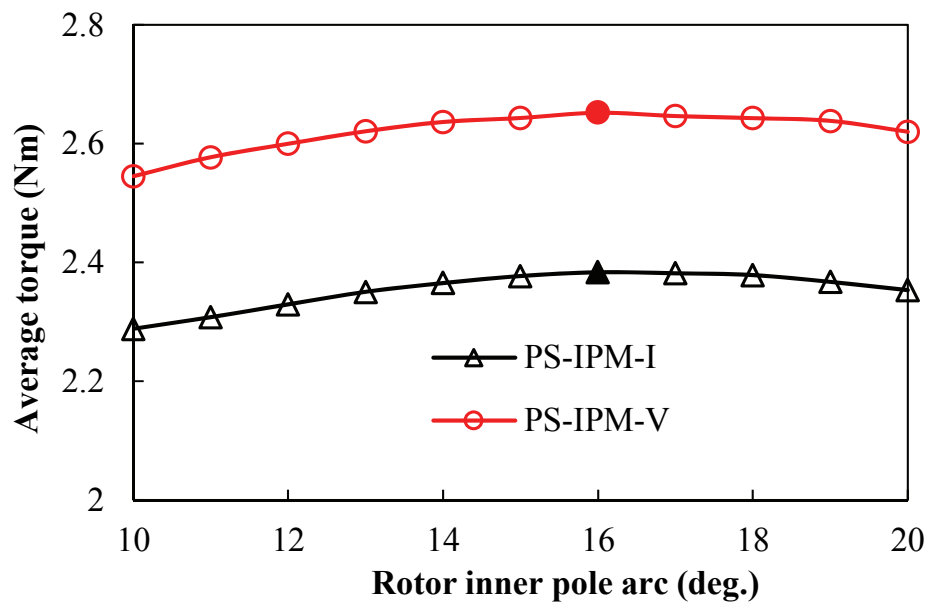


Fig. 2.10 Average torque versus different rotor inner pole arcs.

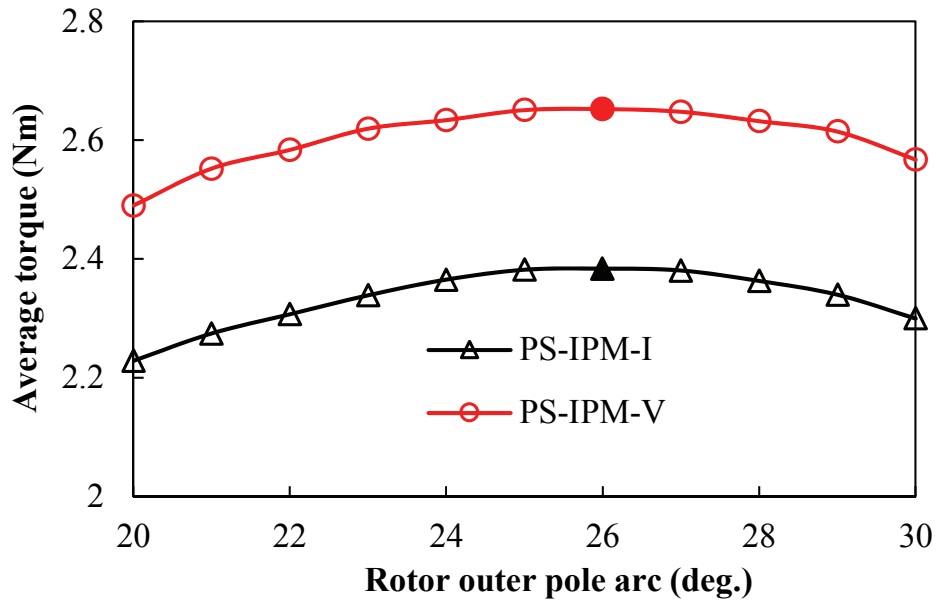


Fig. 2.11 Average torque versus different rotor outer pole arcs.

It can be found that the average torque variation trends with different parameters of the PS-IPM-I and PS-IPM-V machines are quite similar since their structures are intrinsically close, excepting that the PS-IPM-V machine has flux-focusing effect. The average torque of the PS-IPM-V machine is always higher thanks to the flux-focusing effect.

2.4 Comparison of PS Machines

Furthermore, based on sensitivity analysis of the key design parameters illustrated in the previous section, the potential ranges of the key design parameters to obtain the maximum average torque are narrowed down. Accordingly, based on Genetic Algorithm (GA), the global optimizations for maximizing the torque output with the fixed copper losses in armature windings are carried out for the PS-IPM-I and PS-IPM-V machines respectively. The details on the optimization process are summarized as follows:

Model type: 2-D transient model in FE software (ANSYS/Maxwell);

Optimization object: The key design parameters of the PS machines, including split ratio (ratio between stator inner radius to outer radius), outer stator yoke thickness, outer stator tooth arc, rotor outer and inner pole arcs, rotor radial thickness;

Optimization constraint: Fixed 20W copper loss in armature windings, in which the applied phase current will change with the variation of the slot area. If the slot area is increased, the available area for winding is boosted and hence the phase current could be higher for the fixed

copper loss. In addition, the machine dimension is limited with 45mm outer radius, 25mm active axial length;

Optimization strategy: Genetic Algorithm (GA), which is based on an established tool in the optimization package in ANSYS/Maxwell (maximum generation number: 50, individual number: 30);

Optimization goal: Maximizing the average torque during one electric period.

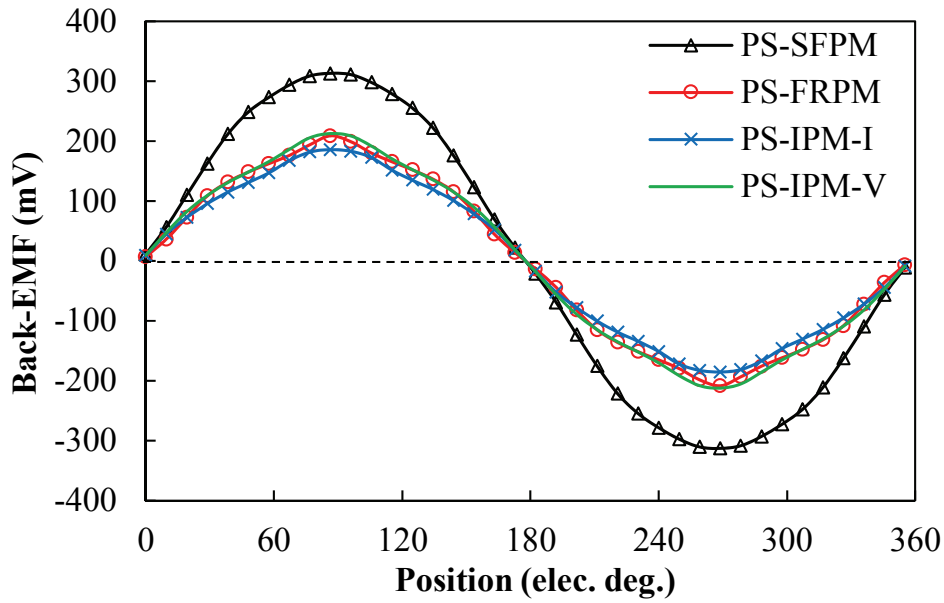
As a result, the optimal design parameters are listed in Table 2.1, accompanied with the optimized parameters of the PS-SFPM and PS-FRPM machines with the same constraints, which are discussed in [EVA15] and [ZHU15b] respectively. Then the optimal models for each machine are built based on the previous optimized geometric parameters. It can be found that the PS-SFPM machine possesses the highest PM usage volume while the PS-IPM-I as well as PS-IPM-V machines have lower PM usage volume. In addition, the inner radius of outer stator in the PS-IPM-I and PS-IPM-V machines is higher as their PM magnetomotive force (MMF) is lower and thus they require less available space for conductors to balance the electric and magnetic loadings. And rotors of the PS-IPM-I and PS-IPM-V machines tend to be thinner as the magnetic saturations are not that severe.

Table 2.1 Optimized key design parameters of four PS machines.

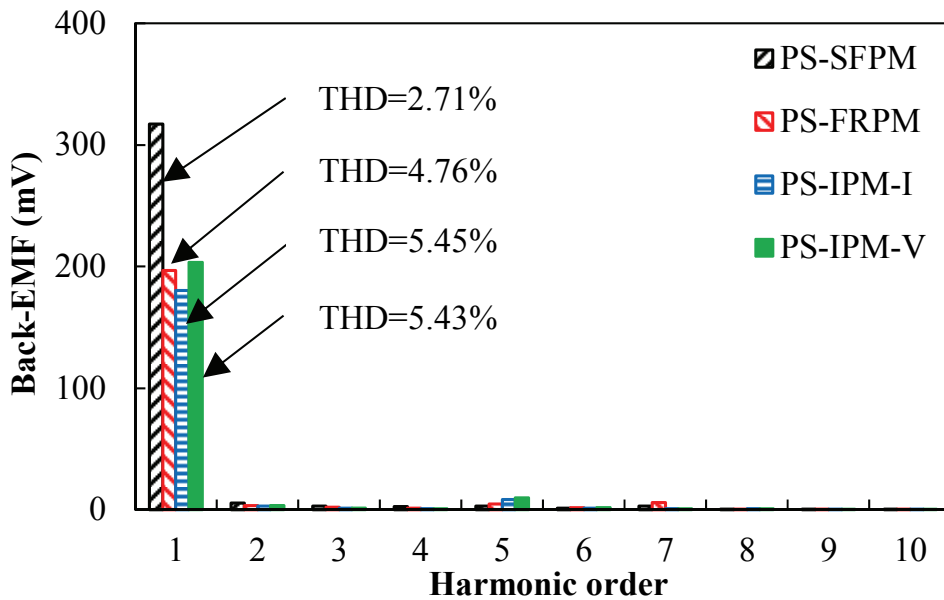
	PS-SFPM	PS-FRPM	PS-IPM-I	PS-IPM-V
Outer stator tooth number			12	
Rotor pole number			10	
Inner stator pole number			12	
Axial length (mm)			25	
Outer stator outer radius, R_{oso} (mm)			45	
Outer stator yoke radius, R_{osy} (mm)	42.5	43	43	43
Outer stator inner radius, R_{osi} (mm)	31	31	33.3	33.3
Outer stator pole arc, β_{ost} ($^{\circ}$)	9	7	6.5	7
Outer stator tip pole arc, β_{tip} ($^{\circ}$)	3	3	3.5	3
Air-gap length, g (mm)			0.5	
Rotor radial thickness, h_r (mm)	4.5	4	3.5	3.5
Rotor outer pole arc, β_{ro} ($^{\circ}$)	25	23	26	26
Rotor inner pole arc, β_{ri} ($^{\circ}$)	20	24	16	16
PM incline angle, δ_{PM} ($^{\circ}$)	N/A	N/A	N/A	50
PM thickness (mm)	5.4	3.5	3.5	2.5
Slot area (mm ²)	80.3	91.5	76.0	75.0
PM volume ($\times 10^4$ mm ³)	2.45	1.34	1.28	1.14

2.4.1 Open-circuit back-EMF

The comparison of open-circuit phase back-EMFs at 400 r/min is shown in Fig. 2.12. As can be seen from the spectra in Fig. 2.12(b), the PS-SFPM machine exhibits the highest peak fundamental value due to the larger PM usage volume and flux-focusing effect. The PS-IPM-I machine has the lowest value due to the reduced PM usage volume and more flux-leakage through iron bridges. It also can be noted that the total harmonic distortion (THD) values of the PS-SFPM machine is the lowest, especially its 5th and 7th harmonics are low, which indicates smaller torque ripple.



(a) Waveforms



(b) Spectra

Fig. 2.12 Phase back-EMFs at 400 r/min. (1 turn number per coil)

2.4.2 Torque characteristics

Fig. 2.13 shows the cogging torques, in which the PS-FRPM and PS-IPM-V machines have higher values while the PS-IPM-I machine exhibits the lowest. The cycle numbers of cogging torque in each machine are identical due to the same slot/pole combinations. The torque waveforms with rated current under zero d -axis current control are compared in Fig. 2.14 and the details are listed in Table 2.2. The results reveal that the PS-SFPM machine exhibits the largest torque while the PS-IPM-I counterpart has the lowest, which correspond to their back-

EMF amplitudes. In addition, the torque ripple of the PS-SFPM machine is low due to its small cogging torque as well as less harmonics. The torque ripple of the PS-IPM-I machine that has the lowest cogging torque is higher since the 5th and 7th back-EMF harmonics are significant.

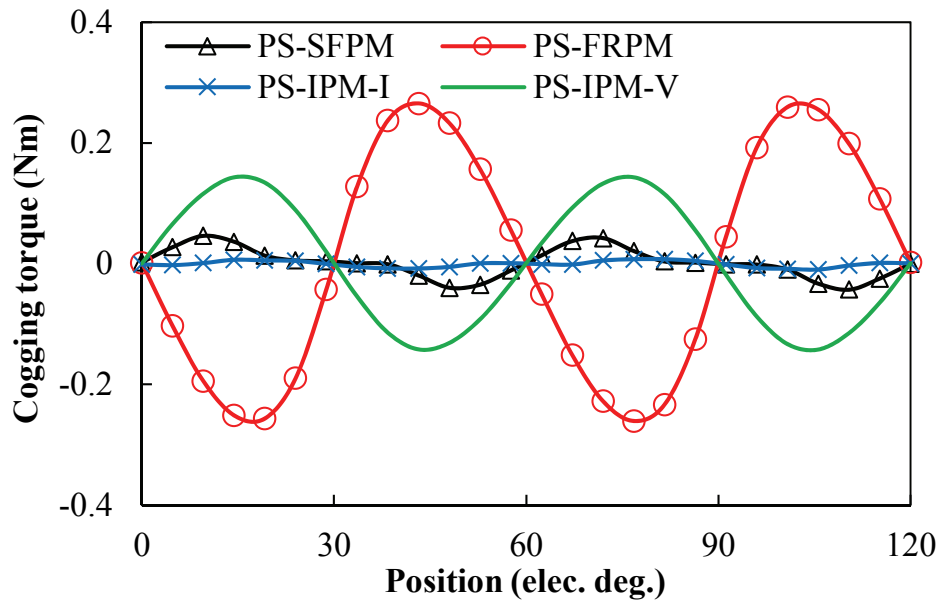


Fig. 2.13 Cogging torque waveforms.

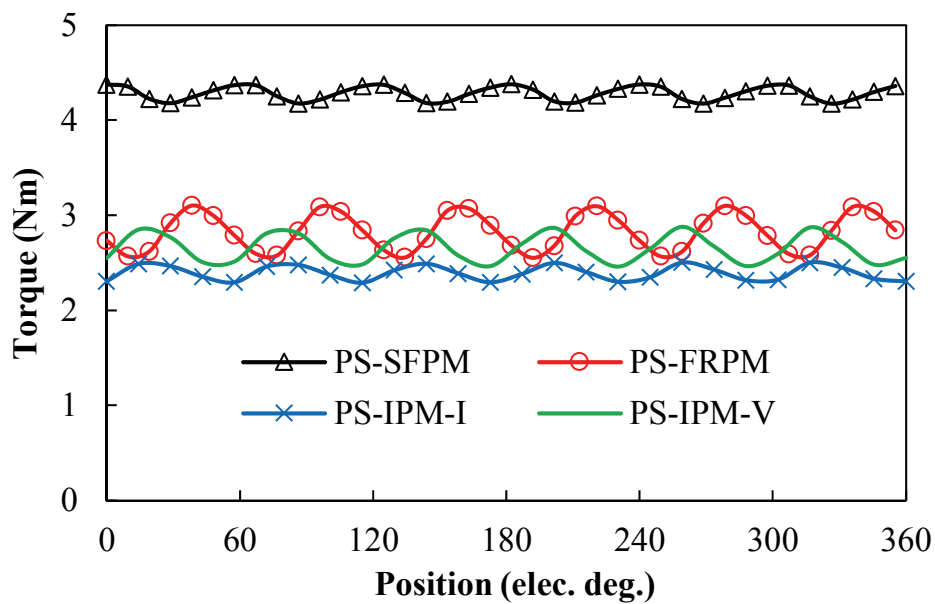


Fig. 2.14 Torque waveforms under zero d -axis current control.

Table 2.2 Details of torque under zero d -axis current control.

	PS-SFPM	PS-FRPM	PS-IPM-I	PS-IPM-V
Average torque (Nm)	4.28	2.82	2.39	2.65
Torque ripple (%)	4.76	19.43	8.87	15.77

Furthermore, the variations of average torque against current advance angle (the phase difference between phase current and open-circuit phase back-EMF) are illustrated in Fig. 2.15. The PS-SFPM machine has the largest torque over all current advance angles and the PS-IPM-I machine always has the lowest value. With V-shaped PM technique, the torque can be improved significantly. It should be emphasized that the maximum torques of all machines occur at the current angle close to 0° (zero d -axis current), implying the fact that reluctance torques of these PS machines are relatively low, which degrades the advantages of the IPM topology. The low reluctance torque in the PS machines is also due to the fact that a small saliency ratio exists.

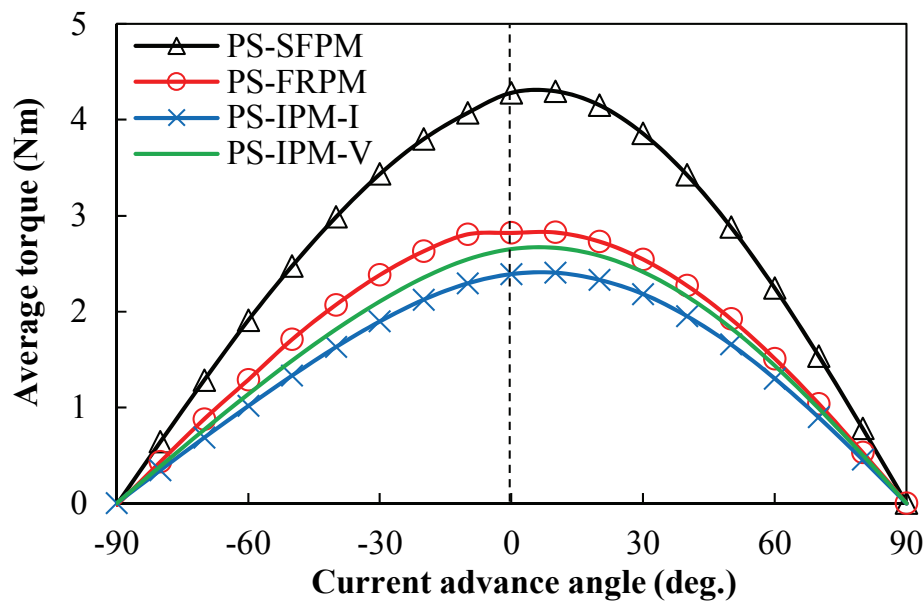


Fig. 2.15 Average torque versus different current advance angles.

Fig. 2.16 shows the average torque with excitations having different copper losses in armature windings, in which the PS-SFPM machine holds the torque advantages over all range, even though the magnetic saturation is quite severe. Nevertheless, considering that the PS-SFPM machine employs larger amount of PM material, it is important to compare the PM usage efficiency of these PS machines. The results are presented in Fig. 2.17 and it can be seen that the PS-IPM-V machine achieves the best PM usage efficiency over the whole copper loss range while the PS-SFPM machine has the lowest over a wide range. It is revealed that the PS-SFPM machine obtains the largest torque at the cost of lower PM usage efficiency. As a result, the appropriate choice of PS machines depends on the torque density and cost *etc.* for a specific application.

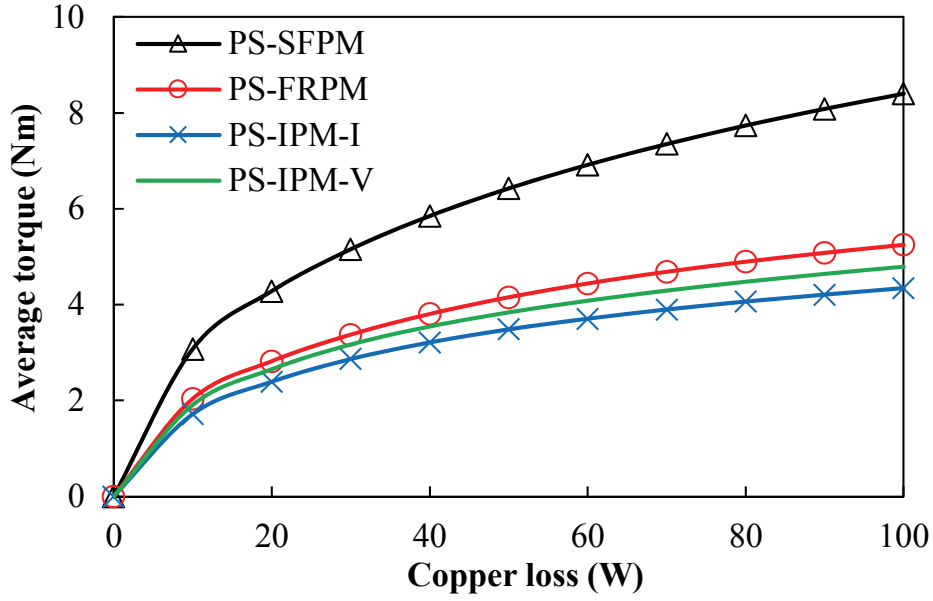


Fig. 2.16 Average torque with different copper losses in armature windings.

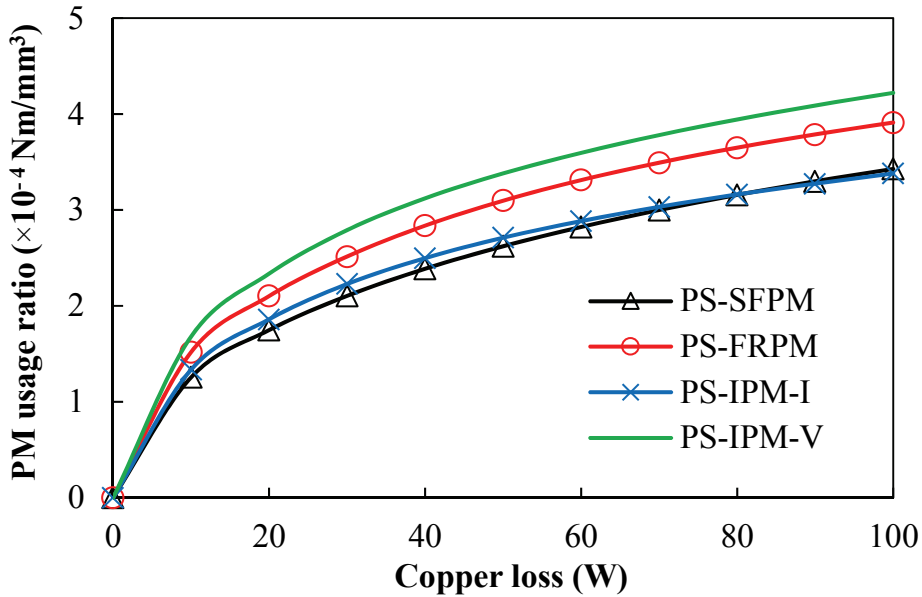


Fig. 2.17 PM usage efficiency with different copper losses.

2.4.3 Flux-weakening factor

Apart from the torque performance, the flux-weakening capability is also an essential characteristic, which can be evaluated as [SOO94]:

$$K_{fw} = \frac{L_d I_d}{\psi_{PM}} \quad (2.3)$$

where L_d , I_d and ψ_{PM} represent the d -axis inductance, d -axis current and PM flux-linkage respectively. The higher flux-weakening factor K_{fw} implies better flux-weakening capability

and hence a wider constant power speed range (CPSR). The PM flux-linkage can be fully weakened and an infinite speed range can be achieved if $K_{fw} \geq 1$. The flux-weakening capabilities of these PS machines are compared in Fig. 2.18, with different excitations. It can be concluded that the PS-IPM-I machine possesses the best flux-weakening potential while the PS-SFPM machine obtains the worst, whilst the PS-IPM-V machine is always better than the PS-FRPM counterpart. The advantages of the PS-IPM-I machine can be attributed to the lower PM flux-linkage.

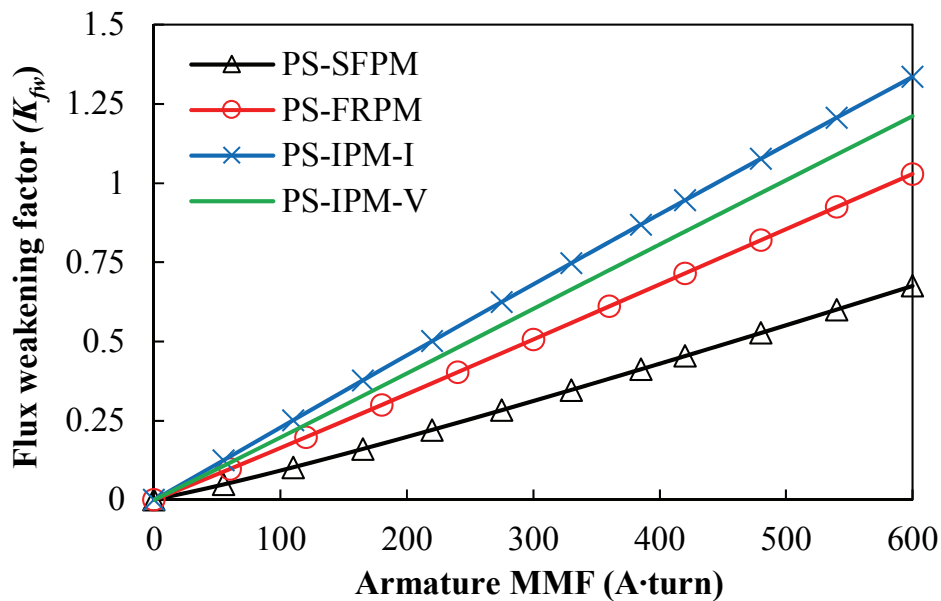


Fig. 2.18 Flux-weakening capabilities with different armature MMFs.

2.5 Comparison of PS Machines Having Identical PM Usage Volume

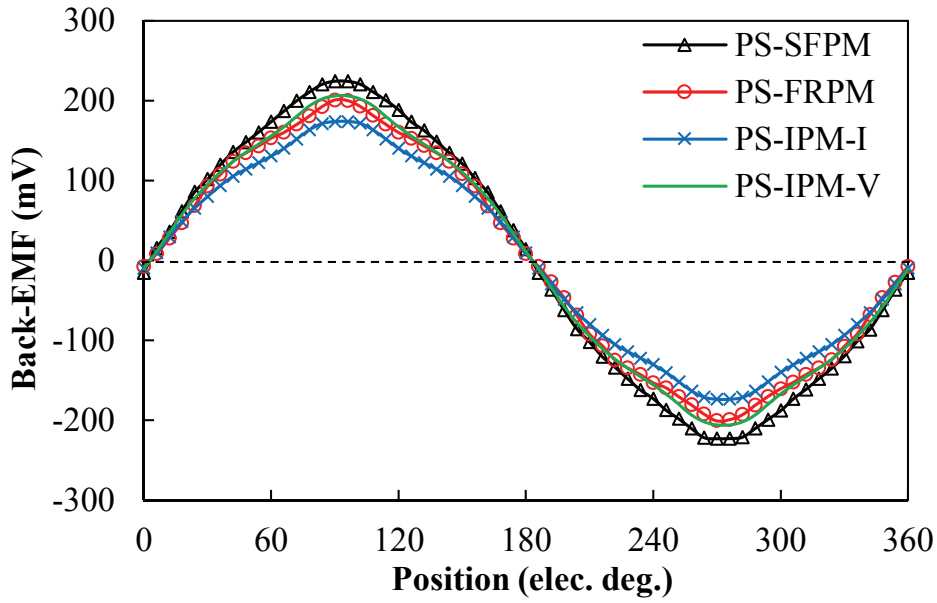
In the foregoing analysis, four individually optimized PS machines are comprehensively compared and their characteristics are highlighted. However, since the PM usage volumes in these machines are significantly different, it is of value to further investigate the machines with the identical PM usage volume. The optimization is carried out again for each machine, with the fixed PM usage volume. The optimized design parameters are listed in Table 2.3, in which the identical PM usage volume can be observed. It is easy to find that the PM thicknesses of the PS-SFPM, PS-FRPM, as well as PS-IPM-I machines are reduced.

Table 2.3 Optimized key design parameters of PS machines having identical PM usage volume.

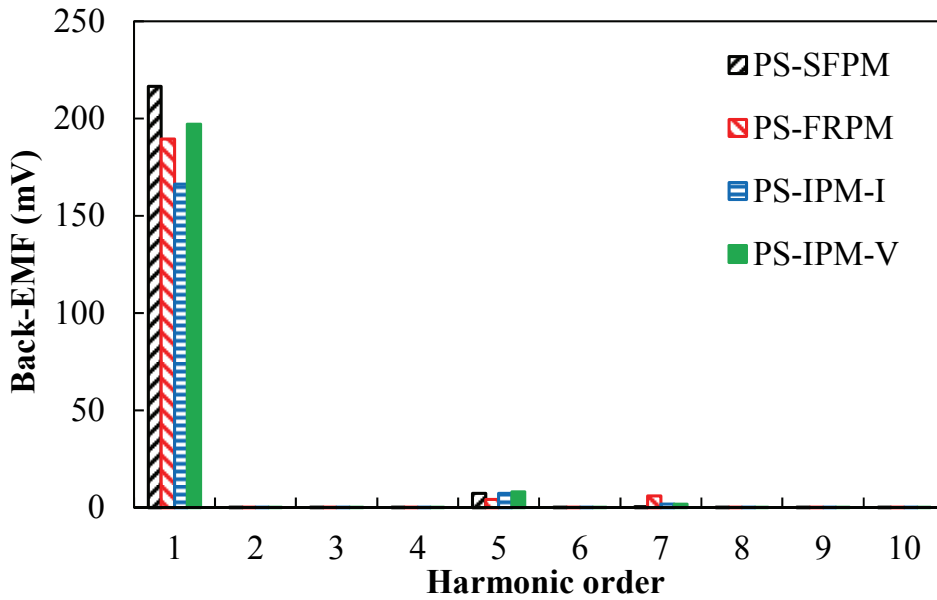
	PS-SFPM	PS-FRPM	PS-IPM-I	PS-IPM-V
Outer stator tooth number			12	
Rotor pole number			10	
Axial length (mm)			25	
Outer stator outer radius, R_{oso} (mm)			45	
Outer stator yoke radius, R_{osy} (mm)	42.5	43	43	43
Outer stator inner radius, R_{osi} (mm)	27	31	32.5	33.3
Outer stator pole arc, β_{ost} ($^{\circ}$)	10	7	6.5	7
Outer stator tip pole arc, β_{tip} ($^{\circ}$)	3.5	3.5	3.5	3
Air-gap length, g (mm)			0.5	
Rotor radial thickness, h_r (mm)	4.5	4	3.5	3.5
Rotor outer pole arc, β_{ro} ($^{\circ}$)	23	23	26	26
Rotor inner pole arc, β_{ri} ($^{\circ}$)	20	24	18	16
PM incline angle, δ_{PM} ($^{\circ}$)	N/A	N/A	N/A	50
PM thickness (mm)	3.4	2.95	3.13	2.5
Slot area (mm ²)	102.5	91.2	78.3	75.0
PM volume ($\times 10^4$ mm ³)	1.14	1.14	1.14	1.14

2.5.1 Open-circuit back-EMF

The open-circuit phase back-EMFs at 400 r/min of these four PS machines are compared in Fig. 2.19, where the amplitude of the PS-SFPM machine is still the highest, although the advantage is not as overwhelming as in section 2.4, due to less PM usage volume.



(a) Waveforms



(b) Spectra

Fig. 2.19 Phase back-EMFs at 400 r/min of four PS machines having identical PM usage volume. (1 turn number per coil)

2.5.2 Torque characteristics

The torque waveforms with the excitations of identical copper losses and zero d -axis current control are presented in Fig. 2.20, and Fig. 2.21 shows the variations of average torque versus copper loss. It can be seen that the PS-SFPM machine still exhibits the highest torque while the PS-IPM-I machine has the lowest, and the PS-FRPM machine always can exhibit higher

torque than the PS-IPM-V counterpart, which are the same as the comparison results in section 2.4.

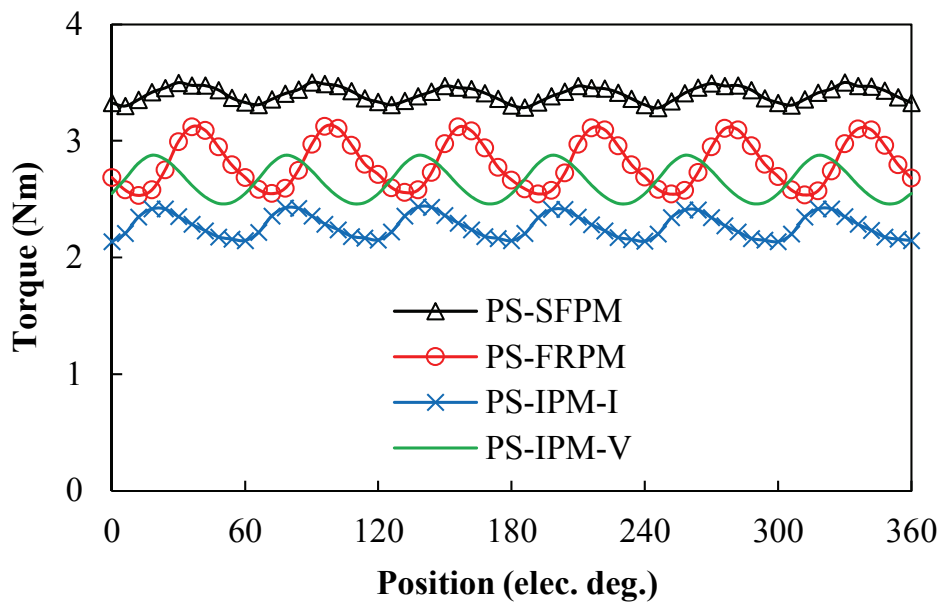


Fig. 2.20 Torque waveforms under zero d -axis current control of four PS machines having identical PM usage volume.

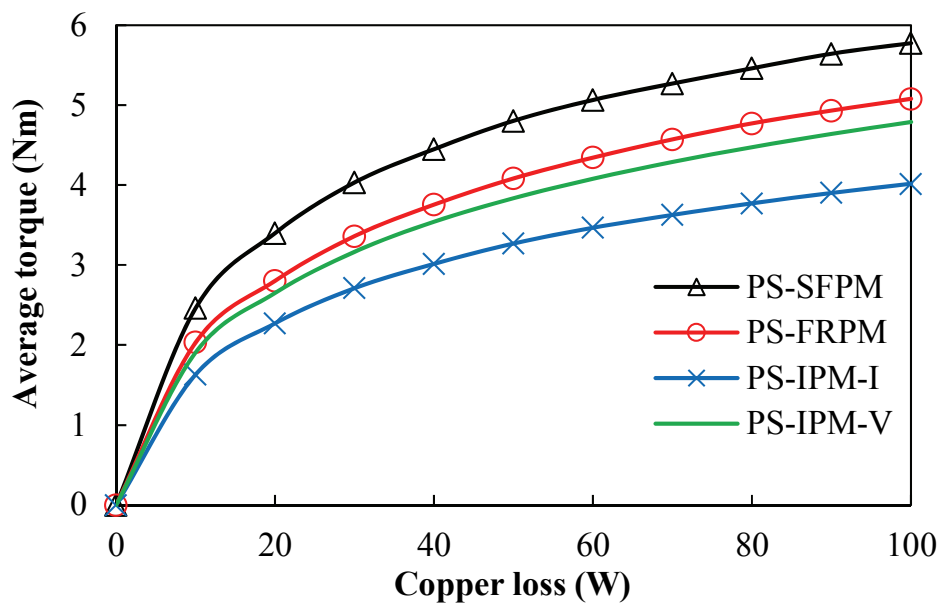


Fig. 2.21 Average torque with different copper losses of four PS machines having identical PM usage volume.

2.5.3 Flux-weakening factor

Further, the flux-weakening capabilities are illustrated in Fig. 2.22, in which the PS-IPM-I machine still benefits from the best flux-weakening potential while the PS-SFPM machine turns to be superior to the PS-IPM-V one.

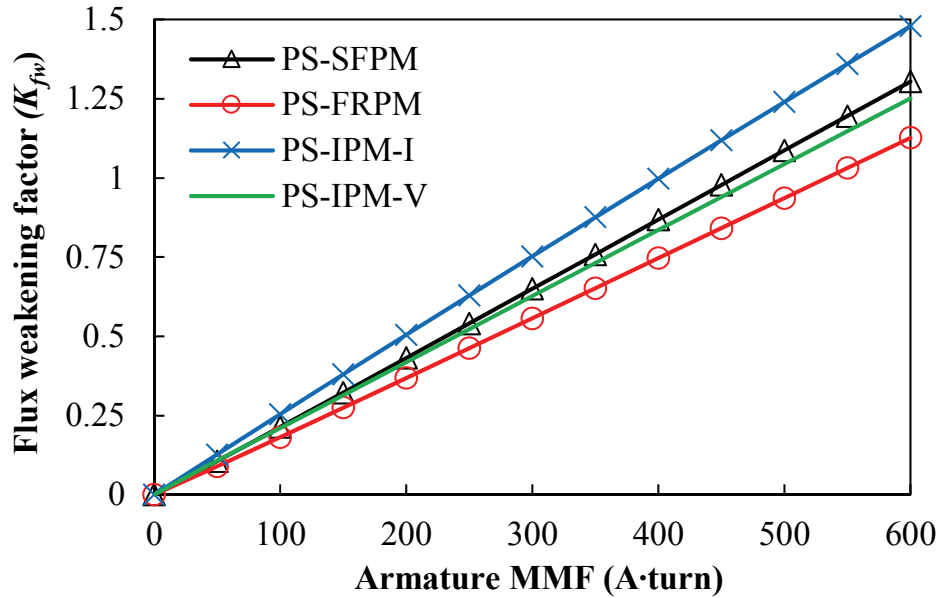


Fig. 2.22 Flux-weakening capabilities with different MMFs of four PS machines having identical PM usage volume.

2.6 Experimental Validation

To validate the FE predictions, four 12/10 PS prototype machines, *i.e.* PS-SFPM, PS-FRPM, PS-IPM-I and PS-IPM-V machine, are manufactured. The major dimensions of the prototypes are listed in Table 2.4, and a little modifications compared with the previously globally optimized parameters are applied to ease manufacture. It should be noted that all machines share the common outer stator as in Fig. 2.23(a) as well as the common rotor as in Fig. 2.23(b), and the distinct inner stators for each machine are shown in Fig. 2.23(c)-(f). Besides, in order to enhance the mechanical strength of the rotor, the iron rib with thickness of 0.5mm is employed to connect the separate rotor iron pieces, as illustrated in Fig. 2.24, which would result in flux-leakage and degrade the performance.

Table 2.4 Design parameters of PS machine prototypes.

	PS-SFPM	PS-FRPM	PS-IPM-I	PS-IPM-V
Axial length (mm)			25	
R_{oso} (mm)			45	
R_{osy} (mm)			42	
R_{osi} (mm)			31.75	
β_{ost} ($^{\circ}$)			8.12	
β_{tip} ($^{\circ}$)			4.94	
g (mm)			0.5	
h_r (mm)			5	
β_{ro} ($^{\circ}$)			18	
β_{ri} ($^{\circ}$)			24	
R_{isi} (mm)			10.19	
δ_{PM} ($^{\circ}$)	N/A	N/A	N/A	50
PM thickness (mm)	5.3	4	3.5	2.5
Turn number per coil			18	



(a) Outer stator



(b) Rotor



(c) IPM-spoke inner stator



(d) SPM inner stator



(e) IPM-I inner stator



(f) IPM-V inner stator

Fig. 2.23 PS machine prototypes with different inner stators.

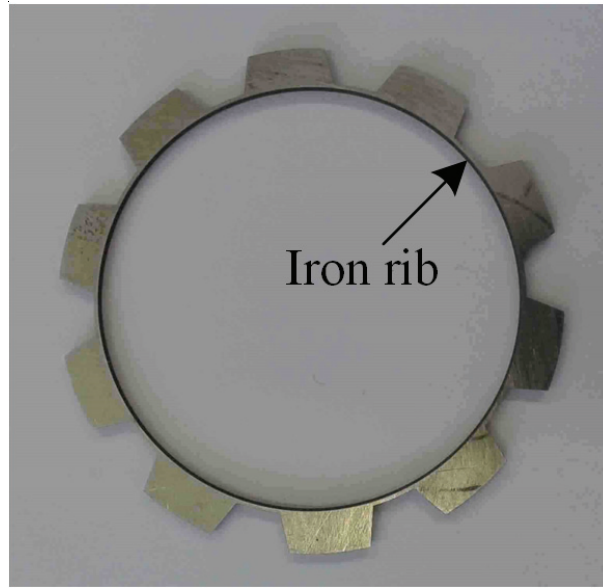


Fig. 2.24 Illustration of rotor lamination with iron rib.

The measured phase back-EMFs at 400 r/min are compared with the 2-D FE predictions in Fig. 2.25. Good agreements are obtained, albeit with slight differences due to end effect. The difference between the measured and FE-predicted peak fundamental back-EMFs are 13.6%, 1.1%, 4.9% and 11.9% in the PS-SFPM, PS-FRPM, PS-IPM-I and PS-IPM-V machines, respectively. More importantly, it is evident that PS-SFPM machine exhibit the highest back-EMF thanks to its larger PM usage volume, which is beneficial to torque output.

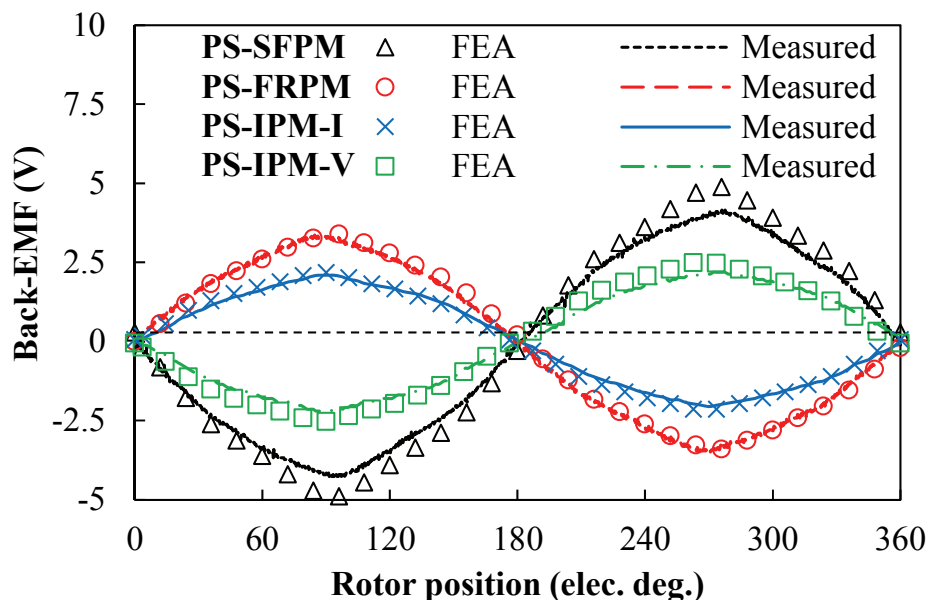


Fig. 2.25 Comparison of FE-predicted and measured phase back-EMF at 400 r/min.

Furthermore, as shown in Fig. 2.26, a test platform is established based on a lathe, which can be employed for measuring the static torque of electric machines [ZHU09]. The frame of the

prototype machine is fixed in the lathe chuck, and the machine shaft is locked with a balanced beam, whose end is connected to a digital weight scale. When the lathe rotates, the static torque at every locked rotor position can be recorded through the weight indicated on the scale. The phase winding connection in the static torque measurement is shown in Fig. 2.27, where Y-type connection is employed and the Phase B and Phase C are connected in parallel. Therefore, the static torque of the prototype machine can be measured. With zero d -axis current control, the FE-predicted and measured static torques versus q -axis current are compared in Fig. 2.28, in which the peak static torques are illustrated. Relatively good agreements can be observed, although the measured values are slightly lower than the predictions due to end effect and tolerances in manufacturing. Since the PS-SFPM machine suffers the most significant difference between the FE and test results, further analysis on the effects of manufacturing tolerance is carried out based on this prototype.

In the prototypes of the PS machines, the air-gap length is an essential parameter, which is challenging to exactly match the design parameter due to the presence of the cup-rotor. Moreover, the thickness of the iron rib for connecting the separated rotor iron pieces, Fig. 2.24, is designed at 0.5mm, however, it may be slightly varied in the cutting. The iron bridges in the inner stators of the PS-SFPM, PS-IPM-I and PS-IPM-V machines also suffer the cutting tolerance. More importantly, it should be noted that although the inner stator is designed to align with the outer stator, a slight shift between the two stators may occur as they are determined by eyes in the assembling. The effects of the key manufacturing tolerances are presented in Fig. 2.29. As can be seen in Fig. 2.29(a), a 0.05mm tolerance of air-gap length (10% compared to the designed air-gap) would result in around 6% difference in the open-circuit back-EMF amplitudes as well as 6% difference in the peak static torque with excitation of 20A q -axis current. Meanwhile, a 0.05mm tolerance of rotor iron rib thickness (10% compared to the designed iron rib) would contribute to around 1.4% difference in the 2D-FE and test back-EMFs and peak static torques, Fig. 2.29(b). A 0.05mm tolerance of inner stator iron bridge thickness (10% compared to the designed iron bridge) results in around 2% difference in the back-EMFs and peak static torques, Fig. 2.29(c). Moreover, as shown in Fig. 2.29(d), the unaligned angle between the two stators has a significant effect on the back-EMFs and static torque performance. With a shift angle of 3° , the open-circuit back-EMF would decrease by around 2% and a reduction of 6% can be observed in the static torque.

In addition to the manufacturing tolerance, the measuring tolerances including the rotor position recording, which is determined by eyes, also may contribute to the difference between FE predictions and test results.

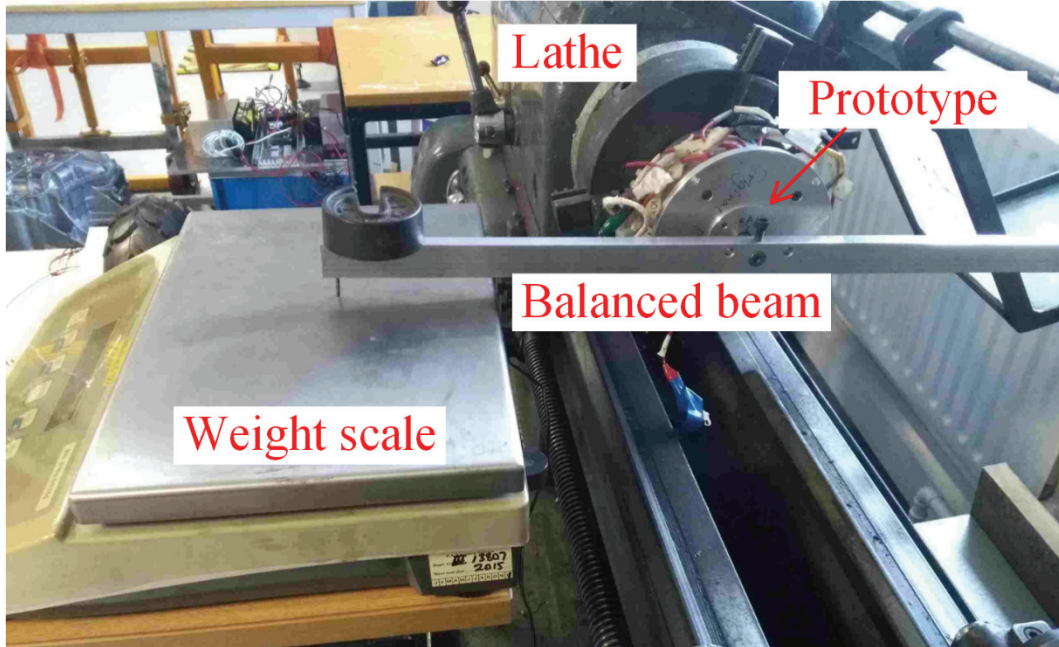


Fig. 2.26 Illustration of test-rig for static torque measurement.

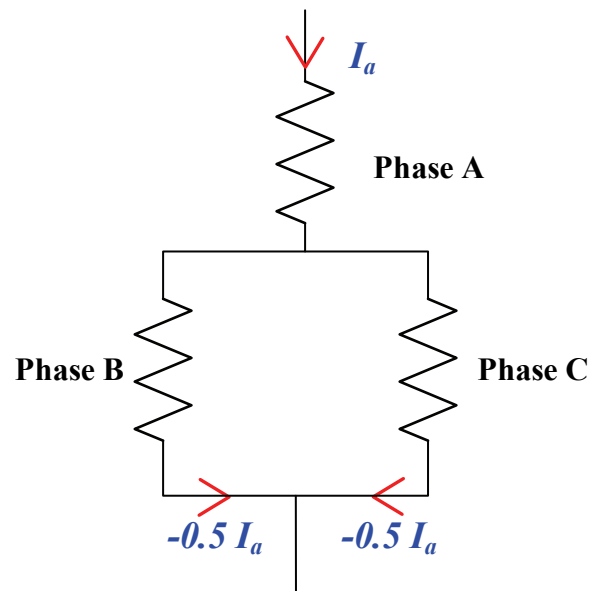


Fig. 2.27 Illustration of the phase windings connection during static torque measurement.

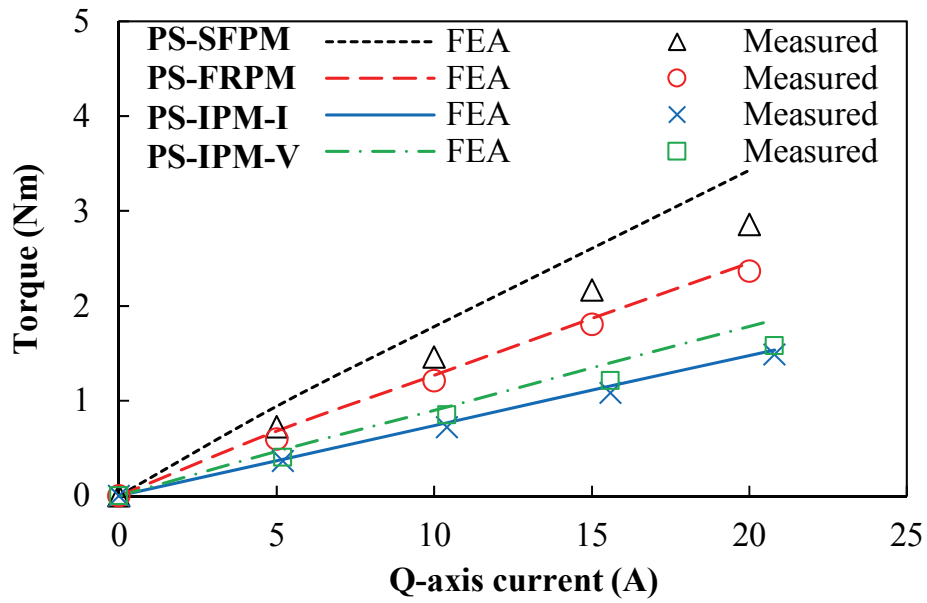
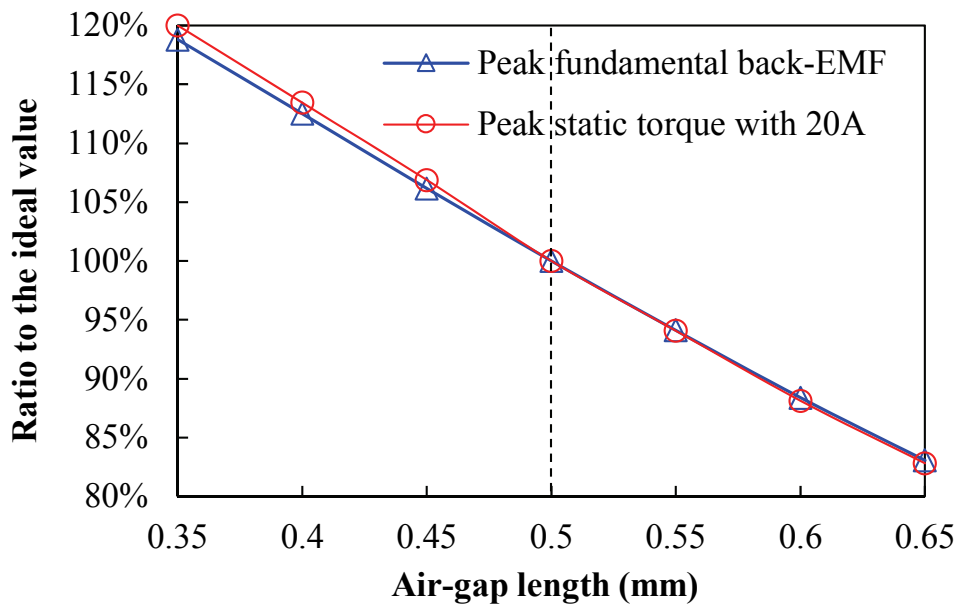
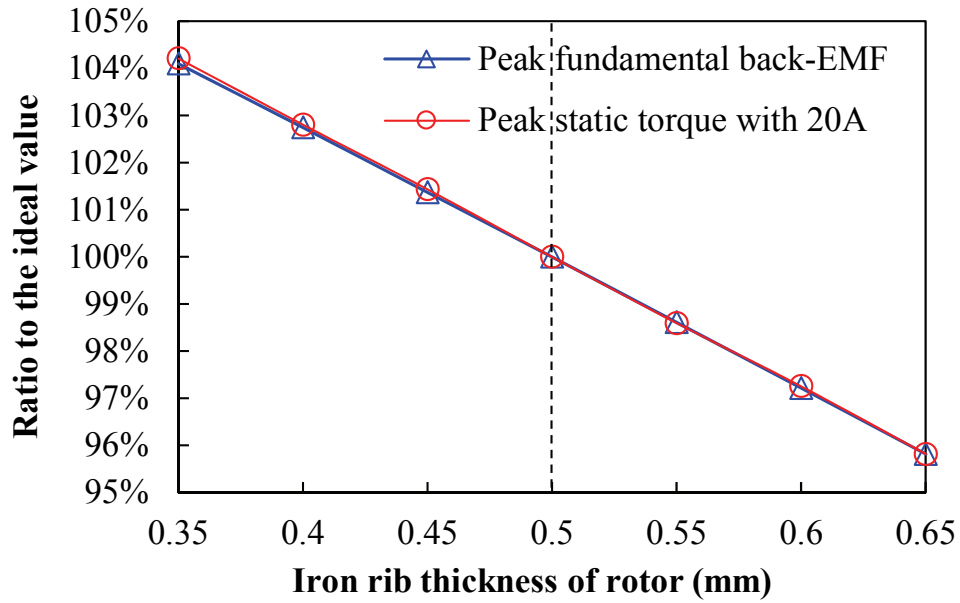


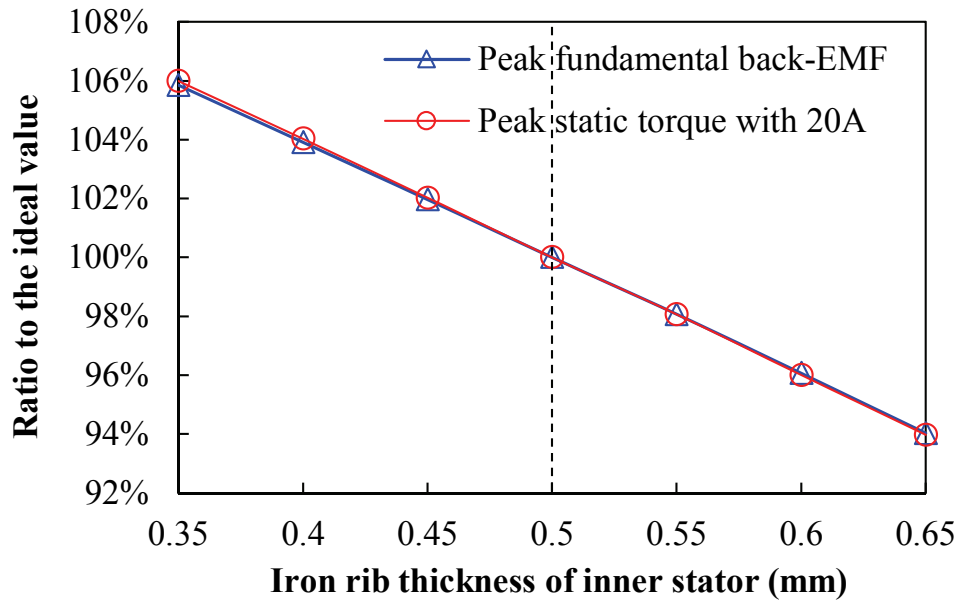
Fig. 2.28 Comparison of FE-predicted and measured peak static torque versus q -axis currents.



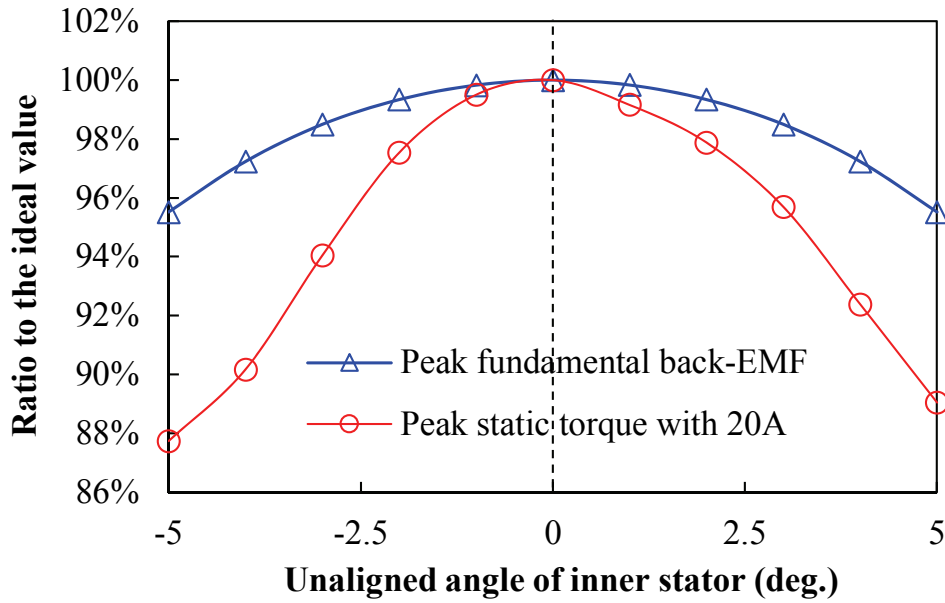
(a) Effect of the air-gap length



(b) Effect of the rotor iron rib thickness



(c) Effect of the inner stator iron rib thickness



(d) Effect of the unaligned inner stator

Fig. 2.29 Effects of the manufacturing tolerances on the prototype performance.

2.7 Conclusion

In this chapter, the PS-SFPM and PS-FRPM machines are proved to share the identical operating principle and they intrinsically belong to one machine type. Then, two new PS machines are proposed, which employ different PM excitation stators. In terms of geometric configuration, the PM excitation stators of PS machines are similar to the rotors of conventional rotor-PM synchronous machines and thus the corresponding topologies can be extended. The comparison results of four 12/10 PS machines reveal that the IPM-spoke inner stator exhibits the largest torque at the cost of poorest PM usage efficiency and limited flux-weakening capability, while the PS-IPM-I machine performs excellent flux-weakening potential and PS-IPM-V machine is most attractive when the cost is important since its PM usage efficiency is the highest. In addition, if the identical PM usage volume is applied to four machines, the PS-SFPM machine still exhibits the highest back-EMF and torque. The appropriate choice of PS machines depends on the specific applications.

Chapter 3. Partitioned Stator Permanent Magnet Machines with Different Magnet Materials

The PS machines employing different PM configurations have been evaluated in Chapter 2, and the results show that the PS-SFPM machine exhibits the highest torque density thanks to the large PM usage volume. Considering the fact that the material cost is also increased with larger PM usage volume, the usage of PS-SFPM machines would be limited in the cost-sensitive applications. Therefore, in order to utilize the large available space in the PS-SFPM machines but reduce the material cost, a rare-earth free solution is proposed in this chapter. The low-cost ferrite PM material is applied to the PS-SFPM machines, with which the cost is reduced due to elimination of expensive NdFeB PMs while a relatively high torque density is still obtained due to the enlarged available space. A pair of PS-SFPM machines employing ferrite and NdFeB PMs respectively are evaluated in this chapter. Further, taking the commercial Prius2010 IPM machine as a baseline, two Prius2010 IPM-sized PS-SFPM machines are presented and compared to better illustrate the performance of the proposed machines. Meanwhile, the demagnetization characteristics and mechanical stress of the large PS-SFPM machine are investigated.

This part has been published in IEEE Transactions on Industry Applications.

3.1 Introduction

The high energy-product PM, e.g. NdFeB, is crucial to guarantee machine performance. In the PS-SFPM machine employing two stators to accommodate PMs and armature windings separately, the space utilization is improved and more PM is applied, with which the high torque density is obtained [EVA15]. However, the supply fluctuation and price rising of such rare-earth PM materials restrict their applications, forcing alternative solutions [McF14], [BOL14], [RAM15], [GAL15]. The machines with low-cost rare-earth-free materials become one focus in the research of PM machines. In this chapter, to achieve the high torque density with rare-earth-free material, the PS-SFPM machines accommodating a large amount of low-cost PM whilst inheriting the nature of stator-PM machines, are presented and evaluated.

The ferrite PM, which is rare-earth-free but with low remanent flux density (B_r) and low coercive force (H_c), has been applied to various machines to substitute NdFeB PM, reducing

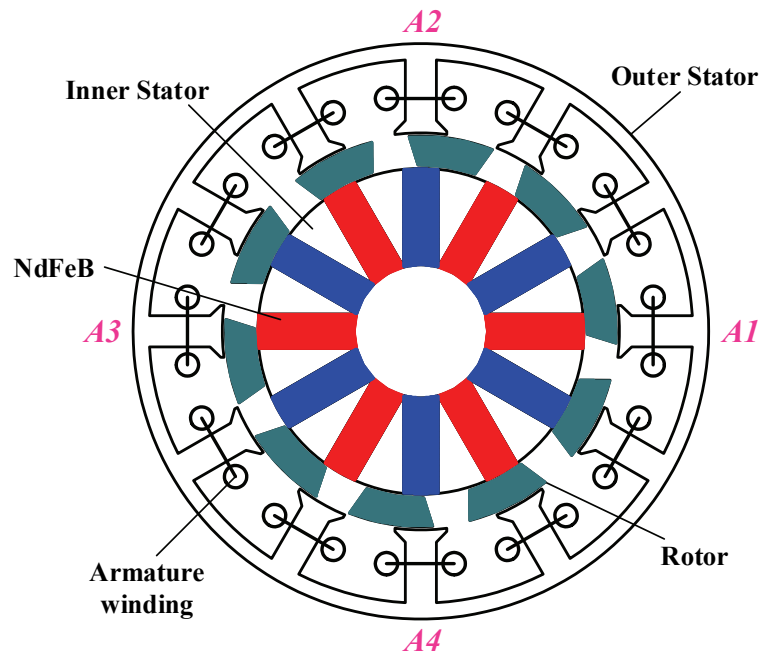
cost but sacrificing performance. The ferrite-assisted synchronous reluctance machines, which accommodate ferrite PMs in flux barriers of the conventional synchronous reluctance machines, exhibit high air-gap flux density and hence increased torque density [BAR14], [BOZ15], [OOI13], [MOR14], [VAG14], [VAR13], [BIA16]. The process of transforming a classic Prius2010 interior-PM (IPM) machine into a ferrite-assisted synchronous machine has been introduced [CAI14]. Moreover, the V-shaped and spoke-type rare-earth-free IPM machines have been evaluated, in which the flux-focusing effect is beneficial and the PMs are thickened to enhance the flux density as well as alleviate the risk of irreversible demagnetization [GAL15], [McF14], [DOR12], [KIM16b], [YOO16], [ZHA15a]. Although a variety of machines with rare-earth-free PMs have been proposed, they always exhibit lower torque density than the corresponding NdFeB PM machines. Therefore, the machines with ferrite PM but exhibiting comparable torque density as an NdFeB PM counterpart, are of great interest. Consequently, the PS-SFPM machine equipped with ferrite PM is an excellent candidate, in which a large amount of ferrite PMs can be allocated thanks to the large available space, which benefits the torque density.

This chapter is organized as follows. In section 3.2, the operation principle of the ferrite PS-SFPM machines, which is similar to the NdFeB counterpart, is briefly introduced, followed by the electromagnetic and economic evaluations of a pair of small PS-SFPM machines employing NdFeB and ferrite respectively, in section 3.3. Then, based on the Prius2010 IPM machine dimensions, the large ferrite and NdFeB PS-SFPM machines are presented and optimized. These two large machines are compared with the Prius2010 IPM machines in section 3.4. The irreversible demagnetization risk of the ferrite one is discussed, and the pole tip is proposed to improve the ability to withstand demagnetization, followed by the mechanical analysis of PS-SFPM machines. Finally, a pair of small-scaled PS-SFPM prototypes with ferrite and NdFeB PMs respectively, are manufactured and tested to validate the predictions.

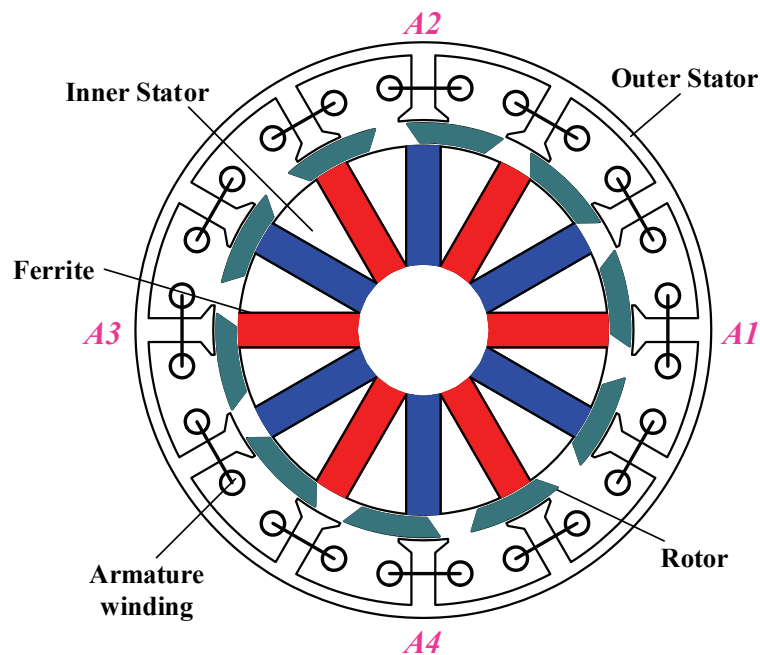
3.2 Machine Structure and Operating Principle

The cross sections of the three-phase 12-stator-slot/10-rotor-piece PS-SFPM machines with NdFeB and ferrite PMs are shown in Fig. 3.1(a) and (b) respectively. In the two PS machines, the outer stator accommodates concentrated non-overlapping armature windings and the inner stator allocates tangentially magnetized PMs, and a cup-rotor consisting of iron pieces is sandwiched between the two stators. The inner and outer stator have the identical pole numbers,

and the PMs are aligned with the outer stator teeth. The difference between these two machines is the employment of NdFeB or ferrite PMs respectively.



(a) NdFeB PS-SFPM machine



(b) Ferrite PS-SFPM machine

Fig. 3.1 Cross sections of NdFeB and ferrite PS-SFPM machines.

The two PS-SFPM machines follow the identical operating principle. Similar to the conventional stator-PM machines, the rotor pole-pair number of the proposed machine is equal

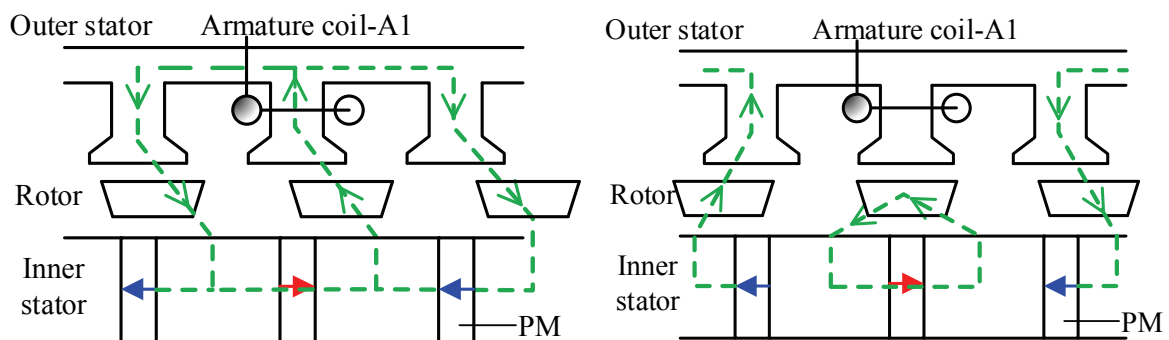
to the rotor piece number. Thus, the relation between rotor electrical position θ_e and mechanical position θ_m follows:

$$\theta_e = N_r \theta_m \quad (3.1)$$

where N_r is the rotor piece number. For the 12/10 PS-SFPM machine, the coils A1, A2, A3, and A4 shown in Fig. 3.1 constitute phase A. Accordingly, Fig. 3.2 illustrates the open-circuit flux paths during one electric cycle. At $\theta_e = 0^\circ$, the PM flux of phase A flows outwards and it reaches the positive maximum value, which is exactly the d -axis rotor position. Then, it tends to be short-circuited by the rotor pieces at $\theta_e = 90^\circ$ and zero flux occurs, which corresponds to the q -axis rotor position. Afterwards, the negative maximum flux is obtained at $\theta_e = 180^\circ$, followed by the zero flux again at $\theta_e = 270^\circ$. As a result, although the PMs are stationary in the inner stator, the flux variation in the armature windings is obtained thanks to the movement of rotor pieces, i.e. the variation of permeance.

Moreover, the PS machine inherits the feature of the even-order harmonic cancellation in the conventional SFPM machines [HUA08]. As shown in Fig. 3.3, the even-order harmonics which exist in the coil flux-linkages, can be cancelled out in the phase flux-linkage and thus the resultant phase flux-linkage is free from even-order harmonics. Based on this bipolar flux-linkages, the back-EMFs can be induced in three-phase windings and thus the electromagnetic torque is produced with currents injected.

The PS-SFPM machine features enlarged available space for conductors and PMs, which contributes to higher torque density at the cost of increased material consumption. Therefore, the ferrite PS-SFPM machine based on the conventional NdFeB one but replacing the NdFeB PM with ferrite PM, can remarkably reduce the material cost although the PM volume is boosted. The ferrite PS-SFPM machine takes advantage of the large PM usage whilst balances the performance and cost.



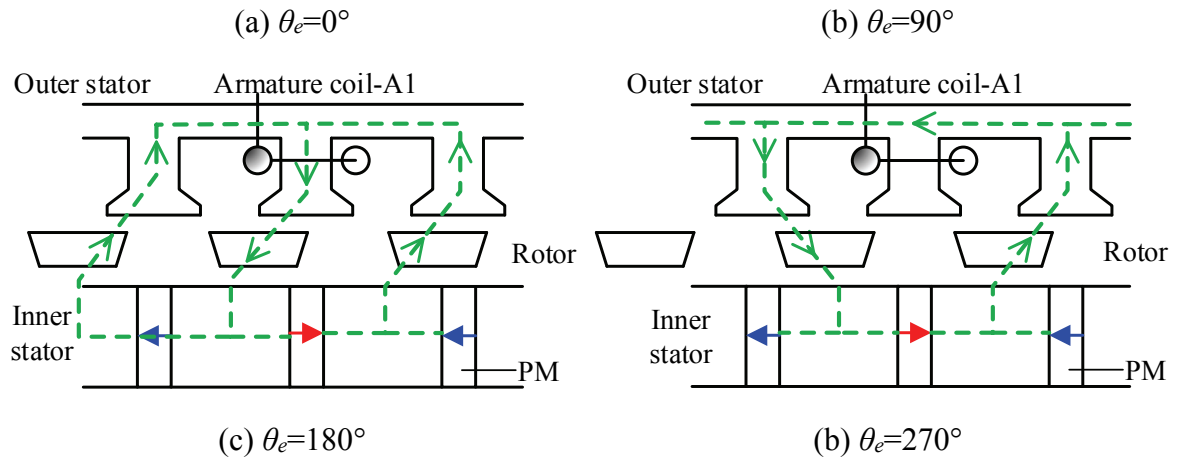


Fig. 3.2 Open-circuit flux paths at four typical rotor positions of the PS-SFPM machine.

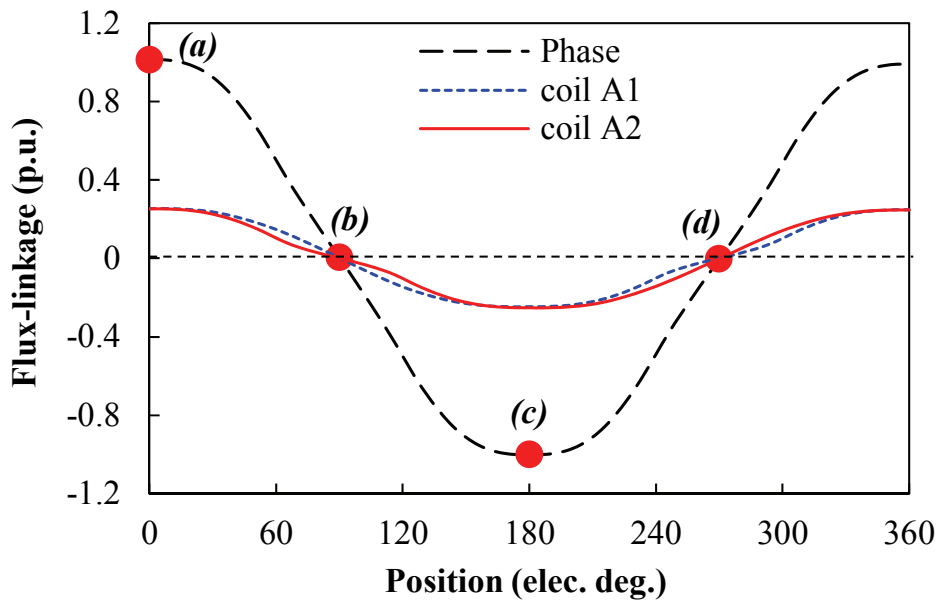


Fig. 3.3 Open-circuit phase flux-linkage of PS-SFPM machine (phase winding=coils A1+A2+A3+A4=2(coils A1+A2)).

3.3 Performance Evaluation of Small PS Machines

Based on 2-D FE analysis, the electromagnetic and economic performances of the NdFeB PS-SFPM and ferrite PS-SFPM machines are evaluated, with which the features of the PS-SFPM machines can be highlighted.

3.3.1 Machine specifications

Based on 25mm axial length and 90mm outer diameter, which is consistent with the overall dimensions of the machines analyzed in chapter 2, a pair of PS-SFPM machines employed

NdFeB and ferrite PMs are presented. Using the genetic algorithm, the two machines are globally optimized with excitation of 20W copper loss in armature windings and zero d -axis current control, to obtain the maximum average torque during one electric period. The definition of the armature winding copper loss can be found in (2.2), and the similar optimization process is applied. It should be noted that the identical copper loss in the two machines does not definitely result in the same temperature rise due to the different iron loss and thermal circuit of the two cases. The optimized design parameters of the two machines are listed in Table 3.1, in which the parameters of the NdFeB one are inherited from those in chapter 2. It can be seen that the inner stator of the ferrite machine is increased to accommodate more PMs whilst the space for coils is reduced to balance the magnetic and electric loadings.

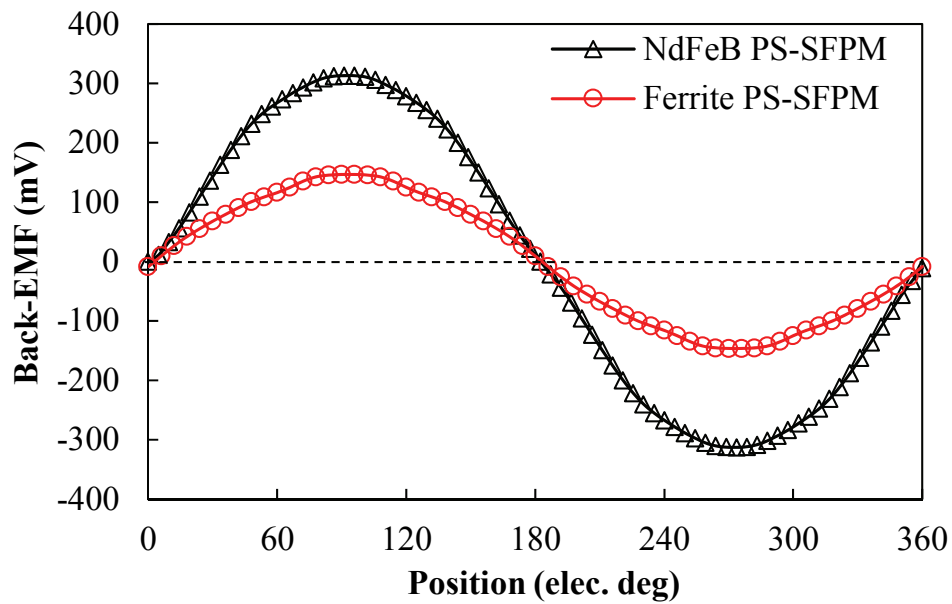
Table 3.1 Key design parameters of NdFeB and ferrite PS-SFPM machines.

Parameters	NdFeB PS-SFPM	Ferrite PS-SFPM
Stator slot number	12	12
Rotor pole-pairs number	10	10
Axial length (mm)	25	25
Stator outer radius (mm)	45	45
Stator yoke radius (mm)	42.5	43
Stator inner radius (mm)	31	32.8
Air-gap length (mm)	0.5	0.5
Rotor radial thickness (mm)	4.5	3
Rotor outer pole arc ($^{\circ}$)	25	27
Rotor inner pole arc ($^{\circ}$)	20	20
Inner stator outer radius (mm)	25.5	28.8
B_r (T)	1.2	0.4
H_c (kA/m)	-910	-295
PM volume ($\times 10^4$ mm 3)	2.45	2.99

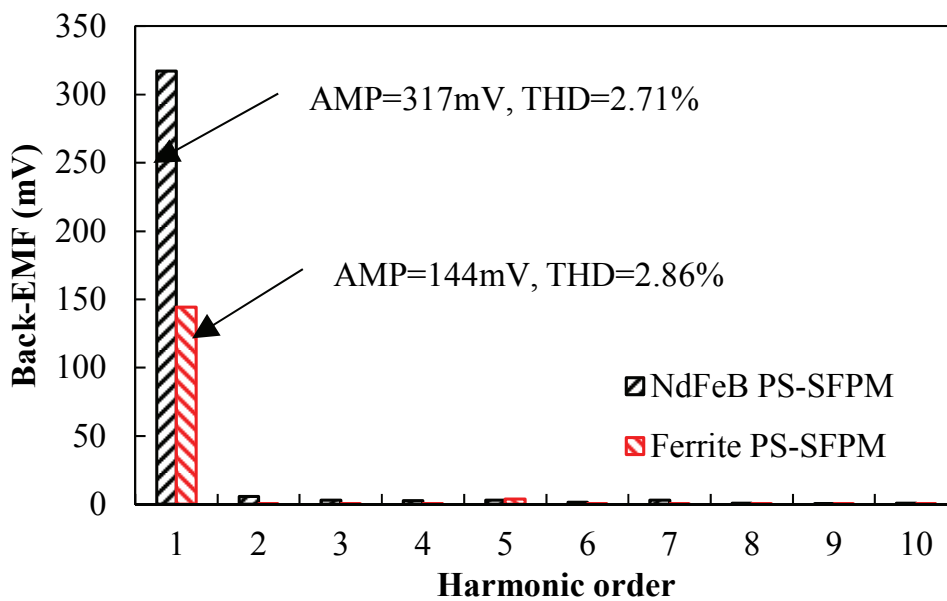
3.3.2 Electromagnetic performance

The phase back-EMFs versus rotor positions at 400 r/min of the two PS-SFPM machines are compared in Fig. 3.4. It can be found the peak fundamental value of the NdFeB PS-SFPM machine (317mV) is more than twice compared with that of the ferrite counterpart (144mV),

due to the strong field of NdFeB PMs. Meanwhile, the THD values of the two machines are both low, which indicate the sinusoidal back-EMFs and thus potentially smooth torque outputs.



(a) Waveforms



(b) Spectra

Fig. 3.4 Open-circuit phase back-EMFs at 400 r/min (1 turn number per coil).

According to the maximum torque per ampere (MTPA) strategy, the torque waveforms with the rated current under zero d -axis current control are shown in Fig. 3.5, in which the NdFeB machine exhibits higher torque than the ferrite one, which is consistent with the back-EMF results. Moreover, the average torque outputs versus different current advance angles of the two machines are illustrated in Fig. 3.6. It can be found that the maximum torques occur when

the current advance angles are close to zero, indicating the negligible reluctance torque in both PS-SFPM machines. Further, with zero d -axis current control, the variations of average torque versus copper loss in armature windings are compared in Fig. 3.7, and the NdFeB machine always has higher torque than the ferrite machine due to the employment of a large amount of NdFeB PM.

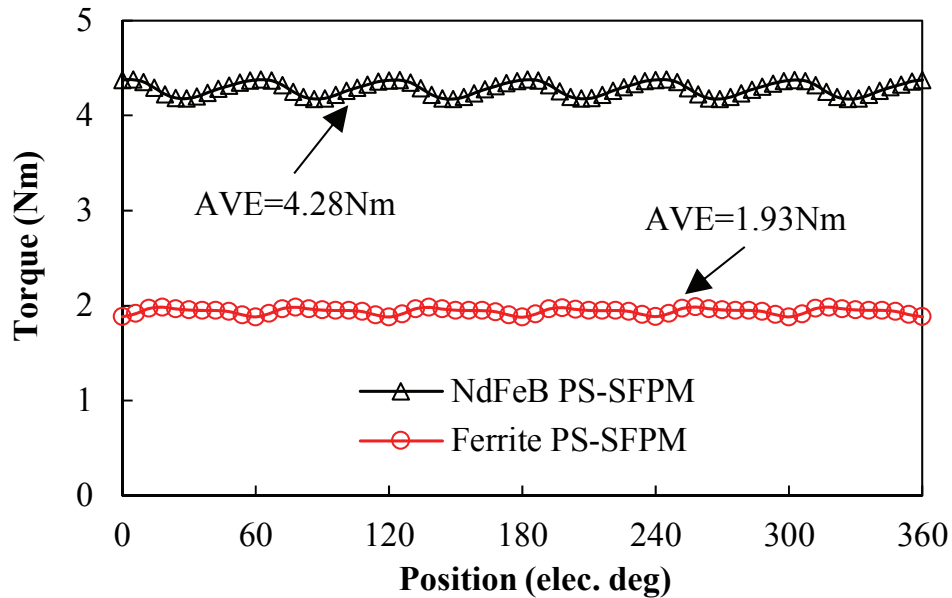


Fig. 3.5 Torque waveforms against rotor positions with rated current and zero d -axis current.

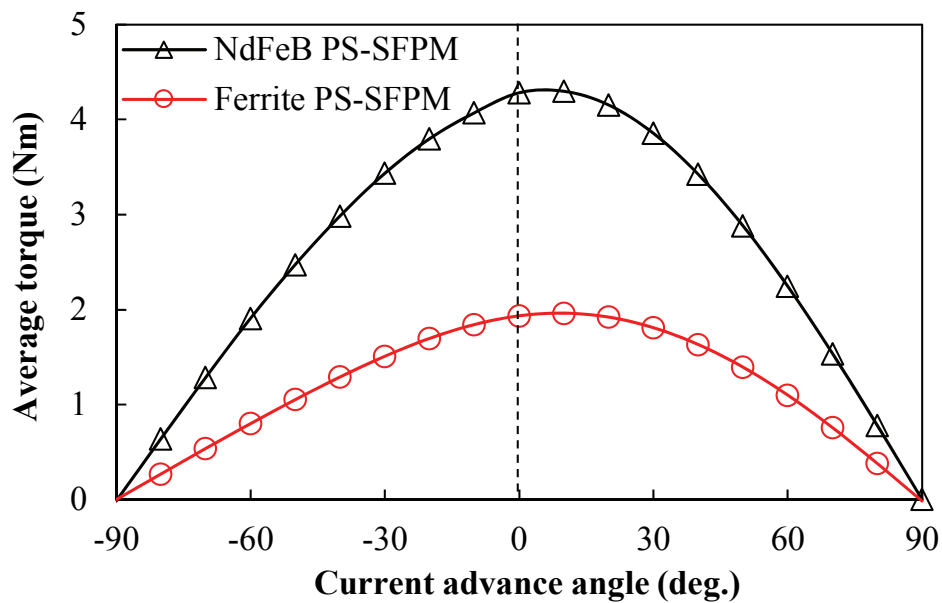


Fig. 3.6 Average torque versus current advance angle with rated current.

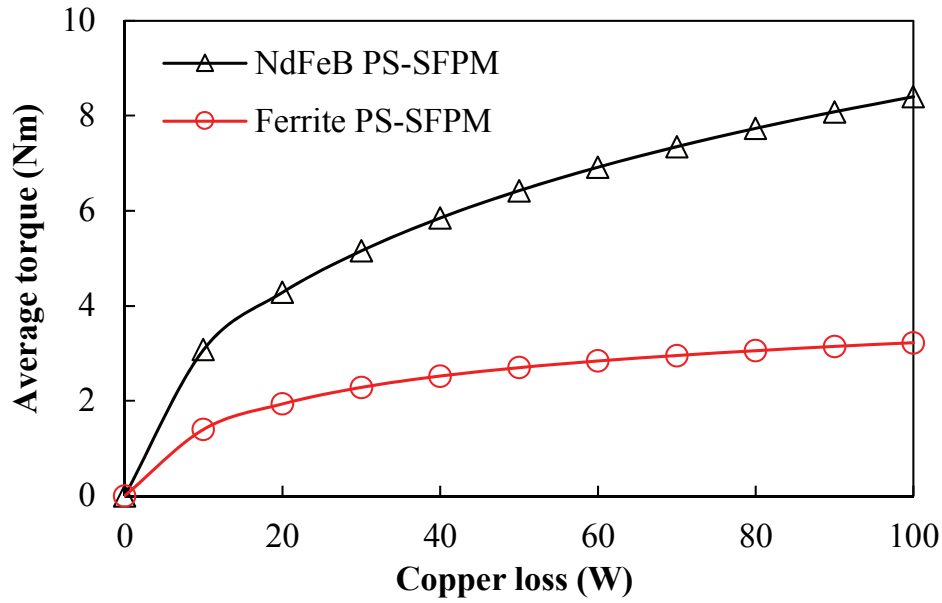


Fig. 3.7 Average torque versus copper loss in armature windings with zero d -axis current control.

The NdFeB PS-SFPM machine exhibits much higher back-EMF and torque due to the strong PM field. Nevertheless, it could be predicted that the flux-weakening capability of the ferrite PS-SFPM would be superior due to the relatively lower PM flux. The flux-weakening factor is defined as:

$$K_{fw} = \frac{L_d I_d}{\psi_{PM}} \quad (3.2)$$

where L_d , I_d and ψ_{PM} are the d -axis inductance, d -axis current and PM flux-linkage respectively. Accordingly, the flux-weakening factors of the two machines with different excitations are compared in Fig. 3.8, in which the ferrite machine has much higher flux-weakening factor with the same armature current, indicating more attractive flux-weakening capability.

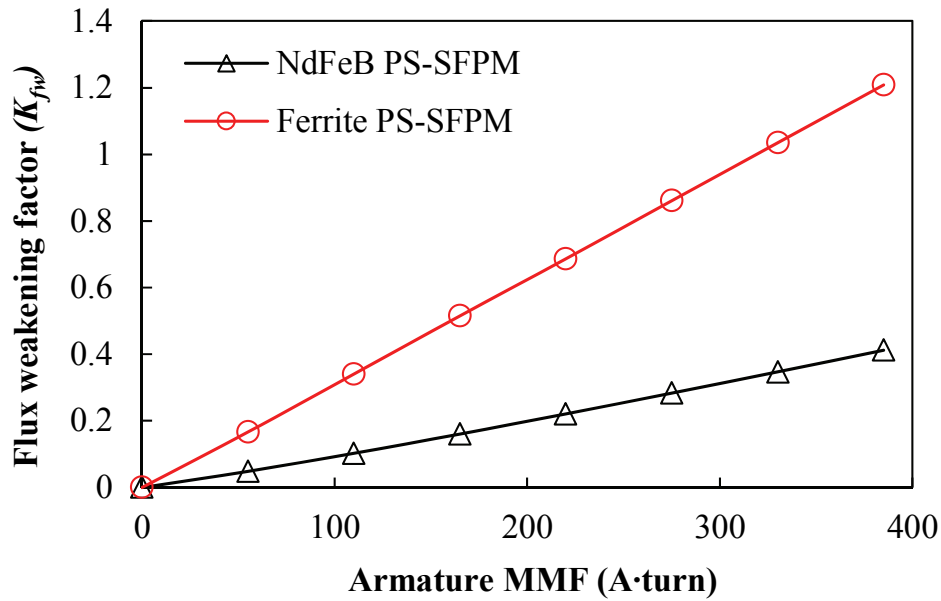


Fig. 3.8 Flux weakening capability with different armature excitations.

3.3.3 Economic issue

The key consideration of replacing the NdFeB PM with ferrite PM is to achieve a low-cost solution. Therefore, to make the comparison more comprehensive, it is of value to assess their economic characteristics. To estimate the active material cost, the price of main materials, based on several sources [SHA15], [MET15], are presented as follows:

- 1) NdFeB PM: 150 USD/kg;
- 2) Ferrite PM: 5 USD/kg;
- 3) Lamination: 2 USD/kg;
- 4) Copper: 11 USD/kg.

The details of the material usage and cost of the two machines are listed in Table 3.2, where the ferrite PS-SFPM machine has a remarkably lower cost due to the absence of the expensive NdFeB PM. Then, the material usage efficiencies (ratio of average torque to material cost) versus different copper losses in armature windings are compared in Fig. 3.9. Thanks to the low cost of the ferrite PM, the ferrite PS-SFPM machine exhibits a higher material usage efficiency than the NdFeB counterpart.

Table 3.2 Material usage and cost of the small NdFeB and ferrite PS-SFPM machines.

Items	NdFeB PS-SFPM	Ferrite PS-SFPM
Copper usage (kg)	0.53	0.57
Copper cost (USD)	5.78	6.12
Lamination usage (kg)	0.50	0.48
Lamination cost (USD)	1.0	0.97
NdFeB usage (kg)	0.18	N/A
NdFeB cost (USD)	27.5	N/A
Ferrite usage (kg)	N/A	0.15
Ferrite cost (USD)	N/A	0.73
Total cost (USD)	34.28	7.82

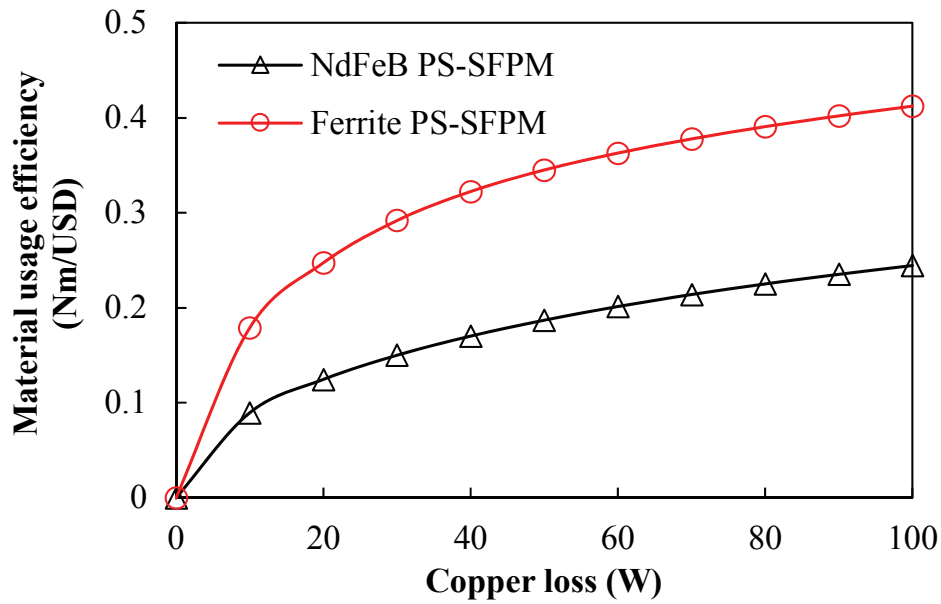


Fig. 3.9 Material usage efficiency versus different excitations.

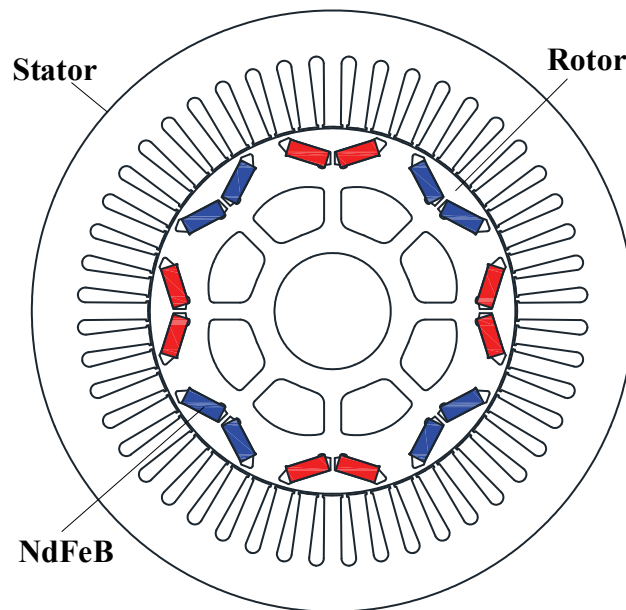
3.4 Performance Comparison of Prius2010 IPM-sized PS Machines

According to the foregoing analysis, the ferrite PS-SFPM machine benefits from higher material usage efficiency and good flux-weakening capability, although suffers lower torque output. It should be noted that the previous investigations are based on the machines having same dimensions as those in chapter 2 (90mm OD×25mm axial length). In this section, in order to provide a more general insight to the machine characteristics, the popular Prius2010 IPM

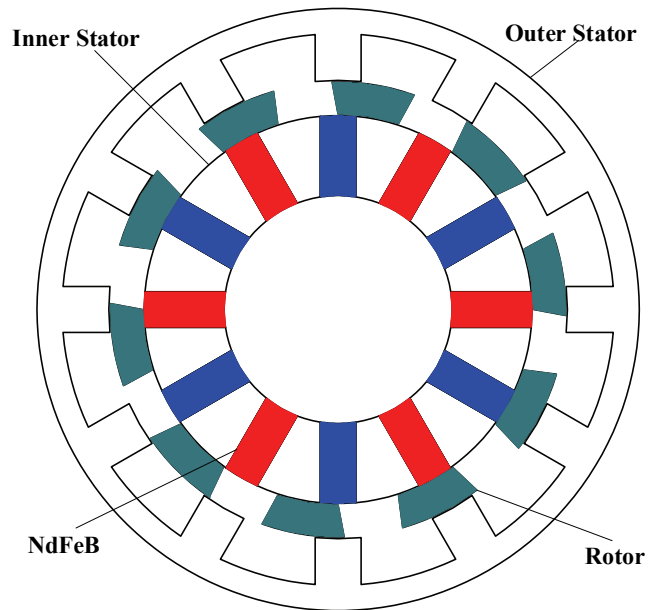
machine (264mm OD×50.8mm axial length) is set as a baseline, and a pair of PS-SFPM machines are designed and compared again.

3.4.1 Machine specifications

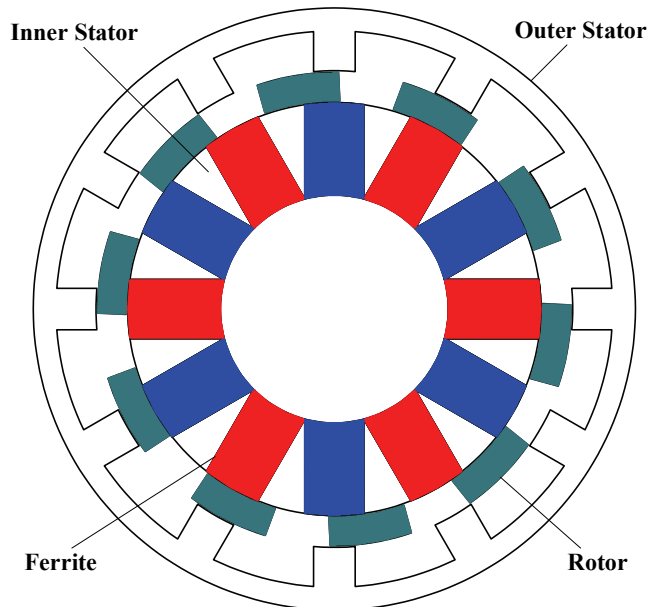
The cross section of the commercial Toyota Prius2010 IPM machine is shown in Fig. 3.10(a), and its key design parameters are summarized in Table 3.3 [OLS11]. With the identical outer diameter, active length, air-gap length, current density and PM material properties, an NdFeB PS-SFPM machine is presented in Fig. 3.10(b). Further, with the same constraints but different PM material, the global optimization based on genetic algorithm is carried out for the ferrite PS-SFPM machine to obtain the maximum average torque, whose optimal cross section is illustrated in Fig. 3.10(c), and the design parameters are all listed in Table 3.3. The PM volume in the NdFeB PS-SFPM machine is much larger than the Prius2010 IPM machine due to the enlarged available space. Although the PM volume in the ferrite PS-SFPM is the largest, its material cost is low thanks to the low price of ferrite PM.



(a) Prius2010 IPM machine



(b) Prius2010 IPM-sized NdFeB PS-SFPM machine



(c) Prius2010 IPM-sized ferrite PS-SFPM machine

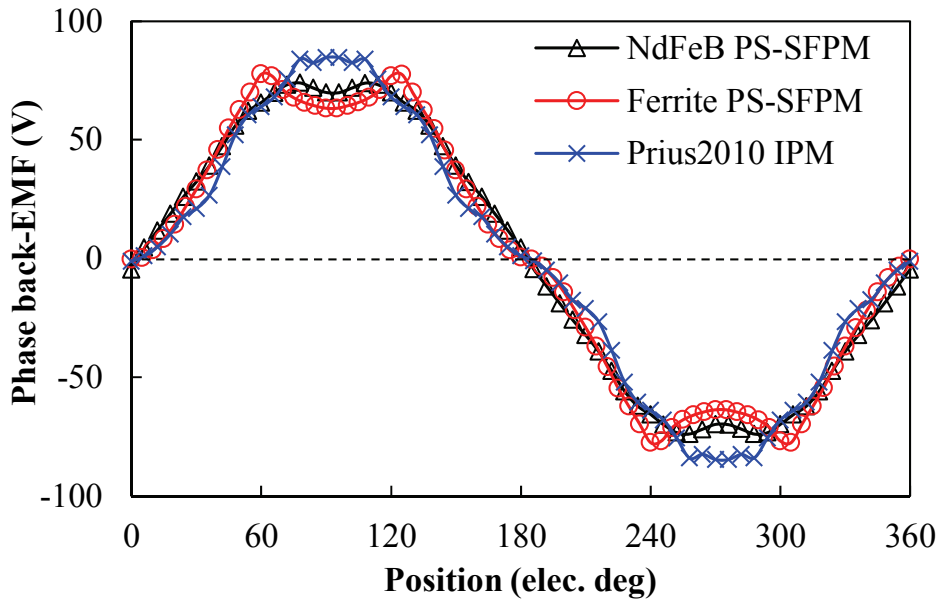
Fig. 3.10 Cross sections of three Prius2010 IPM-sized machines.

Table 3.3 Key design parameters of three Prius2010 IPM-sized machines.

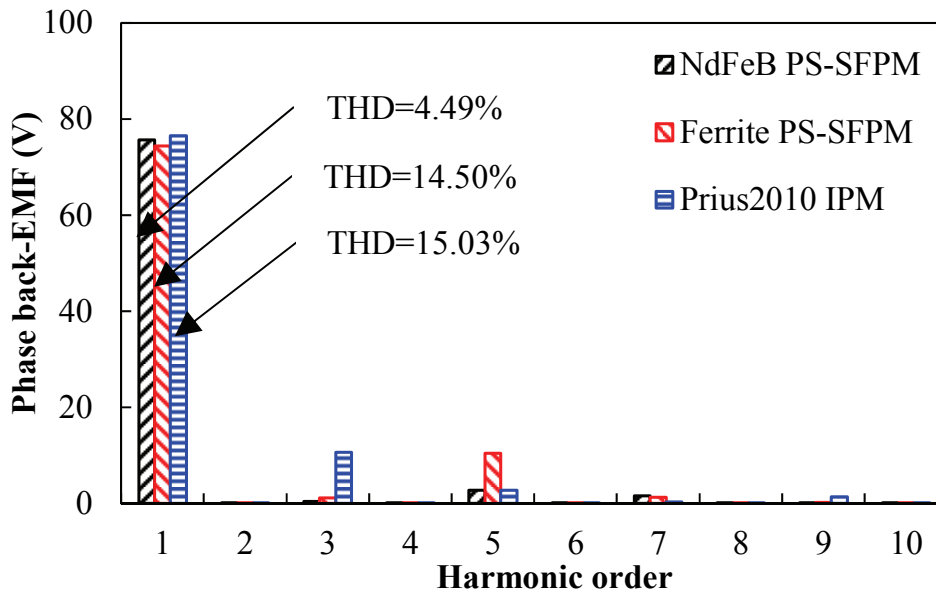
Parameters	Prius2010 IPM	NdFeB PS-SFPM	Ferrite PS-SFPM
Stator slot number	48	12	12
Rotor pole-pairs number	4	10	10
Axial length (mm)	50.8	50.8	50.8
Stator outer radius (mm)	132	132	132
Stator inner radius (mm)	80.95	100.5	104.5
Stator tooth arc (°)	6.15	11.5	10
Air-gap length (mm)	0.73	0.73	0.73
Rotor radial thickness (mm)	N/A	14	12.5
Rotor outer pole arc (°)	N/A	21	20
Rotor inner pole arc (°)	N/A	18	21
Coils number per phase	8	4	4
Turns number per coil	11	9	16
Rated current density (Arms/mm ²)	12.3	12.3	12.3
B_r (T)	1.2	1.2	0.4
H_c (kA/m)	-910	-910	-295
PM volume ($\times 10^4$ mm ³)	10.5	33.2	64.4

3.4.2 Electromagnetic performance

The electrical frequencies of the two PS-SFPM machines are different from the Prius2010 IPM counterpart as their rotor pole-pair numbers are 10 and 4 respectively. Thus, the numbers of turns in both PS-SFPM machines are adjusted to make them have comparable phase back-EMFs with the Prius2010 IPM machine. As a result, their open-circuit phase back-EMFs versus rotor positions at 1500 r/min are compared in Fig. 3.11, in which the similar peak fundamental values are observed. Moreover, it can be found the NdFeB PS-SFPM machine exhibits the lowest harmonics, while the ferrite PS-SFPM machine suffers significant 5th and 7th harmonics. Since only the torque performance is considered while the harmonic suppression is neglected in the optimization, more sinusoidal back-EMF in the ferrite PS-SFPM machine may be obtained with specific attention, especially adjusting the rotor pole arcs.



(a) Waveforms



(b) Spectra

Fig. 3.11 Open-circuit phase back-EMFs at 1500 r/min of three Prius2010 IPM-sized machines.

The ideal sinusoidal currents with the identical frequency to the corresponding back-EMFs are employed to evaluate the torque performance. The torque waveforms with the rated current and the current advance angle generating the highest torque, are compared in Fig. 3.12. It can be noted that the cycle numbers of torque ripple during one electric period are both 6 in the two PS-SFPM machines, which is due to the same slot/pole combinations [ZHU00]. In addition, the NdFeB PS-SFPM machine exhibits much higher average torque than the counterparts thanks to the large PM usage volume, although its torque ripple is higher. The torque output of

the ferrite PS-SFPM machine is around 27% lower than the Prius2010 IPM machine. Further, the variations of average torque versus current angle are illustrated in Fig. 3.13. The peak torques of the NdFeB PS-SFPM and ferrite PS-SFPM machines occur at 0° and -20° respectively, with negligible reluctance torque in the PS-SFPM machines. The ferrite PS-SFPM machine obtains the peak torque with a positive d -axis current, which can be explained by the fact that a slight positive reluctance torque occurs. In fact, this is attractive for employing the ferrite PM since the risk of irreversible demagnetization due to negative d -axis current is alleviated. With zero d -axis current control, the torque of ferrite PS-SFPM machine exceeds the Prius2010 IPM machine, but the reluctance torque is very significant in the Prius2010 IPM machine. At the current advance angles producing the highest average torque for each machine, the variations of average torque versus current density in armature winding slots are presented in Fig. 3.14(a). The NdFeB PS-SFPM machine always exhibits the highest torque, although its phase current is naturally higher thanks to the larger available slot area for armature windings. Meanwhile, it should be emphasized that the ferrite PS-SFPM machine has a little higher torque than the Prius2010 IPM machine with light load but it is easier to be affected by the armature reaction with larger excitations. Besides, the average torques versus copper losses in armature windings are presented in Fig. 3.14(b), in which the NdFeB PS-SFPM machine still exhibits the highest torque whilst the ferrite PS-SFPM and Prius2010 IPM machines have similar torque output with light load but Prius2010 IPM machine is superior when the excitation turns heavy.

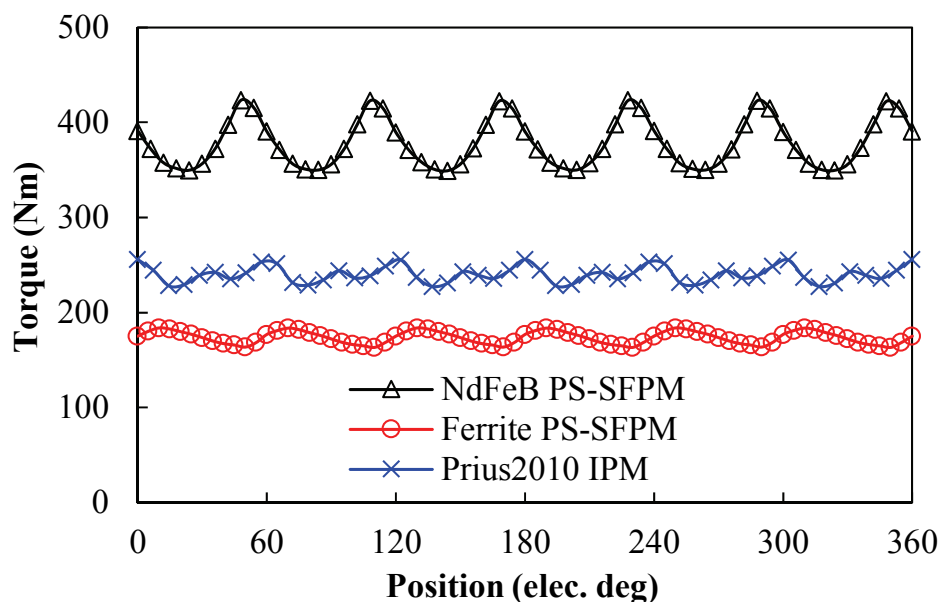


Fig. 3.12 Torque waveforms with rated current density of three Prius2010 IPM-sized machines.

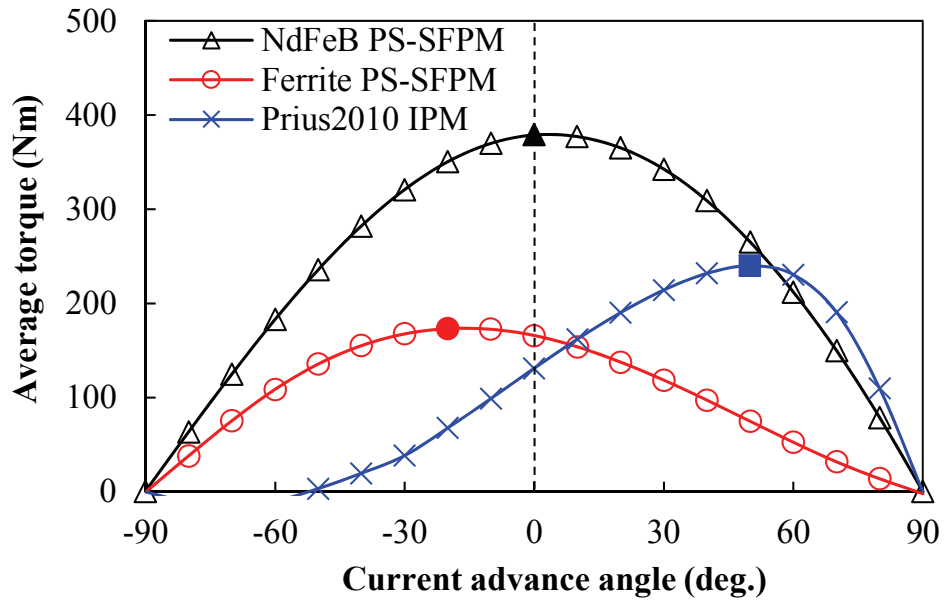
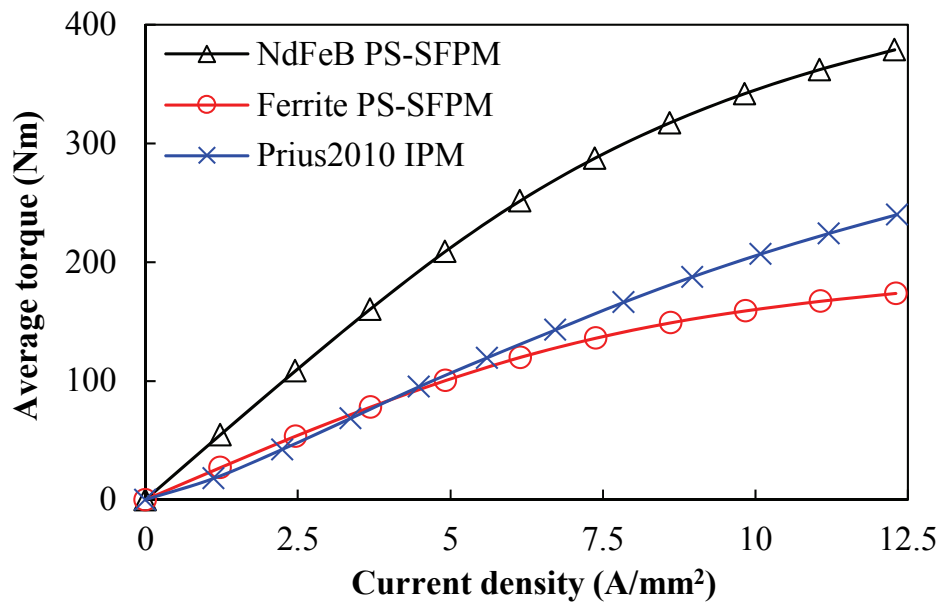
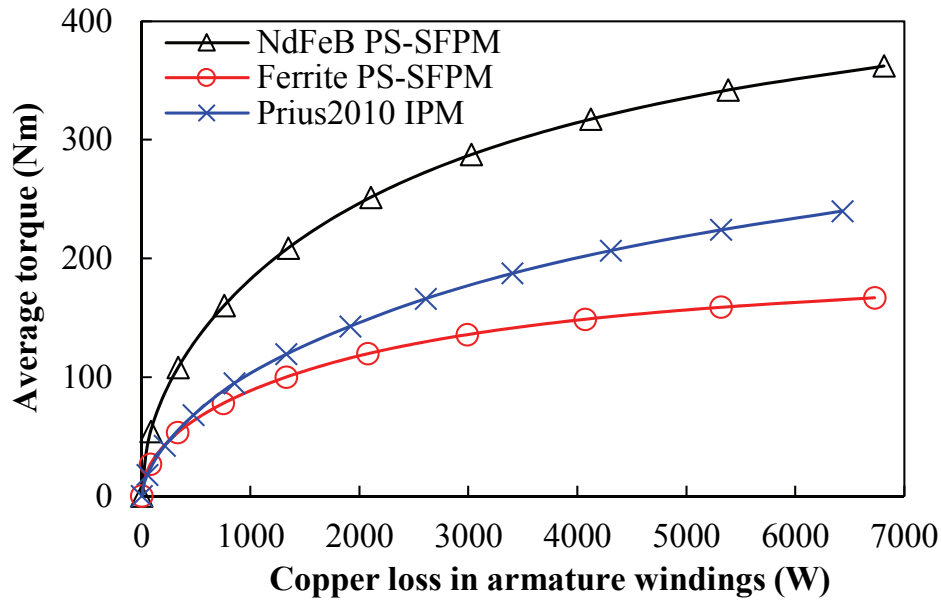


Fig. 3.13 Average torque versus current advance angle of three Prius2010 IPM-sized machines.



(a) Average torque versus current density in armature winding slots

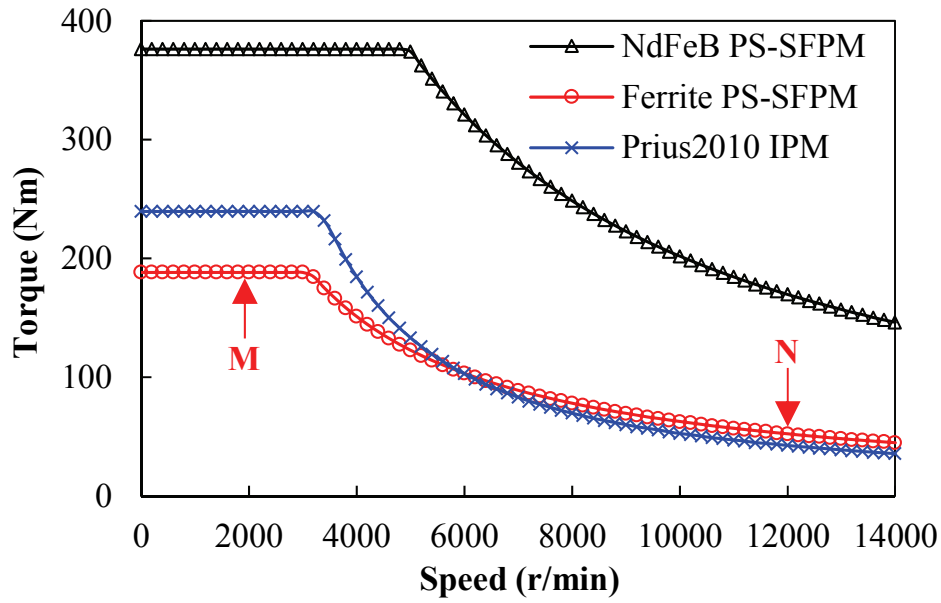


(b) Average torque versus copper loss in armature windings

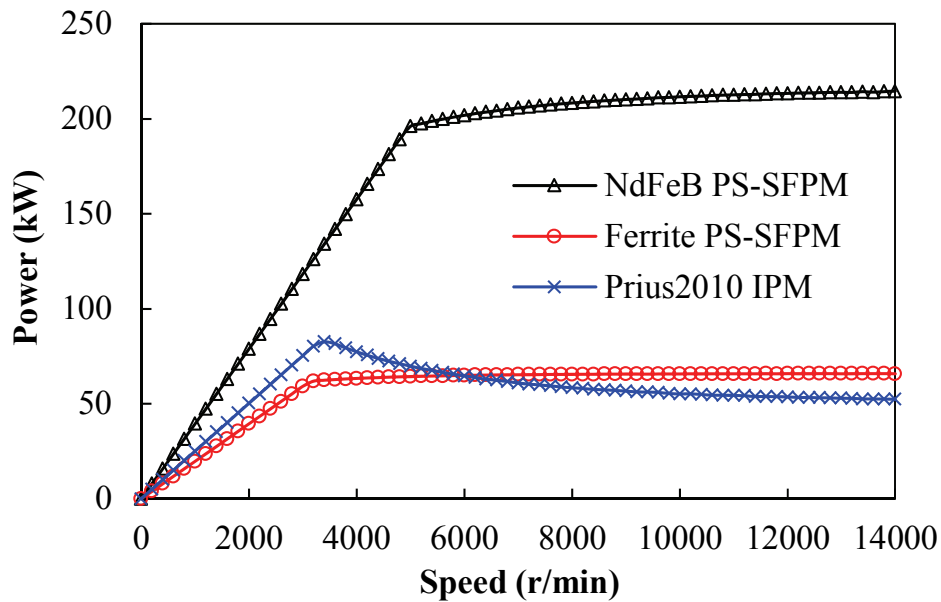
Fig. 3.14 Average torques with different excitations of three Prius2010 IPM-sized machines.

Apart from the torque capability, the flux-weakening performance is important as well. It is known that the Prius2010 IPM machine possesses excellent flux-weakening potential and a wide constant power speed range (CPSR) due to its significant reluctance torque. Thus, the flux-weakening characteristics of the PS-SFPM machines are compared with the Prius2010 IPM machine.

With the identical 650V bus voltage of inverters, the torque-speed and power-speed curves are calculated with flux-linkage method [QI09], and illustrated in Fig. 3.15(a) and (b) respectively. The NdFeB PS-SFPM machine exhibits higher torque over the whole speed range, while the ferrite PS-SFPM machine performs lower torque in the constant torque region but it slightly exceeds the Prius2010 IPM machine in the high speed region. It can be seen from the power-speed behavior in Fig. 3.15(b) that three machines all exhibit wide CPSRs, implying attractive flux-weakening capabilities. Furthermore, the powers at high speed of the two PS-SFPM machines are very close to their peak powers while the Prius2010 IPM machine experiences a significant drop, which reveals that the PS-SFPM machines can guarantee the CPSRs without power falling. Consequently, it can be said that these two PS-SFPM machines possess excellent flux-weakening capabilities.



(a) Torque-speed curves

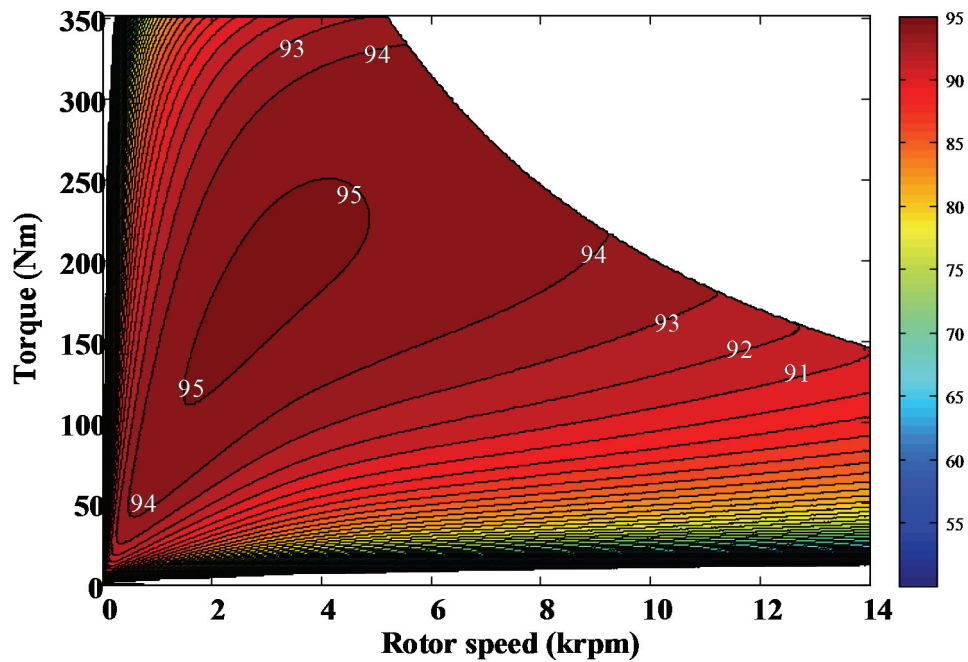


(b) Power-speed curves

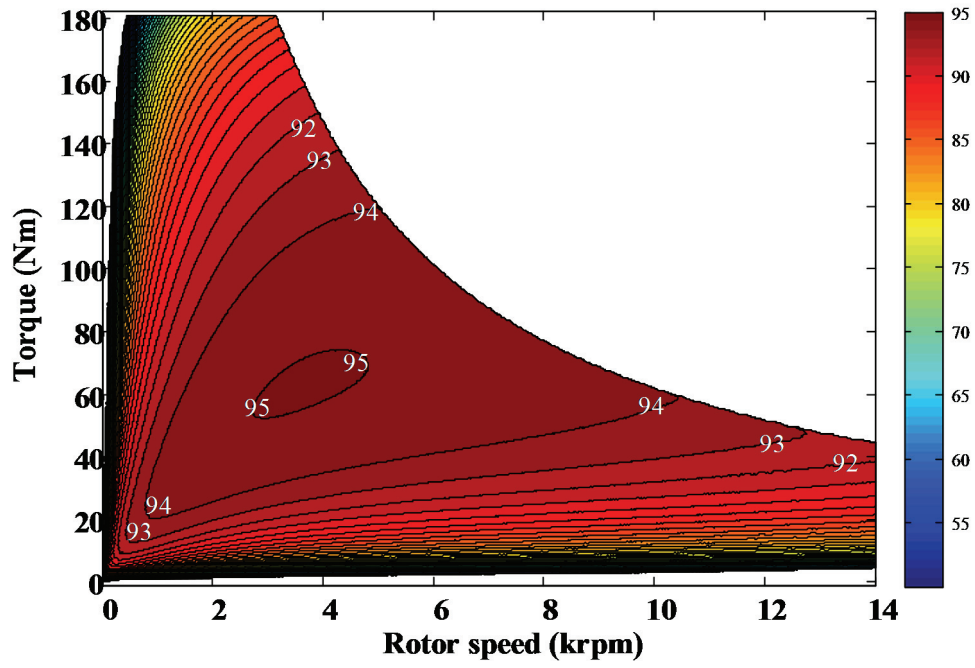
Fig. 3.15 Torque and power characteristics versus speed.

Furthermore, the efficiency maps taking iron losses and copper losses into account among the whole operation range of the three machines are calculated. To obtain the optimum efficiency map, the iron losses and copper losses with different armature currents and current advance angles are swept based on FE analyses, and the highest efficiency at each operating point is obtained. The identical lamination material is used for the three machines to predict the iron loss, and the corresponding hysteresis loss coefficient (K_h), the classic eddy-current loss coefficient (K_c) and the excess eddy-current loss coefficient (K_e) are 261.6W/m^3 ,

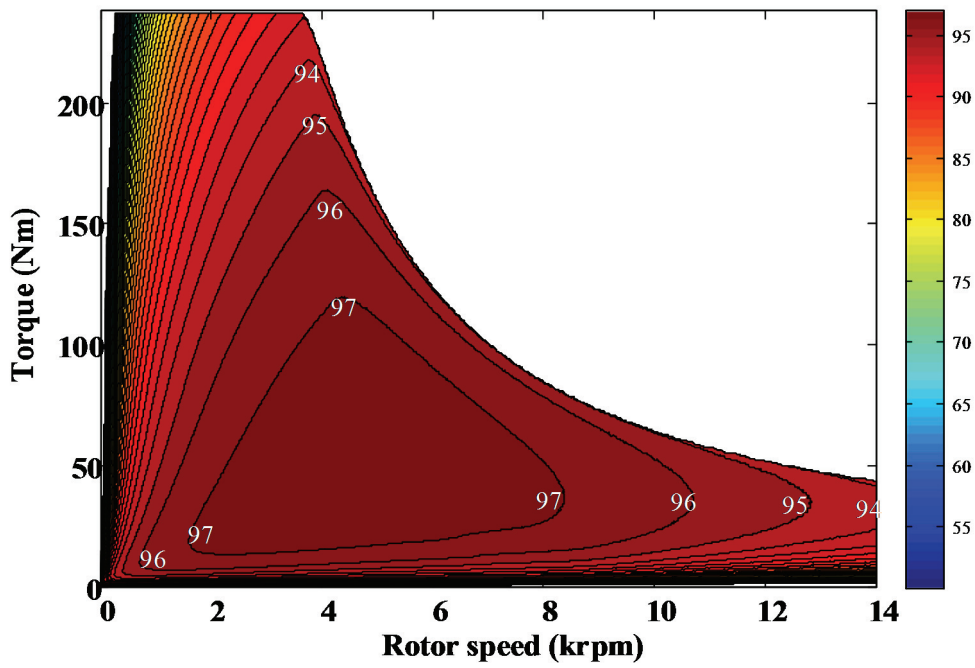
0.10037261.6W/m³ and 3.296261.6W/m³, respectively. Thus, the predicted efficiency maps neglecting PM eddy current losses and mechanical losses of the PS-SFPM and the Prius2010 IPM machines are shown in Fig. 3.16. Although the NdFeB PS-SFPM machine has a very large area exhibiting high efficiency (>94%), the maximum efficiencies of the two PS-SFPM machines are lower than the Prius2010 IPM machine. This can be attributed to the fact that the pole-pair number of the PS-SFPM machines is 10 while the pole-pair number of the Prius2010 IPM machine is 4, with which the iron losses of the two PS-SFPM machines are significantly higher than the Prius2010 IPM counterpart at the same operating speed as the iron loss is remarkably affected by the variation frequency of the flux densities. With the maximum available phase current and the zero *d*-axis current control method for each machine, the calculated iron losses at the operation speed of 1500 r/min of the three machines are shown in Fig. 3.17, where the iron loss on each major component is specified. It can be seen that the iron losses in the two PS-SFPM machines are significantly higher than that in the Prius2010 IPM machine, especially the rotors of the PS-SFPM machines suffer relatively high iron loss due to the significant variation of flux distributions.



(a) NdFeB PS-SFPM machine



(b) Ferrite PS-SFPM machine



(c) Prius2010 IPM machine

Fig. 3.16 Efficiency maps considering iron losses and copper losses.

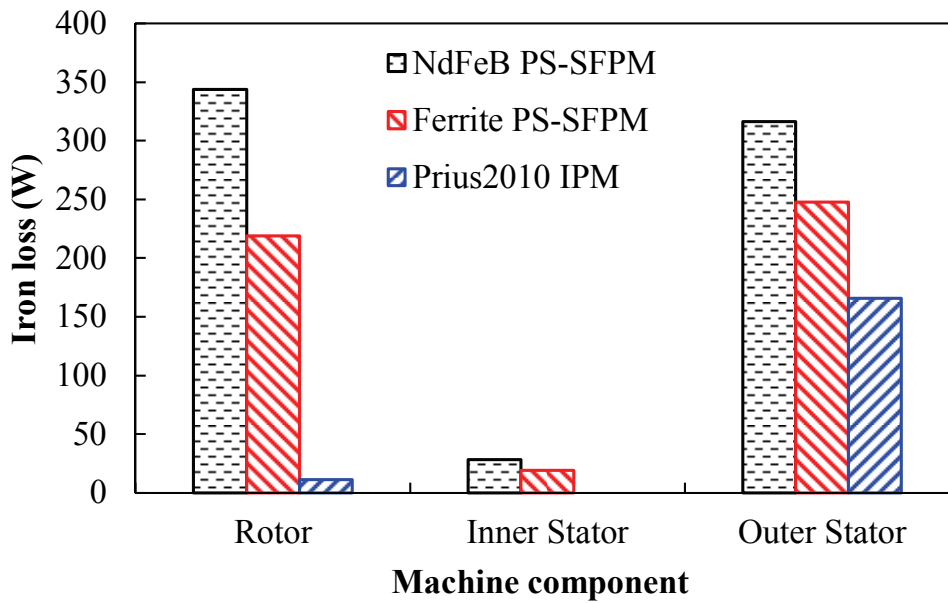


Fig. 3.17 Iron losses at 1500 r/min with maximum available phase current and zero d-axis current control.

3.4.3 Economic issue

The material usage and cost of the three machines are summarized in Table 3.4, in which the cost of the NdFeB PS-SFPM machines is the highest due to the large consumption of expensive NdFeB PM, while the cost of the ferrite machine is significantly lower than the two NdFeB machines. Accordingly, their material usage efficiencies are compared in Fig. 3.18, and it can be observed that the ferrite PS-SFPM machine benefits from low cost and thus excellent material usage efficiency, whereas the NdFeB PS-SFPM and Prius2010 IPM machines are comparable with light load but the NdFeB PS-SFPM is easily affected by magnetic saturations.

Table 3.4 Material usage and cost of three Prius2010 IPM-sized machines.

Items	Prius2010 IPM	NdFeB PS-SFPM	Ferrite PS-SFPM
Copper usage (kg)	4.95	6.50	5.60
Copper cost (USD)	54.5	71.51	61.59
Lamination usage (kg)	14.85	10.29	8.31
Lamination cost (USD)	29.7	20.6	16.6
NdFeB usage (kg)	0.78	2.50	N/A
NdFeB cost (USD)	117.2	374.3	N/A
Ferrite usage (kg)	N/A	N/A	3.15
Ferrite cost (USD)	N/A	N/A	15.8
Total cost (USD)	201.4	466.4	94.0

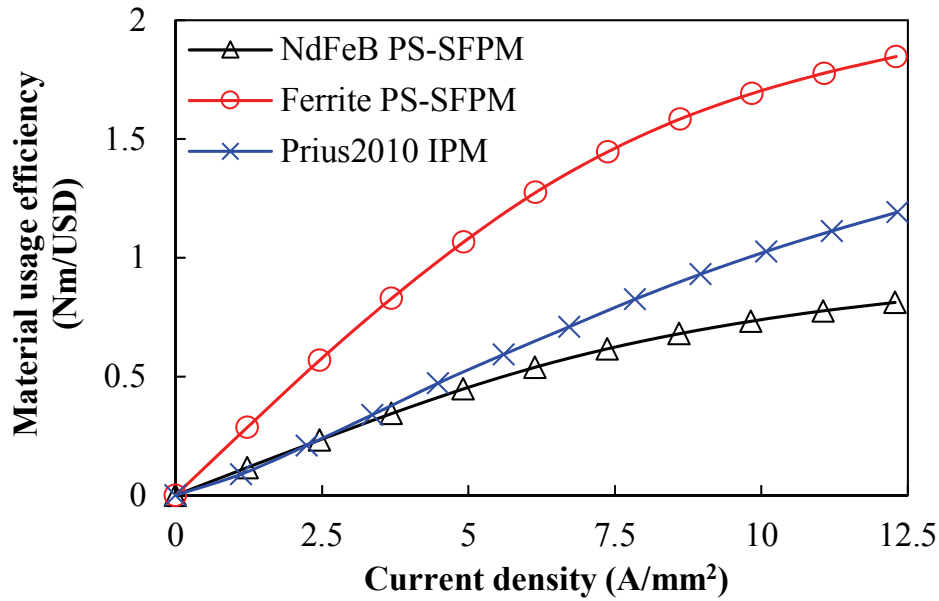


Fig. 3.18 Material usage efficiency versus different excitations of three Prius2010 IPM-sized machines.

3.4.4 Demagnetization of ferrite PS-SFPM machine

Due to the employment of ferrite PM, the irreversible demagnetization behaviour should be evaluated, especially in the Prius2010 IPM-sized ferrite machine with large armature excitations. The ferrite PM is more vulnerable to irreversible demagnetization in low temperature conditions as it has a positive temperature coefficient of coercivity [FAS14],

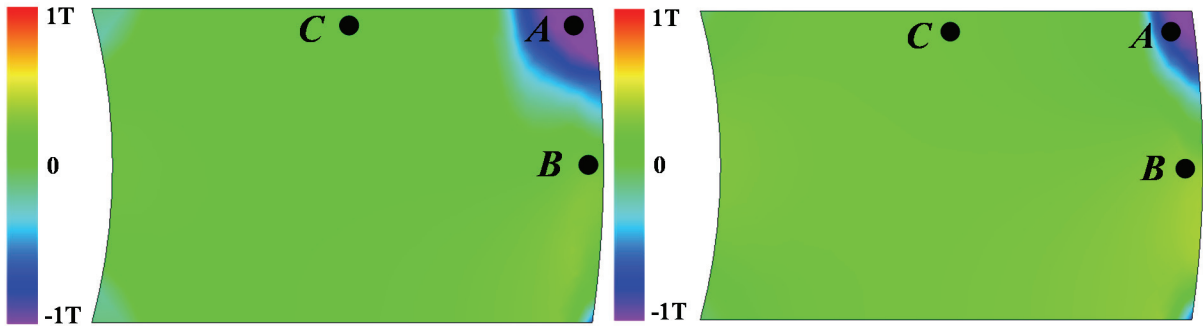
[LI15]. Consequently, the operation with the temperature at $-20\text{ }^{\circ}\text{C}$ is set as the worst conditions to investigate the demagnetization performance.

The negative d -axis current threatens the ferrite PMs directly while the q -axis current can demagnetize the PMs according to the cross-coupling effect. Thus, the operation points have different effects on demagnetization and the most vulnerable points should be found out. In the constant torque region, the current is fully utilized for maximum torque, and the cross-coupling phenomenon is significant. Alternatively, in the high speed region, the negative d -axis current is employed to realize flux-weakening, which also brings a high risk of irreversible demagnetization. Therefore two typical operating points, as “M” and “N” illustrated in Fig. 3.15(a), are picked out, which symbolize the two operating conditions suffering the highest risk of irreversible demagnetization.

The distributions of flux density along the magnetization direction in the ferrite PM, when the ferrite PS-SFPM machine is operated at points M and N, are illustrated in Fig. 3.19(a) and (b) respectively. Although the flux densities among major portions are higher than 0T , which is the demagnetization limit of this ferrite PM, the corner portions close to the air-gap suffer the reversed magnetization. This implies the partially irreversible demagnetization may occur in these portions. Meanwhile, it can be observed that the constant torque operation (point M) has a larger area suffering the partially irreversible demagnetization.

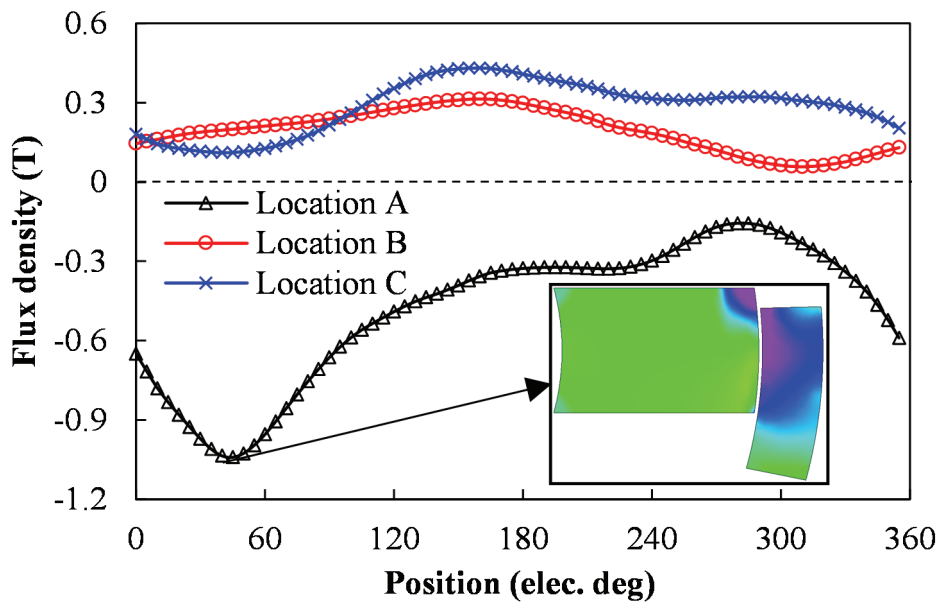
Moreover, the rotor position has an effect on the demagnetization as well, and hence, the worst rotor position should be identified. The flux densities at three typical locations in the PM, marked as “A”, “B”, and “C” in Fig. 3.19, are presented in Fig. 3.20, in which two operations are both evaluated. The location A, which represents the corner portion, suffers the lowest flux densities, while other two locations have the flux densities always higher than the demagnetization limit. Meanwhile, the location A suffers a lower flux density in the constant torque operation. More importantly, it can be found that the minimum flux density at location A always occurs at around 50° electrical degrees, where the rotor is approaching the corner of PM.

According to the previous analysis, the most vulnerable conditions to the irreversible demagnetization have been identified. In the constant torque operation, the minimum flux density at the location A along the magnetization direction during one electric period can be set as the indication of demagnetization. The partially irreversible demagnetization would happen in the ferrite PS-SFPM machine if the minimum flux density is less than 0T .

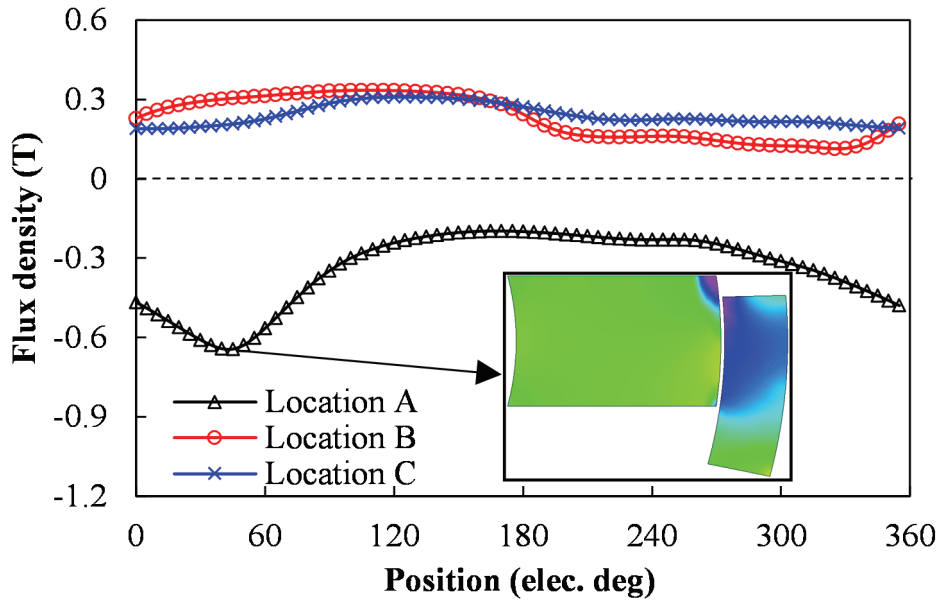


(a) In constant torque region (M), 2000 r/min, I_{rate} , -12° current angle (b) In high speed region (N), 12000 r/min, $0.33 I_{rate}$, 51° current angle

Fig. 3.19 Distributions of flux density along the magnetization direction in the ferrite PMs during operating points M and N respectively.



(a) In constant torque region (operating point M)



(b) In constant power region (operating point N)

Fig. 3.20 Flux density along the magnetization direction at three typical locations in the ferrite PMs.

To improve the capability to withstand demagnetization whilst maintaining the torque output, the pole tip is introduced. The pole tip is located in the inner stator of the Ferrite PS-SFPM machine, which surrounds the corner of PM, as illustrated in Fig. 3.21. As a result, the corner portion of PM is protected by the iron and thus the partially irreversible demagnetization can be alleviated. There are two parameters affecting the shape of pole tip, i.e. pole tip height and pole tip arc. Fig. 3.22(a) shows the minimum flux densities against different pole tip heights and arcs, in which the high flux density and hence the good demagnetization withstand capability can be obtained, especially by increasing the pole tip height. Meanwhile, the effects of pole tip on the average torque are illustrated in Fig. 3.22(b), in which the torque output can be kept at a high value by carefully picking the combination of pole tip parameters.

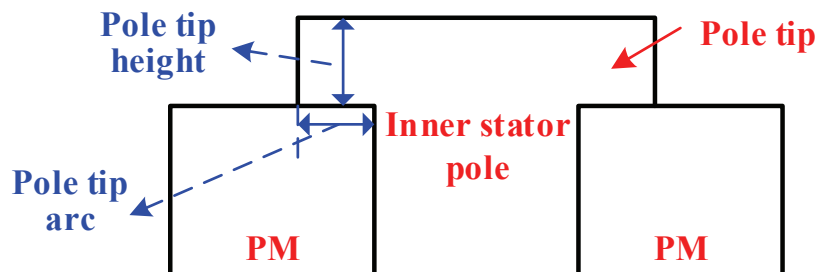
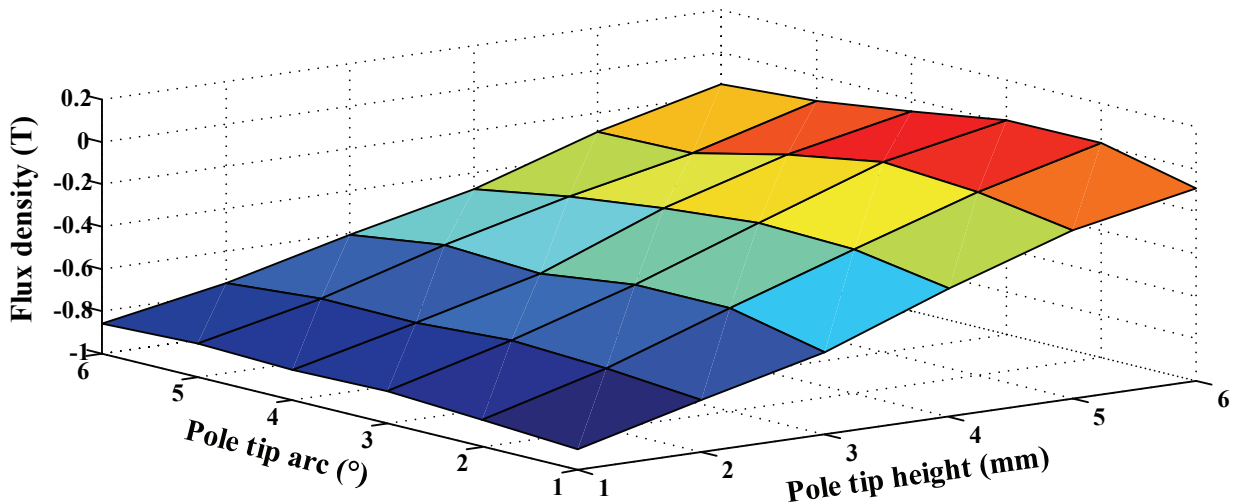
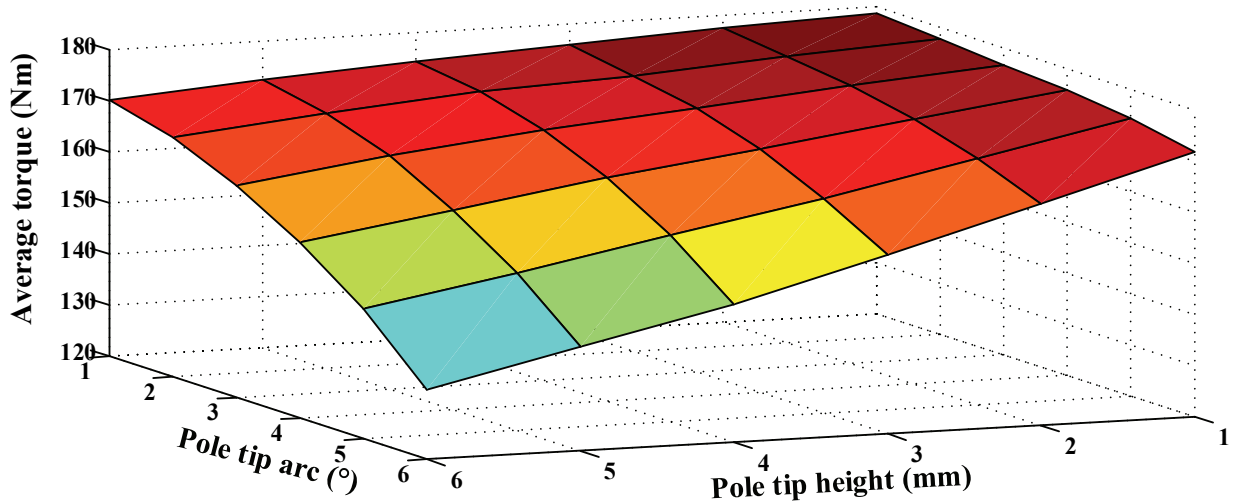


Fig. 3.21 Illustration of improved inner stator with pole tip.



(a) Minimum flux density along magnetization direction at location A.



(b) Average torque with rated current and current angle generating the highest torque

Fig. 3.22 Effects of pole tip parameters on average torque and capability of resisting irreversible demagnetization during operation M.

An optimal Ferrite PS-SFPM machine with the pole tip, compromising the torque output and robustness towards demagnetization, is obtained, whose pole tip height and arc are 6 mm and 2° respectively. Fig. 3.23 shows the flux density distributions of the new design with pole tip in the constant torque operation, and it has much smaller areas suffering irreversible demagnetization, compared with the original design in Fig. 3.19(a). In constant torque operation, the flux densities at location A in ferrite PM are compared in Fig. 3.24, where the new design always exhibits the flux density higher than 0T, which is superior to the original one. Furthermore, as the average torques against excitations shown in Fig. 3.25, the torque of the new design is just a little lower than the original machine (less than 5%). Consequently, it

can be found that the new design with pole tip can greatly enhance the irreversible demagnetization withstand capability while the torque output is maintained.

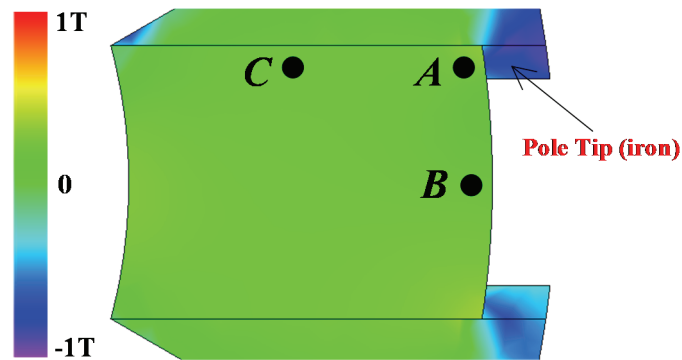


Fig. 3.23 Distributions of flux density along the magnetization direction in the ferrite PMs with optimized pole tip during operation M.

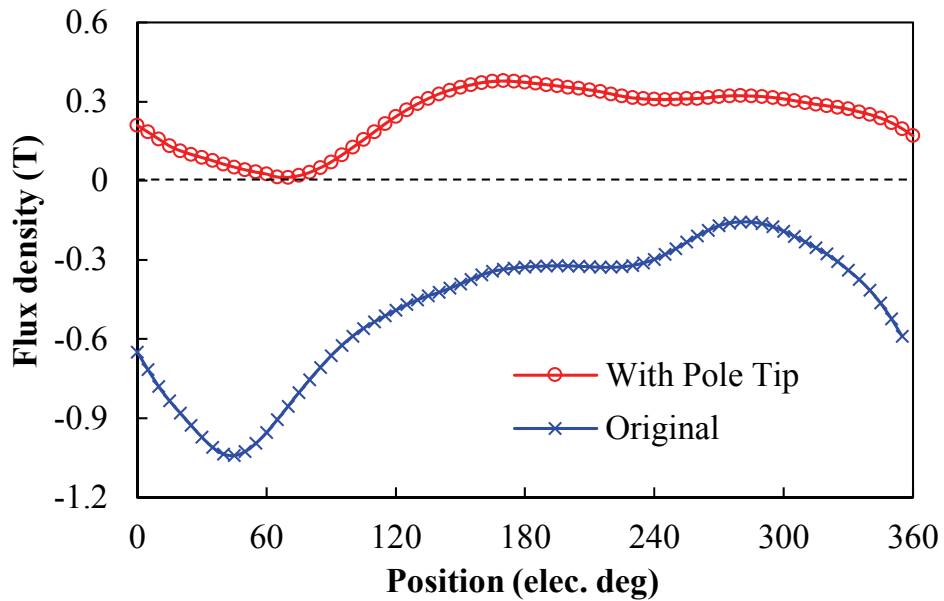


Fig. 3.24 Comparison of flux density along the magnetization direction at location A during operation M.

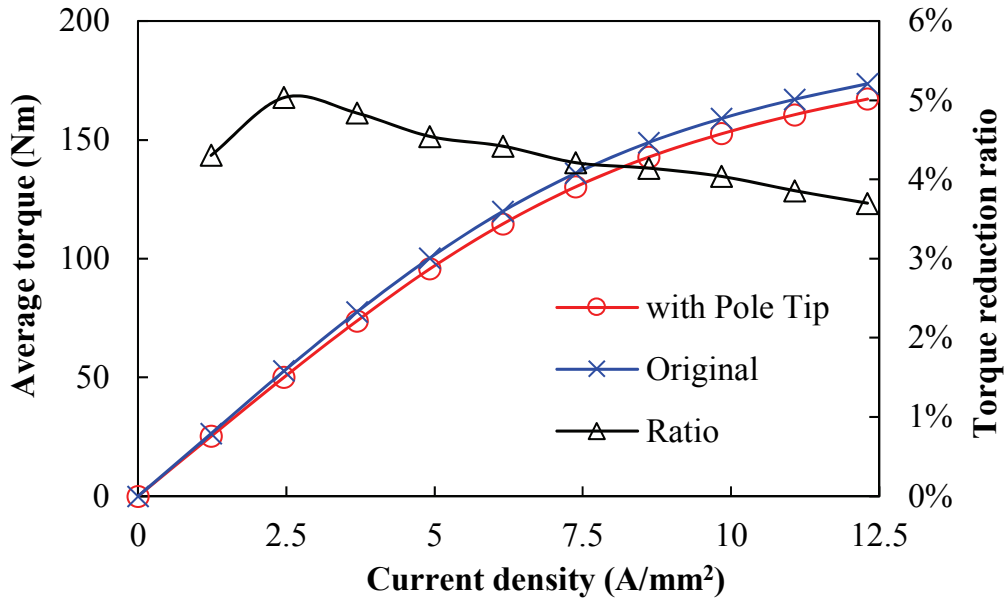


Fig. 3.25 Comparison of average torque versus excitation.

3.4.5 Mechanical analysis of the cup-rotor

Since the cup-rotor is employed, the PS-SFPM machines suffer high mechanical stress [SUN12], [BAI16], [TER16], [SUN15]. Considering the fact that the Prius2010 IPM-sized machine diameter is relatively large, it is of value to have an insight to its mechanical characteristics.

The mechanical structure of the cup-rotor is shown in Fig. 3.26, where the separated rotor pieces are fixed and supported by a bracket. The bracket consists of non-magnetic bars, an end plate and a shaft, in which ten bars are interlaced with the rotor pieces, and the end plate assembled with a shaft is coupled to the bars. Besides, in order to further improve the mechanical strength, a carbon-fiber bandage can be employed to firm the rotor [SUN12], [BIN06]. The mechanical properties of materials used in rotor are listed in Table 3.5.

As the ferrite PS-SFPM machine has the rotor with a larger radius than the NdFeB counterpart, it suffers higher centrifugal force and is more vulnerable to the mechanical failure. Thus its mechanical stress is evaluated, and the rotation speed of 13500 r/min, which is the highest operation speed of the Prius2010 IPM machine, is applied. With the 0.5mm bandage, the Von-Mises stress and deformation of the ferrite PS-SFPM machine are shown in Fig. 3.27. The maximum Von-Mises stress is around 373 MPa, which occurs on the bandage, while the stress on the rotor is always less than 198 MPa. The maximum stress is lower than the stress limits of the corresponding materials, which indicates that the rotor can operate securely. In

addition, the maximum deformation of the rotor is 0.103mm, and it can be seen that the portions farther away from the end plate significantly suffer more severe deformation.

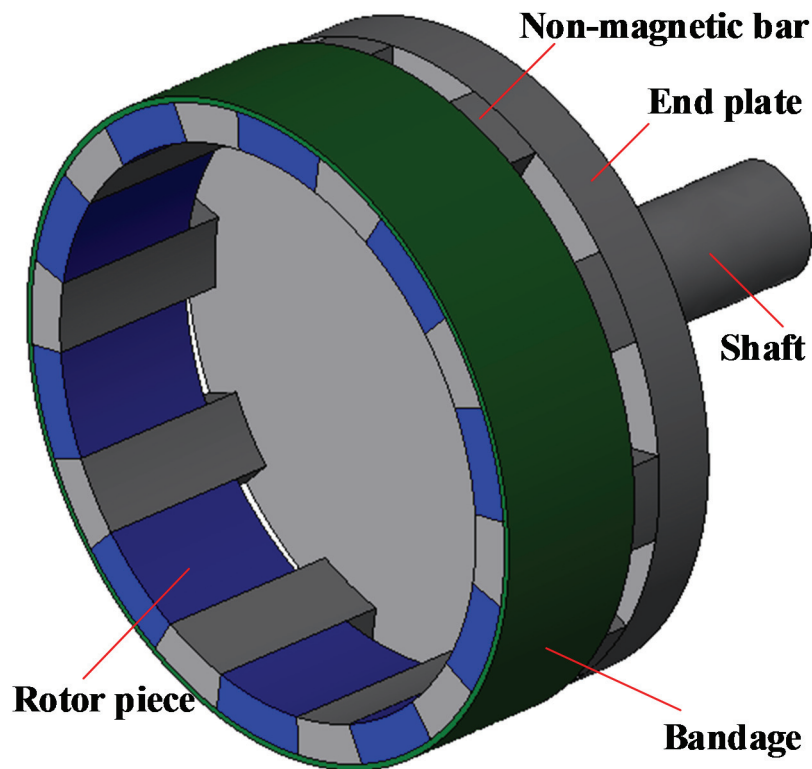
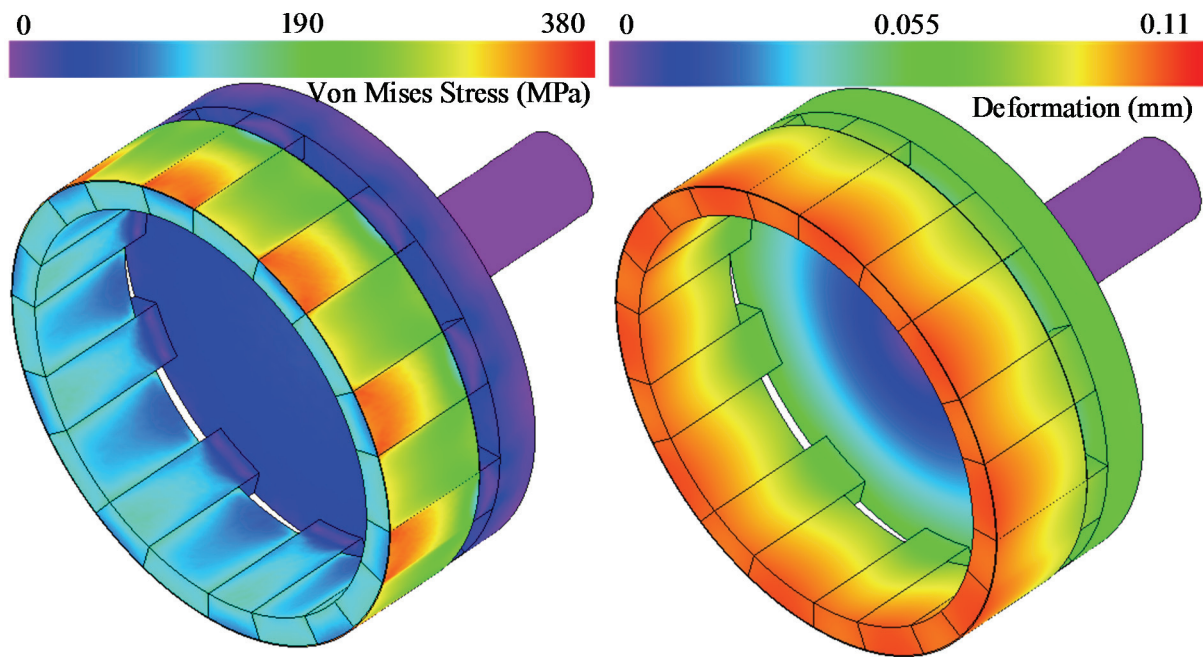


Fig. 3.26 Mechanical structure of the cup-rotor in PS-SFPM machines.

Table 3.5 Mechanical properties of the cup-rotor materials.

	Rotor piece	Bracket	Bandage
Material	Steel lamination	Titanium alloy	Carbon-fiber
Mass density (kg/m^3)	7780	4340	1840
Young's modulus (GPa)	210	116	440
Poisson's ratio	0.33	0.32	0.307
Stress limit (MPa)	412	880	2400

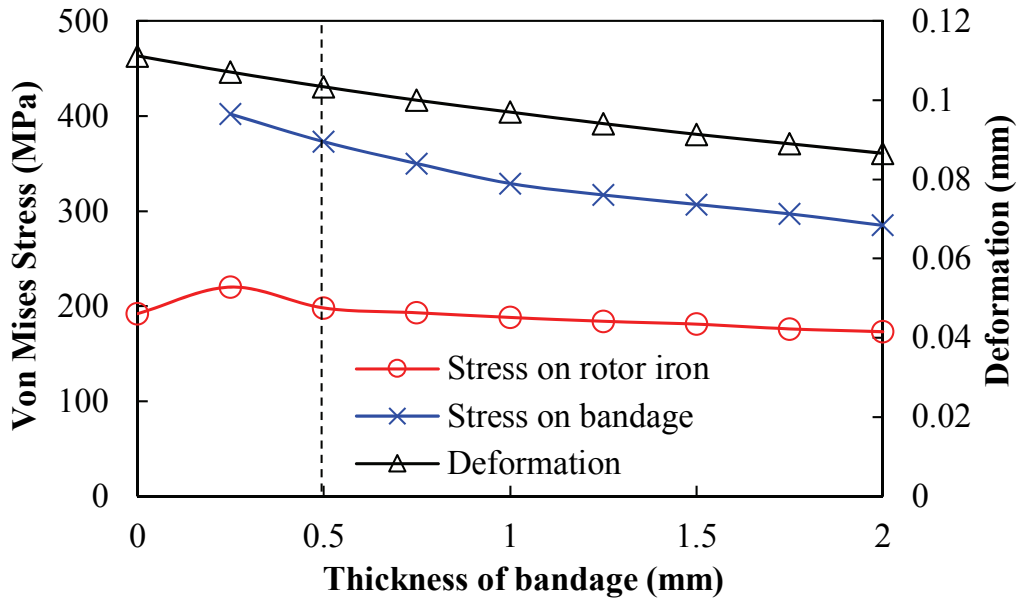


(a) Von-Mises stress

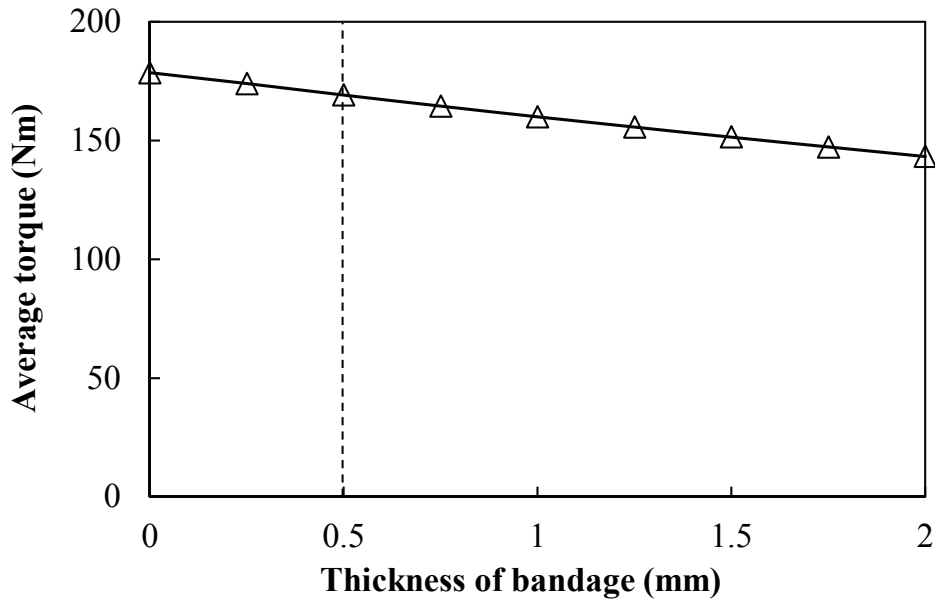
(b) Deformation

Fig. 3.27 Rotor stress and deformation distributions at 13500 r/min.

The 0.5mm bandage is employed in the previous analysis and it is of value to further investigate the effect of bandage thickness. With the fixed air-gap length of 0.73mm, the mechanical characteristics, including the maximum Von-Mises stress on bandage, maximum stress on rotor iron pieces and the maximum deformation, with different bandage thicknesses are illustrated in Fig. 3.28(a). It can be found that the stress and deformation are both reduced by employing a thicker bandage. However, the thicker bandage will contribute to a larger equivalent air-gap length and thus sacrifice the torque output. The average torques versus different bandage thicknesses are shown in Fig. 3.28(b), and the 0.5mm bandage makes the torque decrease by 5.44%. It should be noted that the torsion along the axial direction of the rotor iron-pieces are not taken into account in the calculation of torque output of PS machines.



(a) Rotor stress and deformation at 13500 r/min



(b) Average torque with rated current and the current angle generating the highest torque

Fig. 3.28 Effects of bandage thickness on rotor stress, deformation and average torque.

3.5 Prototyping and Validation

To verify the operation principle and analysis of PS-SFPM machines, a pair of small prototypes, adopting NdFeB and ferrite PMs respectively, are manufactured and tested. The key design parameters of the prototypes are listed in Table 3.6, and the essential components are presented in Fig. 3.29. The outer stators of the PS-SFPM machines are identical to the stator of a classic fractional-slot PM machine, Fig. 3.29(a) and (b), indicating good manufacturability.

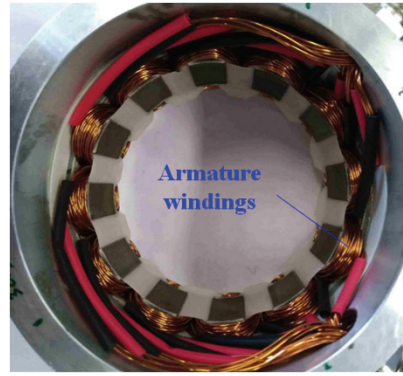
Meanwhile, it can be noted that the stator inner radius of the ferrite PS-SFPM machine is significantly larger than the NdFeB one, with which more space for PMs is provided. The inner stators with 12 pieces of tangentially magnetized PMs are shown in Fig. 3.29(c) and (d), which are similar to the rotor of a spoke-type IPM machine but they are stationary. The volume of ferrite PM is much larger than the NdFeB PM. Further, two cup-rotors, which are the most challenging components in fabrication, are shown in Fig. 3.29(e) and (f). The iron rib is employed to connect the individual rotor iron pieces, which can facilitate the fabrication. Then the rotor pieces are encapsulated in the resin and supported by the non-magnetic bars made of aluminum, which are coupled to the non-magnetic end plate with shaft. Accordingly, the assembled rotor can be connected to the machine frame via bearings.

Table 3.6 Key design parameters of PS-SFPM prototypes.

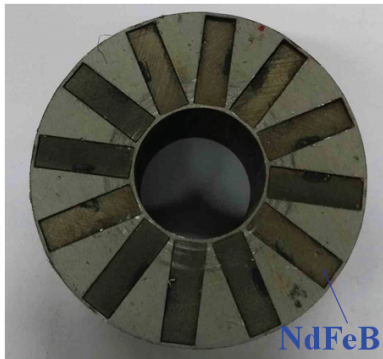
Parameters	NdFeB PS-SFPM	Ferrite PS-SFPM
Axial length (mm)	25	25
Stator outer radius (mm)	45	45
Stator inner radius (mm)	31.75	38
Air-gap length (mm)	0.5	0.5
Rotor radial thickness (mm)	5	4.7
Rotor rib thickness (mm)	0.5	0.35
Inner stator inner radius (mm)	10.19	10.19
Coil number per phase	4	4
Turn number per coil	18	18
B_r (T)	1.2	0.41
H_c (kA/m)	-910	-250



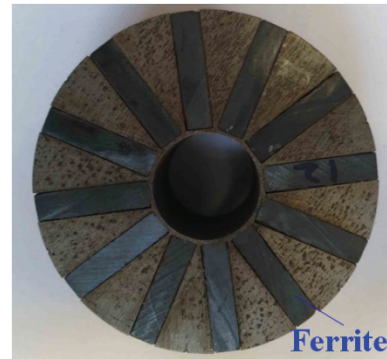
(a) Outer stator, NdFeB machine



(b) Outer stator, ferrite machine



(c) Inner stator, NdFeB machine



(d) Inner stator, ferrite machine



(e) Rotor, NdFeB machine



(f) Rotor, ferrite machine



(g) Assembled stators, NdFeB machine



(h) Assembled stators, ferrite machine

Fig. 3.29 Prototypes of NdFeB and ferrite PM PS-SFPM machines.

The measured phase back-EMFs at 400 r/min of the two prototypes are compared with the 2-D and 3-D FE predictions in Fig. 3.30. Due to the identical rotor piece numbers, the frequencies of back-EMFs are identical in the two prototypes. It can be seen that the cycles of the test results are the same as predictions. The back-EMF amplitude of the NdFeB PS-SFPM machine is higher than the ferrite counterpart due to the strong NdFeB PMs. Meanwhile, since the magnetic saturation is more severe in the NdFeB machine, its end flux-leakage is more significant. By way of example, Fig. 3.31 shows the open-circuit z-axis flux densities, where the NdFeB PS-SFPM machine has significantly higher z-axis flux density, Fig. 3.31(a), which reveals it suffers more severe end effect than the ferrite PS-SFPM counterpart, Fig. 3.31(b). In general, the 3D-FE predicted results agree well with the test results, although they are 4.2% and 5.0% lower than the measurements in the NdFeB and ferrite PS-SFPM machines, respectively. The potential causes of the difference between the FE and test results are similar to the discussion in section 2.6.

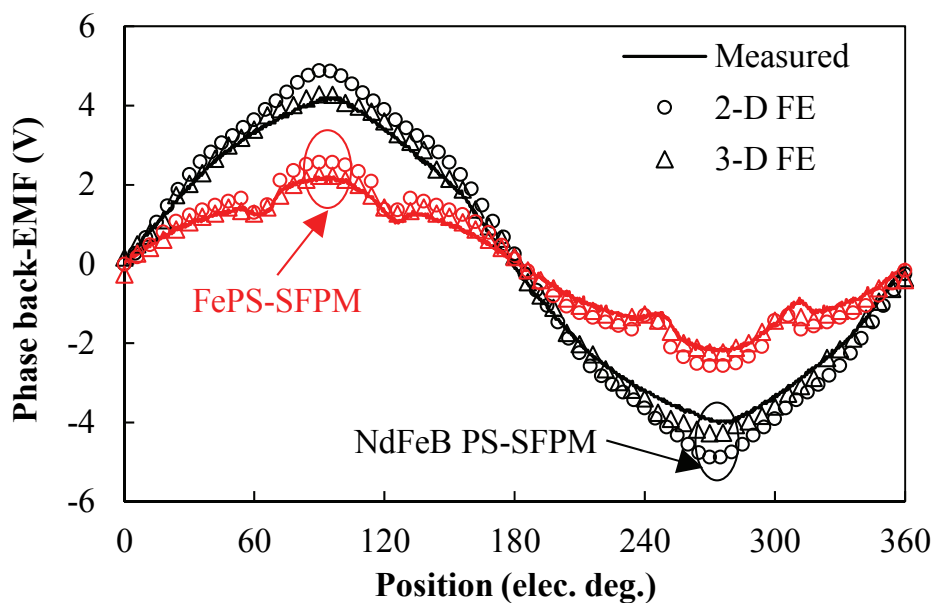
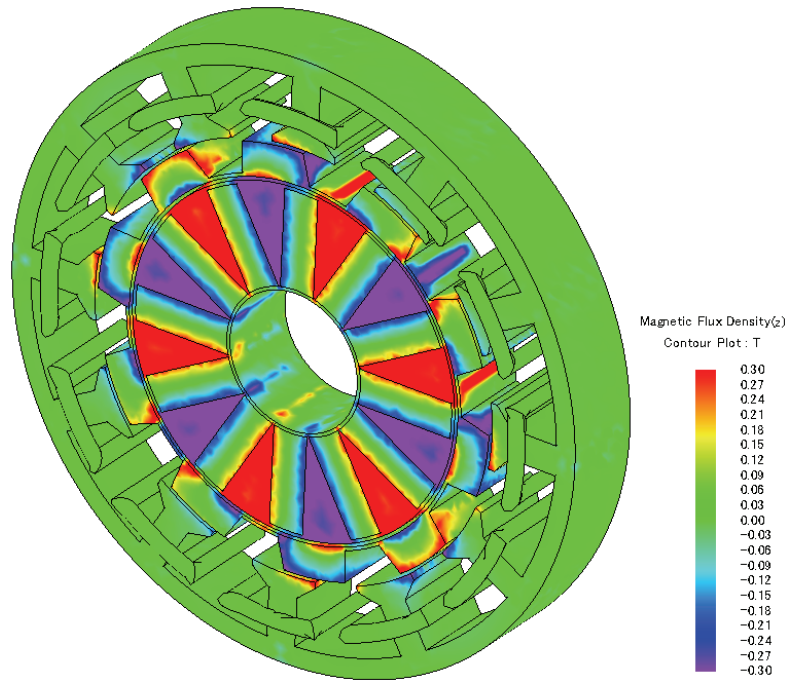
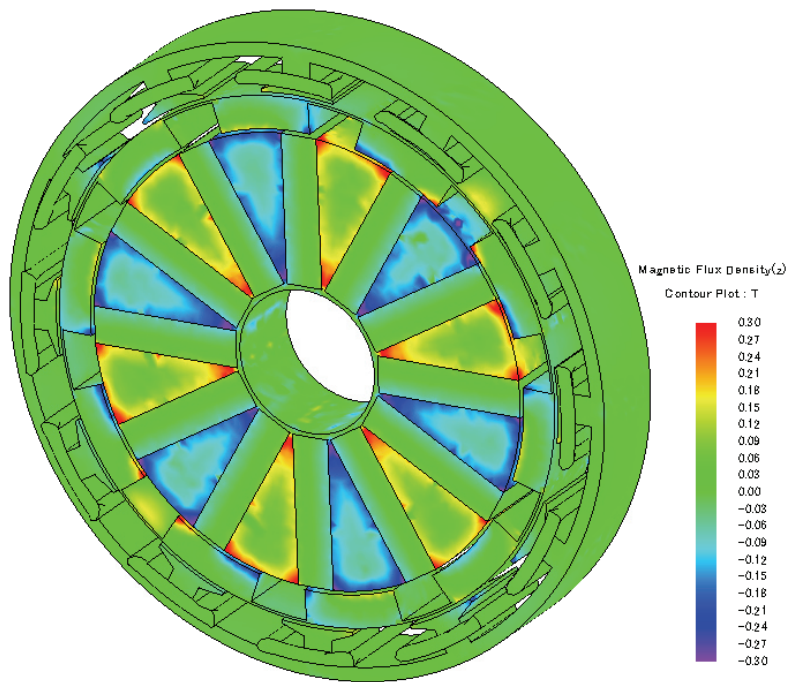


Fig. 3.30 Measured and 2-D, 3-D FE-predicted phase back-EMFs at 400 r/min.



(a) NdFeB PS-SFPM machine

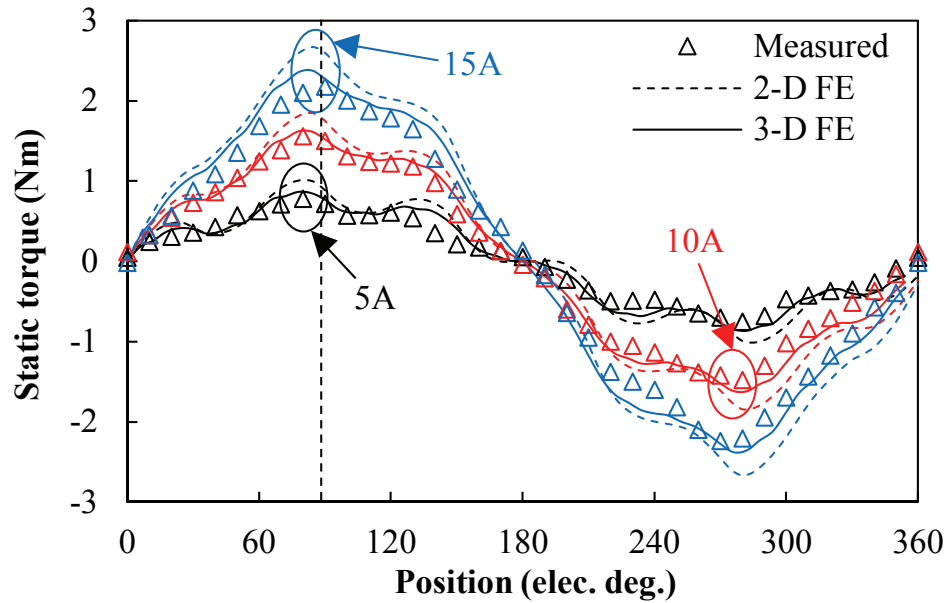


(b) Ferrite PS-SFPM machine

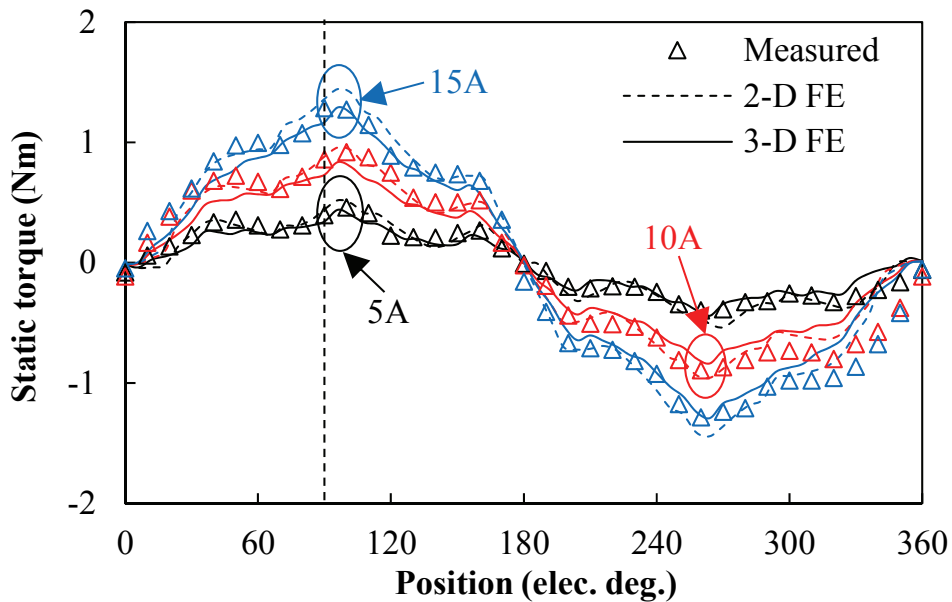
Fig. 3.31 Open-circuit z-axis flux density.

Furthermore, based on the test-rig shown in Fig. 2.26, the static torque waveforms versus rotor positions with different excitations are measured and shown in Fig. 3.32, where the test results agree well with the 3-D FE predictions. Meanwhile, it can be seen that the peak torques always occur around 90° , which is exactly q -axis position and thus indicates that the reluctance torque is negligible. Moreover, the torque waveforms with sinusoidal currents injected into

three-phase armature windings ($I_d=0$ control), are measured and presented in Fig. 3.33. The torque ripples can be observed in the torque waveforms. There are 6 torque ripple cycles during one electric period in both machines, which corresponds to the previous analysis. It should be noted that the current angle of the injected current is related to the rotor position, which may suffer the error in the recording as the rotor position on the lathe is read by eyes.

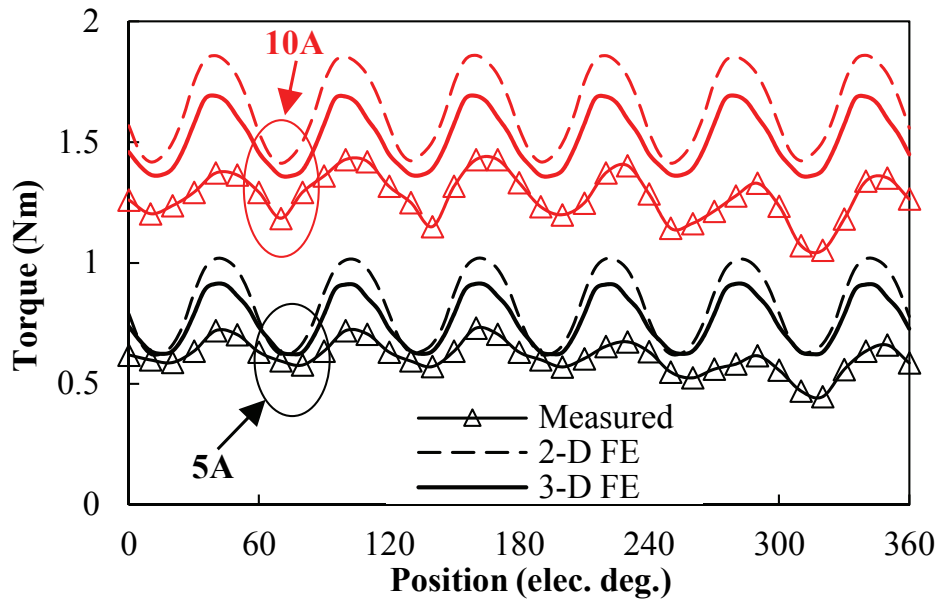


(a) NdFeB PS-SFPM machine

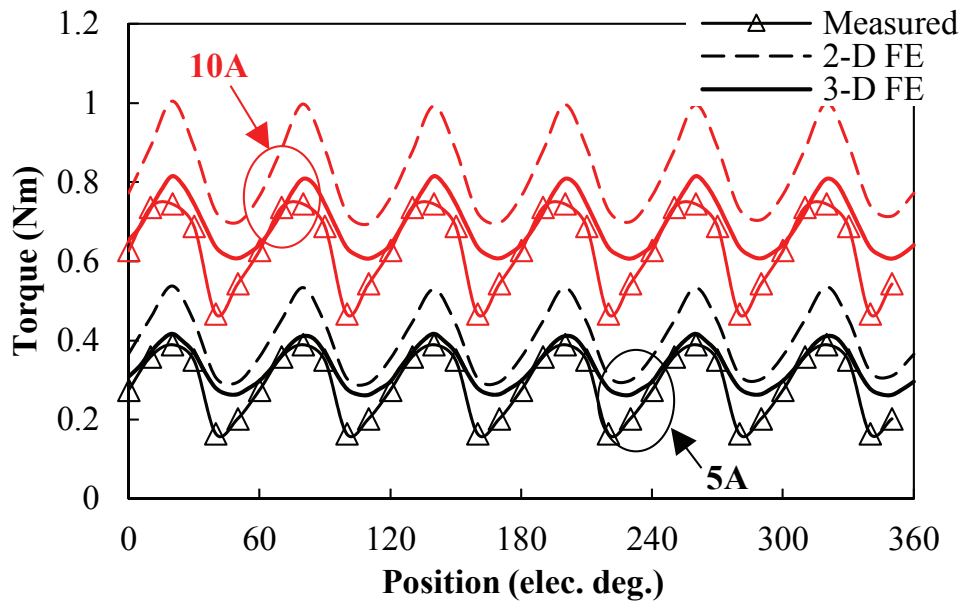


(b) Ferrite PS-SFPM machine

Fig. 3.32 Measured and 2-D, 3-D FE-predicted static torque.



(a) NdFeB PS-SFPM machine



(b) Ferrite PS-SFPM machine

Fig. 3.33 Measured and 2-D, 3-D FE-predicted torque waveforms with $I_d=0$ control.

3.6 Conclusion

In this chapter, the ferrite PS-SFPM machine is proposed to extend the family of the PS machines, and it features with low-cost PM material but high torque density. Then the PS-SFPM machines employing NdFeB and ferrite PMs respectively are evaluated and compared, the small machines and large Prius2010 IPM-sized machines are both investigated. It is found that the ferrite PS-SFPM machine also has high torque density due to the large available space

for accommodating PMs, whilst the cost is greatly reduced and a higher material usage efficiency is obtained, which is attractive in cost-sensitive applications. Meanwhile, the most vulnerable operating points to the irreversible demagnetization are identified in the ferrite PS-SFPM machine, and the pole tip of inner stator is proposed to enhance the irreversible demagnetization withstand capability. However, it should be noted that the PS-SFPM machines suffer the more complicated structure and the mechanical weakness.

Chapter 4. Hybrid Excited Switched Flux Machine with Separate Field Winding Stator

The PS machines employing different PM configurations and PM materials in the excitation stator have been investigated in Chapter 2 and Chapter 3 respectively. It is revealed that the improved torque density is obtained in the PS machines thanks to the enlarged available space. Nevertheless, in the variable-speed applications, the excellent flux controllability is an essential requirement as well. Therefore, a novel HE machine based on the conventional SFPM machine but employing an additional stator equipped with FWs, is proposed in this chapter. The proposed machine benefits from the enlarged available space, and the higher torque density as well as better flux controllability. The electromagnetic performance of the proposed machines is evaluated in detail, together with a conventional stator-excited HE machine as a baseline. Meanwhile, the effects of slot/pole combinations are investigated.

This part has been published in IEEE Transactions on Magnetics.

4.1 Introduction

The employment of PM greatly improves the efficiency and torque density of electric machines. But it also results in a relatively constant air-gap field and thus limits the flux controllability, which restricts the applications in the variable-speed drive systems. Therefore, the HE machines which simultaneously employ PMs and FWs, are being developed to boost the flux-weakening capability [LAL15]. As a result, an additional degree of freedom, i.e. ratio between PM flux and FW flux, is obtained, which is helpful to realize a wide constant power speed range (CPSR) and maintain high power factor [CAP15], [AMA09].

Based on the conventional SFPM machine, the HE switched flux (HESF) machines are proposed to obtain the HE structure, which inherit the benefits of stator-PM machines and avoid sliding contact [AKE01]. In fact, this machine type belongs to the bipolar flux stator-excited machines, as introduced in Fig. 1.8 and Fig. 1.9 in Chapter 1. A variety of HESF machine topologies have been investigated. In [HOA07], an outermost iron ring with concentrated FWs is connected to the stator yoke of conventional SFPM machine, with which the flux-weakening and flux-enhancing can be easily achieved. In addition, based on the identical laminations of SFPM machine, a HESF machine can be obtained by reducing the PM volume whilst placing

FWs in the saved space [HUA09]. The relative locations of PMs and FWs are investigated [OWE09], [HUA15], [ZHA15b]. Meanwhile, the iron bridge neighboring the PM can be employed to facilitate the flux regulation [OWE10a]. However, it can be found that the PM flux would partially short-circuit, sacrificing the torque density. Besides, the HESF machine based on E-core SFPM topology is presented by simply arranging the FWs around the fault-tolerant teeth [CHE11b]. But its flux regulation capability is limited since two field coils beside one armature coil tend to generate the fluxes having reversed polarities. In [GAU14], a simple HESF machine is obtained by directly allocating the FWs in the armature winding slots of conventional SFPM machine, with which only the flux-weakening can be achieved via magnetic saturation. In [DUP16], the claw pole structure combined with a toroidal FW is attached to the stator yokes of a conventional SFPM machine, where the 3-D flux is produced to regulate the air-gap flux.

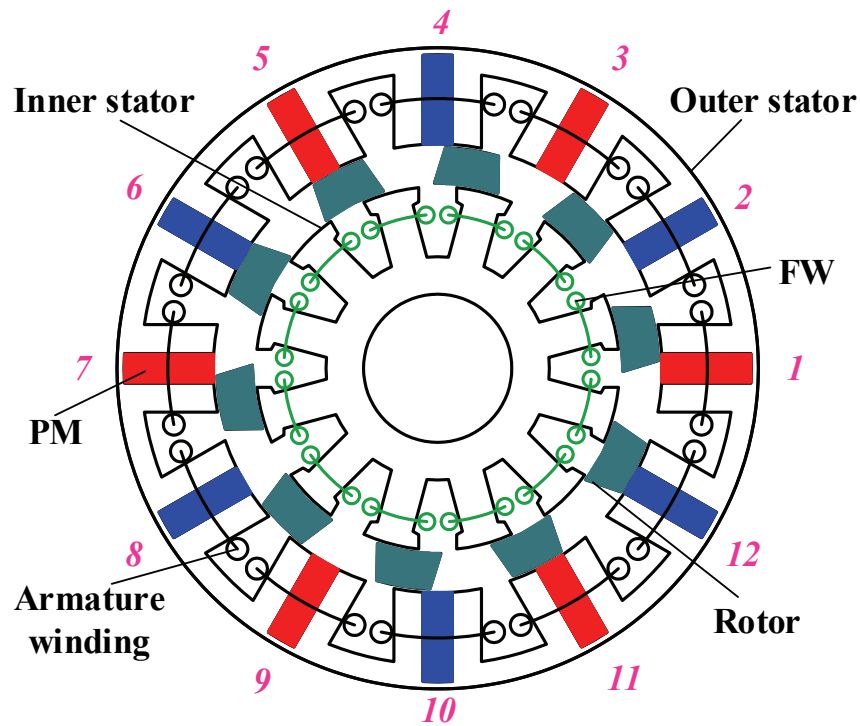
It can be noted that all the previously introduced HESF machines dispose armature windings, FWs as well as PMs on the one stator, suffering from crowded stator and poor space utilization, which greatly sacrifice the torque density and flux regulation capability. Therefore, the dual stator (DS) HESF (DS-HESF) machine having a secondary stator to accommodate FWs, is proposed and investigated in this chapter.

This chapter is organized as follows. The topology and operating principle of the proposed machine will be presented in section 4.2. Afterward, based on 2-D FE analysis, the electromagnetic performances of the DS-HESF machines with different rotor-pole numbers are compared in detail in section 4.3, accompanied with a conventional HESF machine as a baseline. Moreover, the effects of the iron bridge on the hybridization ratio will be clarified in section 4.4. Finally, in section 4.5, a prototype machine is tested to validate the predictions.

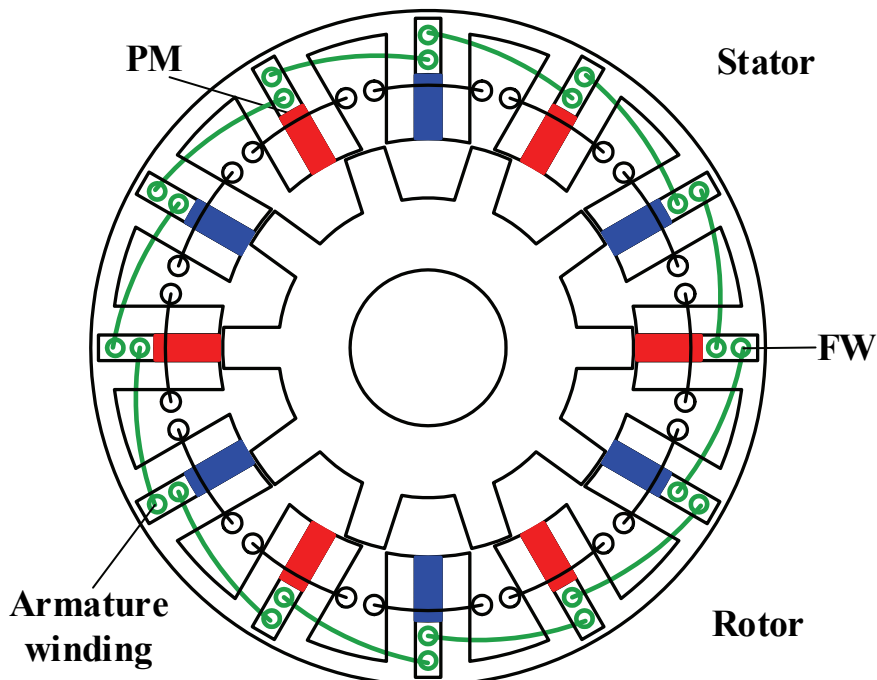
4.2 Machine Topology and Operating Principle

The three-phase 12-stator-slot/10-rotor-pole DS-HESF machine is presented in Fig. 4.1(a), in which two stators are employed and an iron-piece-rotor is sandwiched between them. The outer stator is the same as the stator of the conventional SFPM machine, which accommodates concentrated non-overlapping armature windings as well as tangentially magnetized PMs in stator teeth. Meanwhile, the inner stator has the identical pole number to outer stator, and the inner stator teeth are aligned with the outer stator slots. Moreover, the concentrated non-overlapping FWs are wound around the inner stator teeth. Compared with the conventional

HESF machine shown in Fig. 4.1(b), the feature of the rotor that is free from PM and coil is inherited whilst the space utilization is significantly improved in the DS-HESF machine.



(a) Proposed DS-HESF



(b) Conventional HESF

Fig. 4.1 Cross sections of the proposed and conventional HESF machines.

In the DS-HESF machine, the relation between the rotor electric position θ_e and the mechanical position θ_m also follows:

$$\theta_e = N_r \cdot \theta_m \quad (4.1)$$

where N_r is the rotor pole number. Similar to the conventional SFPM machines [CHE10a], [CHE10b], the stator-slot/rotor-pole number combination of the DS-HESF machines is flexible, and the 10-, 11-, 13-, and 14-pole rotor are all feasible for the 12-stator-slot machines. Combined with the illustration of the armature coil locations shown in Fig. 4.1(a), the coil back-EMF phasors and thus the corresponding winding connections for the 12-stator-slot DS-HESF machines with different rotor pole numbers are shown in Fig. 4.2. According to Fig. 4.2(a), the coils 1, 4, 7, 10 are forward connected to constitute phase A.

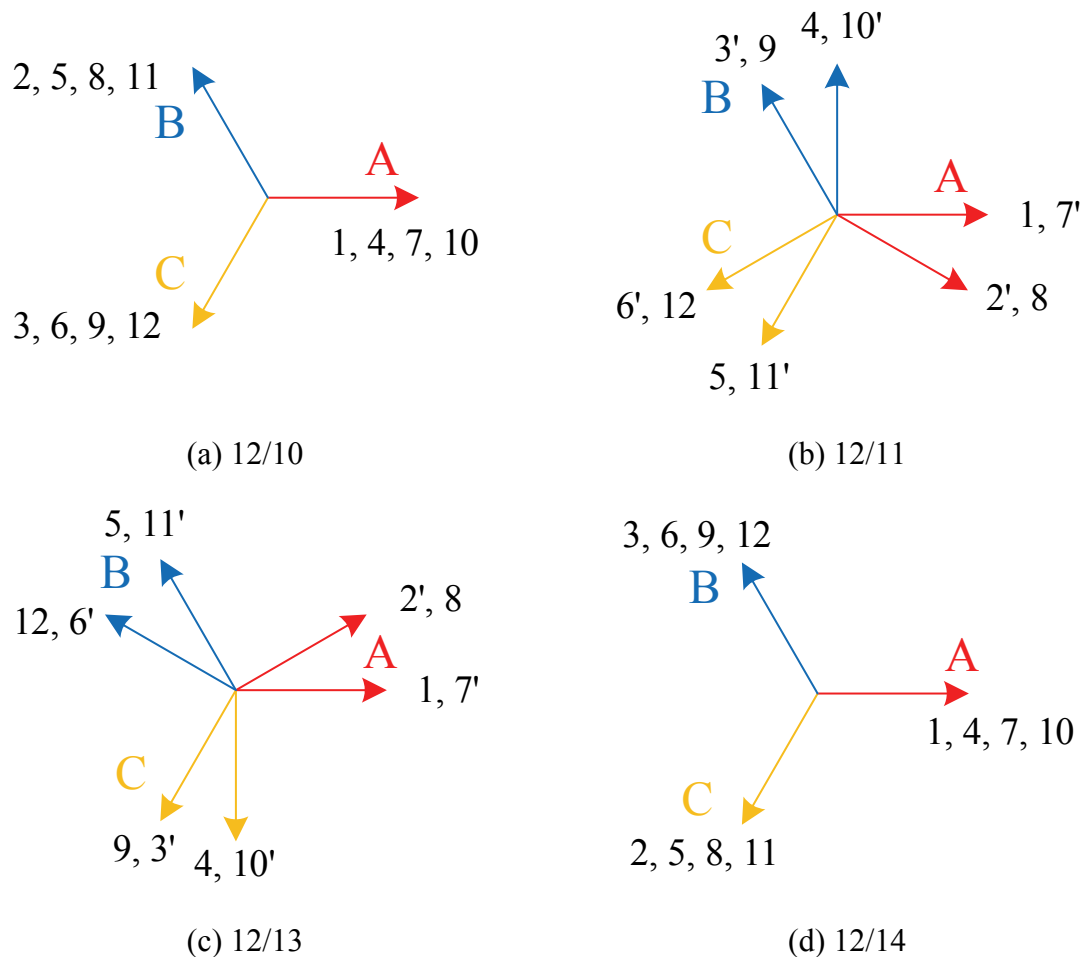


Fig. 4.2 Coil back-EMF phasors for 12-stator-slot DS-HESF machines with different rotor pole numbers.

In order to illustrate the operating mechanism of the proposed machine, the open-circuit field distributions of the 12/10 PS-HESF machine at four typical rotor positions are shown in Fig. 4.3. The variation of the PM field can be observed which is caused by the rotation of the salient rotor. Consequently, the flux linked in the armature coils periodically varies versus rotor position, as illustrated in Fig. 4.4(a), with which the back-EMF is induced and the torque is generated with current injected. Meanwhile, it can be noted that the feature of even order harmonic compensation, which exists in the conventional SFPM machine [HUA08], is inherited in the proposed machine. As shown in Fig. 4.4, the even order harmonics occur in the individual coil flux-linkages but they are cancelled in the resultant phase flux-linkage. As a result, the sinusoidal phase flux-linkage is obtained, with which the brushless AC (BLAC) operation is applicable and the smooth torque output is achievable.

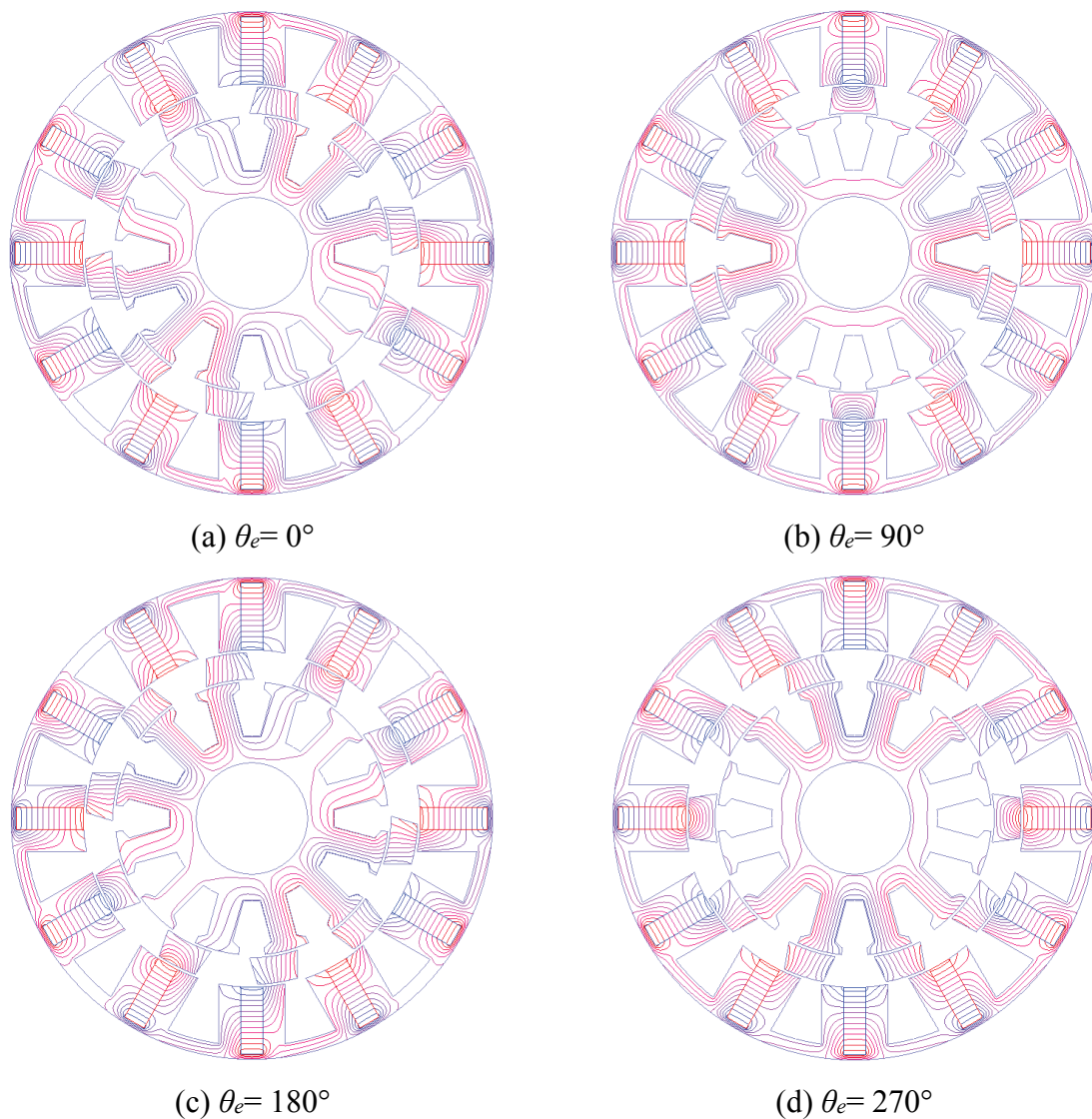
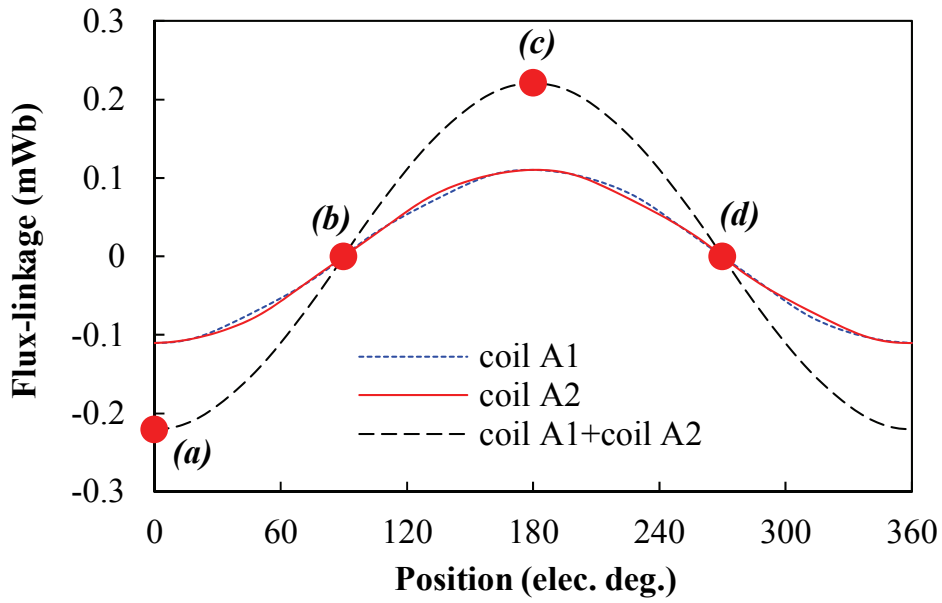
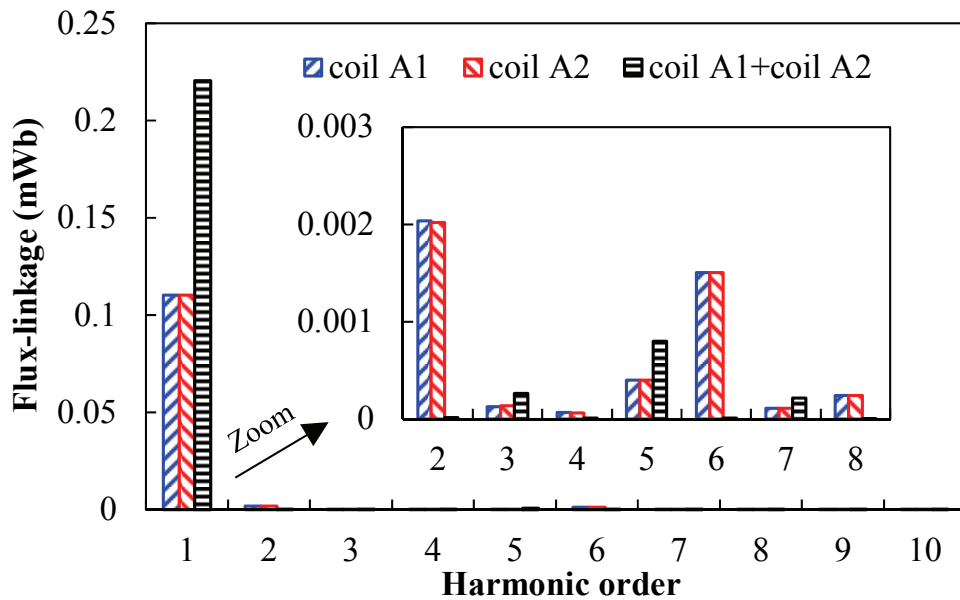


Fig. 4.3 Open-circuit field distributions of the DS-HESF machine at four typical rotor positions.



(a) Waveform



(b) Spectra

Fig. 4.4 Open-circuit coil flux-linkages with only PM excitation.

Moreover, it should be emphasized that the PMs and FWs both can contribute to the flux linked by the armature windings, which is the nature of the HE machines. In order to illustrate the flux regulation effect, the open-circuit flux distributions due to PM excitation and FW excitation respectively, are shown in Fig. 4.5, in which the similar flux paths for two kinds of fluxes can be observed. Furthermore, Fig. 4.6 shows the open-circuit phase flux-linkages of the DS-HESF machine with different field excitations. It can be seen that the resultant phase flux-linkages are easily regulated by injecting the field currents with different polarities.

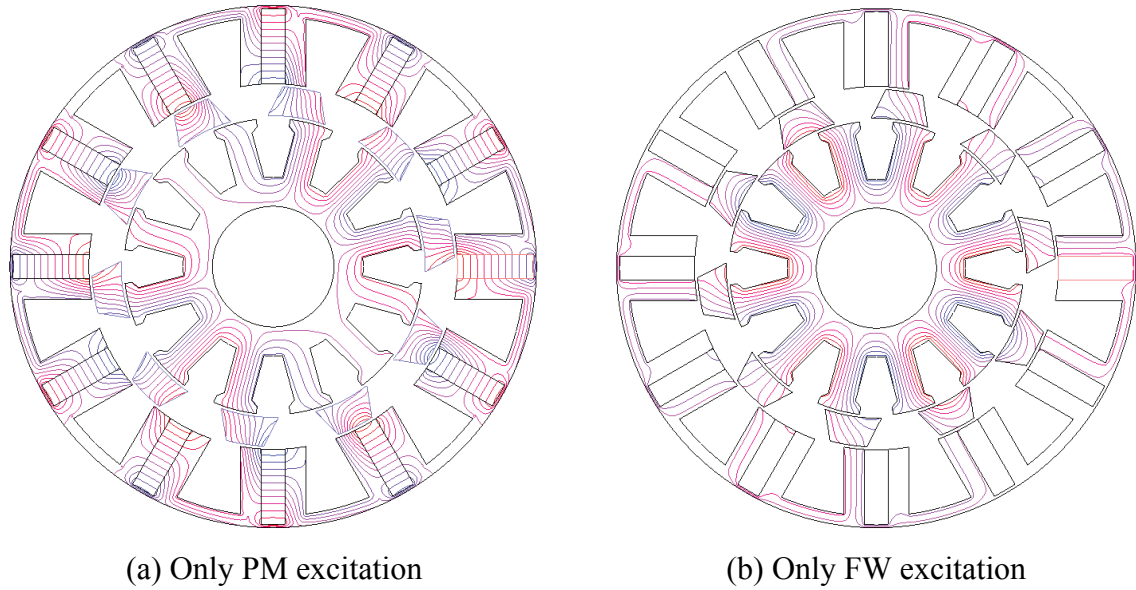


Fig. 4.5 Open-circuit flux distributions with different excitations.

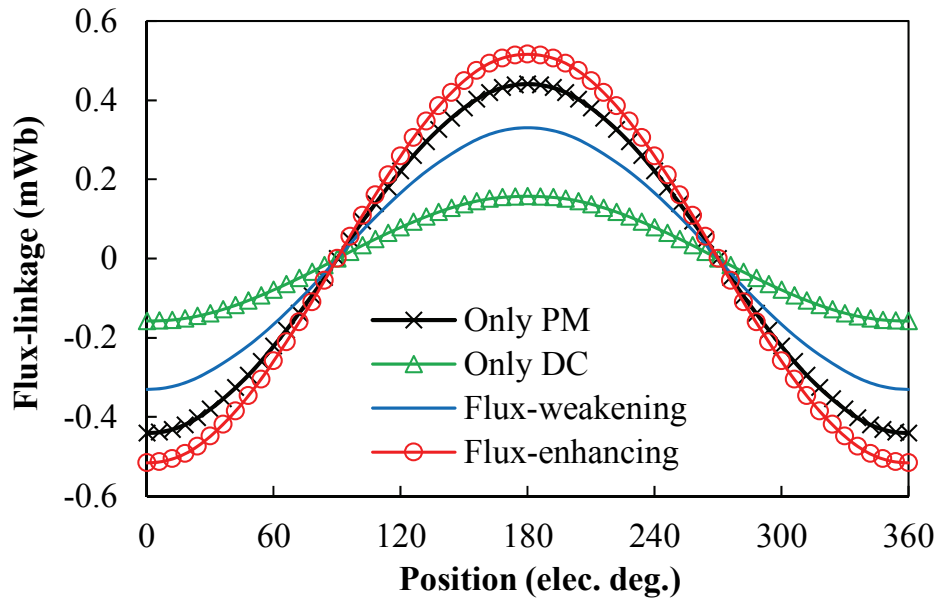


Fig. 4.6 Open-circuit phase flux-linkages with different excitations.

4.3 Electromagnetic Performance

It is essential to evaluate the electromagnetic performance of the proposed machine. Based on 2-D FE analysis, the characteristics of 12-stator-slot DS-HESF machines with different rotor pole numbers (10-, 11-, 13- and 14-rotor) are all investigated. The key geometric parameters of DS-HESF machine are illustrated in Fig. 4.7. Based on genetic algorithm, the optimizations are carried out for each machine to obtain the high average torque during one electric period as well as good flux regulation capability. In the optimizations, the cross section areas for FWs

and PMs are kept the same, whilst $5\text{A}/\text{mm}^2$ current density in FW slots and 20W copper losses in armature windings are applied. The definition of the armature winding copper loss is shown in (2.1), and it should be noted that the slot package factors are kept at 0.5 in both armature coil and field coil slots. The applied armature current is characterized with the sinusoidal waveforms having the same frequency as the open-circuit back-EMFs. The fixed 0.5 mm thick iron bridges neighboring PMs are applied, which can facilitate the flux regulation but short-circuit the PM flux. Firstly, the parametric model is built in FE software (ANSYS/Maxwell), in which the machine geometric parameters can be adjusted flexibly. Afterwards, the sensitivity analysis about each key design parameter is carried out individually to narrow down the potential range of exhibiting the maximum torque output. Then the global optimizations based on the Genetic Algorithm (GA) is used for maximizing the average torque output with the fixed copper losses in armature windings under flux-enhancing operation. In fact, there is a trade-off between the torque and flux regulation capabilities in the HE machine. More available space for PMs is helpful to boost torque output while more space for field windings can improve flux regulation capability. Thus, the maximum torque under flux-enhancing conditions is chosen as the optimization goal in this paper, with which both the torque output and the flux regulation range (the contribution of field current on back-EMF) can be considered. The details on the optimization process are summarized as follows:

Model type: 2-D Transient model in FE software (ANSYS/Maxwell);

Optimization object: The key design parameters of the DS-HESF machines, including split ratio (ratio between stator inner radius to outer radius), outer stator yoke thickness, outer stator tooth arc, rotor outer and inner pole arcs, rotor radial thickness, inner stator tooth arc and etc.;

Optimization constraint: The machine dimension of 45mm outer radius, 25mm active axial length. Moreover, the fixed 20W copper loss in armature windings is applied, in which the applied phase current will change with the variation of the slot area. If the slot area is increased, the available area for winding is boosted and hence the phase current could be higher for the fixed copper loss. The d-axis current is kept at zero. In addition, the fixed $5\text{A}/\text{mm}^2$ current density is injected to field coil slots to realize flux-enhancing operation;

Optimization strategy: Genetic Algorithm (GA), which is based on an established tool in the optimization package in ANSYS/Maxwell (maximum generation number: 50, individual number: 30);

Optimization goal: Maximizing the average torque during one electric period under flux-enhancing operation.

To better evaluate the machine performance, an optimal 12/10 conventional HESF machine based on the same optimization constraints is presented as a baseline machine. The optimized design parameters of the machines are listed in Table 4.1.

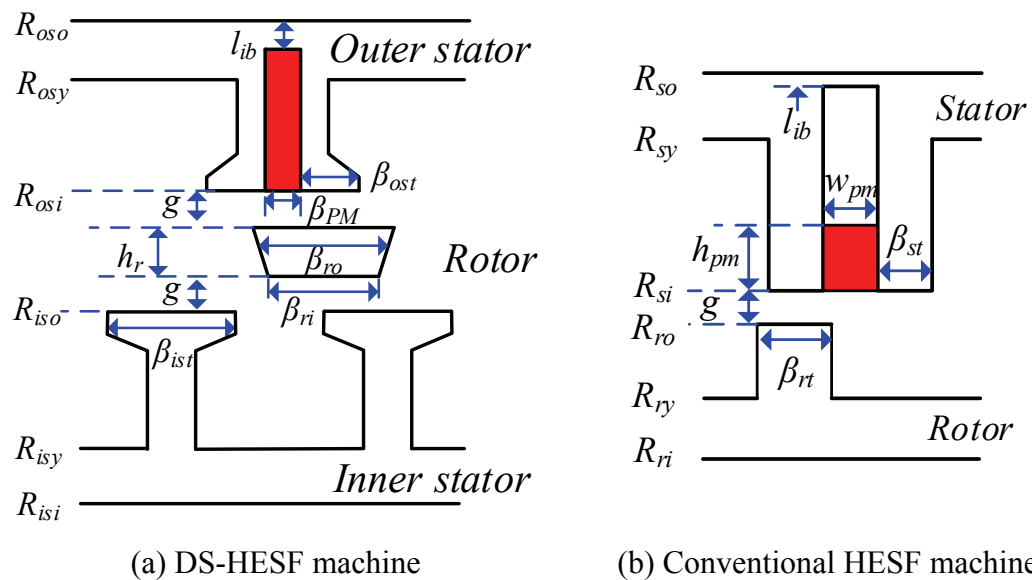


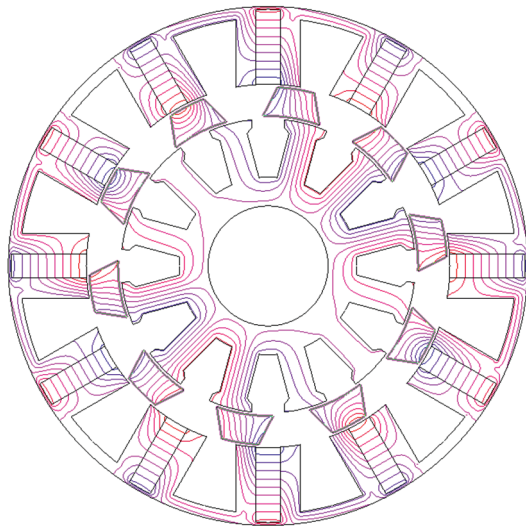
Fig. 4.7 Illustration of key geometric parameters of DS-HESF and conventional HESF machines.

Table 4.1 Key design parameters of DS-HESF machines with different rotor pole numbers.

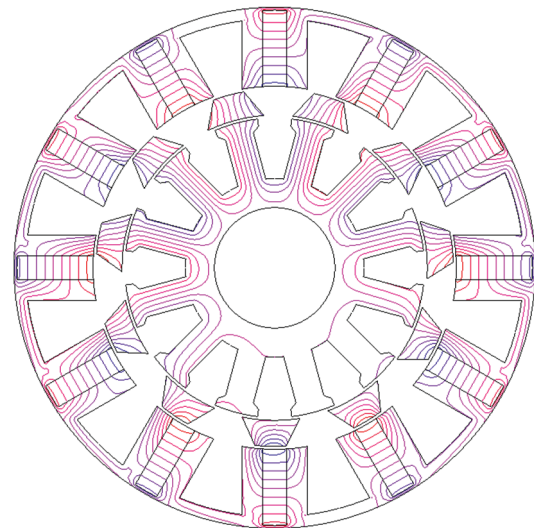
Parameter	10-rotor	11-rotor	13-rotor	14-rotor	Conventional 10-rotor
Stator slot number	12	12	12	12	12
Rotor pole number	10	11	13	14	10
Axial length (mm)	25	25	25	25	25
Stator outer radius (mm), R_{oso}/R_{so}	45	45	45	45	45
Stator yoke radius (mm), R_{osy}/R_{sy}	43	43	43	43	42.5
Stator inner radius (mm), R_{osi}/R_{si}	31.5	31.35	31	31	27.85
Iron bridge thickness (mm), l_{ib}	0.5	0.5	0.5	0.5	0.5
Stator tooth arc ($^{\circ}$), β_{ost}/β_{st}	6.5	6.5	6.5	6.5	8
PM pole arc ($^{\circ}$), β_{PM}	7.5	7.8	8	7.8	9
Air-gap length (mm), g	0.5	0.5	0.5	0.5	0.5
Rotor radial thickness (mm), h_r	5	4.5	4.5	4.5	N/A
Rotor outer pole arc ($^{\circ}$), β_{rol}/β_{rt}	12	10	9	8	14
Rotor inner pole arc ($^{\circ}$), β_{ri}	22	22	20	20	N/A
Inner stator outer radius (mm), R_{iso}	25.5	25.85	25.5	25.5	N/A
Inner stator yoke radius (mm), R_{isy}	15.4	15.4	15.4	15.4	N/A
Inner stator inner radius (mm), R_{isi}	10.4	10.4	10.4	10.4	N/A
Inner stator tooth arc ($^{\circ}$), β_{ist}	17	17	16	16	N/A
PM thickness (mm)	4.1	4.2	4.3	4.2	4.3
PM length (mm)	13	13.2	13.5	13.5	8.3

4.3.1 Open-circuit back-EMF

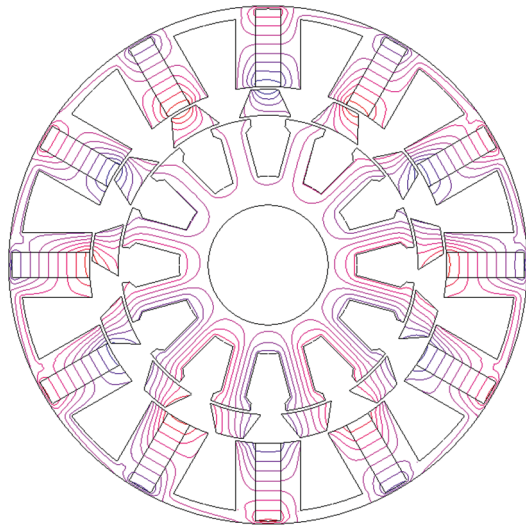
The open-circuit field distributions of the four DS-HESF machines at d -axis rotor position are shown in Fig. 4.8. The open-circuit phase back-EMFs at 400 r/min, without FW excitation, are compared in Fig. 4.9. The sinusoidal back-EMFs are always obtained in the DS-HESF machines. In addition, it can be seen that the back-EMF amplitudes of all the DS-HESF machines are higher than the conventional one. The 13-rotor machine has the highest back-EMFs thanks to its high winding factor and high electric frequency [CHE10a], [CHE10b], which implies good torque capacity.



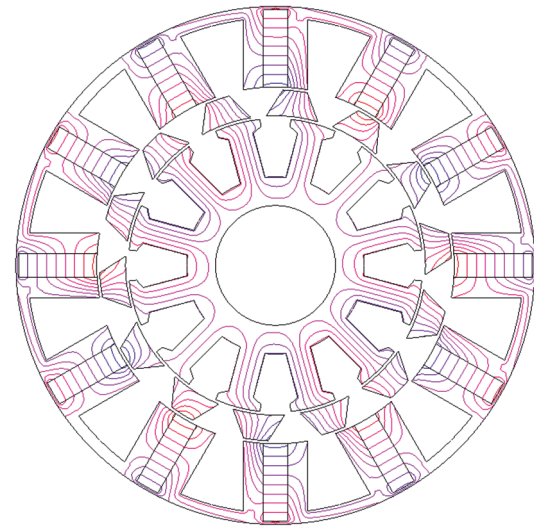
(a) 10-rotor



(b) 11-rotor

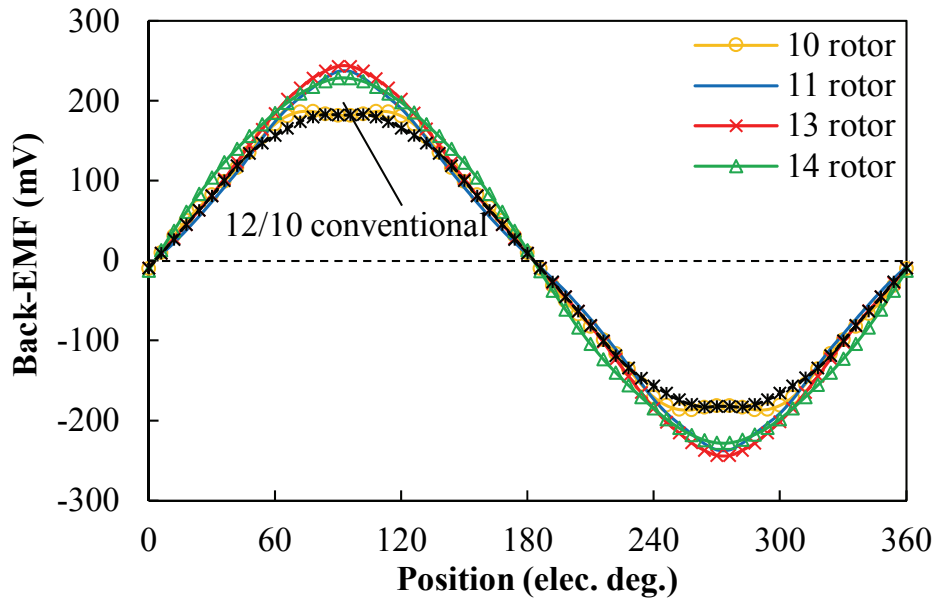


(c) 13-rotor

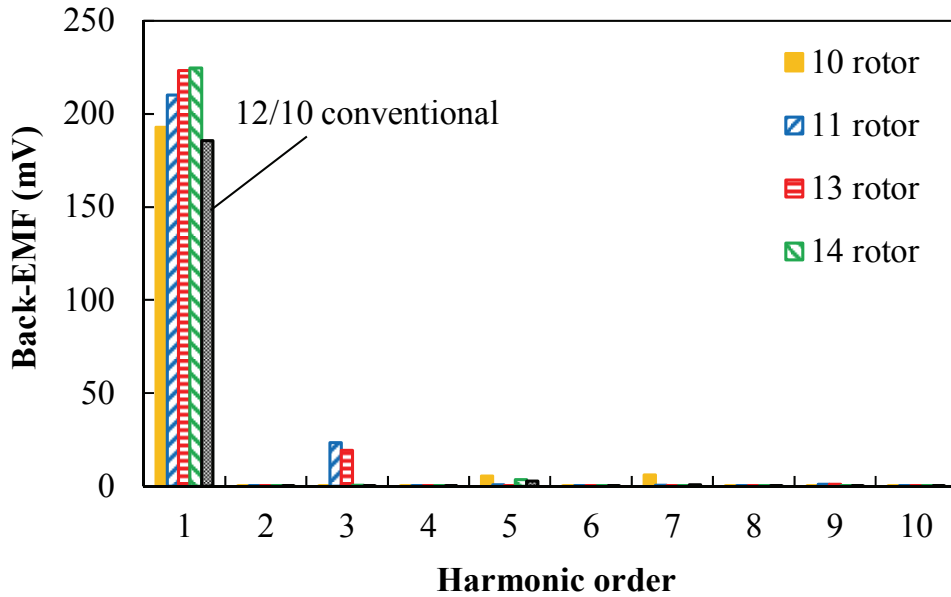


(d) 14-rotor

Fig. 4.8 Open-circuit field distributions of 12-stator-slot DS-HESF machines with different rotor pole numbers at d -axis position ($\theta_e = 0^\circ$).



(a) Waveforms



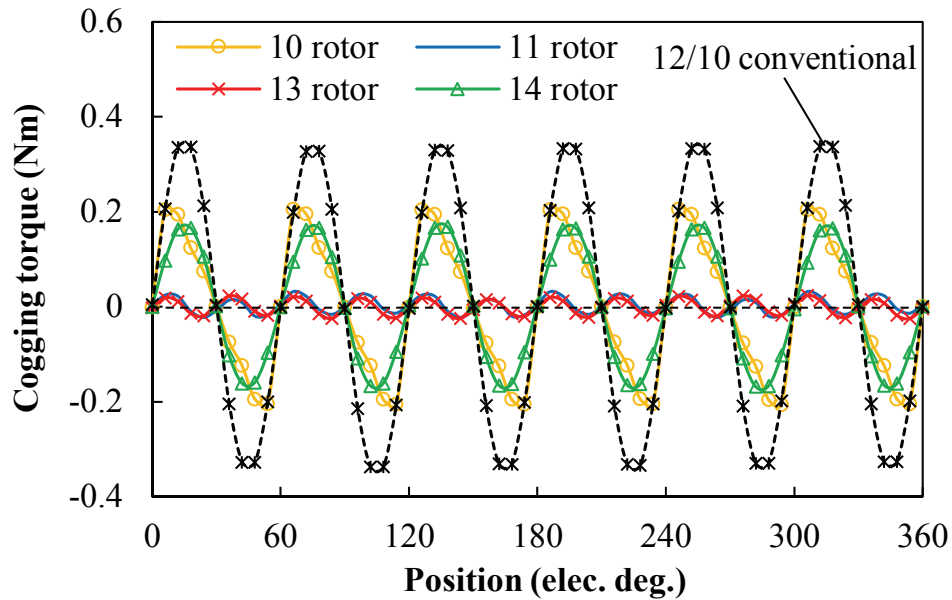
(b) Spectra

Fig. 4.9 Open-circuit phase back-EMFs at 400 r/min (1 turn number per coil).

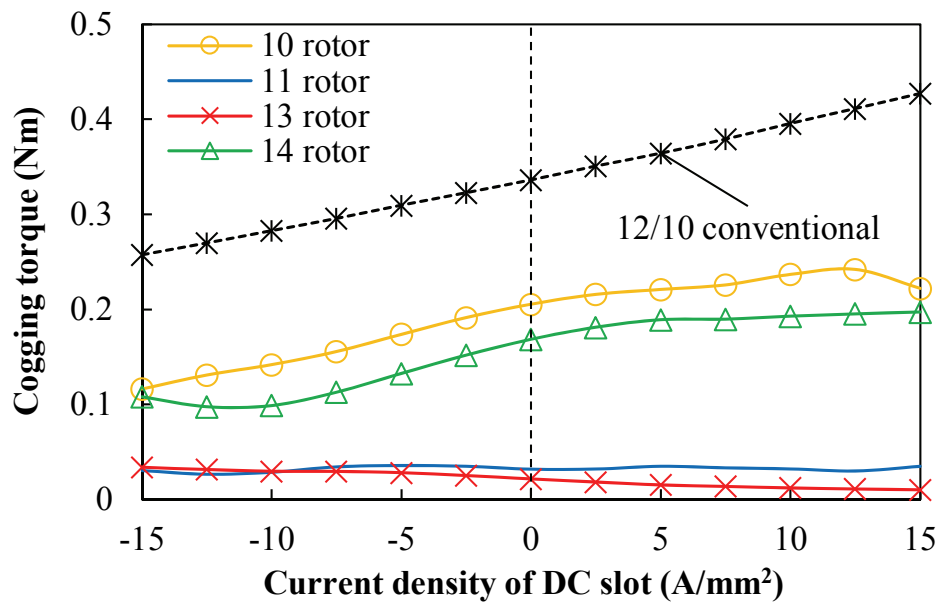
4.3.2 Cogging torque

Fig. 4.10(a) shows the cogging torque waveforms of the four machines with only PM excitation. The cycle number of the cogging torque during one electric period is 6 in the 10- and 14-rotor machines while it is 12 in the 11- and 13-rotor machines, which is due to the corresponding slot/pole combinations [ZHU00]. As a result, the 11- and 13-rotor machines have remarkably lower cogging torques than the counterparts. Meanwhile, it can be noted that the cogging torques of the DS-HESF machines are all lower than the conventional machine.

Moreover, the variations of peak cogging torques versus field currents are compared in Fig. 4.10(b), where the peak cogging torques of the 10- and 14-rotor DS-HESF machines and the conventional machine all increase with the positive field currents but decrease with the negative field currents.



(a) Cogging torque waveforms



(b) Peak cogging torques versus different field currents

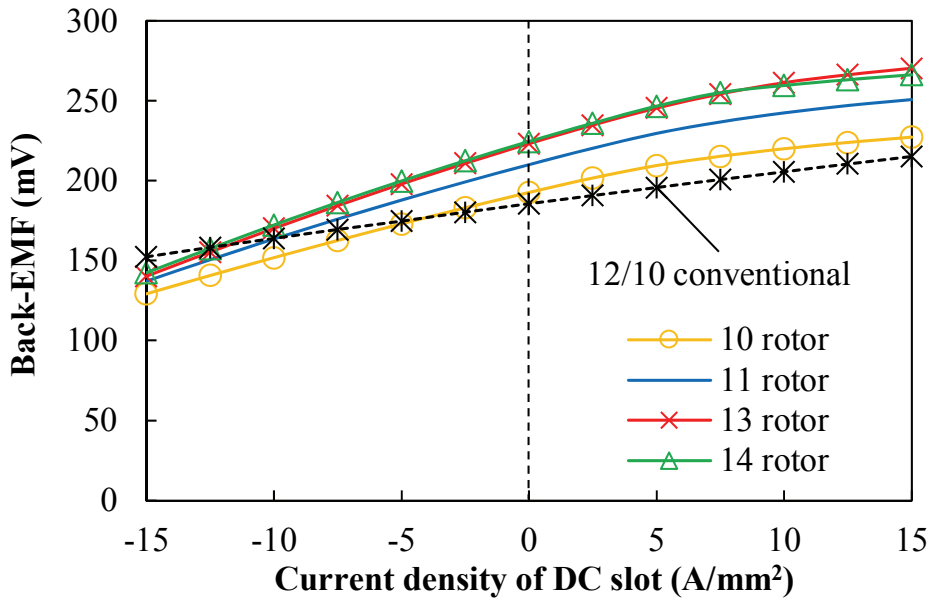
Fig. 4.10 Cogging torques.

4.3.3 Flux regulation capability

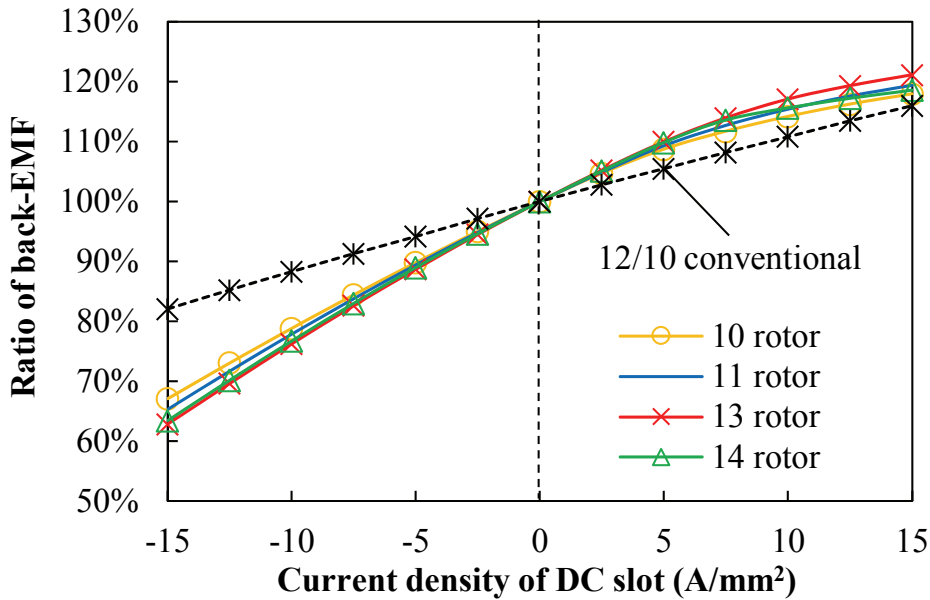
To reveal the flux regulation capability of the proposed machines, the fundamental amplitudes of phase back-EMFs at 400 r/min with different field currents are presented in Fig. 4.11, in which all DS-HESF machines have higher back-EMFs than the conventional one among whole field excitation range. The flux regulation ratio λ is defined:

$$\lambda = \psi_e / \psi_{PM} \quad (4.2)$$

where ψ_{PM} is the open-circuit PM flux-linkage and ψ_e represents the flux-linkage generated by PMs combined with FWs. The flux-weakening operation is achieved if $\lambda < 1$ while $\lambda > 1$ indicates the flux-enhancing condition. Therefore, as the flux regulation ratios versus different field excitations shown in Fig. 4.11(b), the DS-HESF machines always exhibit better flux regulation capabilities than the conventional one (around 82%-116%), among which the 13-rotor DS-HESF machine has the widest flux regulation range (around 62%-121%). In addition, it can be observed that the flux-enhancing is more difficult than the flux-weakening in all machines due to the magnetic saturation.



(a) Back-EMFs



(b) Ratio of back-EMFs

Fig. 4.11 Variation of fundamental back-EMFs versus field excitations (1 turn number per coil).

4.3.4 On-load torque

The developed DS-HESF machines not only exhibit better flux regulation capability, but also benefit from higher torque density thanks to the enlarged space for PMs and windings. With zero d -axis current control and fixed 20W copper losses in armature windings, the torque waveforms are compared in Fig. 4.12. It can be found that all DS-HESF machines exhibit higher torque than the conventional one. Furthermore, the average torques versus field currents

are shown in Fig. 4.13(a), in which the 13- and 14-rotor DS-HESF machines hold the advantages among all field excitations. Moreover, the torque ripple factor is defined as:

$$T_{ripple} = \frac{T_{max} - T_{min}}{T_{ave}} \quad (4.3)$$

where T_{max} , T_{min} and T_{ave} represent the maximum, minimum and average torque during one electric cycle. The torque ripple factors of all machines with different field excitations are compared in Fig. 4.13(b), in which the 11- and 13-rotor DS-HESF machines exhibit the lowest torque ripples while the conventional machine always has the highest. The benefits of the lower torque ripples in the 11- and 13-rotor DS-HESF machines should be attributed to the inherently low cogging torque and less 5th and 7th back-EMF harmonics.

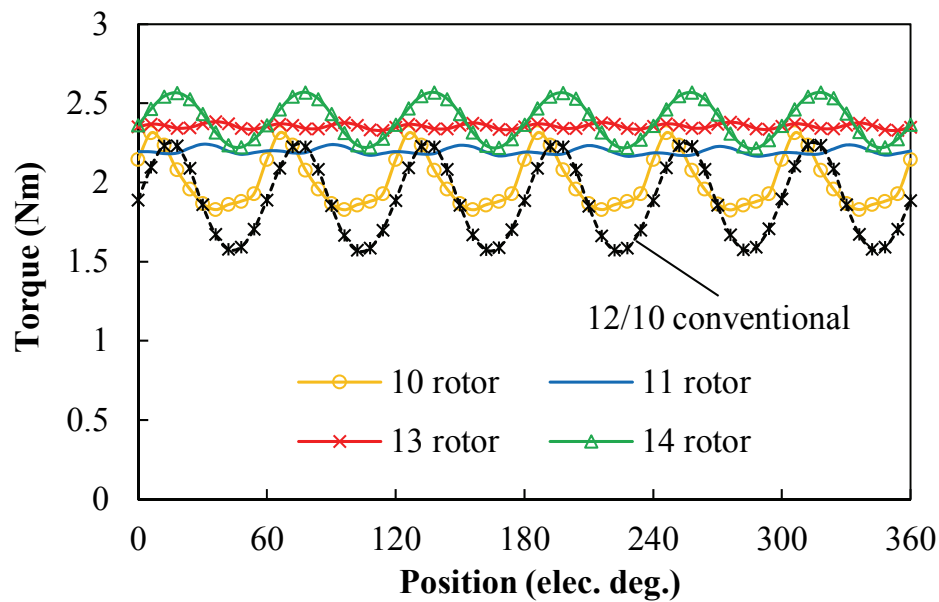
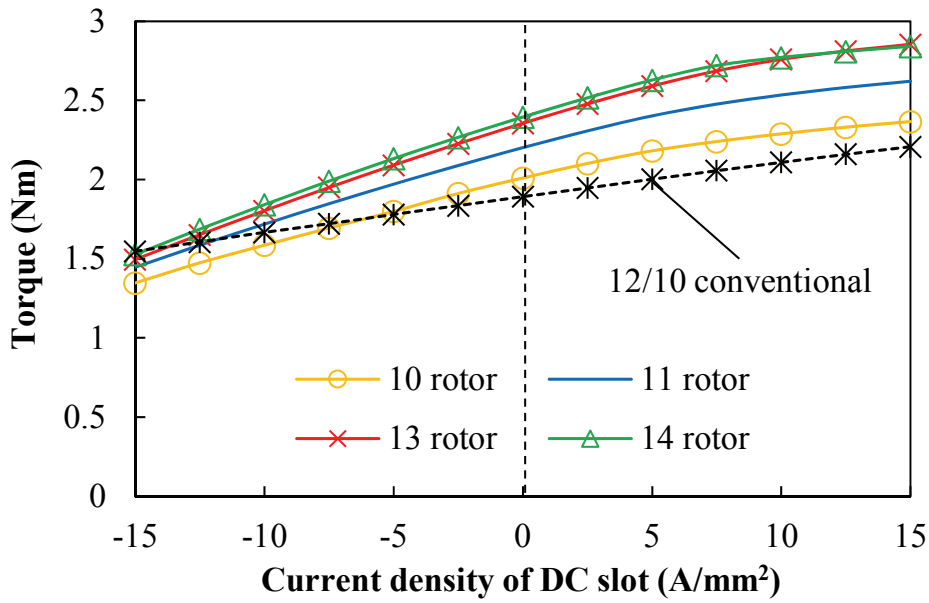
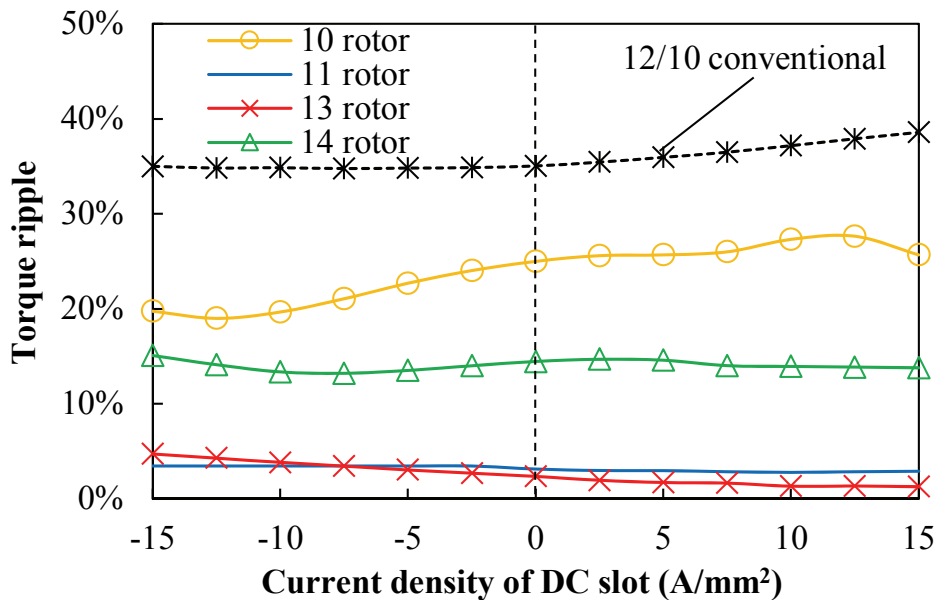


Fig. 4.12 Torque waveforms with 20W copper losses in armature windings (zero d -axis current control).



(a) Average torque



(b) Torque ripple

Fig. 4.13 Variation of average torques and torque ripples versus field excitations.

Besides, Fig. 4.14 shows the average torques versus current advance angles of all machines, in which the peak torque always occurs at around 0° in each machine, indicating that the reluctance torque is negligible and the zero d -axis current control is suitable for the maximum torque per ampere (MTPA) strategy. Further, without FW excitation, the average torques with different copper losses in armature windings are compared in Fig. 4.15. It can be found that the torques of all DS-HESF machines are higher than the conventional one and the 14-rotor DS-HESF machine is more advantageous than the counterparts.

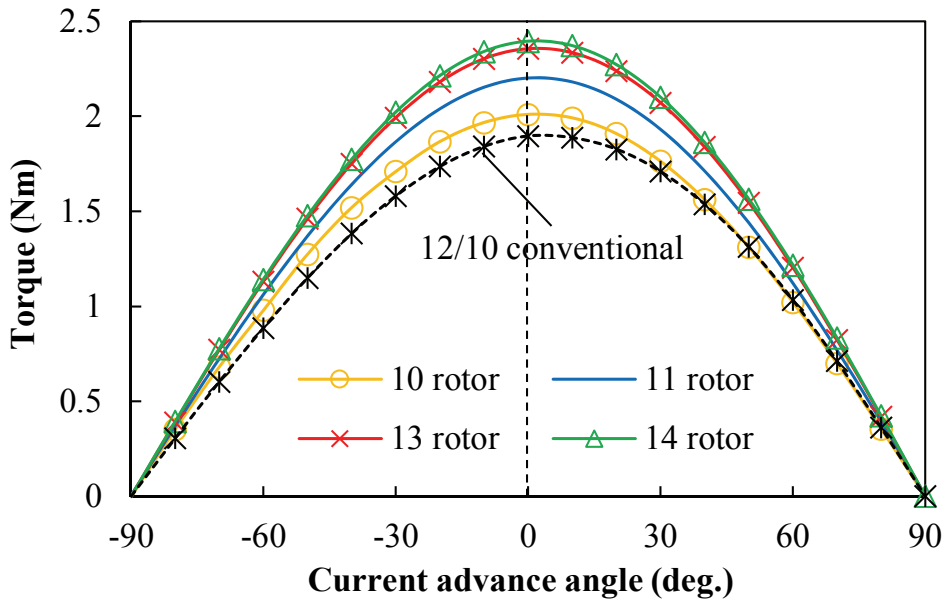


Fig. 4.14 Variation of average torques versus current advance angles.

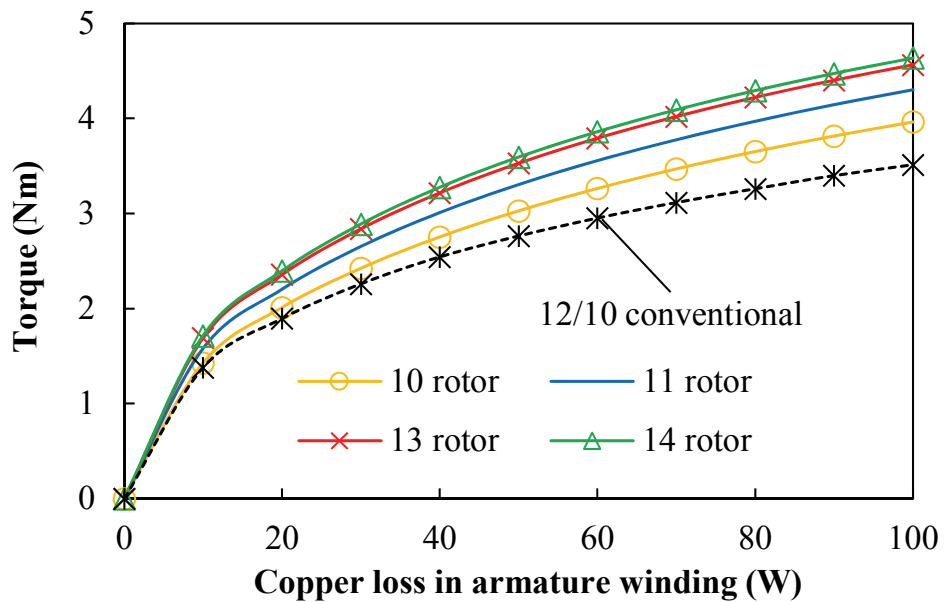
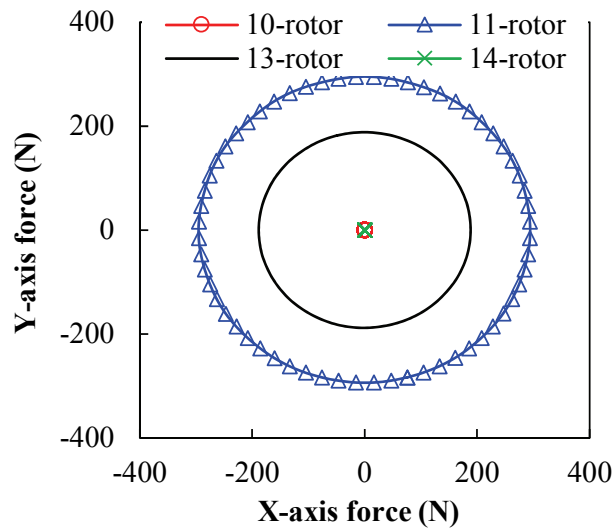


Fig. 4.15 Variation of average torques versus copper losses in armature windings.

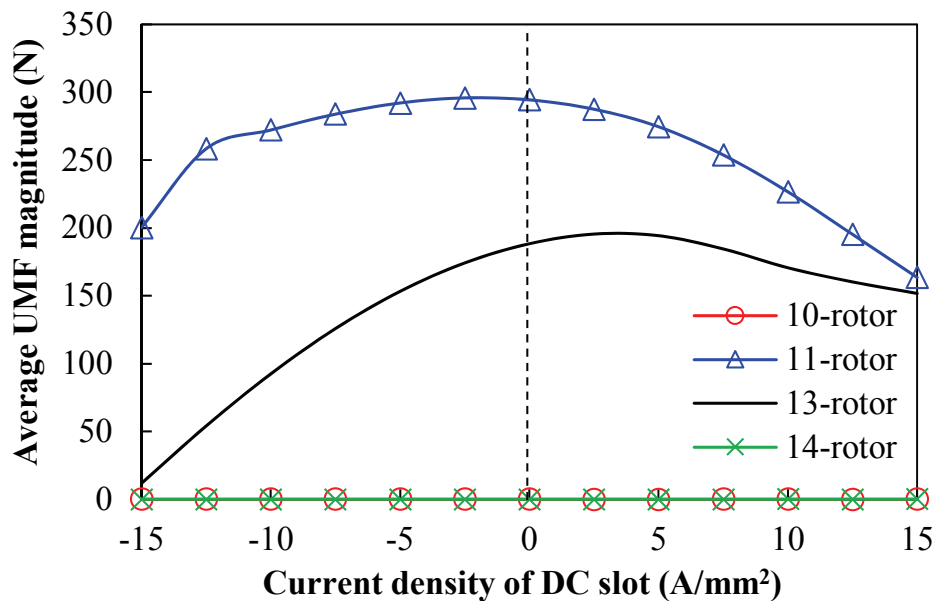
4.3.5 Unbalanced magnetic force

The unbalanced magnetic force (UMF) on the rotor is undesirable as it may cause the additional noise and vibration as well as reduce the bearing life. The 11- and 13-rotor DS-HESF machines would suffer the remarkable UMFs due to the odd rotor pole numbers. This is illustrated in Fig. 4.16(a) and Fig. 4.17(a), in which the UMFs under open-circuit and on-load conditions of the 10- and 14-rotor machines are always negligible but they are significant in the 11- and 13-rotor machines. In addition, the variations of the average UMFs against field

excitations are shown in Fig. 4.16(b) and Fig. 4.17(b), in which the UMFs in the 11- and 13-rotor DS-HESF machines are affected by the field current and the lower UMFs can be obtained by injecting field currents. It should be noted that the UMFs in the 11- and 13-rotor DS-HESF machines can be eliminated by multiplying their stator slot and rotor pole numbers at the same time to obtain the even rotor pole numbers.

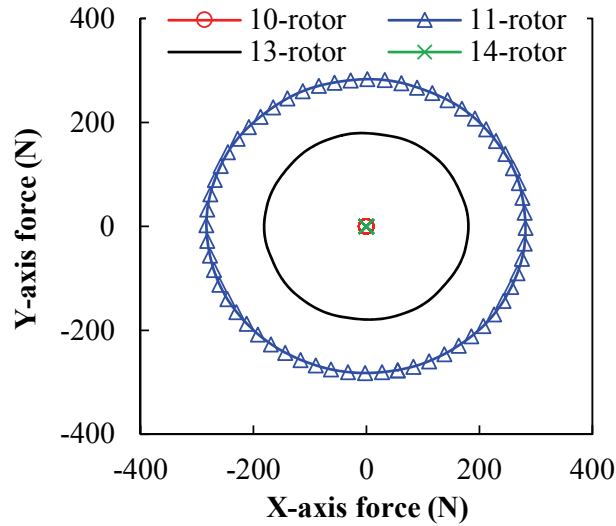


(a) UMF without FW excitation

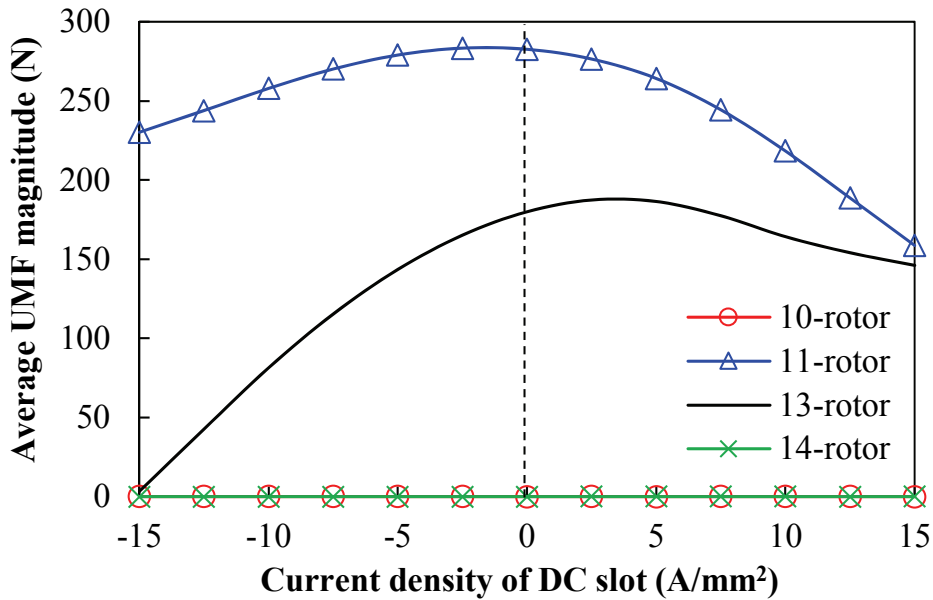


(b) Average UMF magnitudes with different field currents

Fig. 4.16 Open-circuit UMFs of 12-stator-slot DS-HESF machines with different rotor pole numbers.



(a) UMF without FW excitation



(b) Average UMF magnitudes with different field currents

Fig. 4.17 On-load UMFs of 12-stator-slot DS-HESF machines with different rotor pole numbers (20W copper losses in armature windings, zero d -axis current control).

4.4 Influence of Hybridization

It was mentioned that the iron bridge is employed on the outer stator, which is adjacent to the PM and offers a bypass path for the FW flux. The flux regulation capability tends to be improved by applying this iron bridge but the torque density will be sacrificed since the PM flux automatically short-circuits through the iron bridge. The field distributions due to the PM excitation and FW excitation in the models with or without iron bridge are shown in Fig. 4.18. From Fig. 4.18(a) and (b), it can be identified that the iron bridge greatly reduces the magnetic

reluctance of the FW flux path and hence facilitate the flux regulation. In fact, the parallel connection between FW and PM fluxes is obtained due to the presence of the iron bridge as the FW flux can bypass the PM, Fig. 4.18(a). If the iron bridge is removed, Fig. 4.18(b), only the series connection is presented. Moreover, based on Fig. 4.18(a) and (d), it is easy to observe the short-circuited PM flux due to the iron bridge. Hence, it is of value to carefully investigate the influence of the iron bridge thickness.

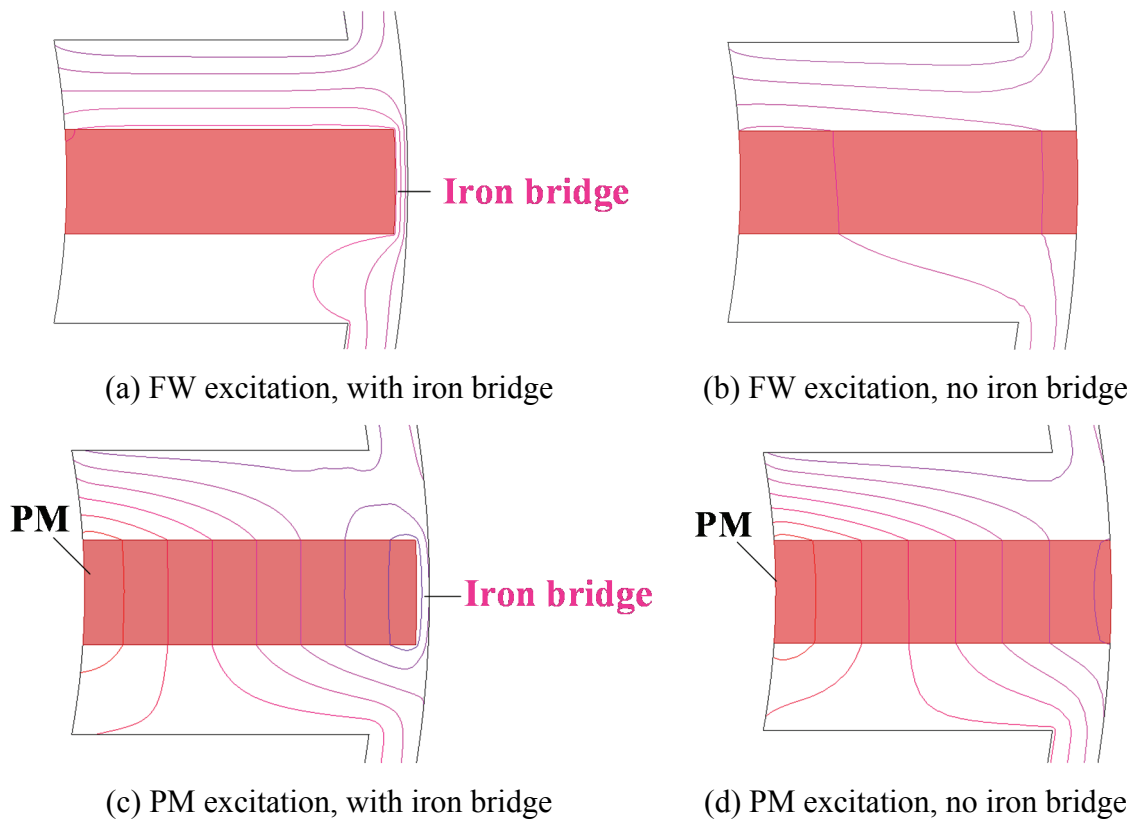


Fig. 4.18 Open-circuit field distributions with or without iron bridge.

The flux regulation capability δ of the HE machines is defined as follows:

$$\delta = \frac{E_{FE} - E_{FW}}{E_{PM}} \quad (4.4)$$

where E_{FE} , E_{FW} , and E_{PM} represent the open-circuit back-EMFs under flux-enhancing, flux-weakening, and sole PM excitation respectively. The higher δ implies a better flux regulation capability. The variations of the average torque and flux regulation capability of the 12/10 DS-HESF machine with different iron bridge thicknesses are shown in Fig. 4.19, in which the average torque with 20W copper loss in armature windings and δ with 5A/mm² in FW slots are included. As can be seen, the torque decreases gradually with the iron bridge thickened, while the flux regulation capability is improved. Thus, it can be said that the appropriate design of

the DS-HESF machine depends on the compromising requirements of the torque output and flux regulation capability.

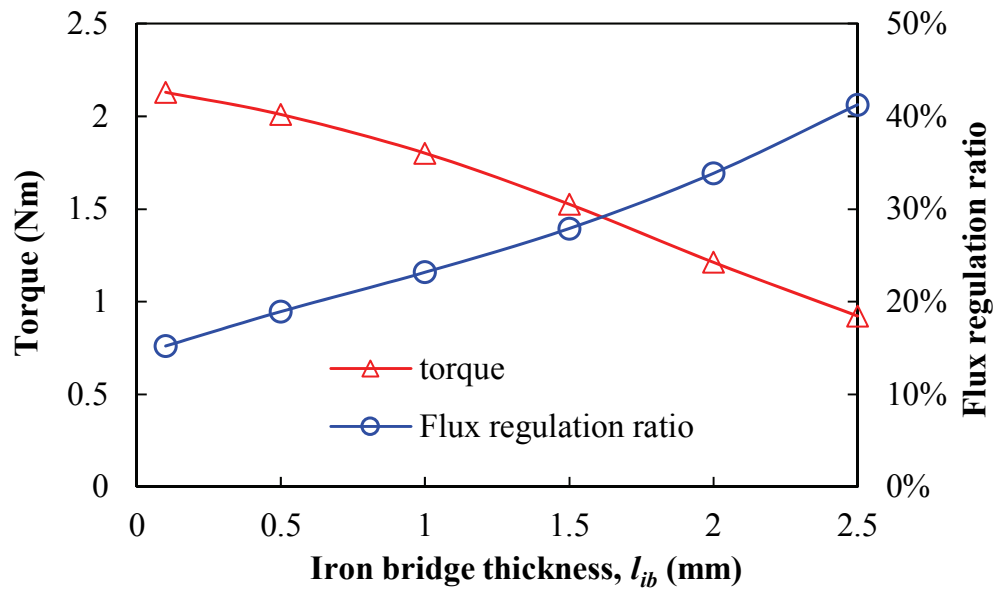


Fig. 4.19 Effect of iron bridge thickness of 12/10 DS-HESF on torque and flux regulation.

4.5 Experimental Validation

In order to validate the FE predictions, a 12/10 DS-HESF prototype machine is manufactured and the test is carried out. The key design parameters of the prototype are listed in Table 4.2, whilst the essential machine components, including the outer stator with PMs and armature windings, the cup-rotor and the inner stator wound with FWs, are shown in Fig. 4.20.

Table 4.2 Key design parameters of 12/10 DS-HESF prototype machine.

Parameter	Value	Parameter	Value
Stator slot number	12	g (mm)	0.5
Rotor pole number	10	h_r (mm)	5
Axial length (mm)	25	β_{ro} ($^\circ$)	18
R_{oso} (mm)	45	β_{ri} ($^\circ$)	24
R_{osy} (mm)	42.5	R_{iso} (mm)	25.75
R_{osi} (mm)	31.75	R_{isy} (mm)	15
l_{ib} (mm)	0.45	R_{isi} (mm)	10.08
β_{ost} ($^\circ$)	7.5	β_{ist} ($^\circ$)	17
β_{PM} ($^\circ$)	5.5	N_{ac} / N_{dc}	13/9

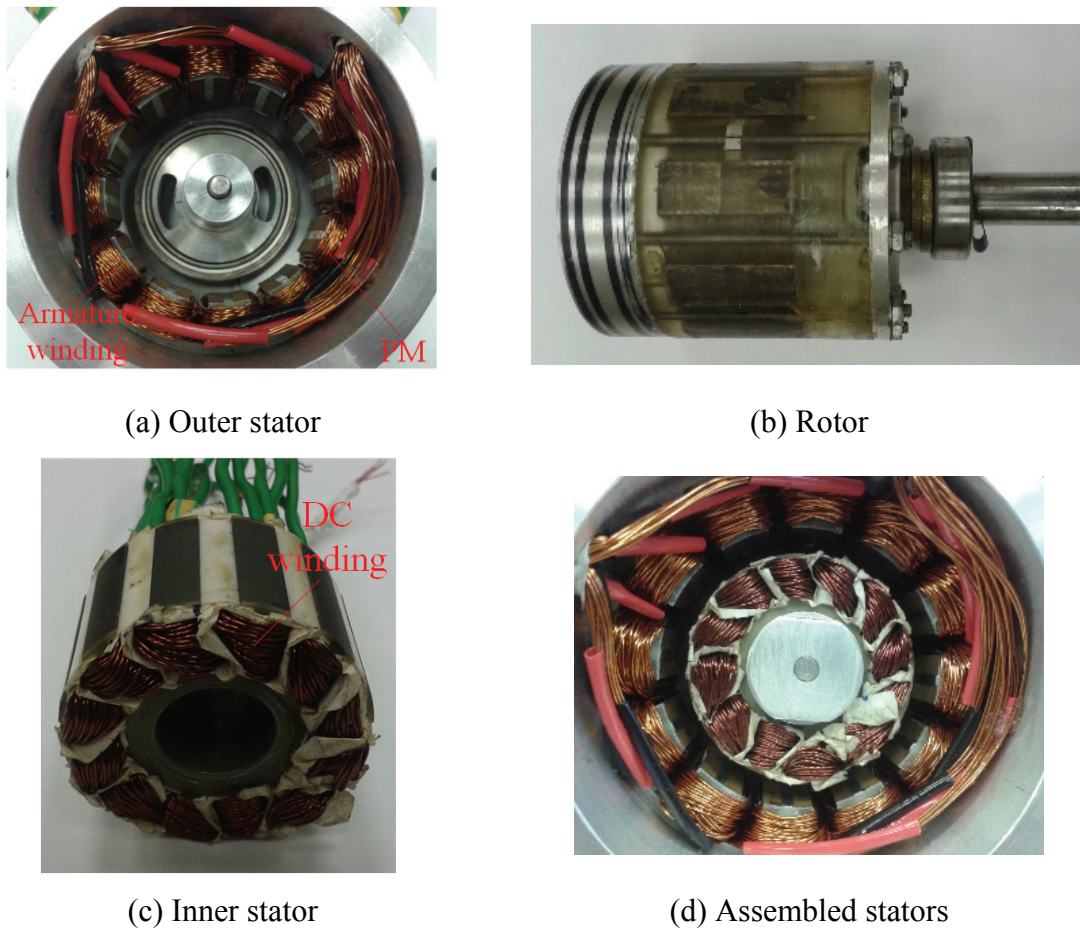


Fig. 4.20 Essential components of proposed 12/10 DS-HESF machine prototype.

The open-circuit phase back-EMF at 400 r/min is measured and compared with the 2-D FE predictions in Fig. 4.21, in which there is an around 7.6% difference between the peak fundamental amplitudes in the 2-D FE and test results. Furthermore, the measured and 2-D FE-predicted fundamental back-EMFs with different field excitations are presented in Fig. 4.22, in which the variation of open-circuit back-EMFs versus field currents can be observed, indicating the flux regulation capability of the proposed machine. It can be found that the difference of back-EMFs between the FE predictions and test results tend to be more significant with the negative FW currents. This may be attributed to the fact that the FW flux generated by the negative FW currents counters against the PM flux in the lamination portions adjacent to the air-gap, which results in more severe end leakage-flux. Furthermore, based on the test-rig shown in Fig. 2.26, the static torque versus rotor position, with different armature currents of the prototype machine, is measured in Fig. 4.23, and the corresponding FE predictions are included. The possible causes include the end effect, potential cutting tolerances on laminations and the unaligned inner stator, which were discussed in section 2.6.

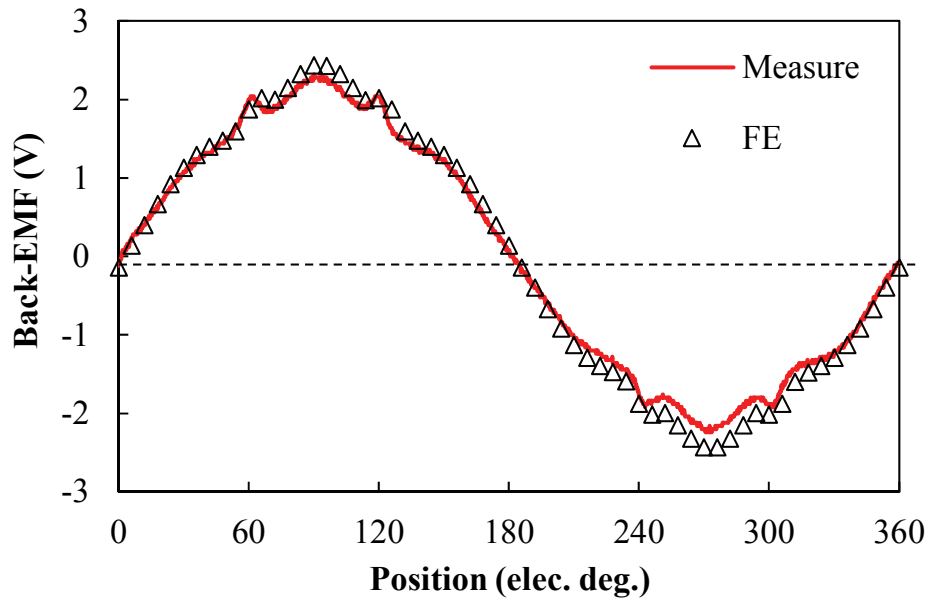


Fig. 4.21 Measured and 2-D FE-predicted phase back-EMFs at 400 r/min.

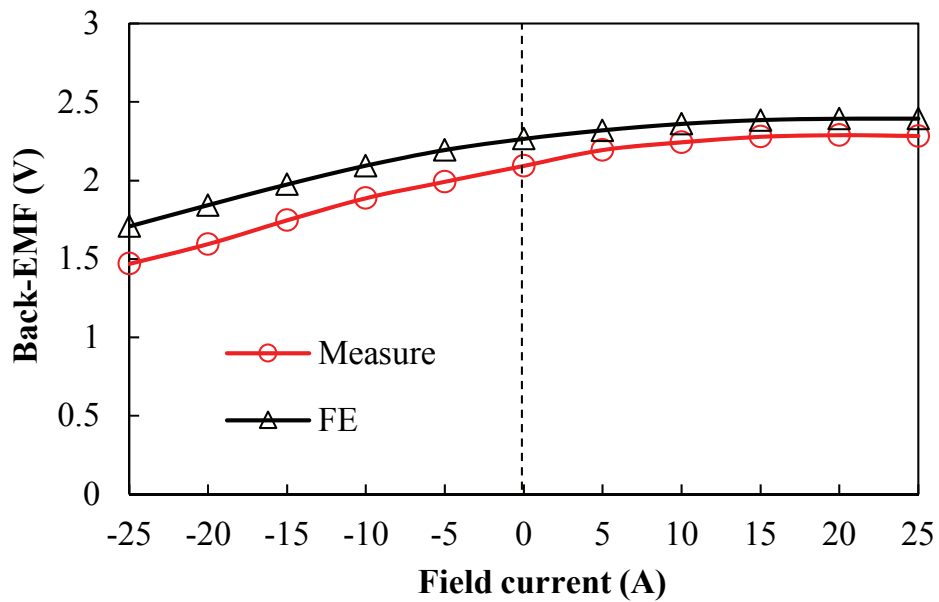


Fig. 4.22 Measured and 2-D FE-predicted fundamental phase back-EMFs at 400 r/min versus different FW excitations.

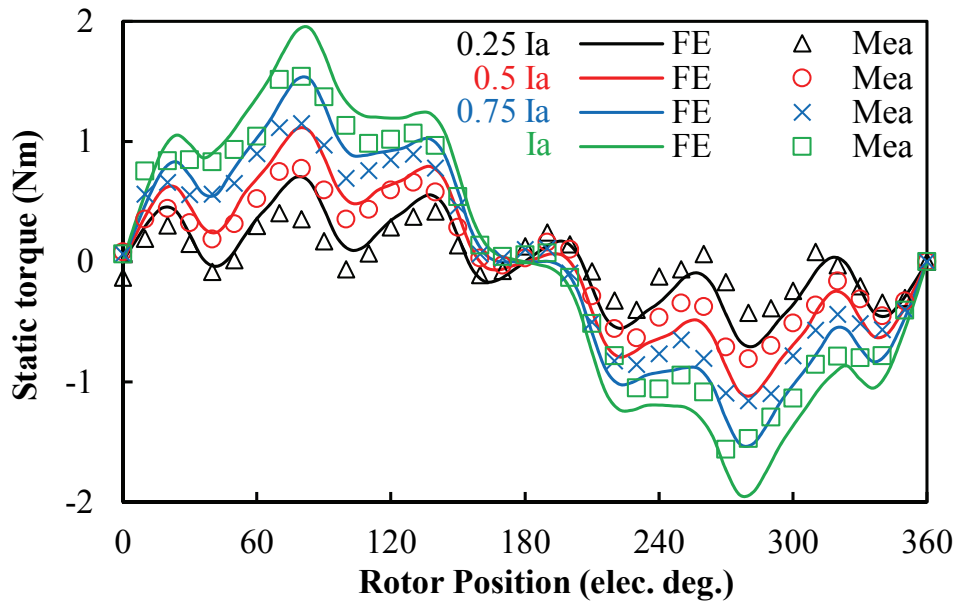


Fig. 4.23 Measured and 2-D FE-predicted static torque.

4.6 Conclusion

In this chapter, a novel DS-HESF machine is proposed, which has the armature windings and PMs on one stator while the FWs on the other stator. The comparison results between the DS-HESF machines and the conventional HESF machine reveal that the proposed machines exhibit not only higher torque densities but also better flux regulation capabilities, due to the superior space utilization. Meanwhile, the influence of rotor pole number has been investigated and it is found the 13- and 14-rotor DS-HESF machines are more advantageous thanks to lower torque ripples as well as good flux regulation capability.

Chapter 5. Partitioned Stator Hybrid Excited Switched Flux Machines

In the previous Chapter 4, a novel dual stator HESF machine with PMs and armature windings on one stator whilst FWs on the other stator has been presented and evaluated. In fact, the PM location is flexible and can also be moved to the inner stator adjacent to the FWs. Therefore, a partitioned stator (PS)-HESF machine is proposed in this chapter, in which one stator accommodates the armature windings whilst the other stator equips with the excitation sources (including both PMs and FWs). Compared with the conventional PS-SFPM machines, an additional degree of freedom, i.e. the hybridization ratio between PM and FW flux is obtained in the proposed PS-HESF machine. Meanwhile, the good space utilization contributes to a high torque density as well as excellent flux regulation capability. In this chapter, the electromagnetic performance of the PS-HESF machines will be investigated, with due account for the effects of rotor pole numbers. Moreover, the hybridization ratio, which is affected by several machine design parameters, are discussed.

This part has been published in IEEE Transactions on Energy Conversion.

5.1 Introduction

The HE machines having both PM and FW excitations, inherit the high efficiency and high torque density of PM machines and meanwhile enhance the flux controllability [CAP15]. Based on the conventional SFPM machines, Fig. 1.16, the HESF machine is firstly introduced in [AKE01], which simply replaces half number of PMs with FWs, and hence the PMs and field coils alternately contribute to the air-gap flux. A HESF machine employing an additional iron ring with FWs outside a conventional SFPM machine is proposed in [HOA07], which sacrifices the available slot space of armature windings. Further, with the identical laminations to the conventional SFPM machines, the HESF machines reducing PM width and having FWs in the saved space are presented in [HUA09], Fig. 1.9. Meanwhile, the locations of PMs and FWs [OWE09], [HUA15], [ZHA15b], and the effects of iron bridges are investigated [OWE10a]. The operating principle and performance of this kind of HESF machines are summarized [HUA14], [HUA15], [ZHA16]. In addition, based on the E-core SFPM machine [CHE11e], a HESF machine with field coils wound around the fault-tolerant teeth is proposed, and the available stator slot/rotor pole combinations are investigated [CHE11b]. Moreover, a simple HESF machine is presented, which directly arranges the FWs on the armature winding

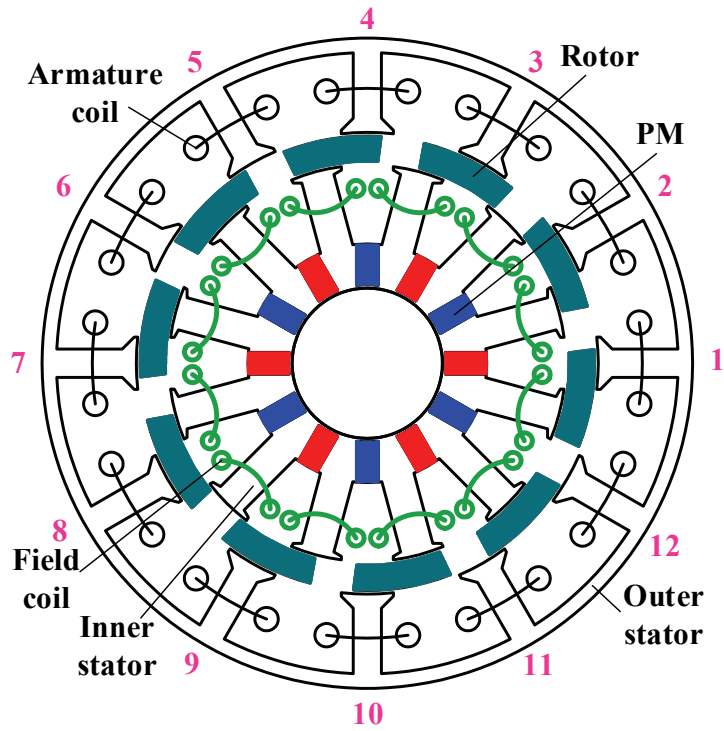
slots in the conventional SFPM machine to share the slot area [GAU14]. However, this machine can only realize flux-weakening via magnetic saturation and cannot achieve flux-enhancing. In [DUP16], the claw pole structure combined with a toroidal FW is attached to the stator yokes of a conventional SFPM machine, where the 3-D flux is produced to regulate the air-gap flux. Furthermore, a two-stack HESF machine is proposed, which is axially the combination of a conventional SFPM machine and a wound-field switched flux machine [WAN12a].

All the existing HESF machines allocate PMs, FWs and armature windings on one stator, suffering serious space conflict and thus the sacrificed performance. Therefore, the partitioned stator (PS) HESF (PS-HESF) machine, which employs two separated stators to accommodate armature windings and excitations (PM and FW) respectively, is proposed in this chapter. The space utilization of the proposed machine is greatly improved and hence the performance can be enhanced.

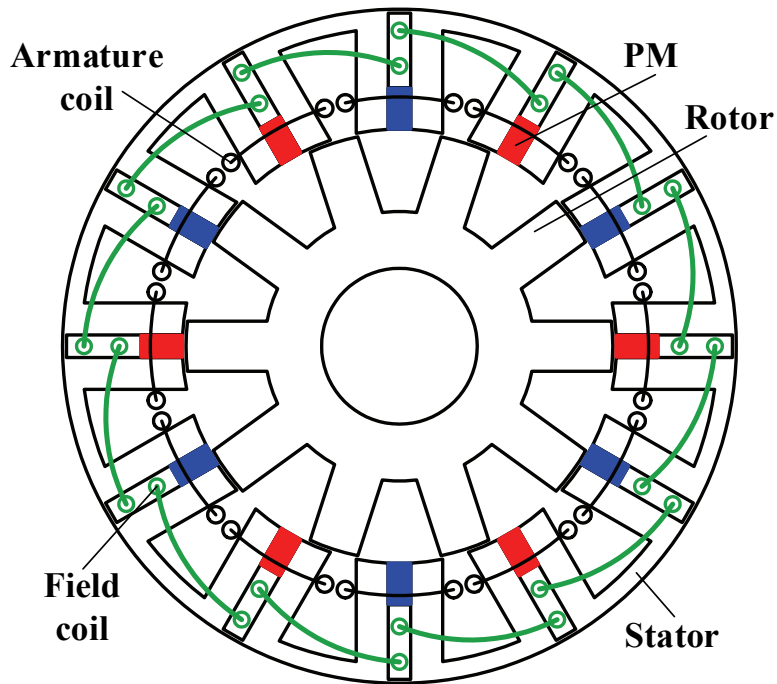
This chapter is organized as follows. In section 5.2, the topology and operating principle of the PS-HESF machines are illustrated. Then, in section 5.3, based on 2-D FE analysis, the electromagnetic performance of the proposed PS-HESF machines with different slot/pole combinations is evaluated, together with the comparison with a conventional HESF machine. Afterwards, the effects of key design parameters on torque density and flux regulation capability are investigated in section 5.4. Finally, a prototype machine is manufactured and tested to validate the predictions.

5.2 Machine Topology and Operating Principle

The proposed three-phase 12-stator-slot/10-rotor-pole PS-HESF machine is illustrated in Fig. 5.1(a), which employs an outer stator to accommodate armature windings, an inner stator to allocate PMs and FWs (the inner stator and outer stator are exchangeable), and an iron-piece-rotor sandwiched between the two stators. The armature windings and FWs both consist of concentrated non-overlapping coils. The PMs are all tangentially magnetized and inserted in the yokes of inner stator. Meanwhile, the outer stator and inner stator have the identical pole number, whilst the inner stator teeth align with the outer stator slots. Compared with the conventional HESF machine shown in Fig. 5.1(b), the PS-HESF machine benefits from more available space for armature windings and/or excitations, resulting in the improved torque density and flux regulation capability.



(a) Proposed PS-HESF machine.



(b) Conventional HESF machine.

Fig. 5.1 Cross sections of proposed 12-stator-slot/10-rotor-pole PS-HESF machine and the conventional HESF machine.

The PS-HESF machine follows the similar operating principle to the conventional HESF machine. The rotor electrical position θ_e is expressed as follows:

$$\theta_e = N_r \theta_m \quad (5.1)$$

where θ_m is the rotor mechanical position and N_r represents the rotor piece number. Meanwhile, as illustrated in the coil back-EMF phasor in Fig. 5.2(a), the armature coils 1, 4, 7 and 10 are forward connected to constitute phase A for this 12/10 PS-HESF machine, which is the same as the corresponding conventional HESF machine.

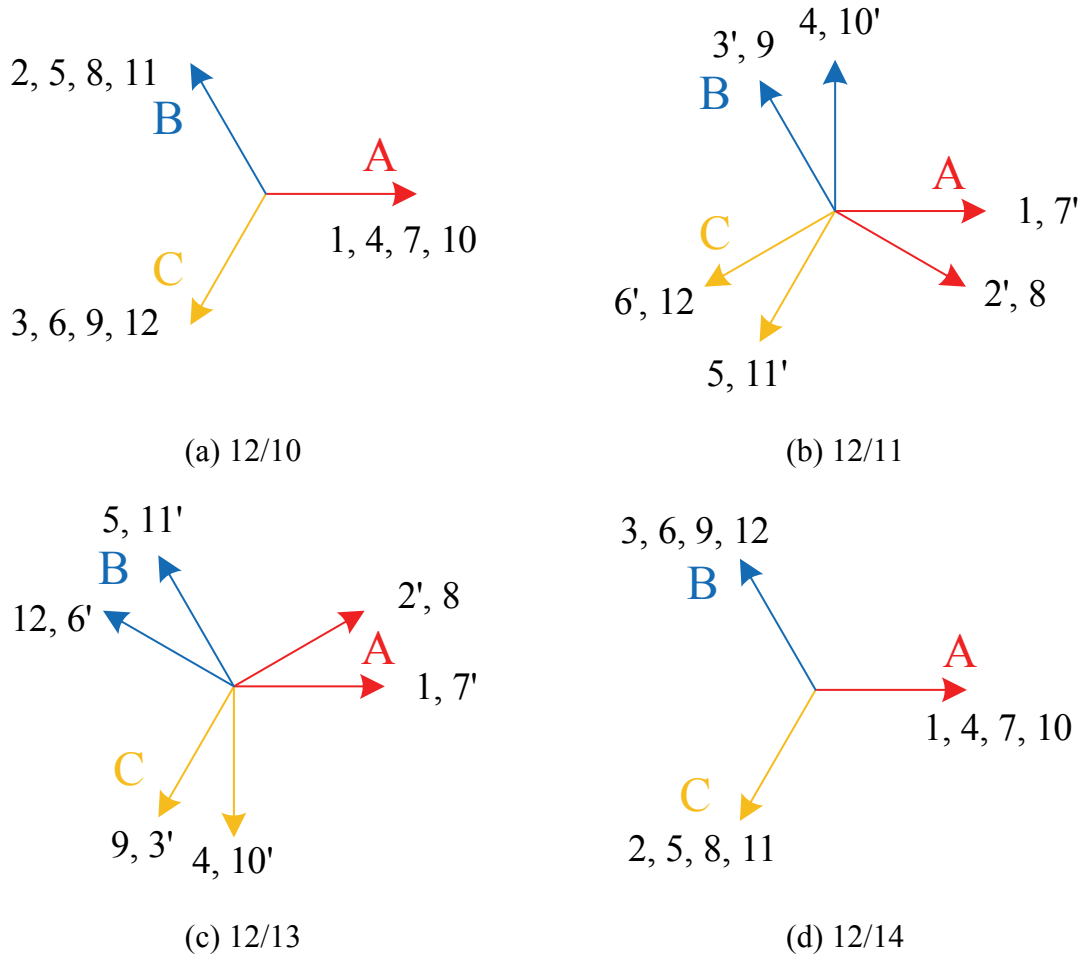


Fig. 5.2 Coil back-EMF phasors for 12-stator-slot PS-HESF machines with different rotor pole numbers.

Based on 2-D FE analysis, the open-circuit field distributions of the proposed machine at four typical rotor positions with only PM excitation are shown in Fig. 5.3. With the salient rotor rotating, the variation of magnetic field can be observed. The positive and negative maximum flux-linkages for phase A occur at $\theta_e = 0^\circ$ (see Fig. 5.3(a)) and $\theta_e = 180^\circ$ (see Fig. 5.3(c)) respectively, whilst the zero flux-linkage is obtained at $\theta_e = 90^\circ$ (see Fig. 5.3(b)) and $\theta_e = 270^\circ$ (see Fig. 5.3(d)) respectively. Therefore, the open-circuit coil flux-linkages are obtained in Fig. 5.4. It should be emphasized that the feature of even order harmonics compensation in the

SFPM machines is inherited [HUA08]. Although each coil flux-linkage (coil 1 or coil 4) contains even order harmonics, the resultant flux-linkage of coil group (coil 1+4), which is the half of the corresponding phase flux-linkage, is sinusoidal and free from even order harmonics, Fig. 5.4(b). Accordingly, the PS-HESF machine can exhibit sinusoidal phase flux-linkage and hence the sinusoidal back-EMF waveforms, revealing the brushless AC (BLAC) operation is applicable.

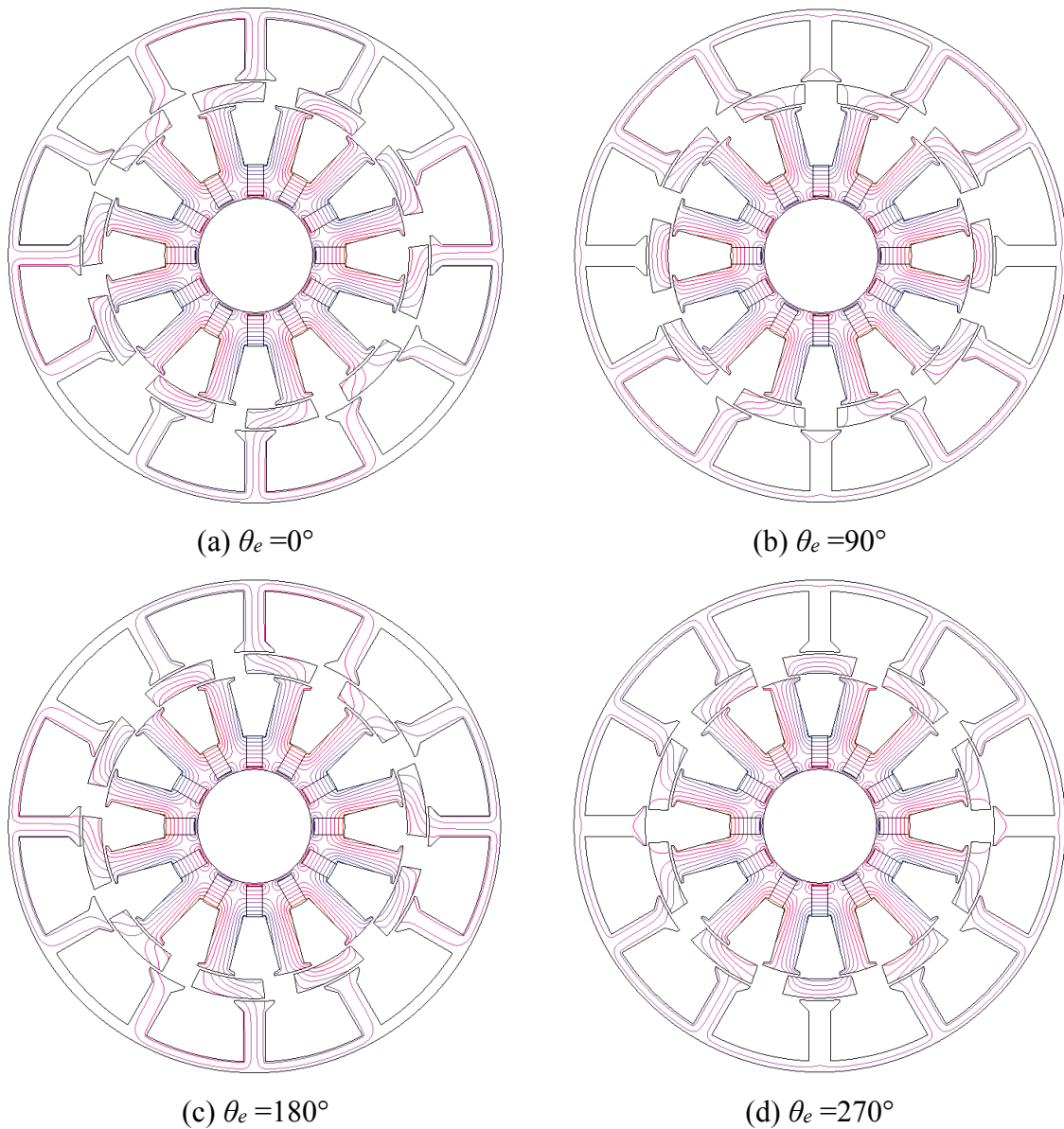
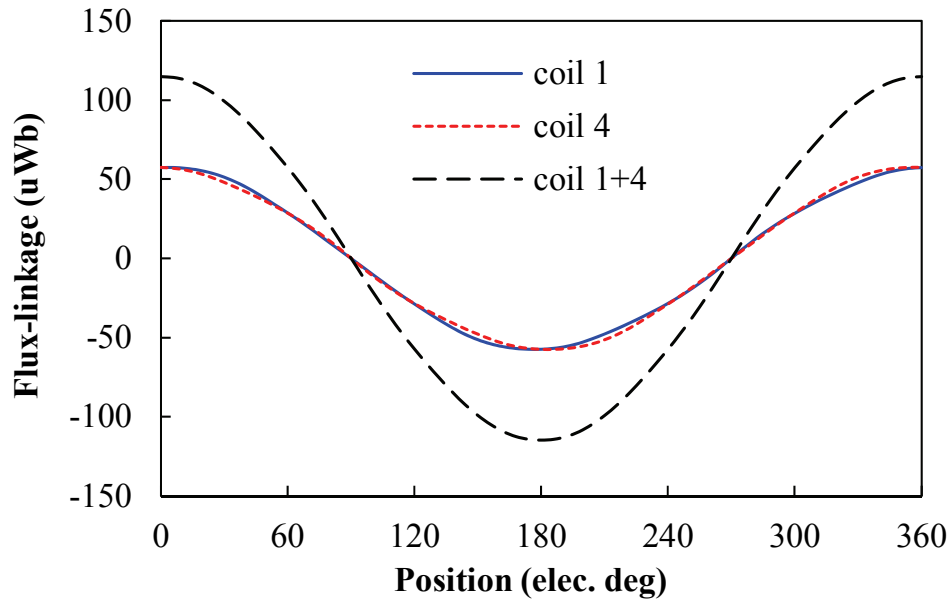
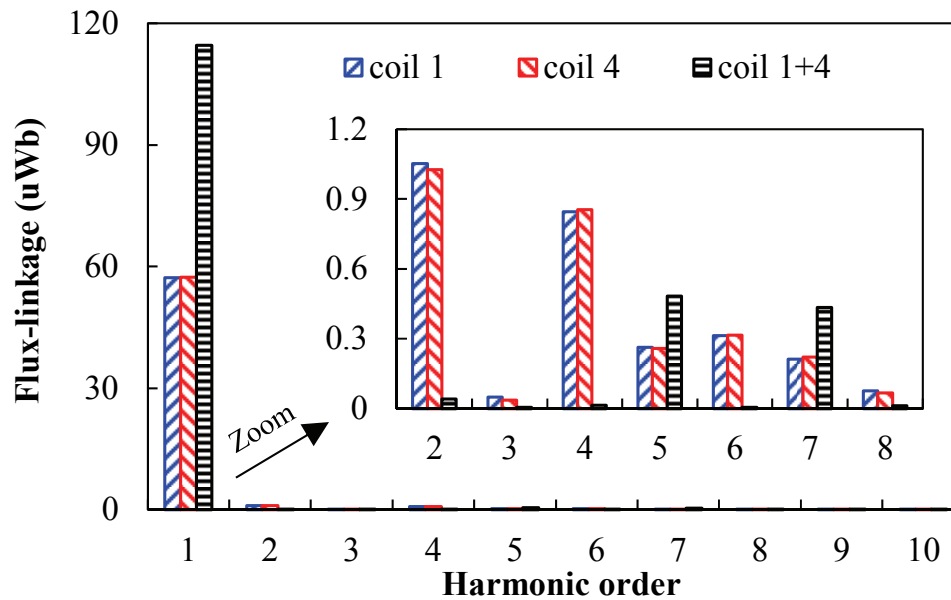


Fig. 5.3 Open-circuit field distributions due to only PM excitation at four typical rotor positions of the 12/10 PS-HESF machine.



(a) Waveforms



(b) Spectra

Fig. 5.4 Open-circuit flux-linkages due to PM excitation only of the 12/10 PS-HESF machine.

The flux regulation principle of the PS-HESF machine is illustrated in Fig. 5.5, in which the flux paths under flux-enhancing and flux-weakening operations are specified. The PMs and FWs can contribute to the air-gap flux simultaneously, thus the accumulative flux can be easily regulated by applying currents with different polarities to the FWs. At $\theta_e = 0^\circ$ (d -axis rotor position), the field distributions under flux-enhancing and flux-weakening conditions are shown in Fig. 5.6, in which the effects of flux regulation can be observed. Furthermore, the

open-circuit phase flux-linkage waveforms under different excitations are compared in Fig. 5.7, and the current density of 5A/mm^2 in FW slots are applied. As the FW flux experiences the same paths as the PM flux, the even order harmonic compensation is also effective. It can be seen that the amplitudes of phase flux-linkages can be flexibly varied while the harmonics are always tiny thanks to the advantages of even order harmonics compensation.

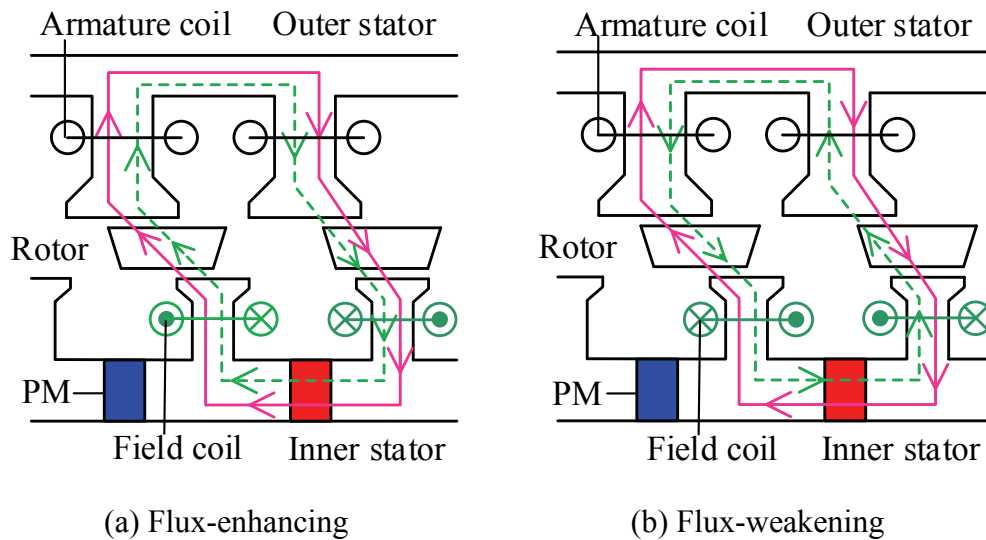


Fig. 5.5 Flux paths of flux-enhancing and flux-weakening operations.

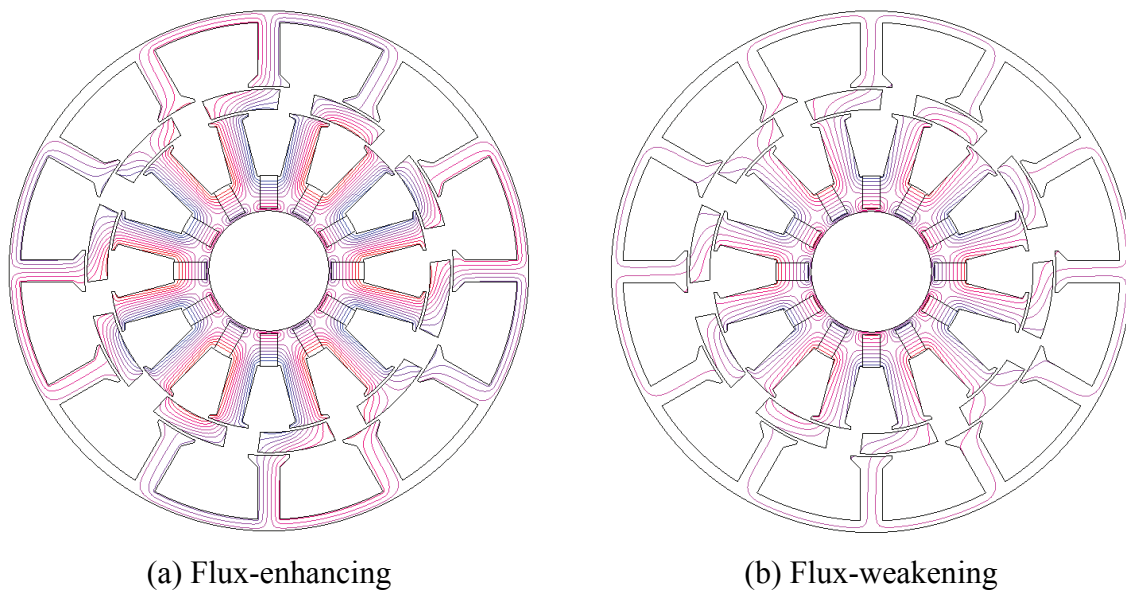
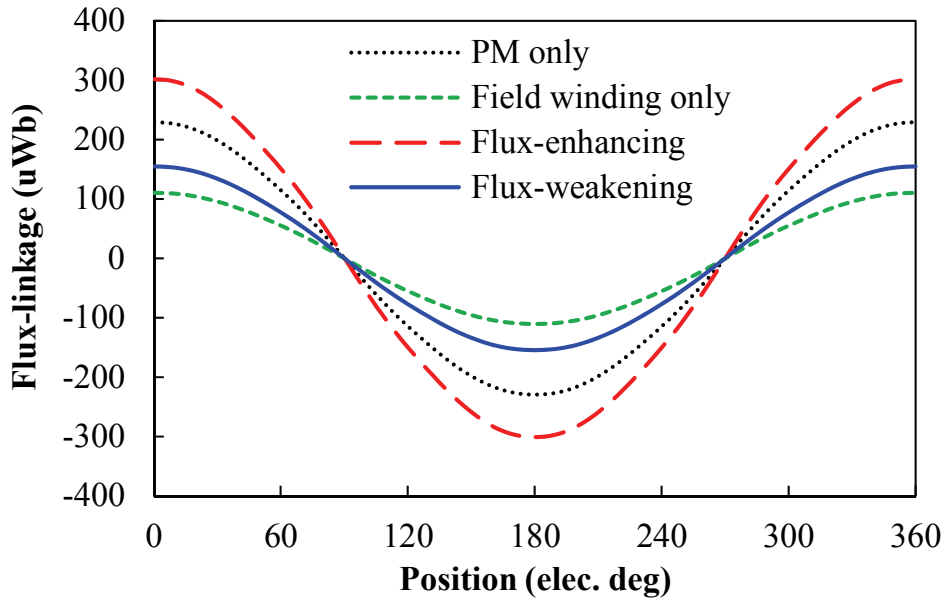
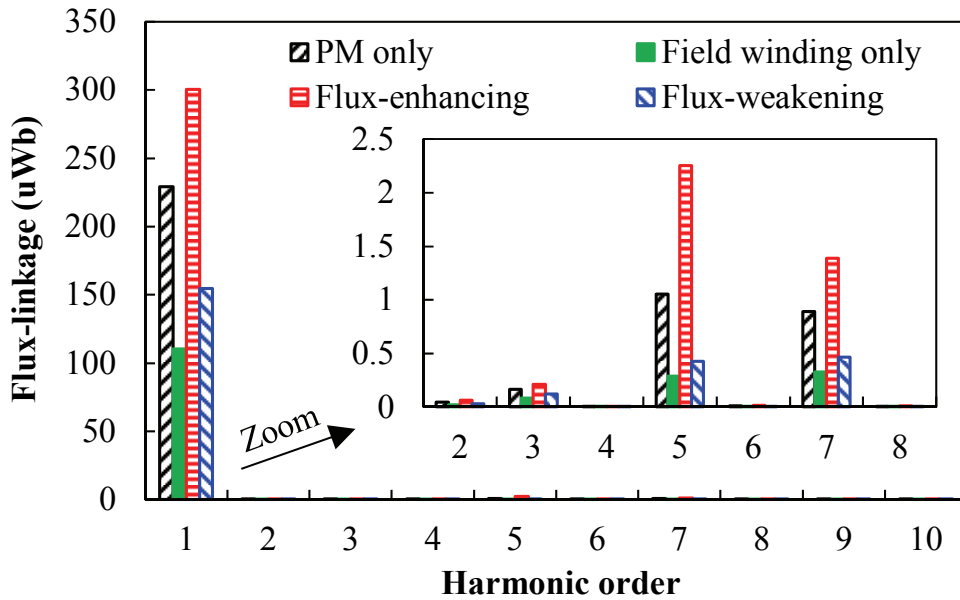


Fig. 5.6 Open-circuit field distributions of the 12/10 PS-HESF machine under flux-enhancing and flux-weakening operations at d -axis rotor position.



(a) Waveforms



(b) Spectra

Fig. 5.7 Open-circuit phase flux-linkages of the 12/10 PS-HESF machine under different excitations.

5.3 Electromagnetic Performance

Based on 2-D FE analysis, the electromagnetic performance of the proposed machines are evaluated in this section. Apart from the 12/10 configuration, the 11-, 13- and 14-pole rotors are also feasible for the 12-stator-slot machine, and their armature winding configurations are shown in Fig. 5.2. The key design parameters of the PS-HESF machine are illustrated in Fig.

5.8(a), and the iron bridge adjacent to the PMs is employed to facilitate flux regulation. The design of PS-HESF machine is flexible as there is a trade-off between the torque output and flux regulation capability. With the constraints including 25mm active axial length, 45mm outer radius, 5000 mm³ PM volume, 20W copper losses in armature windings and zero *d*-axis current control, the global optimization based on genetic algorithm is carried out for maximizing the average torque during one electric period under the flux-enhancing operation with 5A/mm² current density in the FW slots. The definition of the armature winding copper loss is expressed in (2.1), and it should be noted that the slot package factors are kept at 0.5 in both armature coil and field coil slots. In addition, the thickness of iron bridge is fixed at 0.5 mm since the thicker iron bridge would boost the short-circuited flux and thus degrade the torque output while the thinner one would limit the flux regulation. The optimization process of the PS-HESF machines is similar to that introduced in the section 4.3. In addition, the thickness of iron bridge is fixed at 0.5 mm since the thicker iron bridge would boost the short-circuited flux and thus degrade the torque output while the thinner one would limit the flux regulation. The optimized stator inner radius should be moderate as a higher value sacrifices the available space for armature windings while a lower value reduces the space for excitations (PM and FW). Similarly, the optimal stator yoke thickness and tooth arc should be moderate to compromise the space for windings and magnetic saturation. Moreover, the rotor pole arcs are determined to avoid more severe saturation and leakage-flux, while the compromising rotor thickness is obtained to maintain the necessary saliency ratio and the space for windings and PMs. After global optimization, the optimal geometric parameters for the 10-, 11-, 13- and 14-rotor PS-HESF machines are listed in Table 5.1. In addition, in order to better evaluate the machine performance, a conventional HESF machine as shown in Fig. 5.1(b), which has been proved to have better performance than its counterparts [OWE10a], [ZHA11], [HUA15], is taken as a baseline. The optimization with the identical strategy and constraints is carried out for this machine, and its optimized parameters are listed in Table 5.1 as well.

Table 5.1 Key design parameters of optimal PS-HESF machines with different rotor pole numbers and the conventional HESF machine.

Machines	10-rotor	11-rotor	13-rotor	14-rotor	Conventional 10-rotor
Stator slot number, N_s	12	12	12	12	12
Rotor pole-pair number, N_r	10	10	10	10	10
Active axial length (mm), l_a	25	25	25	25	25
Stator outer radius (mm), R_{oso}/R_{so}	45	45	45	45	45
Stator yoke radius (mm), R_{osy}/R_{sy}	43	43	43	43	42.5
Stator inner radius (mm), R_{osi}/R_{si}	31.95	32.25	32.85	33.2	29
Stator tooth arc ($^\circ$), β_{ost}/β_{st}	13	13	13.5	13	8.5
Air-gap length (mm), g	0.5	0.5	0.5	0.5	0.5
Rotor radial thickness (mm), h_r	3.5	3	3	3	N/A
Rotor outer pole arc ($^\circ$), β_{ro}/β_{rt}	25	24	20	18	13.5
Rotor inner pole arc ($^\circ$), β_{ri}	24	22	20	19	N/A
Inner stator outer radius (mm), R_{iso}	27.45	28.25	28.85	29.2	N/A
Inner stator yoke radius (mm), R_{isy}	16.5	16.5	16.5	16.5	N/A
Inner stator inner radius (mm), R_{isi}	10.4	10.4	10.4	10.4	N/A
Inner stator tooth arc ($^\circ$), β_{ist}	15	14	14	14	N/A
PM height (mm), h_{pm}	5.6	5.6	5.6	5.6	5.6
PM thickness (mm), w_{pm}	3	3	3	3	3
PM volume (mm ³)	5000	5000	5000	5000	5000
Iron bridge thickness (mm), l_{ib}	0.5	0.5	0.5	0.5	0.5
Rotor outer radius (mm), R_{ro}	N/A	N/A	N/A	N/A	28.5
Rotor yoke radius (mm), R_{ry}	N/A	N/A	N/A	N/A	18
Rotor inner radius (mm), R_{ri}	N/A	N/A	N/A	N/A	10.4

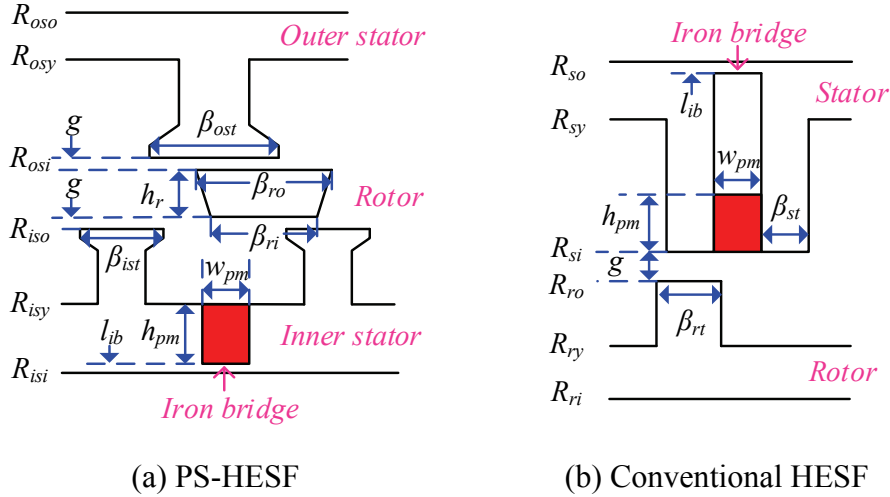
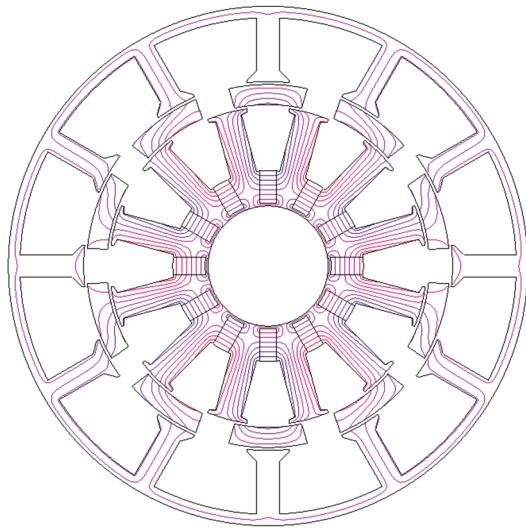


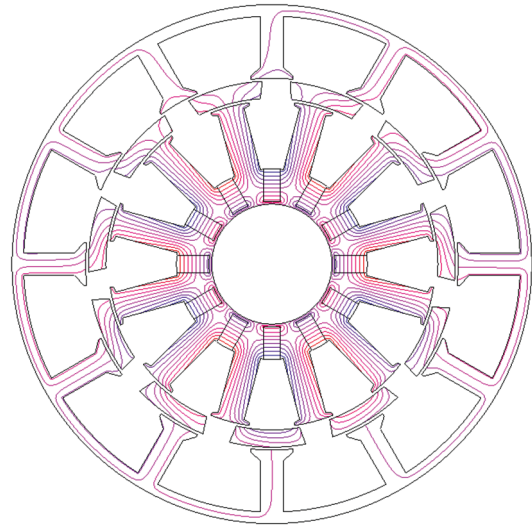
Fig. 5.8 Illustration of design parameters of PS-HESF and HESF machines.

5.3.1 Open-circuit back-EMF

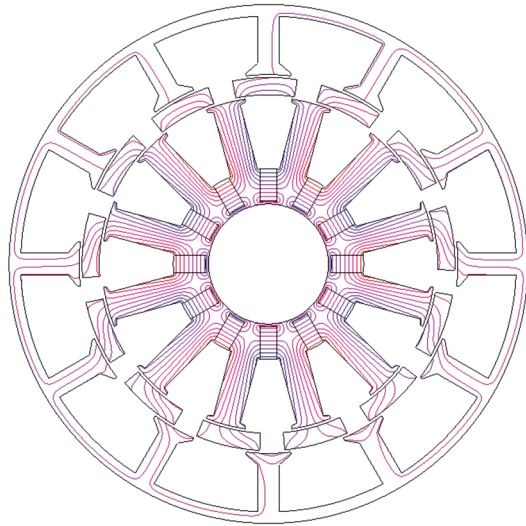
Fig. 5.9 shows the open-circuit field distributions of the four optimized PS-HESF machines with different rotor pole numbers, at d -axis rotor position. Without field current, the open-circuit phase back-EMFs at 400 r/min of the proposed PS-HESF and conventional HESF machines are compared in Fig. 5.10. It can be seen that the back-EMFs of all machines are sinusoidal and the even order harmonics are negligible, which is corresponding to the previous analysis. Moreover, the peak fundamental amplitudes of the 11- and 13-rotor PS-HESF machines are higher than the counterparts, which can be attributed to the high winding factors. The peak fundamental back-EMF value of the conventional HESF machine is slightly higher than the PS-HESF machines.



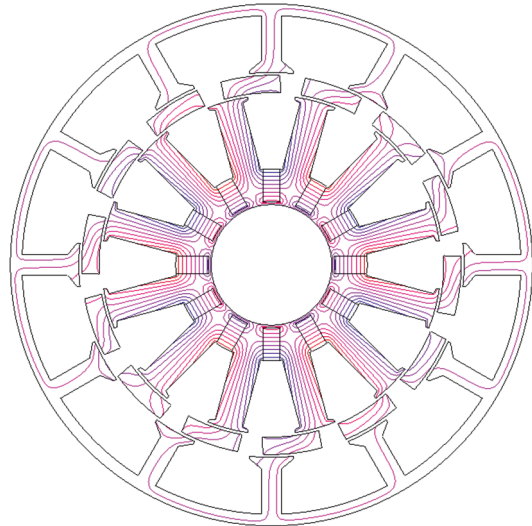
(a) 10-rotor



(b) 11-rotor

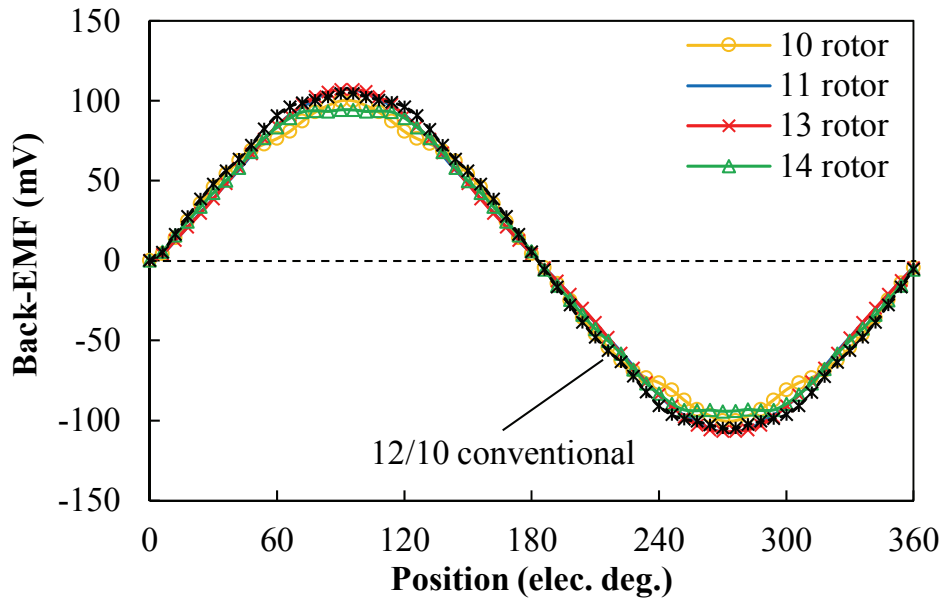


(c) 13-rotor

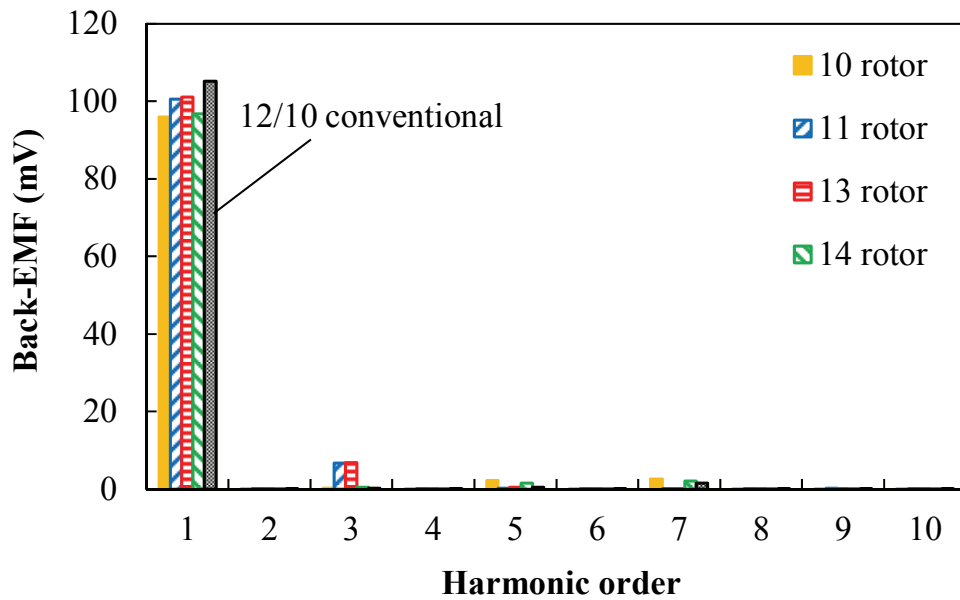


(d) 14-rotor

Fig. 5.9 Open-circuit field distributions of 12-stator-slot PS-HESF machines with different rotor pole numbers at d -axis position ($\theta_e = 0^\circ$).



(a) Waveforms



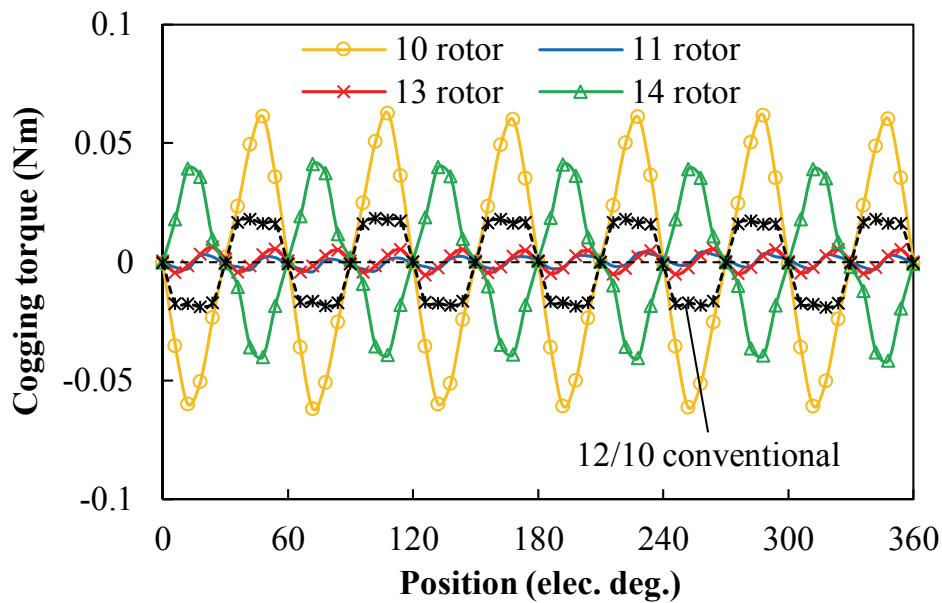
(b) Spectra

Fig. 5.10 Open-circuit phase back-EMFs at 400 r/min without field current (1 turn number per coil).

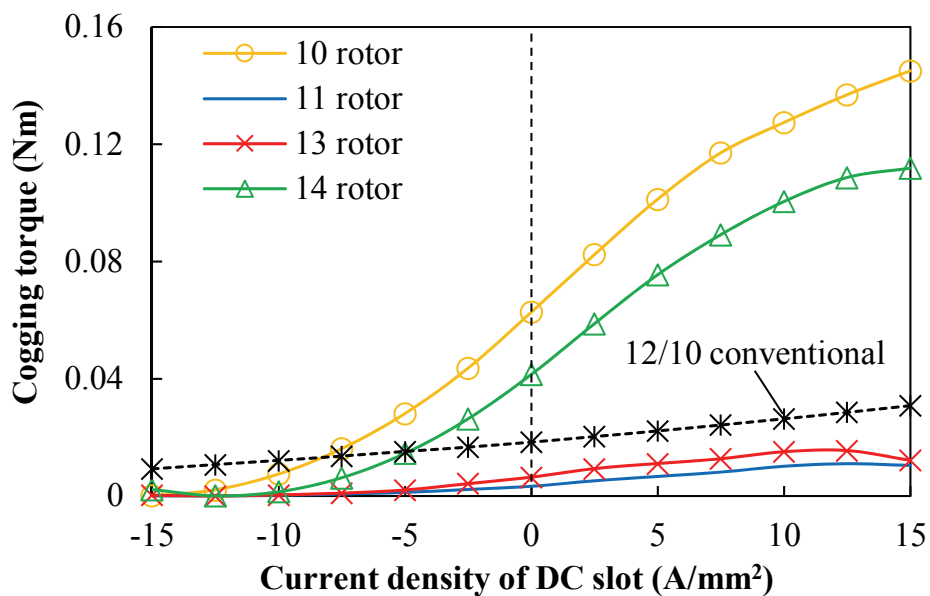
5.3.2 Cogging torque

Fig. 5.11 shows the cogging torques with only PM excitation, in which the cycle numbers of cogging torque in each electric period are 6 for the 10- and 14-rotor HE machines while it is 12 for the 11- and 13-rotor machines, which follows the cogging torque principle of machines having corresponding slot/pole combinations [ZHU00]. It can be seen that the 11-rotor PS-HESF machine exhibits the lowest cogging torque. However, the 10-rotor PS-HESF machine

exhibits higher cogging torques than the conventional one. It should be mentioned that only the maximum torque is considered in the optimization and the cogging torque suppression is neglected. As shown in Fig. 5.12, the reduced cogging torque can be obtained by carefully adjusting the rotor outer and inner pole arcs, but the average torque may be slightly sacrificed. In addition, the peak cogging torques versus different field currents of all machines are shown in Fig. 5.11(b), in which the 11- and 13-rotor PS-HESF machines always have lower cogging torques. Meanwhile, it can be found that the peak cogging torques are increased with positive field currents but decreased with negative field currents.



(a) Cogging torque waveforms



(b) Peak cogging torques versus field currents

Fig. 5.11 Cogging torques.

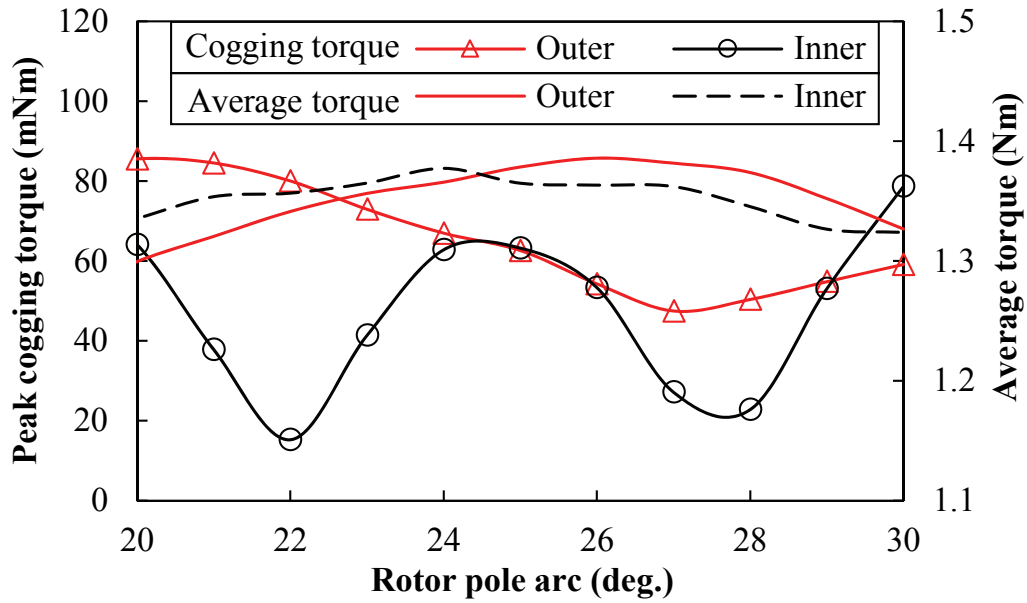
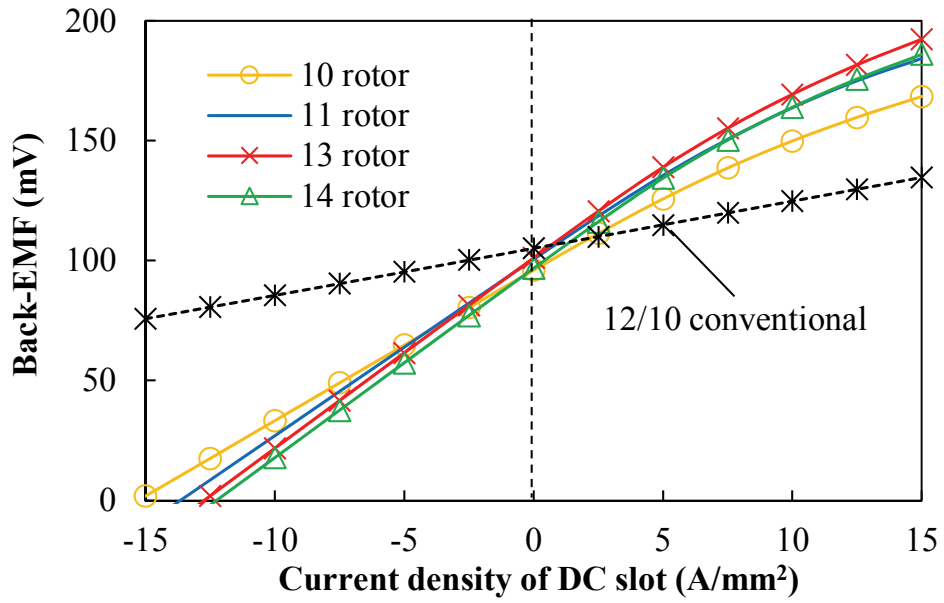


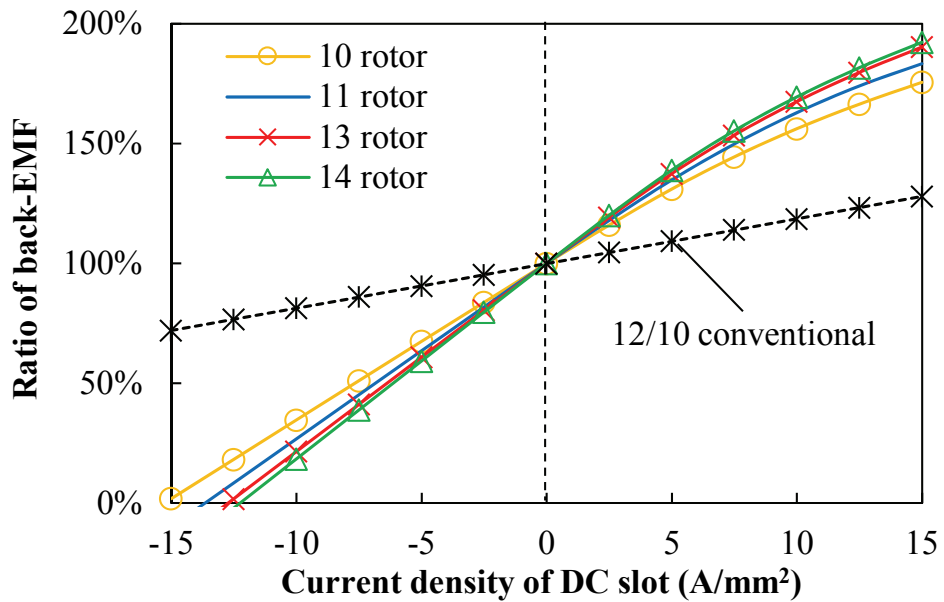
Fig. 5.12 Peak cogging torques and average torques of 12/10 PS-HESF machine with different rotor outer and inner pole arcs.

5.3.3 Flux regulation capability

The flux regulation capability is an essential characteristic of HE machines, which should be investigated in detail. The variations of peak fundamental back-EMFs versus field excitations are compared in Fig. 5.13(a), and Fig. 5.13(b) shows the ratios of the back-EMFs with different field excitations to the back-EMF without field current. The proposed PS-HESF machines always have wider flux variation ranges than the conventional one in both flux-enhancing and flux-weakening operations, among which the 14-rotor PS-HESF machine exhibits the widest flux variation range. With around -12.5A/mm^2 current density in the FW slots, the zero back-EMF can be achieved, while around 185% back-EMF can be obtained with $+15\text{A/mm}^2$ FW excitation. It can be noted that the flux-enhancing is more challenging than the flux-weakening due to the magnetic saturation. More specifically, Fig. 5.14 illustrates the phase back-EMF waveforms at 400 r/min of the 12/10 PS-HESF and conventional HESF machines with different field excitations. The labels “ $J_s=-5$ ” and “ $J_s=+5$ ” represent the current density of 5A/mm^2 in the FW slots, with negative and positive polarities respectively. It can be found that the 12/10 PS-HESF machine exhibits a much wider variation range of back-EMFs than the conventional one, which is due to the enlarged area for the FW slots.



(a) Peak fundamental back-EMFs.



(b) Ratios of back-EMFs.

Fig. 5.13 Variations of peak fundamental back-EMFs at 400 r/min versus field excitations.

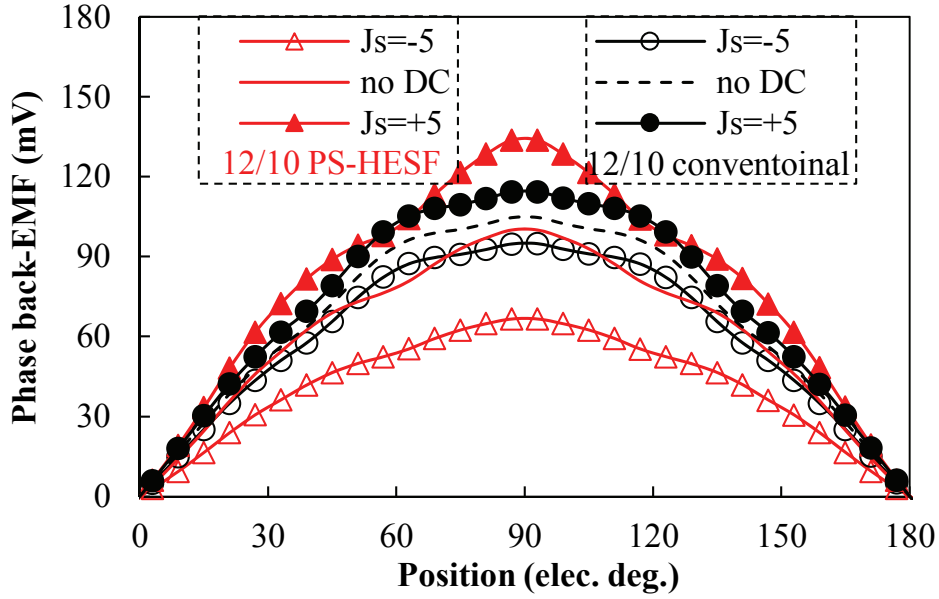


Fig. 5.14 Phase back-EMF waveforms at 400 r/min with different field excitations of the 12/10 PS-HESF and conventional HESF machines.

5.3.4 On-load torque

Apart from the outstanding flux regulation capability, the torque output of the proposed PS-HESF machine is improved as well. With fixed 20W copper losses in armature windings and zero d -axis current control, the torque waveforms of the four PS-HESF machines and the conventional machine are compared in Fig. 5.15. It is found that all PS-HESF machines benefit from higher torques than the conventional one. Although the open-circuit back-EMF of the conventional HESF machine is higher, Fig. 5.10, it suffers serious space conflict in the stator and the available area for armature windings is limited, which results in lower torque.

Further, the variations of the average torques versus field currents are shown in Fig. 5.16(a), which corresponds to the back-EMF variations. The PS-HESF machines always have higher torques than the conventional one during the flux-enhancing region, and the 13-rotor PS-HESF machine exhibits the highest torque. In addition, the torque ripple factor is defined as:

$$T_{ripple} = \frac{T_{max} - T_{min}}{T_{ave}} \quad (5.2)$$

where T_{max} , T_{min} , and T_{ave} represent maximum, minimum and average torque during one electric cycle respectively. Fig. 5.16(b) shows the torque ripples versus field currents, in which the 11- and 13-rotor PS-HESF machines always have remarkably lower torque ripples than the counterparts.

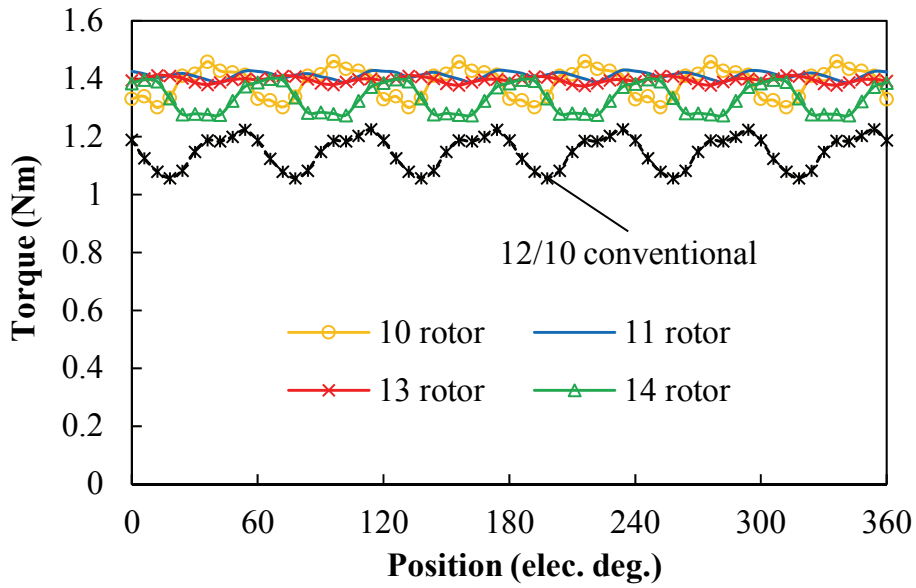
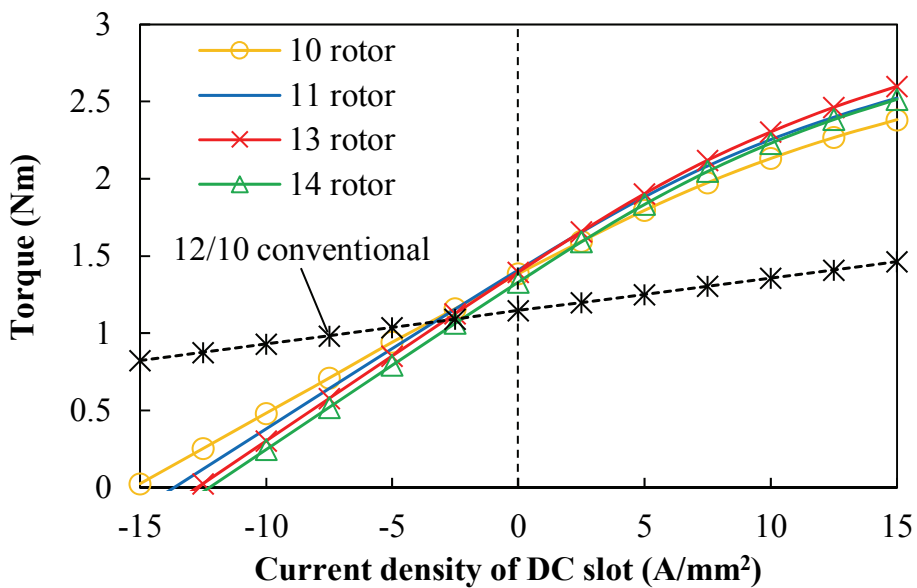
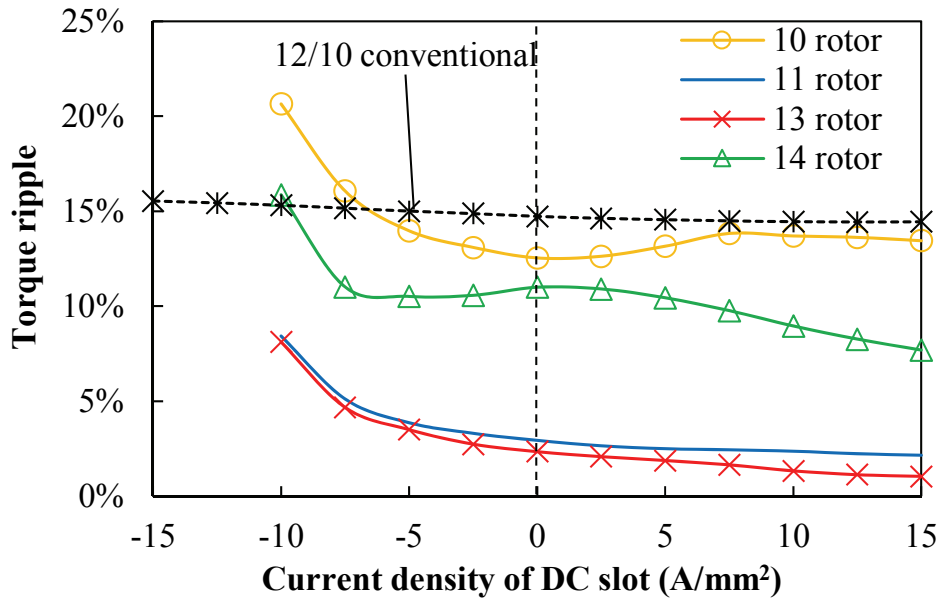


Fig. 5.15 Torque waveforms with 20W copper losses in armature windings and zero d -axis current control.

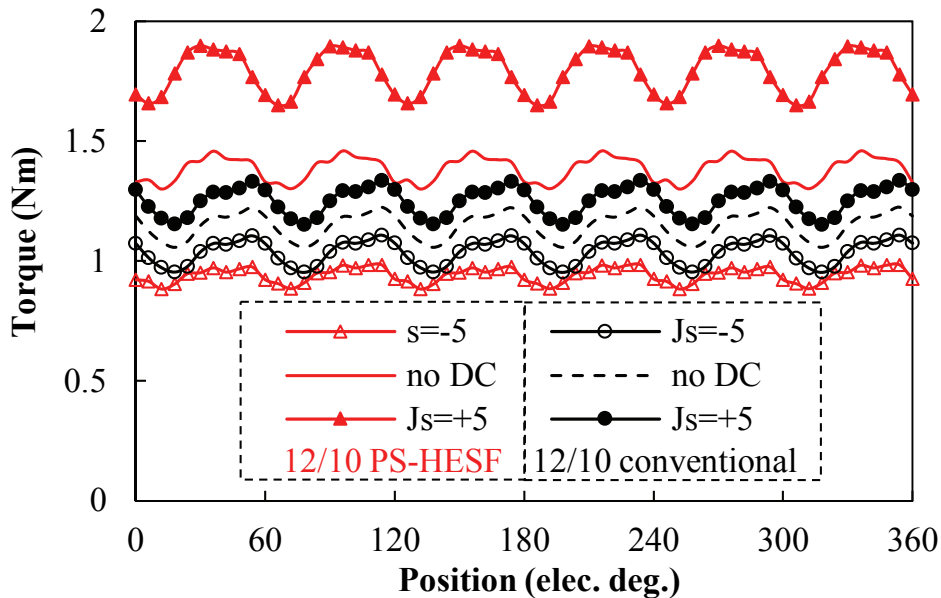
More specifically, Fig. 5.16(c) compares the electromagnetic torque waveforms of the 12/10 PS-HESF and conventional HESF machines with 20W copper losses in armature windings and zero d -axis current control. Three typical field excitations are applied individually. The torques of the PS-HESF machine are significantly higher than the conventional HESF machine under sole PM excitation and flux-enhancing conditions (20% and 43% higher respectively), which is due to better space utilization and enlarged slot area for windings. Meanwhile, the PS-HESF machine has lower torque under flux-weakening operation since its back-EMF is greatly weakened by the negative field current.



(a) Average torques versus field excitations.



(b) Torque ripples versus field excitations

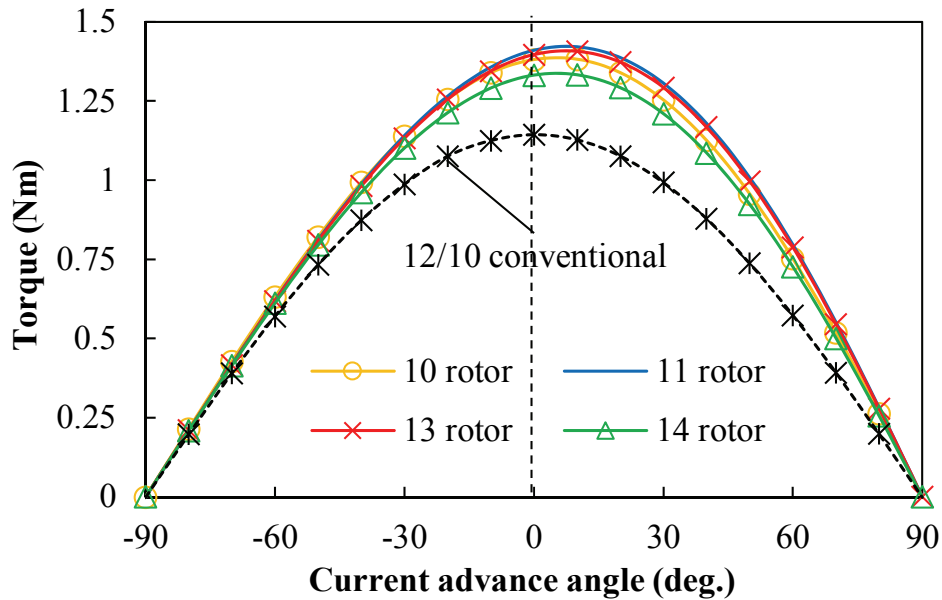


(c) Torque waveforms of the 12/10 PS-HESF and conventional HESF machines

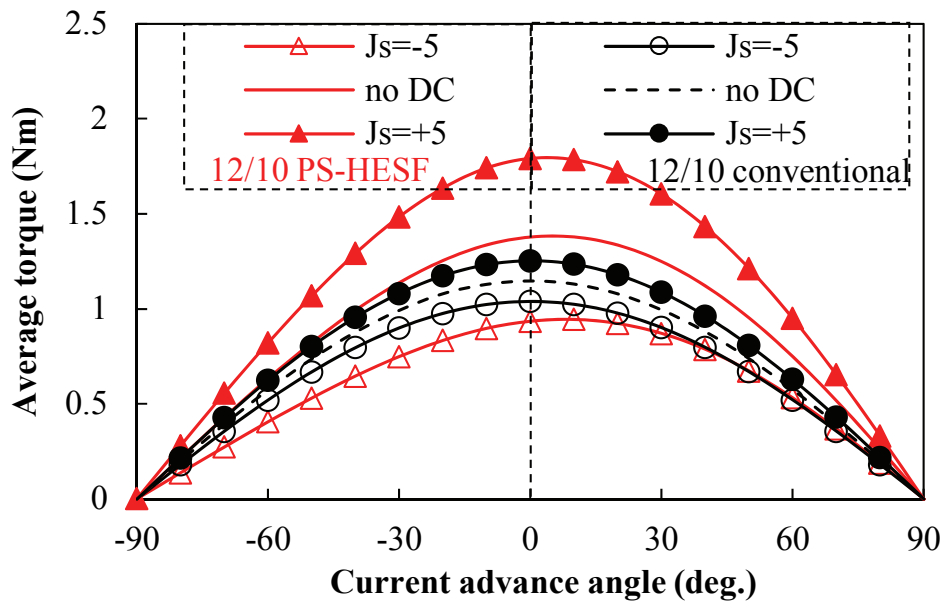
Fig. 5.16 Torques with different field excitations. (20W copper loss in armature windings, zero d -axis current control)

The variations of average torques versus current advance angles are compared in Fig. 5.17(a), where the PS-HESF machines always have higher torques than the conventional one. More importantly, it can be seen that the peak torques occur at the current angle close to 0° , indicating low reluctance torque in all machines. Further, the average torques against current advance angles of the 12/10 PS-HESF and conventional HESF machines, under three typical field excitation conditions, are compared in Fig. 5.17(b). Similarly, the peak torques still occur at

around 0° , which is not influenced by the field excitations. Therefore, the zero d -axis current control strategy is suitable for these machines to achieve maximum torque per ampere. Besides, the average torques of the PS-HESF machines are always higher than the conventional one under sole PM excitation and flux-enhancing conditions.



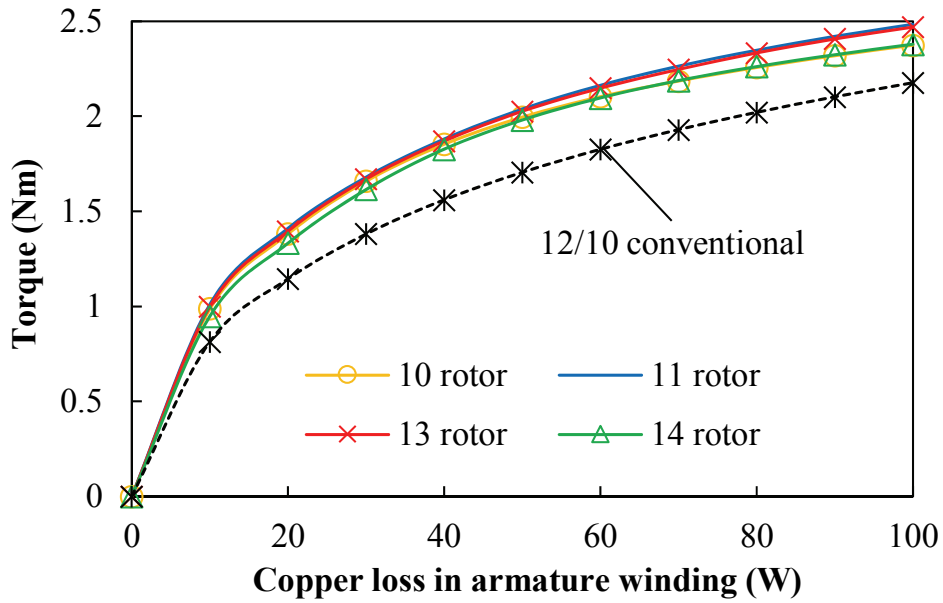
(a) Average torques versus current advance angles without FW excitation



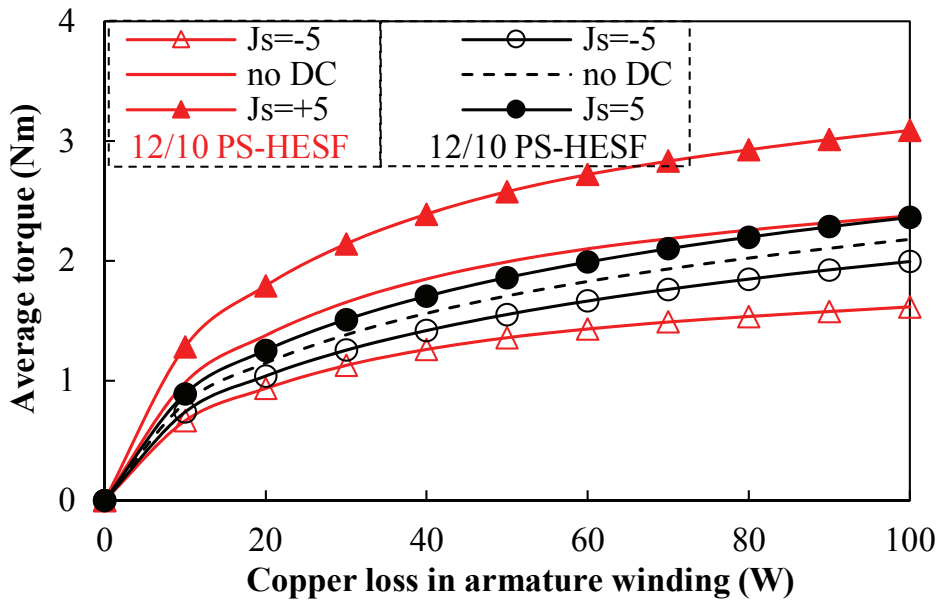
(b) Average torque versus current advance angle of the 12/10 PS-HESF and conventional HESF machines

Fig. 5.17 Variations of average torques versus current advance angles. (20W copper loss in armature windings)

Without FW excitation, the variations of average torques versus copper losses in armature windings of all HE machines are shown in Fig. 5.18(a), where the PS-HESF machines have higher torque among the whole copper loss range. Meanwhile, the average torques versus armature winding copper losses of the 12/10 PS-HESF machine and the conventional one, under three field excitation conditions, are illustrated in Fig. 5.18(b). The torques of the PS-HESF machine are advantageous under flux-enhancing and sole PM excitation conditions. It should be mentioned that the copper loss in the FW slots with 5A/mm^2 current density is around 19W.



(a) Average torques versus copper losses in armature windings without FW excitation



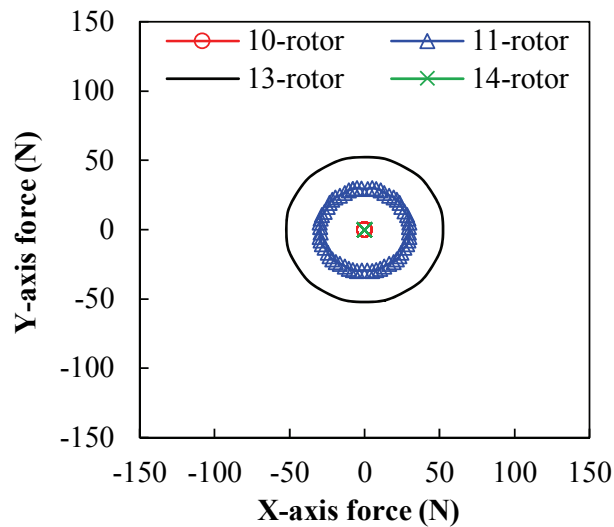
(b) Average torques versus copper losses in armature windings of the 12/10 PS-HESF and conventional HESF machines

Fig. 5.18 Variations of average torques versus copper loss in armature windings. (zero d -axis current control)

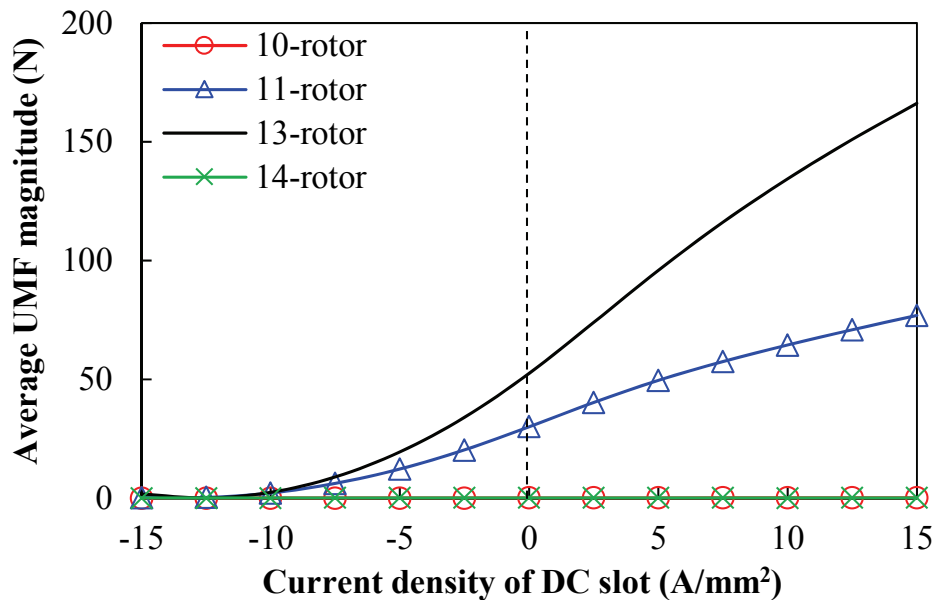
5.3.5 Unbalanced magnetic force

The unbalanced magnetic force (UMF) on the rotor can cause additional vibration and noise as well as threaten the bearing life. Without FW excitation, the open-circuit and on-load UMFs of the four PS-HESF machines are shown in Fig. 5.19(a) and Fig. 5.20(a), respectively. It can be seen that the 11- and 13-rotor machines suffer significant UMFs due to their odd rotor pole

numbers, while the UMFs are negligible in the 10- and 14-rotor counterparts. Meanwhile, the UMFs in the 11- and 13-rotor machines are increased with the load. More importantly, the variations of the average UMF magnitudes versus field currents are shown in Fig. 5.19(b) and Fig. 5.20(b), where the 10- and 14-rotor PS-HESF machines are always free from the UMFs, whereas the 11- and 13-rotor machines have the increased UMFs with positive field currents but the decreased UMFs with negative field currents. Furthermore, it should be emphasized that the UMFs in the 11- and 13-rotor PS-HESF machines will be eliminated by multiplying their stator slot and rotor piece numbers to obtain the even rotor piece numbers.

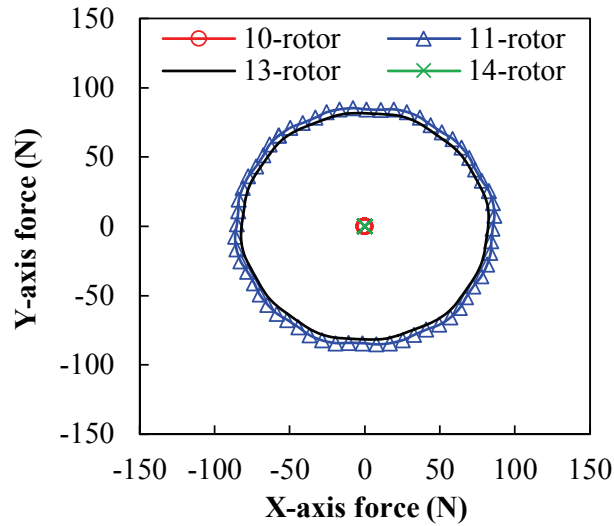


(a) UMF without FW excitation

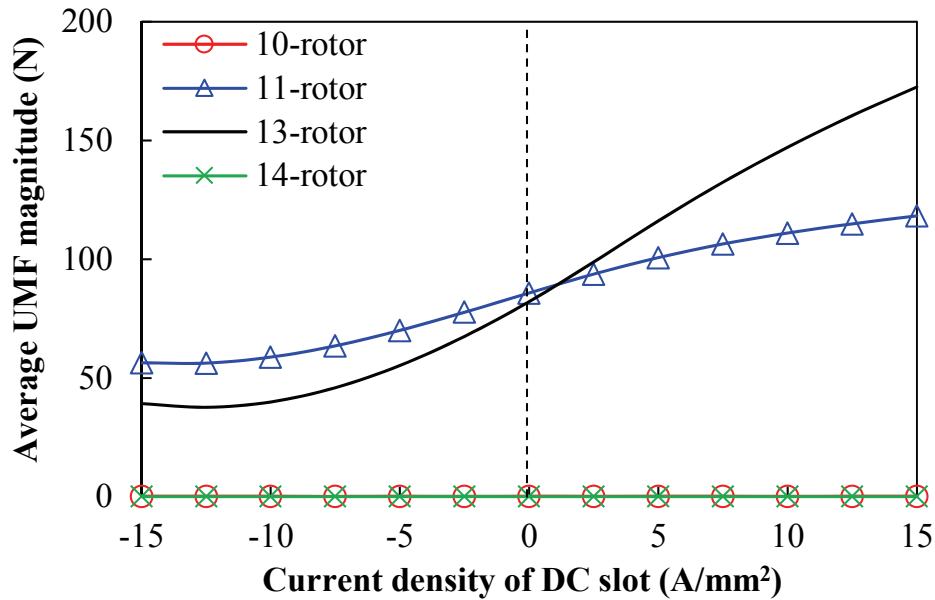


(b) Average UMF magnitudes with different field currents

Fig. 5.19 Open-circuit UMFs of 12-stator-slot PS-HESF machines with different rotor pole numbers.



(a) UMF without FW excitation



(b) Average UMF magnitudes with different field currents

Fig. 5.20 On-load UMFs of 12-stator-slot PS-HESF machines with different rotor pole numbers (20W copper losses in armature windings, zero d -axis current control).

5.4 Influence of Hybridization

According to the previous analysis, it can be found that the proposed PS-HESF machine can exhibit better flux regulation capability as well as higher torque output than the conventional HESF counterpart. However, since the design of the HE machine is flexible, it is worth investigating the effects of key geometric parameters on the hybridization ratio, which reflects the split between PM and FW fluxes. The trade-off between the torque output and flux regulation capability is significantly affected by this ratio. In this section, based on the proposed

12/10 PS-HESF machine, the essential design parameters including PM length factor k_{PM} and iron bridge thickness l_{ib} , are analyzed. k_{PM} is defined as:

$$k_{PM} = \frac{h_{PM}}{R_{iso} - R_{isi}} \quad (5.3)$$

The higher k_{PM} implies larger PM usage volume and thus higher torque density while sacrificed flux regulation capability. In fact, the PS-HESF machine can be transformed to a sole PM PS machine [EVA15] if $k_{PM}=1$ and a wound-field PS machine [ZHU15c] if $k_{PM}=0$. Meanwhile, to evaluate the flux regulation potential, the flux regulation capability δ is defined as:

$$\delta = \frac{E_{FE} - E_{FW}}{E_{PM}} \quad (5.4)$$

where E_{FE} , E_{FW} and E_{PM} represent the open-circuit back-EMFs under flux-enhancing, flux-weakening and sole PM excitation respectively. The higher δ indicates better flux regulation capability.

Without FW excitation, the average torques with 20W copper losses in armature windings and zero d -axis current control are presented in Fig. 5.21, where different k_{PM} are applied. The torque increases significantly with the increase of k_{PM} . However, as δ with $5A/mm^2$ current density in FW slots shown in Fig. 5.21, the flux regulation capability is degraded with higher k_{PM} since the PM volume is increased and the available space for FWs is reduced.

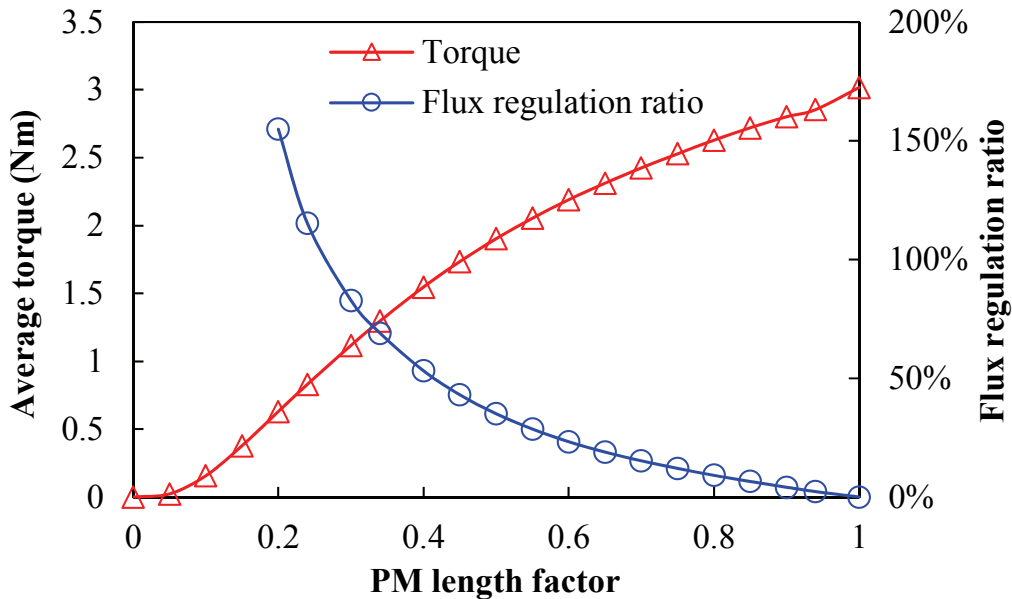


Fig. 5.21 Variations of average torque and flux regulation ratio with different PM length factors.

Besides, the iron bridge can assist the flowing of the flux generated by the FWs, enhancing the flux regulation. But it also short-circuits the PM flux and hence reduces the torque output. Fig. 5.22 shows the effects of the iron bridge thickness, in which the average torque without FW excitation and δ with 5A/mm^2 current density in FW slots are both illustrated. As can be seen, δ increases significantly with iron bridge thickness increasing, while the torque capability is sacrificed.

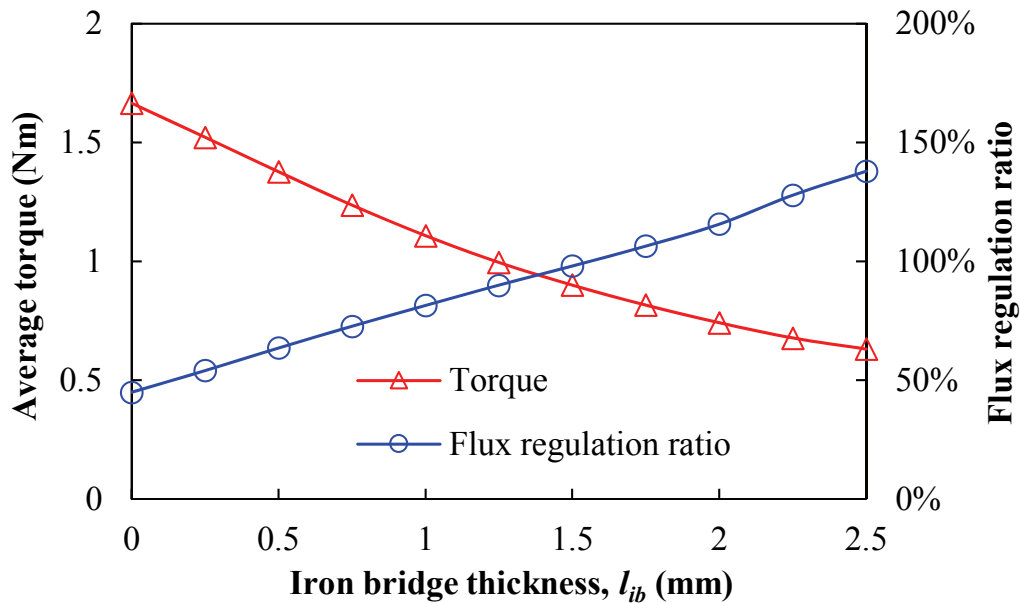


Fig. 5.22 Variations of average torque and flux regulation ratio with different iron bridge thicknesses.

In fact, the presence of iron bridge influences the magnetic connection configurations between PM and FW excitations in the PS-HESF machine. It is known that the HE machines can be classified into series hybrid and parallel hybrid [AMA09], where the FW flux goes across the PM in the series hybrid while it bypasses the PM in the parallel hybrid. If the PS-HESF machine is equipped with the iron bridge, the flux generated by the FWs can flow through the iron bridge and thus bypass the PM, as shown in Fig. 5.23(a) in which the field current is applied and the PM is set as air. As a result, parallel hybrid and thus better flux regulation capability are achieved. However, the PS-HESF machine having iron bridge suffers the short-circuited PM flux, Fig. 5.23(c), and hence the sacrificed torque. Alternatively, the FW flux has to go through the PM if the iron bridge is absent, and therefore the series hybrid is obtained, Fig. 5.23(b).

Therefore, the hybridization ratio of this PS-HESF machine is flexible, which can be easily adjusted by the PM length factor or iron bridge thickness. Besides, the parallel hybrid can be

achieved by employing iron bridge while the series hybrid is obtained if the iron bridge is eliminated. As a result, the appropriate design of the PS-HESF machine depends on the requirements of the torque density and flux regulation capability, for a specific application.

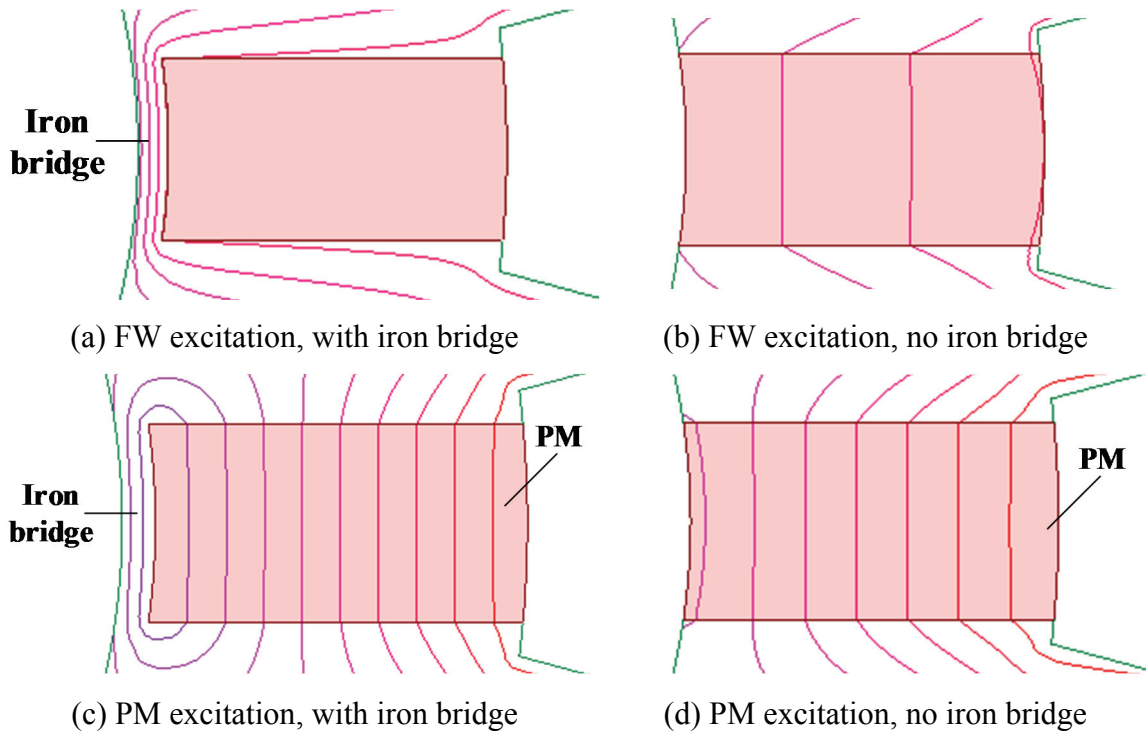


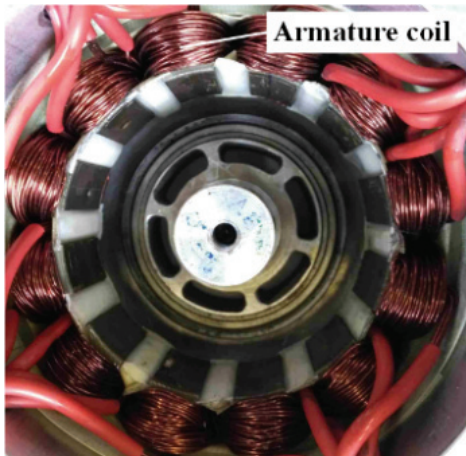
Fig. 5.23 Open-circuit field distributions with field current only or PM only.

5.5 Experimental Validation

In this section, a 12/10 PS-HESF prototype machine is manufactured and tested to validate the FE predictions. The key design parameters of the prototype machine are listed in Table 5.2, whilst the essential machine components are shown in Fig. 5.24. The outer stator assembled with the armature windings is illustrated in Fig. 5.24(a), while the inner stator having field coils and PMs are presented in Fig. 5.24(c). Besides, it should be noted that a 0.5 mm iron rib as shown in Fig. 5.24(d) is employed to connect the separated rotor pieces, which can enhance the mechanical strength and facilitate the fabrication. Moreover, the rotor coupled with the shaft is illustrated in Fig. 5.24(e).

Table 5.2 Key design parameters of prototype 12/10 PS-HESF machine.

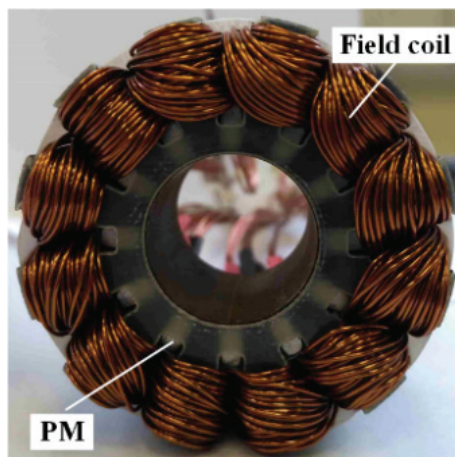
Item	PS-HESF	Item	PS-HESF
N_s	12	N_r	10
l_a	25 mm	R_{oso}	45 mm
R_{osy}	42 mm	R_{osi}	31.75 mm
β_{ost}	18°	g	0.5 mm
h_r	5 mm	β_{ro}	18°
β_{ri}	24°	R_{iso}	25.75 mm
R_{isy}	16 mm	R_{isi}	10.1 mm
β_{ist}	15°	h_{pm}	5.4 mm
w_{pm}	3 mm	l_{ib}	0.5 mm
Number of turns in armature coil	18	Number of turns in field coil	11



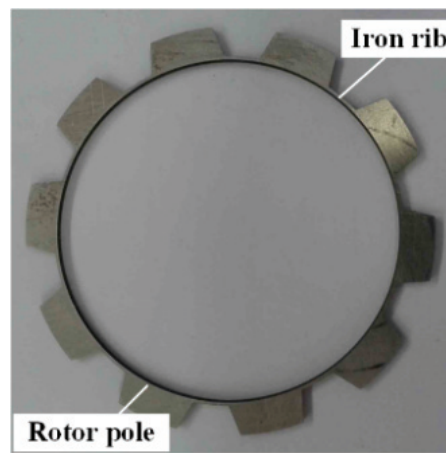
(a) Outer stator



(b) Inner stator lamination



(c) Inner stator



(d) Rotor lamination



(e) Rotor



(f) Assembled stators

Fig. 5.24 Prototype of 12/10 PS-HESF machine.

The open-circuit phase back-EMFs at 400 r/min without field current are measured and compared with the FE predictions in Fig. 5.25, in which the two waveforms agree well while the amplitude of the measured result is around 9.7% lower than the 2-D FE predictions. Furthermore, in order to validate the flux regulation capability, the peak fundamental back-EMFs with different field excitations are presented in Fig. 5.26. The significant variation of back-EMFs is realized, indicating good flux regulation capability. Moreover, based on the test-rig in Fig. 2.26, the static torques without field current are measured by locking the rotor at different positions. Fig. 5.27 shows the comparison between the measured and FE-predicted static torques with different armature currents, where good agreement can be seen. Apart from the end effect that is neglected in 2-D FE calculations, the manufacturing and measuring tolerances discussed in section 2.6 also may result in the difference between the test and FE results.

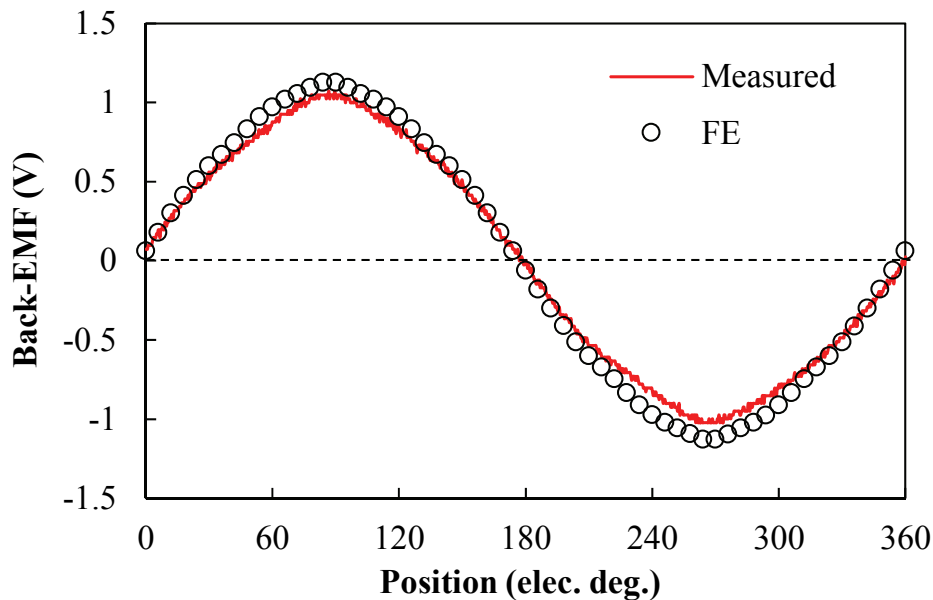


Fig. 5.25 Measured and 2-D FE-predicted back-EMF waveforms at 400 r/min without field current.

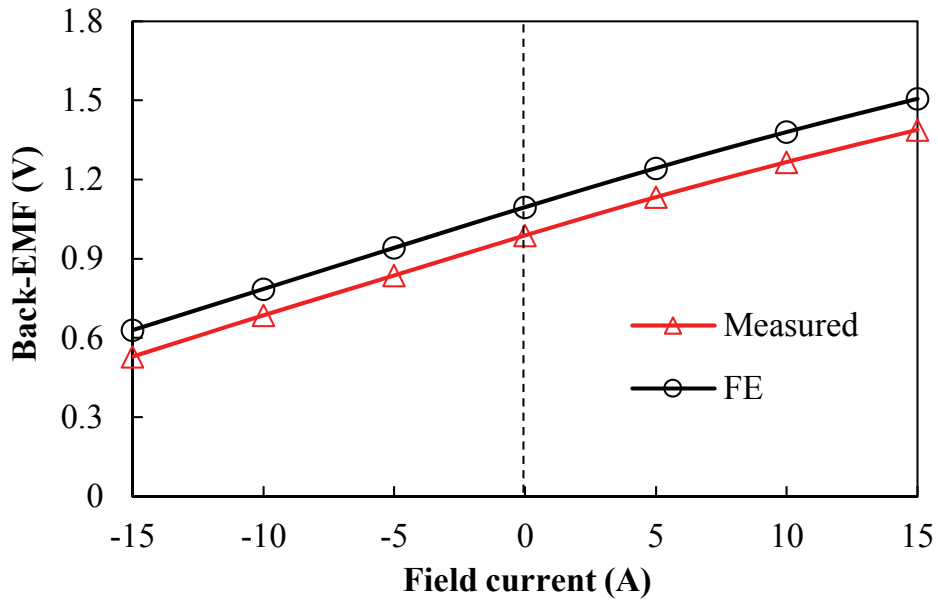


Fig. 5.26 Measured and 2-D FE-predicted peak fundamental back-EMFs versus different FW excitations at 400 r/min.

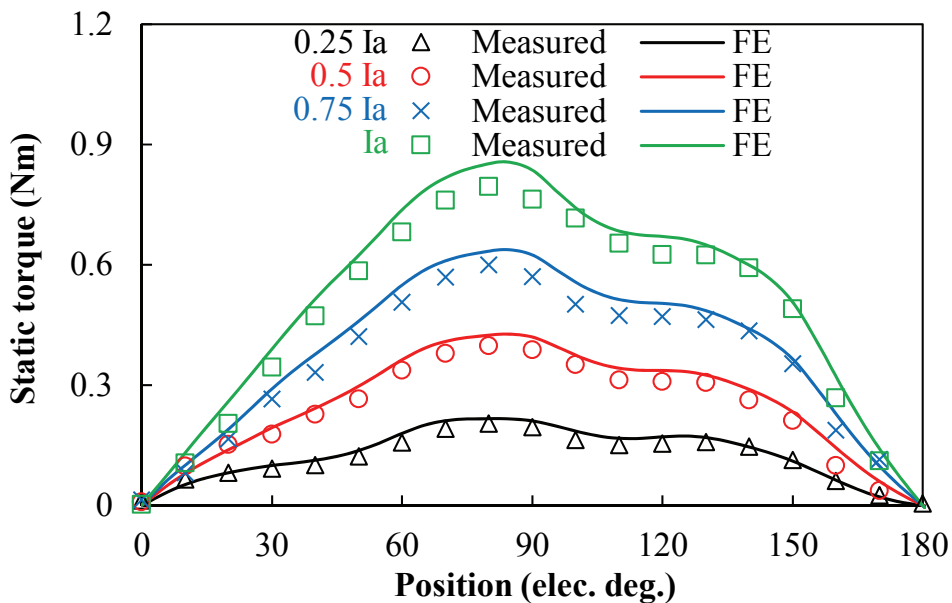


Fig. 5.27 Measured and 2-D FE-predicted static torques without FW current.

Further, in order to fully illustrate the effect of flux regulation, the test platform shown in Fig. 5.28 is set up to measure the torque-speed curves. The prototype machine is connected to a regular brushed DC generator as load. The operating point of the prototype can be flexibly adjusted by varying the field current of the generator as well as the resistance of the load bank linked to the generator armature windings. Besides, an encoder and a torque transducer are employed to detect the rotor position and torque output respectively. A DC power supply is used to feed the three-phase inverter, which is based on the dSPACE controller and intelligent

power module. Further, an individual adjustable current source is connected to the field winding of the prototype and hence the field current can be continuously adjusted. Due to the limit of inverter capacity (10V/8A bus voltage/current), the torque-speed curves are measured with the maximum 8A peak phase current. The torque-speed curves under the no field current operation and the flux-enhancing operation with positive 7.5A field current are both measured and presented in Fig. 5.29. Although the extremely low torque cannot be achieved due to the inherent friction torque of the load machine, the trends of the two curves can be observed. The flux-enhancing operation contributes to a significantly higher torque output in the low speed region, but its base speed is lower. The FE-predicted torque-speed curves based on flux-linkage method [QI09] are shown in Fig. 5.29 as well.

Due to the dual-stator and cup-rotor structure, only one shaft end is available in the proposed PS machines. Therefore, the encoder and load are coupled to the prototype machine at the same end, as shown in Fig. 5.28. In order to relieve the vibration of the encoder, the encoder is supported by a tie bar that is linked to the end plate of the machine frame. However, the prototype machine and the encoder still suffer observable vibration during the operation due to the inherently complicated machine structure and the assembling of the platform. As a result, the rotor position that is feedback to the controller would suffer the error, which may degrade the machine torque output. In addition, it should be noted that the initial rotor position is determined by synchronizing the triangle signal from the encoder and the open-circuit back-EMFs of Phase A, and this is checked by eyes, which may introduce errors to the practical rotor position and the practical current angle. Consequently, apart from the end effect and the manufacturing tolerance introduced in the previous section, the error in the drive system also contributes to the difference between FE predictions and test results in Fig. 5.29.

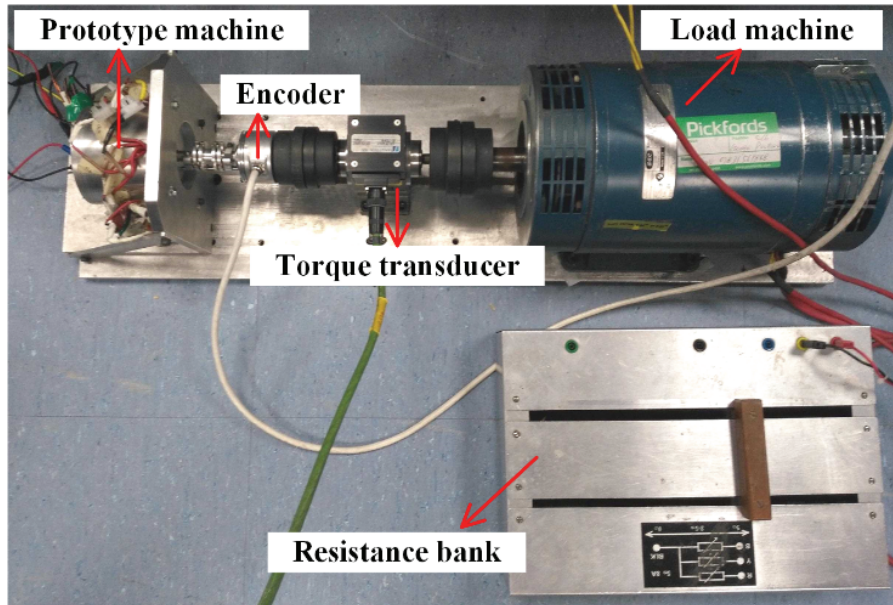


Fig. 5.28 Test platform for torque-speed measurement.

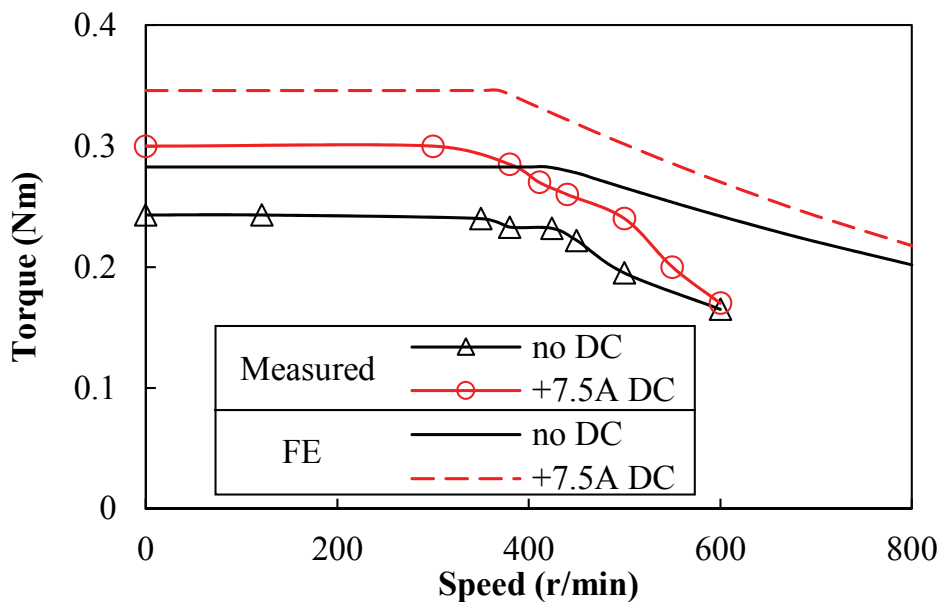


Fig. 5.29 Measured and 2-D FE-predicted torque-speed curves under two field operations.

5.6 Conclusion

In this chapter, the novel PS-HESF machines are proposed to improve the limited flux regulation capability and sacrificed torque density of the conventional HE machines. The proposed PS-HESF machine employs two stators to accommodate armature windings and excitations (PMs and FWs) separately, resulting in better space utilization. The comparison results reveal that the PS-HESF machine exhibits not only the enhanced flux regulation capability but also the increased torque output than the conventional HESF machine. Further,

the magnetic couplings between PMs and FWs in the PS-HESF machines are identified, and the influences of key design parameters on the hybridization ratio are investigated, which implies that the design of the PS-HESF machines is flexible and depends on the requirements for a specific application.

Chapter 6. Series Hybrid Excited Machines with Separate Excitation Stator

The novel HE machines originating from the SFPM machine have been investigated in the previous Chapter 4 and Chapter 5, which inherit the features of brushless machines and benefit from better space utilization. In fact, by allocating FWs to the inner stator by the side of the PM poles, the PS-FRPM machine can be transformed to HE configurations as well. Moreover, the series or parallel connection between PM flux and FW flux can be obtained flexibly in the corresponding HE machines by carefully arranging the relative locations of the PMs and FWs. In this chapter, a novel HE machine based on the PS-FRPM machine is proposed, where the PM poles and FW poles are alternately placed on the inner stator and thus their series connection is obtained. The operating principle and the effects of slot/pole number combinations of the proposed machine will be investigated. Further, based on 2-D FE analysis, the electromagnetic performances, including back-EMF, cogging torque, flux regulation, torque capability, power factor and torque-speed curve, are evaluated. The results reveal that the proposed machines can exhibit wide flux regulation range as well as good torque density.

This part has been published in IEEE Transactions on Industrial Electronics.

6.1 Introduction

The PM machines benefit from high torque density and high efficiency. Nevertheless, in variable speed applications such as spindle drives, household appliances and electric vehicles (EVs), good flux-weakening capability and hence wide constant power speed range (CPSR) are required as well. Based on the principle of vector control, the flux-weakening is achieved by injecting a negative d -axis armature current ($-I_d$) to counter the PM flux [JAH86], [SOO94]. As a result, the PM machines can obtain a wide CPSR, especially the interior-PM (IPM) machines that benefit from reluctance torque and high inductance [NER14]. Moreover, extensive studies on fractional-slot PM machines reveal that they have enhanced flux-weakening capabilities [REF10]. However, the flux-weakening with $-I_d$ requires precise d -axis and q -axis current separation, and $-I_d$ has the potential to cause irreversible demagnetization of the PMs. Meanwhile, since I_d expends the armature current capacity, the available q -axis current is reduced and thus torque capability and power factor may be sacrificed [CAP15].

Consequently the HE machines, which combine the high efficiency and high torque density of PM machines together with the good field controllability of electrical-excited (EE) machines, are presented [McC87]. The HE machines employ PMs and FWs at the same time. Compared with conventional PM machines, an additional degree of freedom, i.e. the ratio between PM flux and FW flux, is obtained in HE machines [AMA09]. Normally, the positive field current can be applied in the FWs among the low speed operating range to boost the torque output, while the negative field current is used to extend the constant power speed range (CPSR) and maintain a high power factor.

Recently, the PS machines were investigated, which are characterized with the separated stators to accommodate armature windings and excitations (PMs or/and FWs) respectively. The comparison between the PS machines and corresponding conventional stator-PM machines indicates that the PS structures can greatly boost the torque density. Besides, the consequent-pole technique can be applied to PS-FRPM machine, which significantly decreases the PM volume whilst keeping the torque output almost unchanged [WU15b]. The PM-free PS EE machine having FWs and armature windings on different stators is presented as well [ZHU15c]. It is beneficial to apply the PS structure to HE machines, in which FWs are located on the stator and thus the sliding contact is avoided. Moreover, the available space for coils and PMs is enlarged thanks to the employment of two stators, which is helpful to boost the torque output. Therefore in this chapter, a novel PSHE machine originating from the PS-FRPM machine but featuring with series connection between PM and FW flux, is proposed. It employs a primary stator to accommodate armature windings and a secondary stator to locate FWs as well as PMs, and the consequent-pole technique is applied to reduce the PM usage as well as to facilitate flux regulation.

The chapter is organized as follows. In section 6.2, the topology and operating principle of the novel series PSHE machines are presented, followed by the effects of slot/pole number combinations in section 6.3. In section 6.4, the electromagnetic performances of proposed machines with different slot/pole combinations are comprehensively evaluated based on 2-D FE analysis. Finally, in section 6.5, a prototype is manufactured and tested to validate the predictions.

6.2 Machine Topology and Operating Principle

The proposed three-phase 12-stator-slot/11-rotor-pole consequent-pole PSHE machine is illustrated in Fig. 6.1. The concentrated non-overlapping armature windings are located on the outer stator, whilst the PMs and concentrated non-overlapping FWs are alternately placed on the inner stator. The surface-mounted PMs on the inner stator are all magnetized with an identical polarity to achieve the consequent-pole structure. The outer stator and inner stator have the same pole number, and the inner stator teeth are aligned with the center of the outer stator slots. Meanwhile, the iron-piece-rotor is sandwiched between the two stators.

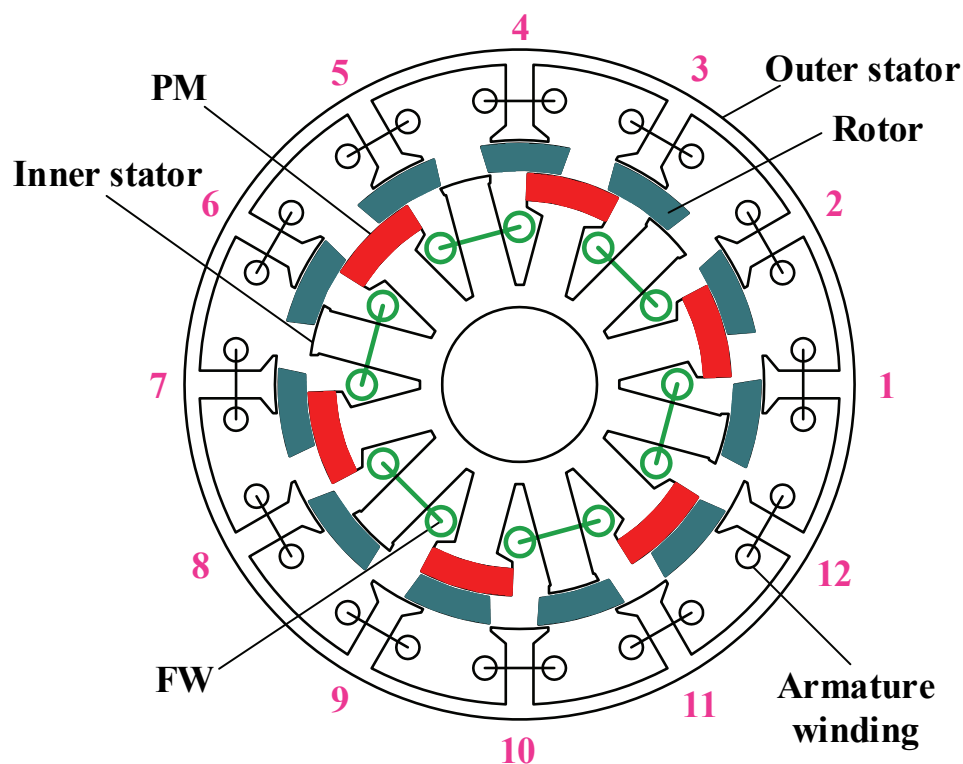


Fig. 6.1 Cross section of proposed three-phase 12-stator-slot/11-rotor-pole series PSHE machine.

This machine naturally is a stator-PM machine but employs a secondary stator to accommodate PMs as well as FWs. The coil back-EMF phasors of the proposed 12/11 machine are presented in Fig. 6.2(b), where coils 1, 2, 7, 8 as illustrated in Fig. 6.1 are employed to constitute phase A. Rotor electrical position θ_e can be expressed as:

$$\theta_e = N_r \theta_m \quad (6.1)$$

where θ_m and N_r are rotor mechanical position and rotor iron piece number respectively. It should be noted that the frequency of the proposed machine depends on the rotor iron piece number, i.e. the machine rotor pole pair number equals to the rotor iron piece number.

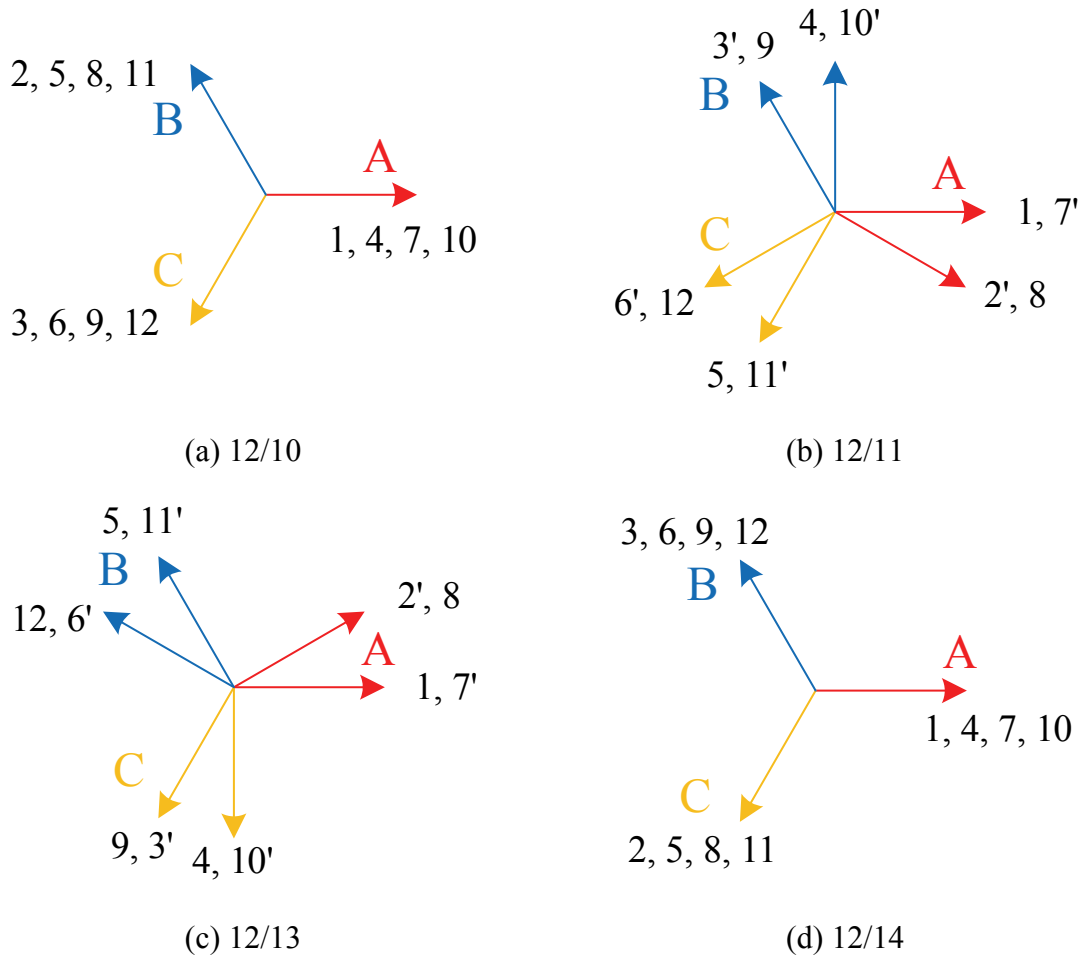
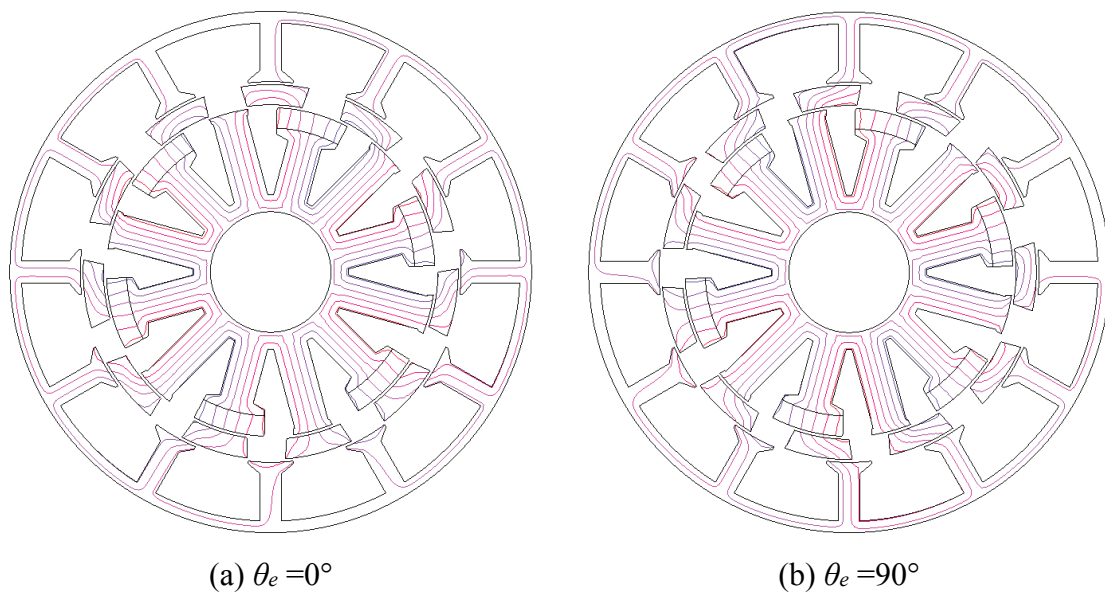


Fig. 6.2 Coil back-EMF phasors for 12-stator-slot consequent-pole PSHE machines with different rotor iron piece numbers.

Based on 2-D FE analysis, the open-circuit field distributions are obtained. Fig. 6.3(a)-(d) show the field distributions at four typical rotor positions with only PM excitation. At $\theta_e = 0^\circ$ as shown in Fig. 6.3(a), the flux-linkage of phase A reaches the maximum negative value. Then it is short-circuited by the rotor iron pieces at $\theta_e = 90^\circ$. Afterwards, the maximum positive flux-linkage is obtained with the rotor rotating by another 90° , as illustrated in Fig. 6.3(c). Finally, the flux is short-circuited and zero flux-linkage occurs again at $\theta_e = 270^\circ$. Hence, the sinusoidal phase flux-linkage waveform with only PM excitation is obtained in Fig. 6.4(a). The harmonics of flux-linkage can be significantly reduced with specific slot/pole combinations and winding configurations, which will be discussed in the following section 6.3.

The PM and FW flux paths are illustrated in Fig. 6.5, and it can be found that the series connection between them is obtained. The accumulative air-gap field is the sum of PM flux and FW flux. The reluctance for FW flux is reduced by employing a consequent-pole structure, which can enhance the flux regulation capability, although the magnetic saturation and flux leakage would degrade the performance. At $\theta_e = 0^\circ$, the field distributions with only FW excitation are presented in Fig. 6.6(a), in which the PMs are non-magnetized and treated as air. In addition, combining the PM field with the field generated by positive or negative field current in FWs, the flux-enhancing or flux-weakening operation can be achieved respectively. Their field distributions are shown in Fig. 6.6(c) and (d) respectively, from which the effects of flux regulation can be observed. Meanwhile, the open-circuit phase flux-linkages with different field excitations are presented in Fig. 6.4. The sinusoidal waveforms always can be obtained, which reveals that the brushless AC (BLAC) operation is suitable. More importantly, the phase flux-linkages are flexibly regulated by field currents.



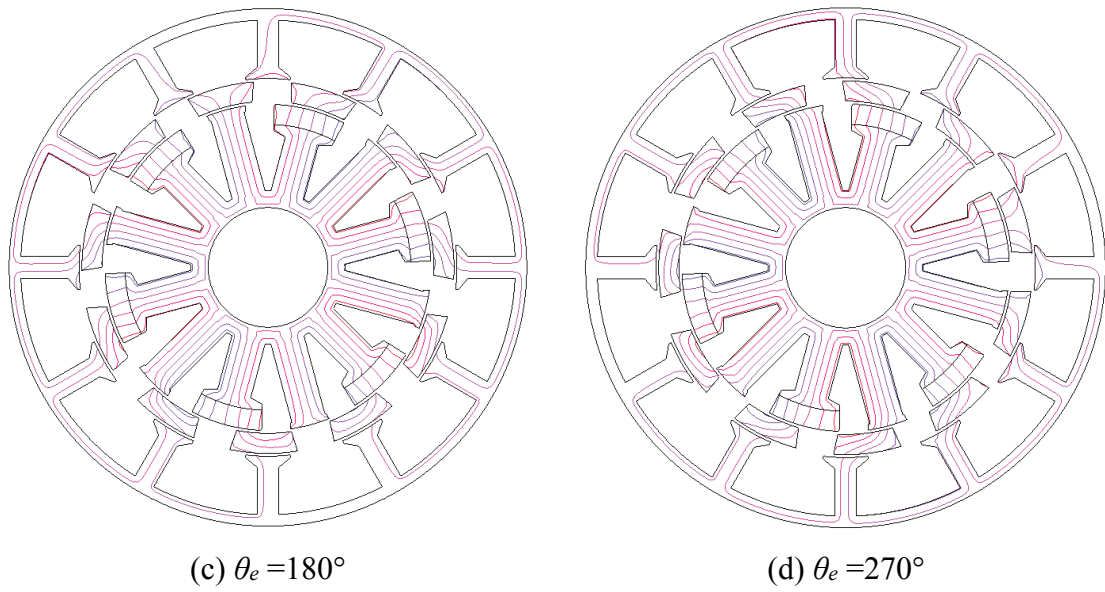
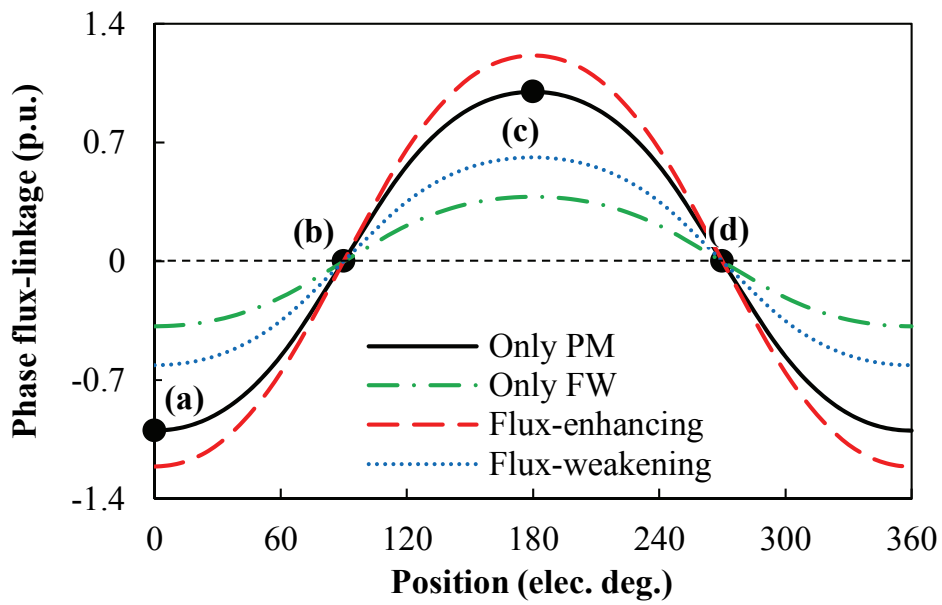
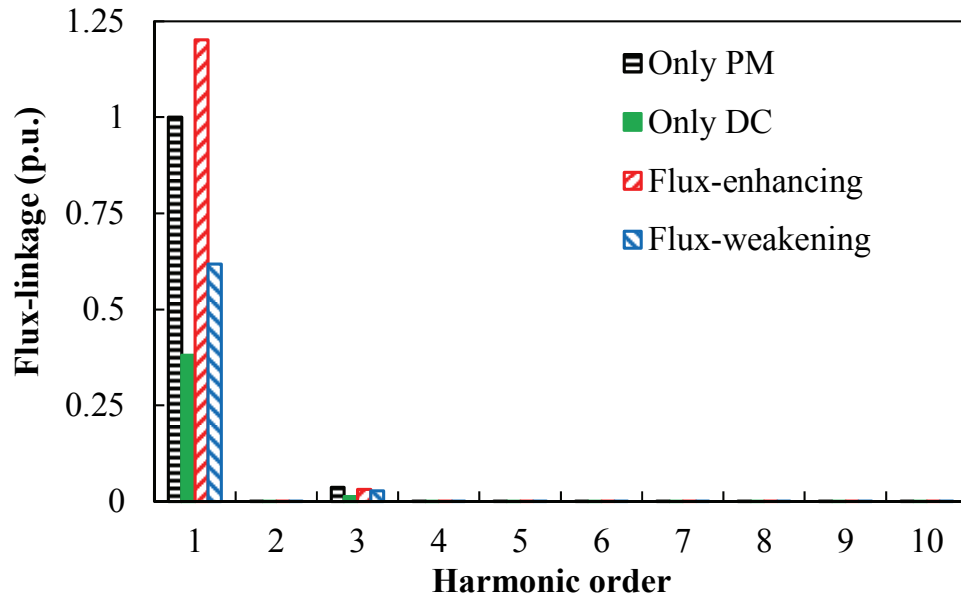


Fig. 6.3 Open-circuit field distributions of 12/11 consequent-pole PSHE machine at four typical rotor positions with only PM excitation.

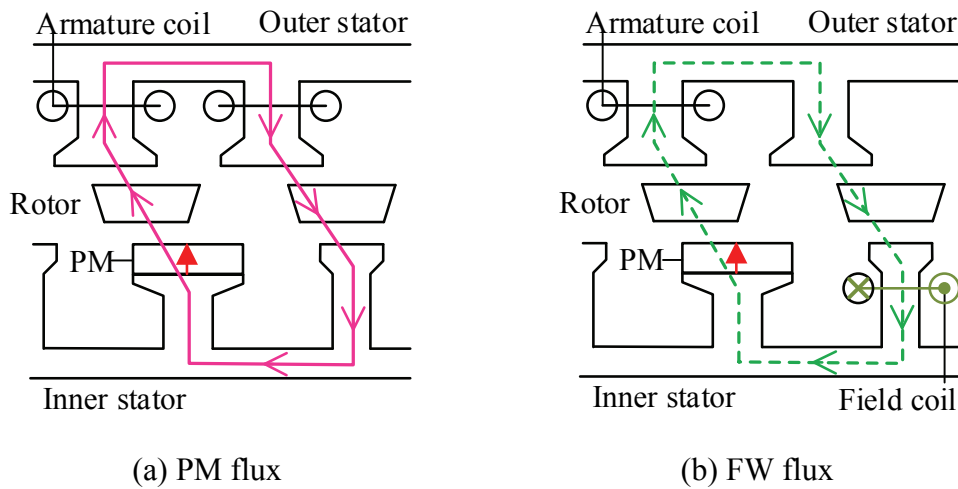


(a) Waveforms



(b) Spectra

Fig. 6.4 Phase flux-linkages of 12/11 consequent-pole PSHE machine with different excitations.



(a) PM flux

(b) FW flux

Fig. 6.5 Flux paths of PMs and FWs.

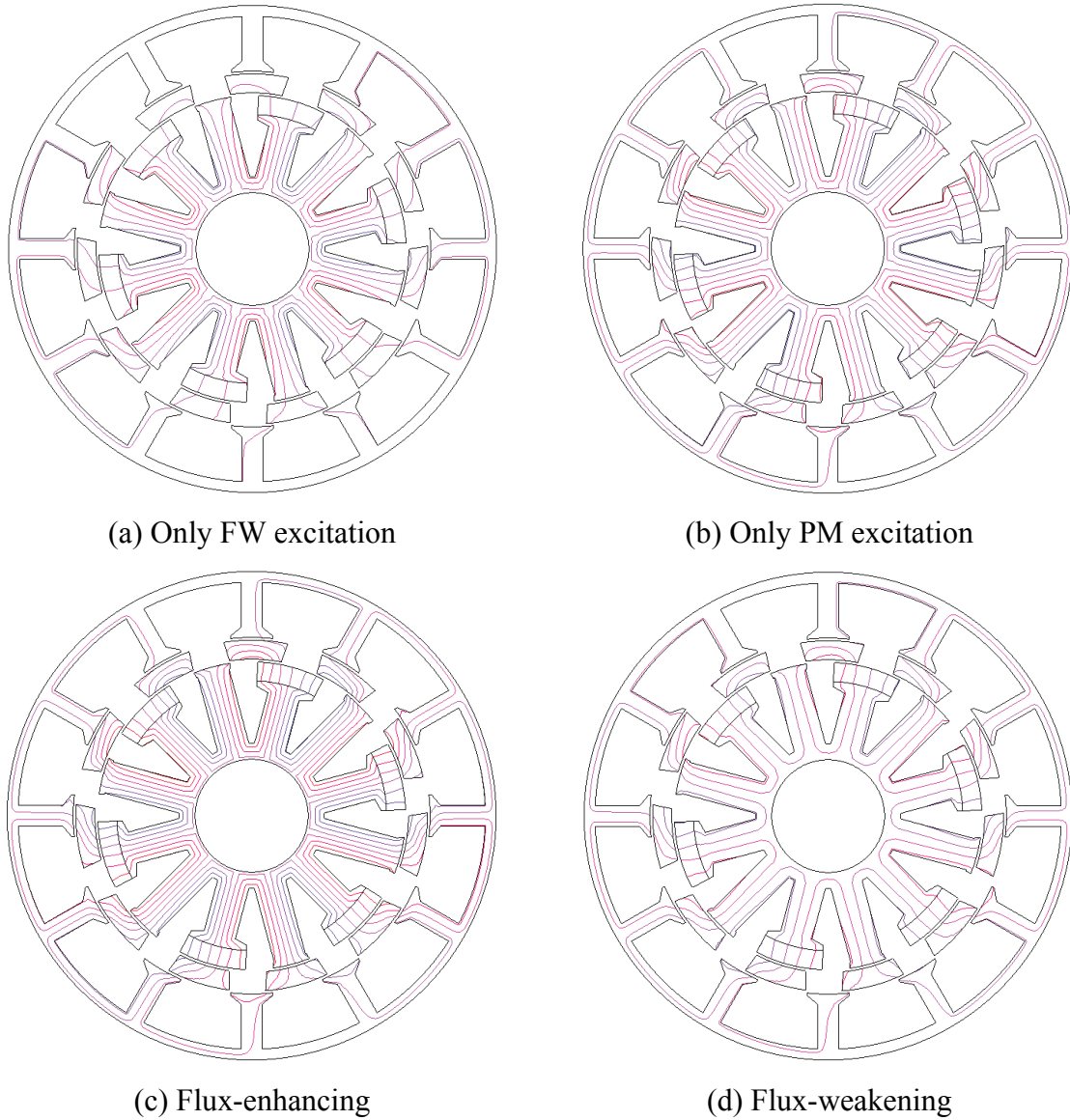


Fig. 6.6 Open-circuit field distributions of 12/11 consequent-pole PSHE machine at $\theta_e = 0^\circ$ (d -axis rotor position) with different excitations.

6.3 Slot/Pole Number Combinations

The slot/pole number combinations of the proposed consequent-pole PSHE machines have significant effects on performance. The selected combinations (12/11 and 12/13) can exhibit phase flux-linkages with significantly less harmonics, while others (12/10 and 12/14) suffer from a wealth of even order harmonics. Therefore the conditions to obtain sinusoidal flux-linkage in the proposed consequent-pole PSHE machine will be described in this section.

It is known that the naturally sinusoidal phase flux-linkage is an important advantage of stator-PM machines [HUA08]. Although the even order harmonics usually exist in the coil

flux-linkages, they can cancel each other out and result in phase flux-linkages free from even order harmonics. The proposed PSHE machines are inherently characterized as a consequent-pole stator-PM machines. Thus, the principle of harmonic cancellation in the consequent-pole stator-PM machines is firstly investigated.

According to the coil back-EMF phasors of stator-PM machines with different slot/pole combinations shown in Fig. 6.2, the coil arrangements for phase A are illustrated in Table 6.1. The reverse connections occur in 11- and 13-rotor machines while all coils are forward connected in 10- and 14-rotor machines. The flux-linkages of coil A1 (Φ_{A1}) and coil A2 (Φ_{A2}) are expressed with Fourier series as:

$$\Phi_{A1}(t) = \sum_{v=1}^{\infty} \Phi_v \cdot \cos(\omega \cdot v \cdot t + \varphi_v) \quad (6.2)$$

$$\Phi_{A2}(t) = \sum_{v=1}^{\infty} \Phi_v \cdot \cos(\omega \cdot v \cdot t + \varphi_v - \theta_v) \quad (6.3)$$

$$\theta_v = \frac{2\pi}{N_s} \cdot N_r \cdot S_n \cdot v + k_1 \cdot \pi + k_2 \cdot \pi \quad (6.4)$$

where Φ_v and φ_v represent the amplitude and phase for v^{th} harmonic, and ω is electrical angular speed. In addition, θ_v is the lag angle between Φ_{A2} and Φ_{A1} , N_s and N_r are the stator slot number and the rotor pole number respectively, and S_n represents the slot number between coils. Moreover, k_1 symbolizes the relative coil polarity while k_2 is the symbol for relative PM polarity. More specifically, k_1 equates to 1 when the coil polarities between coils A1 and A2 are reversed while it is 0 if the polarities are the same. k_2 is 1 if PMs facing coils A1 and A2 have opposite polarities but 0 if they are identical. Different from the conventional stator-PM machine, the PMs are all magnetized with the same polarity in the consequent-pole stator-PM machine, which makes k_2 never equal to 1. Consequently, according to the coil locations shown in Fig. 6.1, the resultant θ_v of the proposed machines with different rotor iron piece numbers is listed in Table 6.2. It can be found that there is an additional “ π ” in the 11- and 13-rotor machines due to the reversed coil polarities, with which the even order harmonics can be cancelled. Therefore, the proposed consequent-pole PSHE machines with 11- and 13-rotor benefit from the phase flux-linkages free from even order harmonics while the harmonics are significant in 10- and 14-rotor machines.

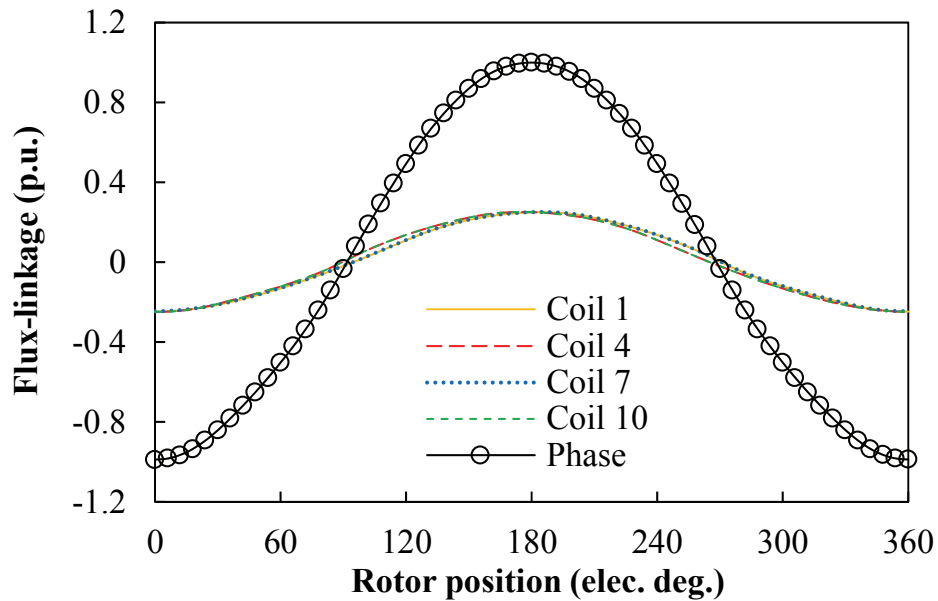
Table 6.1 Coil arrangement for phase A.

Rotor number	A1	A2	A3	A4
10-/14- rotor	1	4	7	10
11-/13- rotor	1	7'	2'	8

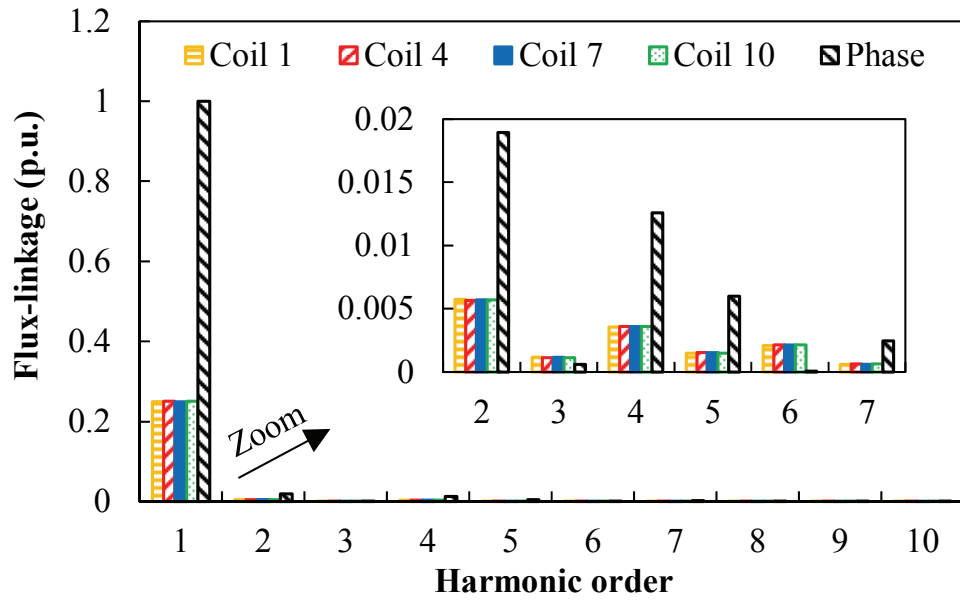
Table 6.2 Lag angle between coils A1 and A2.

Rotor number	S_n	k_1	k_2	θ_v
10- rotor	3	0	0	$5 v \pi$
11- rotor	6	1	0	$11 v \pi + \pi$
13- rotor	6	1	0	$13 v \pi + \pi$
14- rotor	3	0	0	$7 v \pi$

To illustrate the previous analysis, the coil and phase flux-linkages of the proposed PSHE machines with 10- and 11-rotor under sole PM excitation, are presented in Fig. 6.7 and Fig. 6.8 respectively. As shown in the spectra, the even order harmonics in coil flux-linkages are added together in the 10-rotor machine and result in quite significant harmonics in the phase flux-linkages. Alternatively, in the 11-rotor machine, although the even order harmonics still exist in coil flux-linkages, they cancel each other out in the resultant phase flux-linkages.

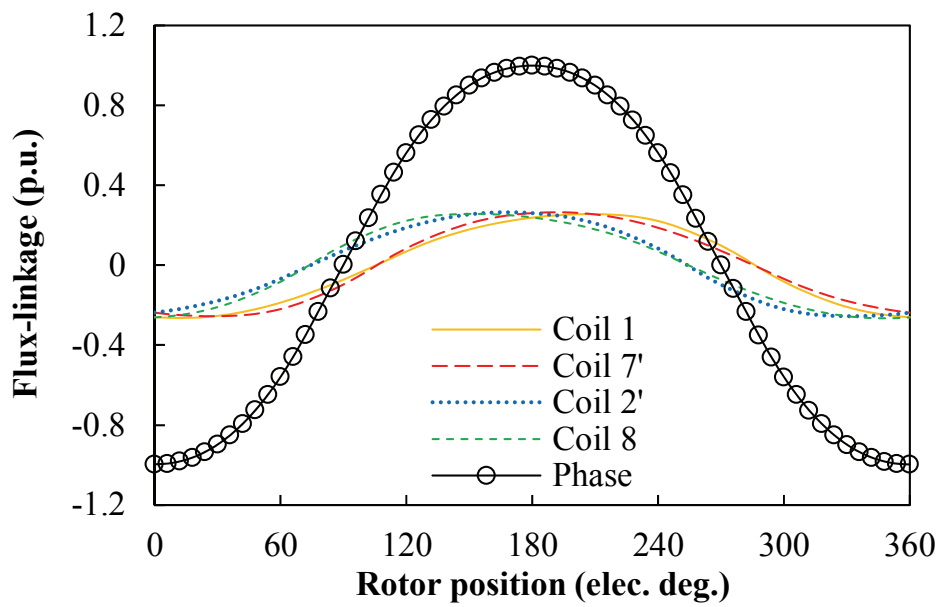


(a) Waveforms

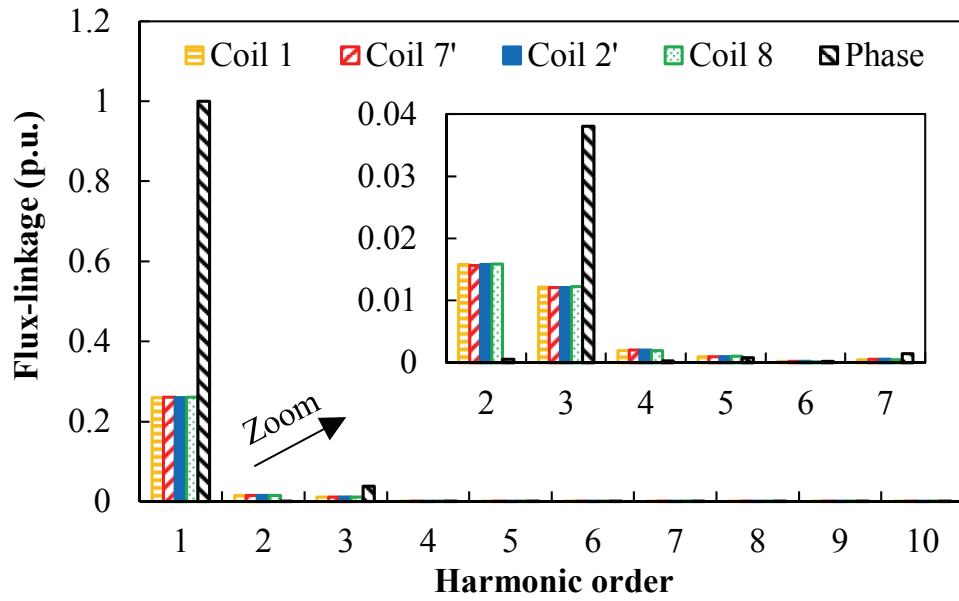


(b) Spectra

Fig. 6.7 Open-circuit flux-linkages of coils and corresponding phase of the proposed machine with 10-rotor.



(a) Waveforms



(b) Spectra

Fig. 6.8 Open-circuit flux-linkages of coils and corresponding phase of the proposed machine with 11-rotor.

6.4 Electromagnetic Performance

Based on 2-D FE analysis, the electromagnetic characteristics of the proposed consequent-pole PSHE machines with different rotor iron piece numbers are evaluated in this section. The machine geometric parameters are illustrated in Fig. 6.9. It should be emphasized that there is always a trade-off between the torque and flux regulation capability in HE machines. In general, more PM usage is beneficial to improve the torque output while a better flux regulation can be achieved by allocating more available space to FWs. Meanwhile, increasing the PM usage is favourable to machine efficiency but increases the cost. In this chapter, the optimization is carried out for each machine to obtain the maximum average torque during one electrical period under flux-enhancing operation. The torque capability and the effect of flux regulation can then be simultaneously taken into consideration. With the constraints including 25mm active axial length, 45mm outer radius, 10.4mm inner radius, 20W copper loss in armature windings and zero I_d control, the key geometric parameters are globally optimized based on the genetic algorithm. The definition of the armature winding copper loss is shown in (2.1), and the current density of $5\text{A}/\text{mm}^2$ is applied to the field coil slots to realize the flux-enhancing operation. The slot package factors are kept at 0.5 in both armature coil and field coil slots. It should be emphasized that the 20W copper loss in armature windings and $5\text{A}/\text{mm}^2$ current density in

FWs are determined with the rough consideration of the thermal conditions of the machines with the corresponding size. The detailed optimization process of the series PSHE machine is similar to that introduced in section 4.3. The optimal design parameters and materials employed in FE models are listed in Table 6.3.

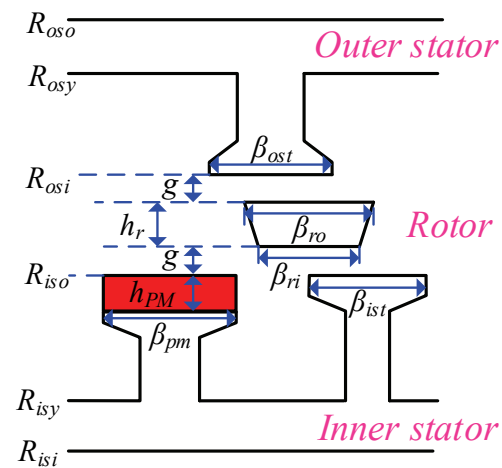


Fig. 6.9 Essential design parameters of consequent-pole PSHE machine.

Table 6.3 Key design parameters of proposed machines with different rotor iron piece numbers.

Parameter	10-rotor	11-rotor	13-rotor	14-rotor
Stator slot number, N_s	12	12	12	12
Rotor iron piece number, N_r	10	11	13	14
Axial length (mm), l_a	25	25	25	25
Outer stator outer radius (mm), R_{oso}	45	45	45	45
Outer stator yoke radius (mm), R_{osy}	43	43	43	43
Outer stator inner radius (mm), R_{osi}	32.4	32.9	33.3	33.5
Outer stator tooth arc ($^\circ$), β_{ost}	10 $^\circ$	10 $^\circ$	9.5 $^\circ$	10.5 $^\circ$
Air-gap length (mm), g	0.5	0.5	0.5	0.5
Rotor radial thickness (mm), h_r	3.5	3.5	3	3
Rotor outer pole arc ($^\circ$), β_{ro}	24 $^\circ$	21 $^\circ$	19 $^\circ$	18 $^\circ$
Rotor inner pole arc ($^\circ$), β_{ri}	23 $^\circ$	19 $^\circ$	18 $^\circ$	17 $^\circ$
Inner stator outer radius (mm), R_{iso}	27.9	28.4	29.3	29.5
Inner stator yoke radius (mm), R_{isy}	13.4	13.4	13.4	13.4
Inner stator inner radius (mm), R_{isi}	10.4	10.4	10.4	10.4
Inner stator tooth arc ($^\circ$), β_{ist}	13 $^\circ$	13 $^\circ$	13 $^\circ$	13 $^\circ$
PM height (mm), h_{pm}	3.5	3.5	3.5	3.5
PM pole arc ($^\circ$), β_{pm}	25.5	25.5	25.5	25.5
PM remanence (T)	1.2	1.2	1.2	1.2
PM coercivity (kA/m)	910	910	910	910
Turns number in armature coil, N_{ac}	18	18	18	18

6.4.1 Open-circuit back-EMF

The open-circuit field distributions of the four consequent-pole series PSHE machines with different rotor pole numbers, at d -axis rotor position, are shown in Fig. 6.10. The open-circuit phase back-EMFs at 400 r/min without FW excitation, are presented in Fig. 6.11. It can be observed that the 10- and 14-rotor machines suffer from significant harmonics, especially the even order items. Although the 3rd harmonics exist in the 11- and 13-rotor machines, they will be eliminated in the line back-EMFs if the Y-type winding connection is applied. In addition,

the fundamental amplitude of the 13-rotor machine is higher than the 11-rotor counterpart due to the higher rotor iron piece number and hence higher frequency, which implies a better torque capacity.

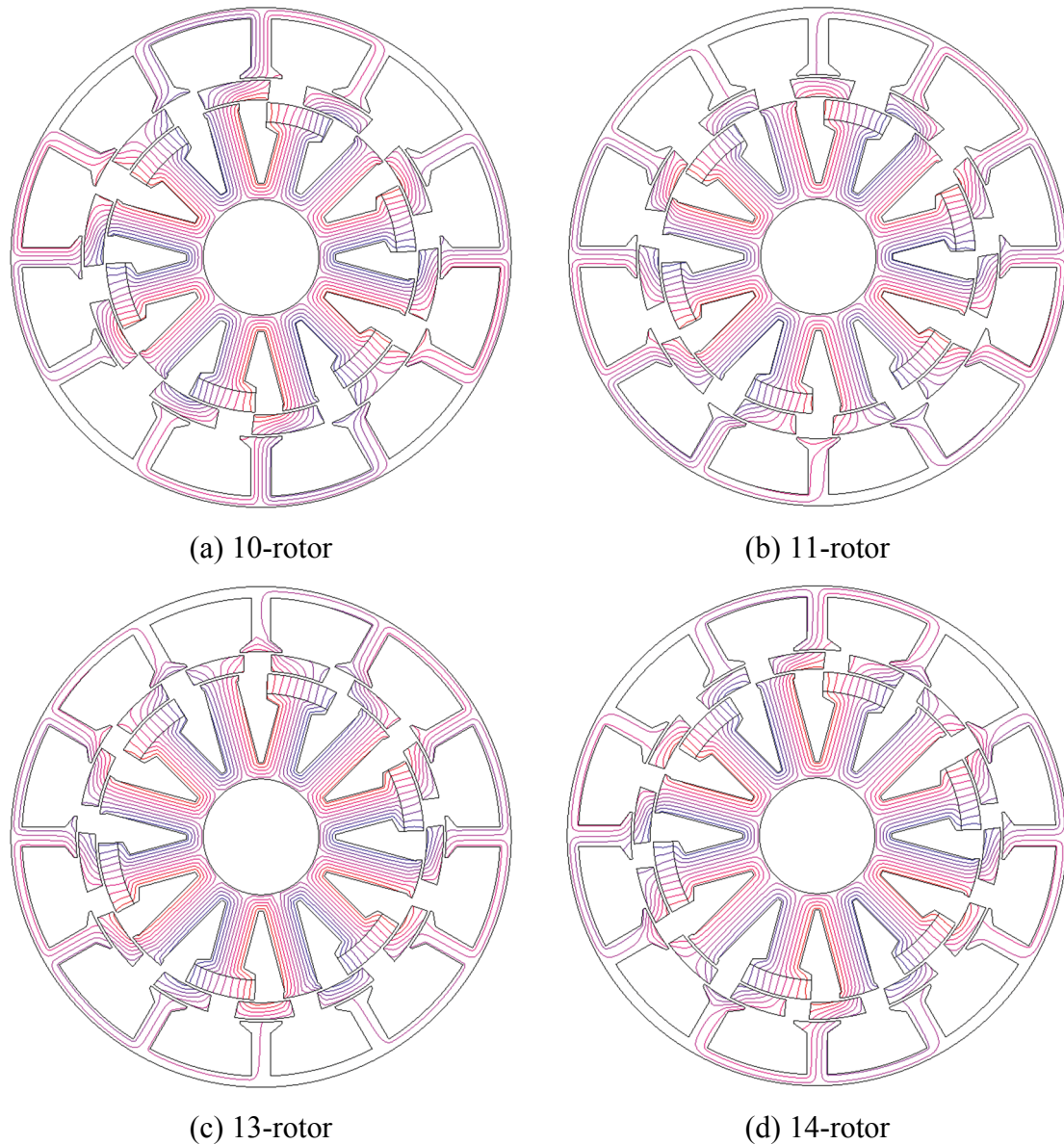
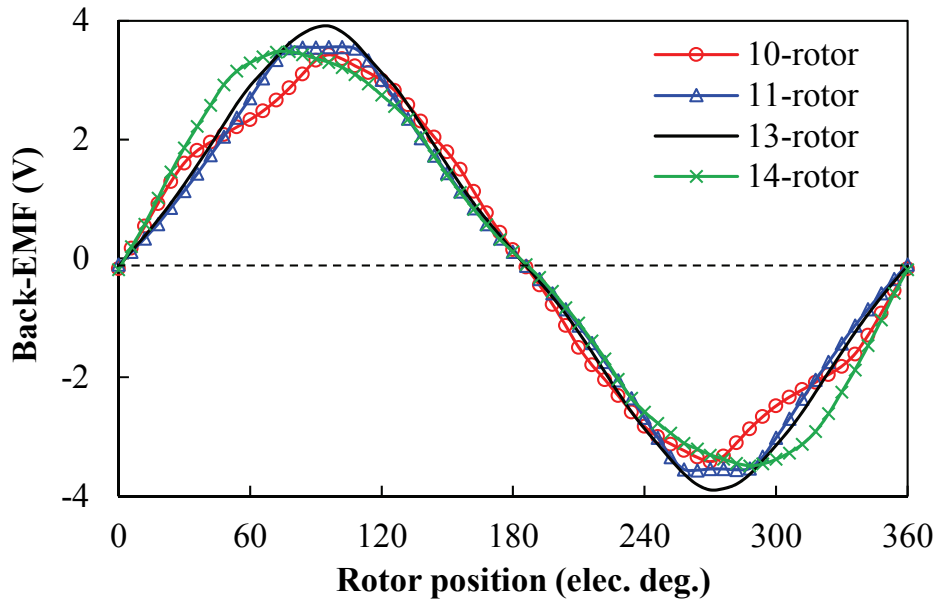
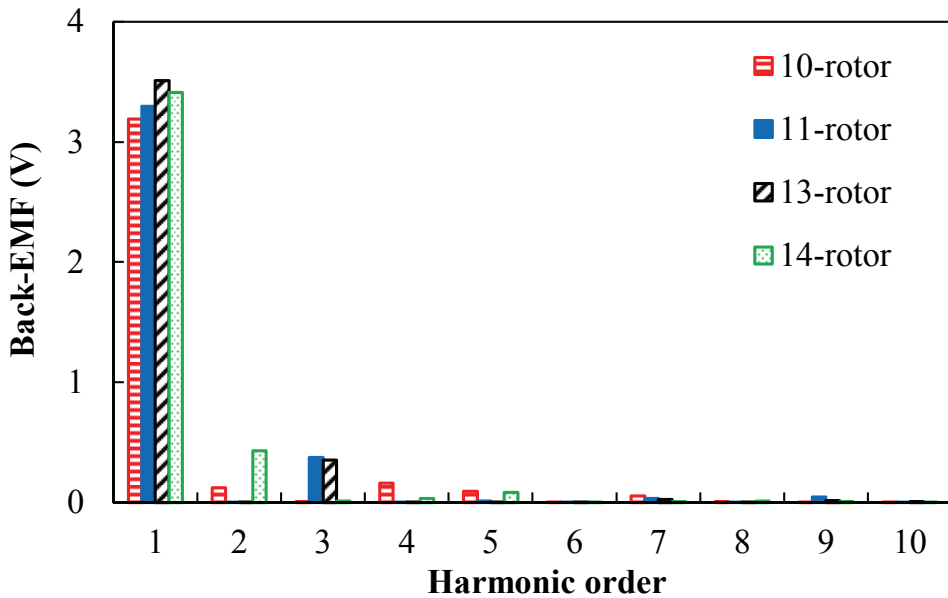


Fig. 6.10 Open-circuit field distributions of 12-stator-slot consequent-pole series PSHE machines with different rotor pole numbers at d -axis position ($\theta_e = 0^\circ$).



(a) Waveforms



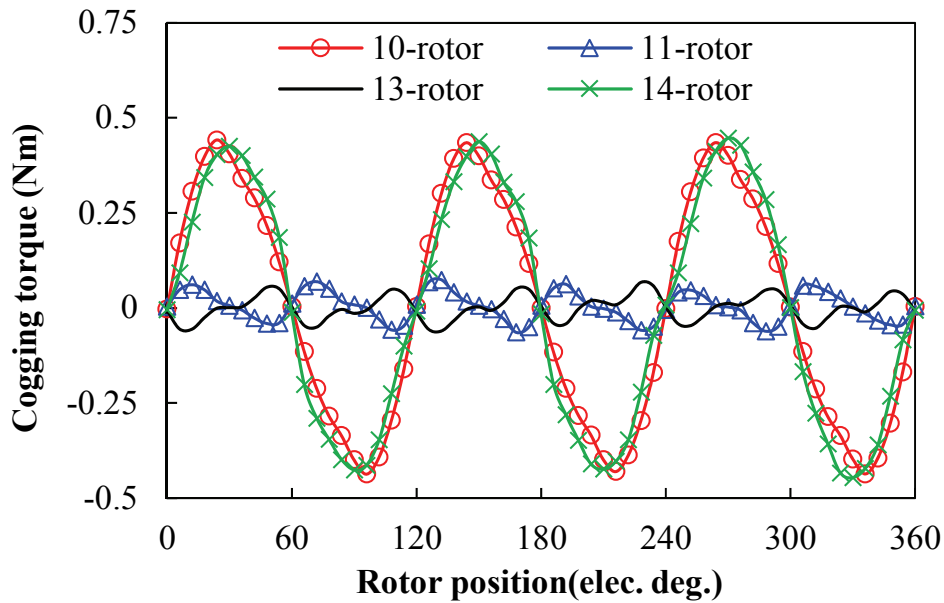
(b) Spectra

Fig. 6.11 Phase back-EMFs at 400 r/min without field currents.

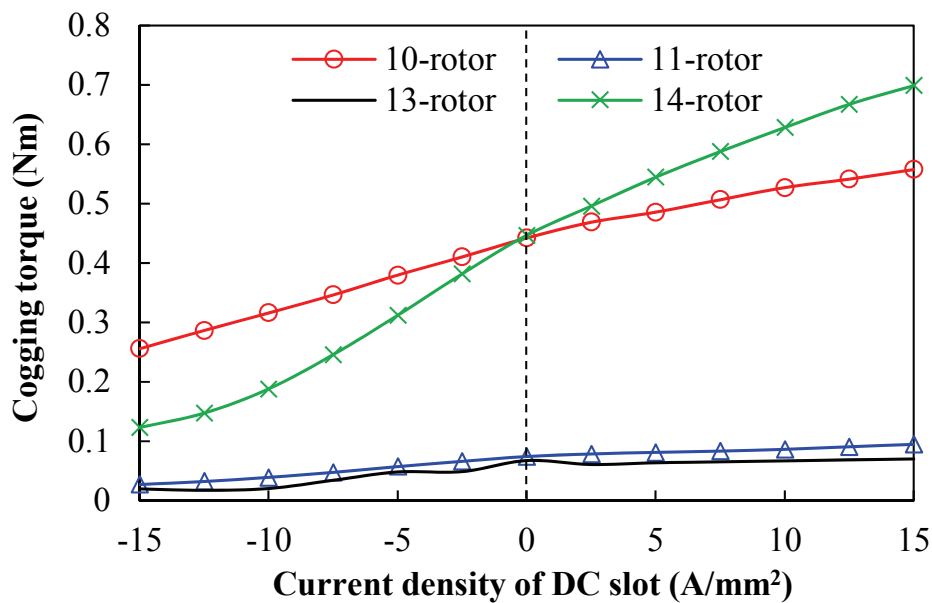
6.4.2 Cogging torque

Fig. 6.12(a) shows the cogging torque without field current. The ratios of peak cogging torque to rated average torque are listed in Table 6.4. The cogging torques of 10- and 14-rotor machines are significantly higher and their cycle numbers per electrical period are halved, compared with their 11- and 13-rotor counterparts. This can be attributed to the inherently higher ‘goodness’ factor in 10- and 14-rotor machines, which is defined as the greatest common divisor between N_s and N_r [ZHU00]. In addition, it should be noted that the cogging torque

mitigation is not involved in the optimization. The reduced cogging torque can be obtained by adjusting the geometric parameters, especially the rotor pole arcs. But the cogging torques of the 10- and 14-rotor machines are inherently higher. Furthermore, the peak cogging torques versus different field currents are summarized in Fig. 6.12(b), where the cogging torques of the 11- and 13-rotor PSHE machines are always lower than those in the 10- and 14-rotor counterparts. More importantly, it can be seen that the cogging torques decrease with negative field currents while they are boosted when the positive field currents are applied.



(a) Cogging torque waveforms without field current



(b) Peak cogging torques versus field currents

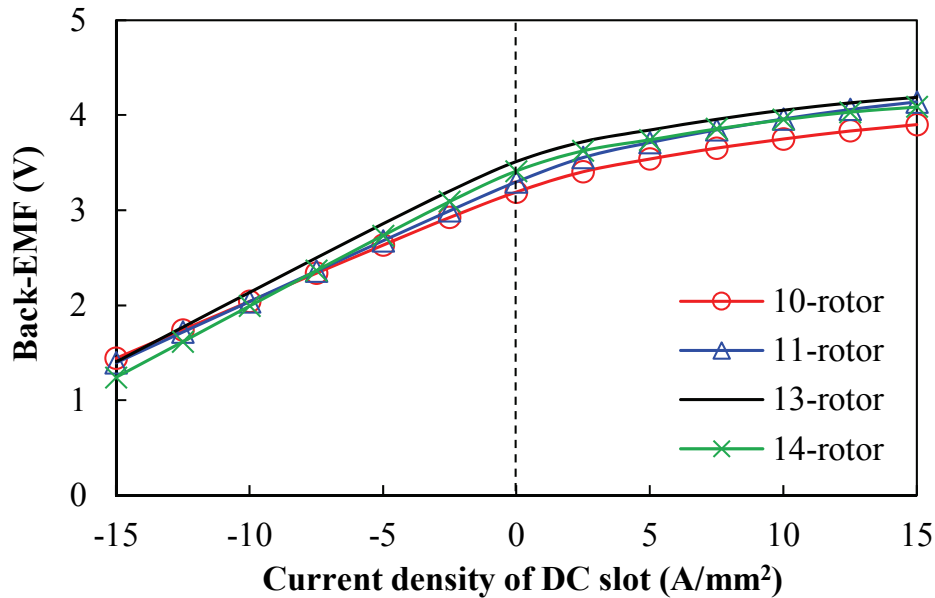
Fig. 6.12 Cogging torque.

Table 6.4 Torque characteristics.

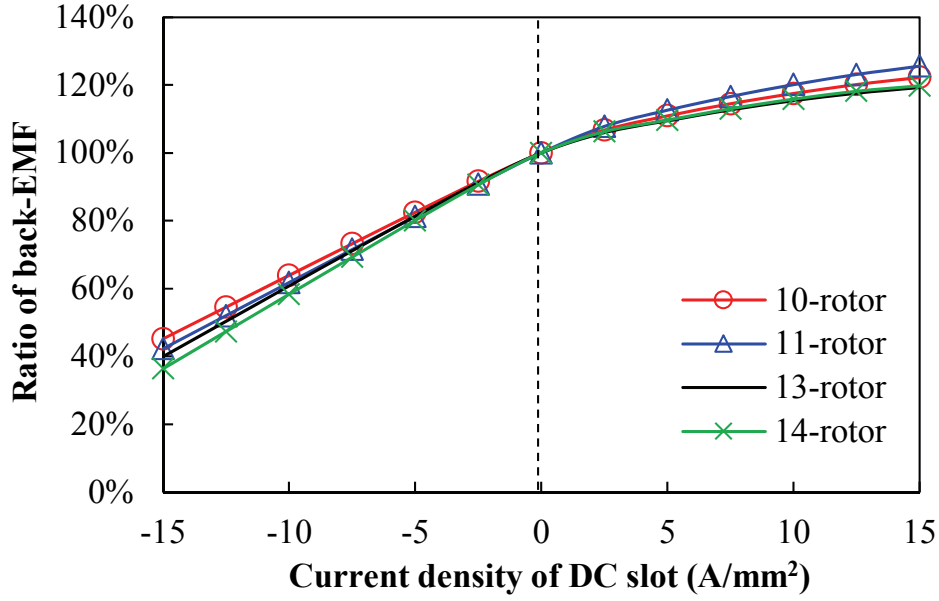
	10-rotor	11-rotor	13-rotor	14-rotor
Peak cogging torque (N·m)	0.44	0.07	0.06	0.45
T_{ave} (N·m)	2.44	2.47	2.57	2.49
Ratio of cogging torque	18%	2.8%	2.3%	18%
T_{ripple}	45%	5.8%	5.4%	50%

6.4.3 Flux regulation capability

With different field currents, the peak fundamental phase back-EMFs at 400 r/min are compared in Fig. 6.13, and excellent flux regulation capabilities can be observed. As shown in Fig. 6.13(b), with 15A/mm² current density in FW slots, the back-EMFs can be regulated between approximately 40% and 120%. The flux-enhancing is more challenging than the flux-weakening due to the magnetic saturation.



(a) Back-EMFs.



(b) Ratio of back-EMFs.

Fig. 6.13 Variations of peak fundamental back-EMFs at 400 r/min versus field excitations.

6.4.4 On-load torque

With the fixed 20W copper loss in armature windings and zero I_d control strategy which corresponds to around 21.5A q -axis current, the torque waveforms are shown in Fig. 6.14. It can be found that the 10- and 14-rotor topologies suffer from much larger torque ripples due to their significant cogging torques and harmonics. The torque ripple factor T_{ripple} is defined as

$$T_{ripple} = \frac{T_{max} - T_{min}}{T_{ave}} \quad (6.5)$$

where T_{max} , T_{min} , and T_{ave} represent maximum, minimum and average torque during one electric cycle respectively. The detailed torque characteristics are listed in Table 6.4 and it is found that the 13-rotor machine exhibits higher average torque than the 11-rotor counterpart due to higher back-EMFs. Besides, the average torques against different field currents with 20W copper loss in armature windings are shown in Fig. 6.15(a), which corresponds to the back-EMF variations, and the 13-rotor machine holds the advantages of higher torque. Meanwhile, the torque ripples with different field currents are compared in Fig. 6.15(b), in which the 11- and 13-rotor PSHE machines always exhibit significantly lower torque ripples than the 10- and 14-rotor counterparts.

Furthermore, with 20W copper loss in armature windings, the average torque versus current advance angle are illustrated in Fig. 6.16, in which the peak torques always occur at around 0° ,

indicating the negligible reluctance torque. Meanwhile, the average torques versus different excitations in armature windings are presented in Fig. 6.17, in which the variations of average torque against armature winding copper loss and q -axis current are both included. It can be found that the 13-rotor machine always has higher torque.

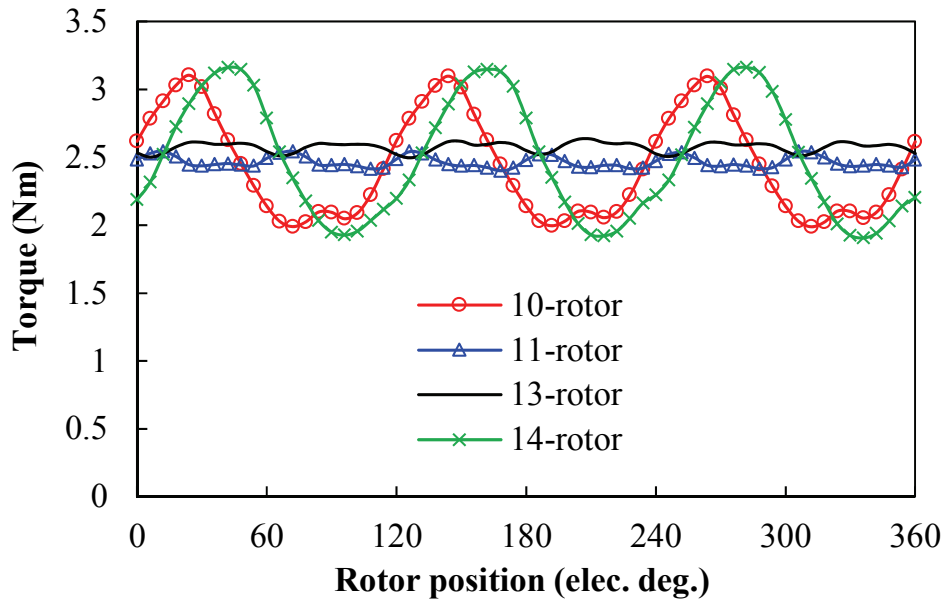
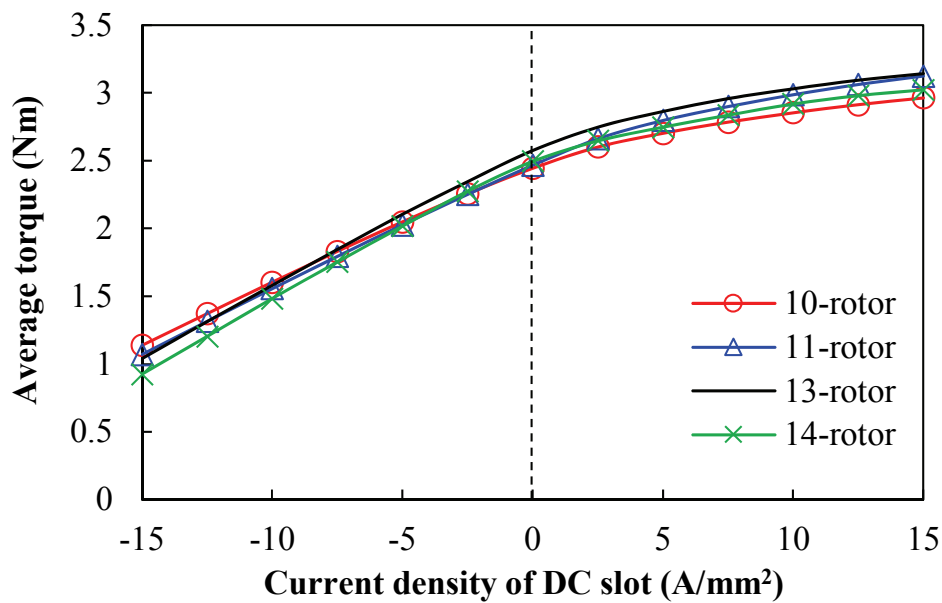
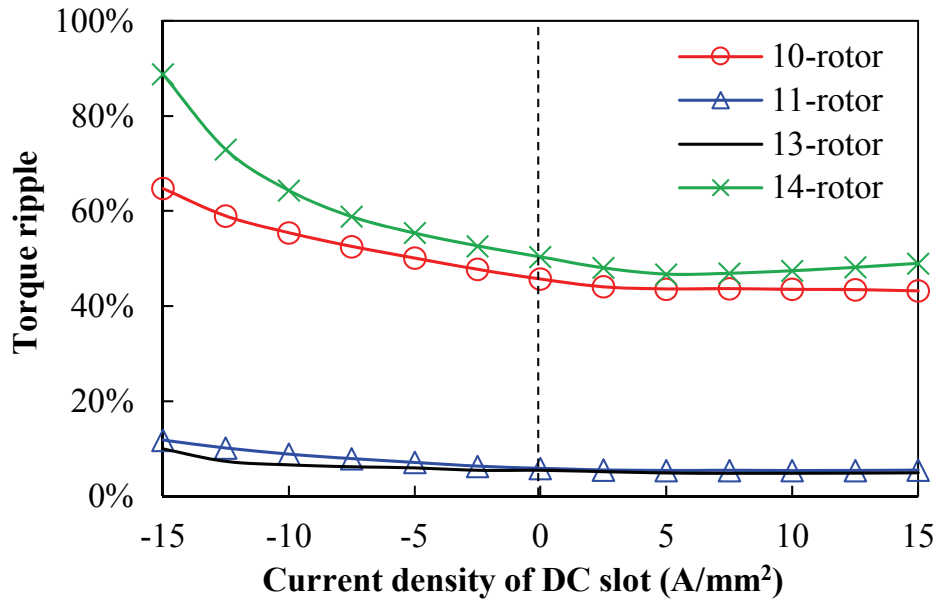


Fig. 6.14 Torque waveforms with 20W copper loss in armature windings and zero d -axis current control.



(a) Average torque



(b) Torque ripple

Fig. 6.15 Average torque versus field excitation with 20W copper loss in armature winding and zero d -axis current control.

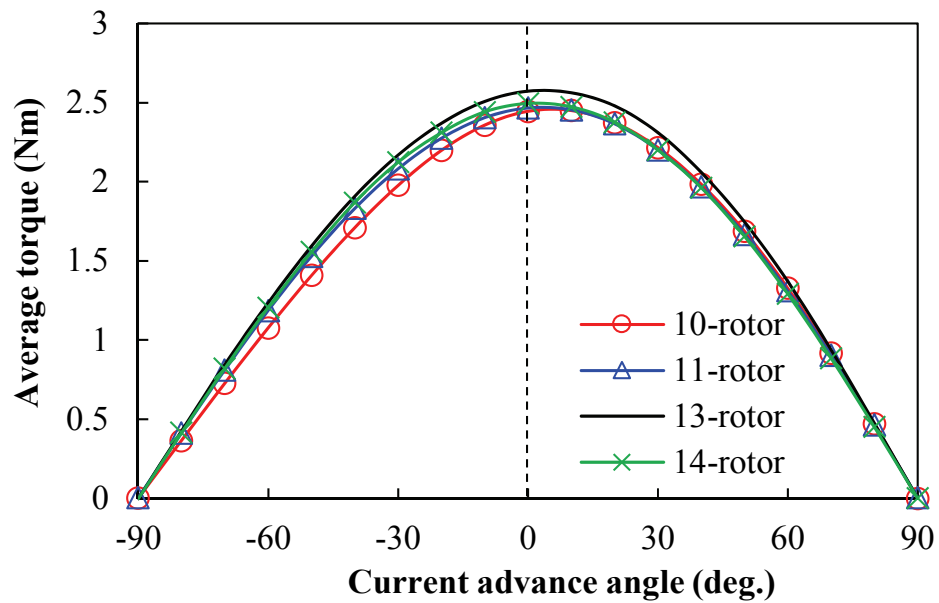
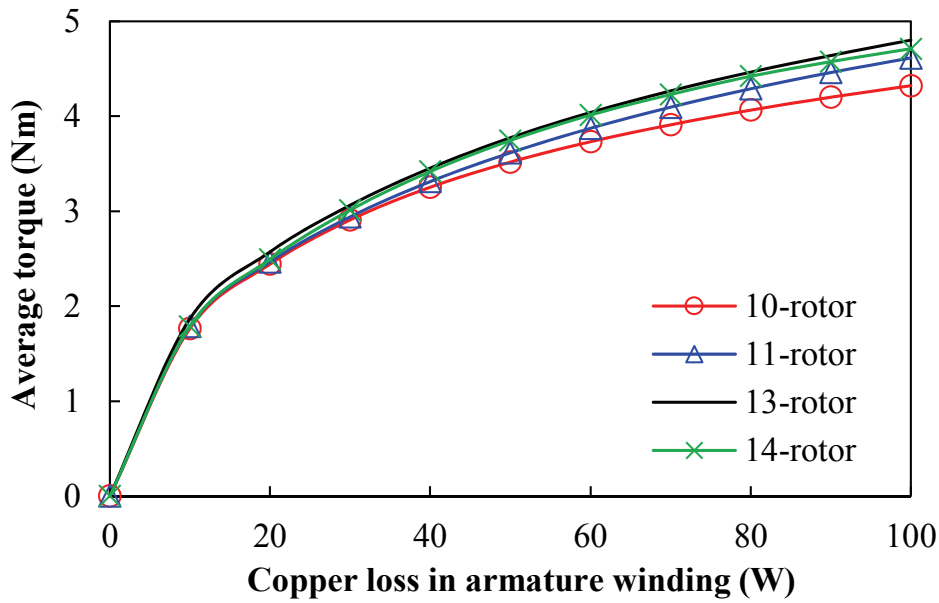
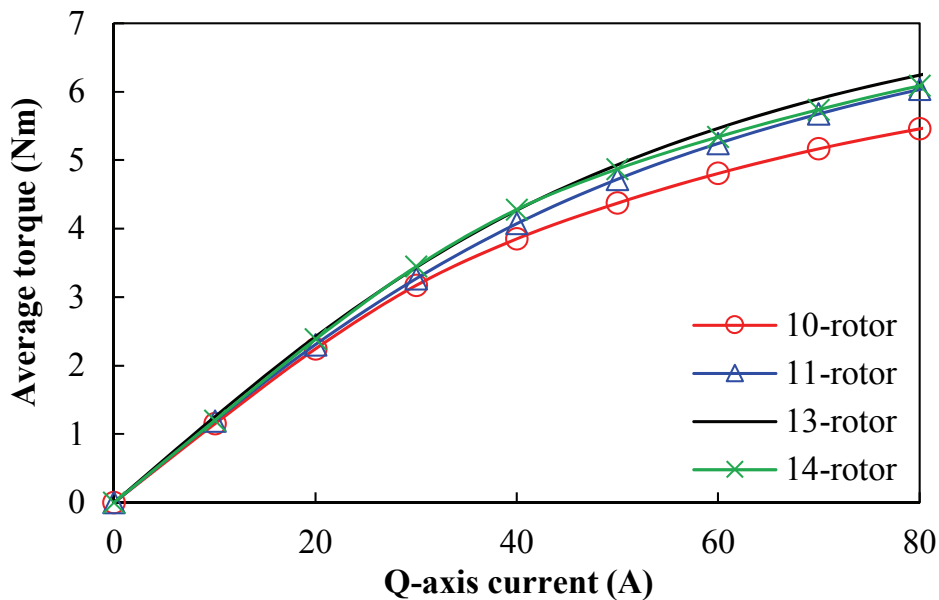


Fig. 6.16 Average torque versus current advance angle with 20W copper loss in armature windings.



(a) Average torque versus copper loss in armature windings



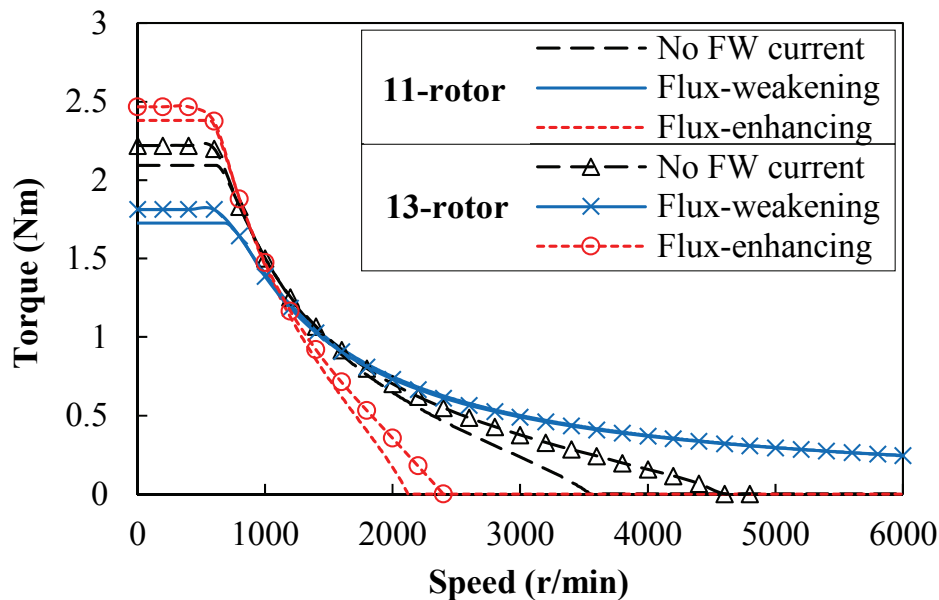
(b) Average torque versus q -axis current

Fig. 6.17 Variations of average torque versus armature winding excitations.

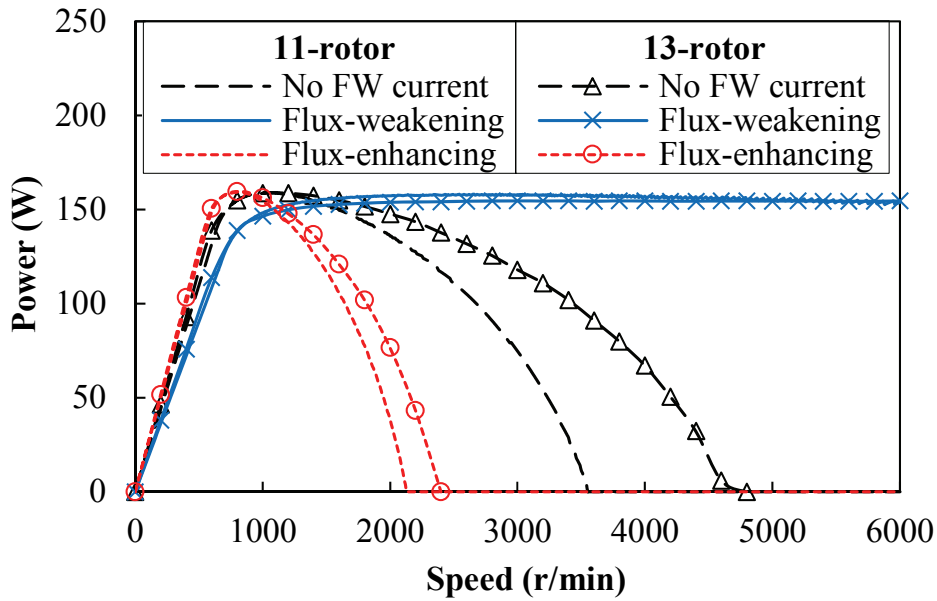
6.4.5 Torque-speed envelop

An essential benefit of the HE machine is a wide constant power speed range (CPSR). Thus, the torque-speed curves of the proposed machines are evaluated. Thanks to the advantages of even order harmonics cancellation, the 11- and 13-rotor machines inherently exhibit much less harmonics and lower torque ripples than the 10- and 14-rotor counterparts. Therefore, these two machines are further investigated.

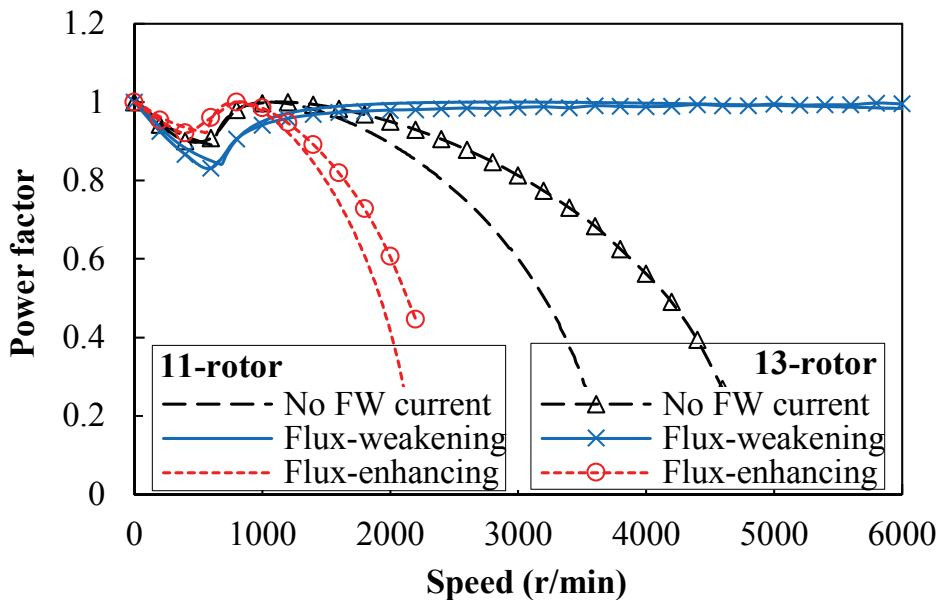
With the identical limit on bus voltage and phase current (12V/18A), the torque-speed curves of the 11- and 13-rotor PSHE machines are calculated by using the flux-linkage method [QI09]. Three typical field excitation conditions were applied. These were, respectively, the sole PM excitation without field current, the flux-weakening with negative 5A/mm² current density in FW slots and the flux-enhancing with positive 5A/mm². Fig. 6.18(a) and (b) present the predicted torque-speed and power-speed curves, in which the constant power speed range (CPSR) can be significantly extended under flux-weakening operation, while the flux-enhancing operation is beneficial to improve torque output in the low speed region. Consequently, with the flexible control of field current, the high torque output and wide CPSR can be obtained in the proposed machines. Furthermore, as shown in Fig. 6.18(c), the power factor can be greatly improved in the high speed region by applying flux-weakening control with negative field current, which can reduce the requirement on inverter capacity.



(a) Torque-speed curve



(b) Power-speed curve



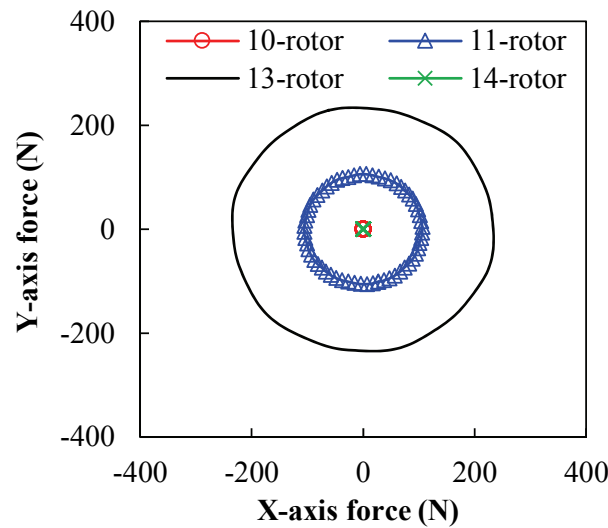
(c) Power factor-speed curve

Fig. 6.18 Torque, power and power factor versus operation speed under three typical field excitation conditions.

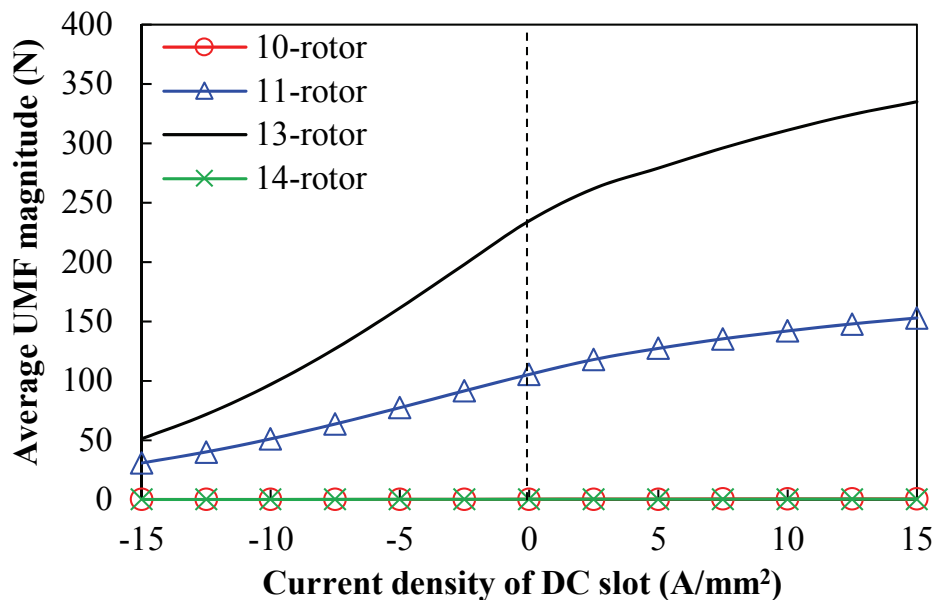
6.4.6 Unbalanced magnetic force

The unbalanced magnetic force (UMF) on the rotor is of importance to be evaluated as well. Without FW excitation, the open-circuit and on-load UMFs of the series PSHE machines equipped with different rotor pole numbers are compared in Fig. 6.19(a) and Fig. 6.20(a) respectively. There is no UMF in the 10- and 14-rotor machines but it is significant in the 11- and 13-rotor counterparts due to the odd rotor pole numbers. Meanwhile, there is negligible

effect due to the load. More importantly, the variations of UMFs versus field currents are illustrated in Fig. 6.19(b) and Fig. 6.20(b), in which the UMFs are always negligible in the 10- and 14-rotor machines, while they are increased in flux-enhancing operations but decreased in flux-weakening operations in the 11- and 13-rotor series PSHE machines. It should be noted that the UMFs in the 11- and 13-rotor machines will be greatly alleviated by multiplying both the stator slot and rotor piece numbers to obtain the even rotor piece numbers.

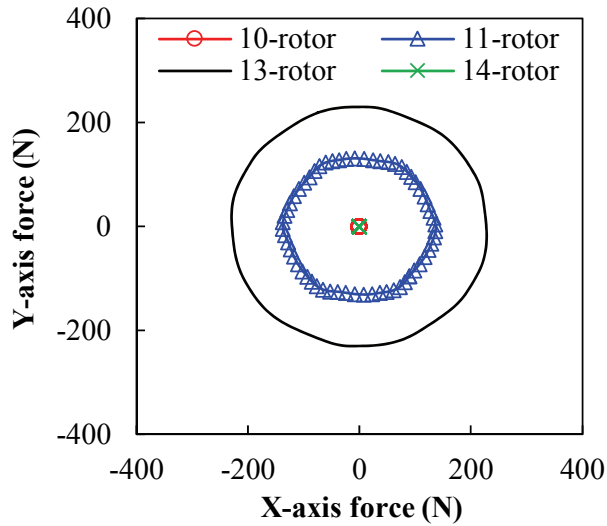


(a) UMF without FW excitation

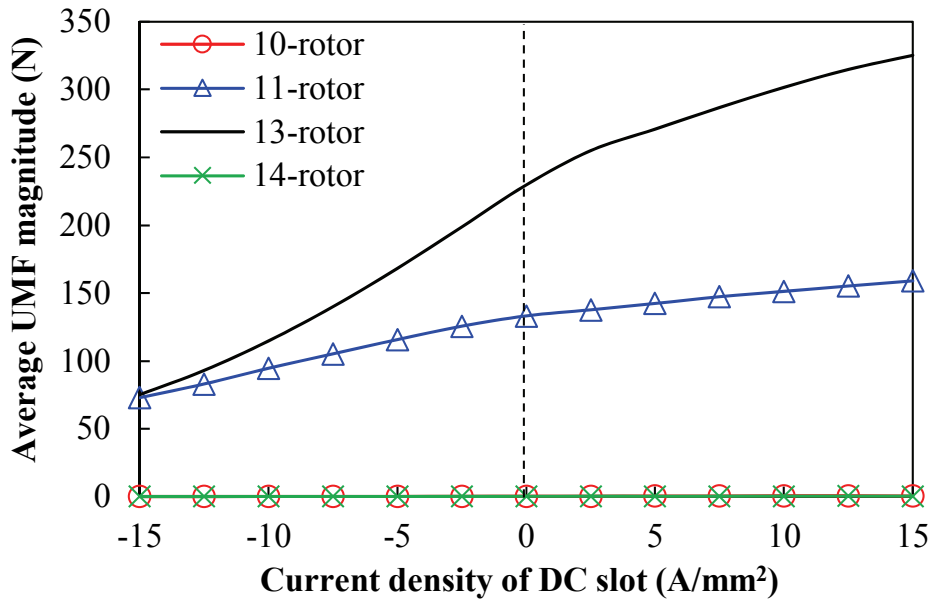


(b) Average UMF magnitudes with different field currents

Fig. 6.19 Open-circuit UMFs of 12-stator-slot series PSHE machines with different rotor pole numbers.



(a) UMF without FW excitation



(b) Average UMF magnitudes with different field currents

Fig. 6.20 On-load UMFs of 12-stator-slot series PSHE machines with different rotor pole numbers (20W copper losses in armature windings, zero d -axis current control).

6.5 Experimental Validation

In order to validate the previous analysis on electromagnetic performances, a 12/11 consequent-pole PSHE prototype machine was manufactured and tested. The essential parameters of this prototype machine are listed in Table 6.5, and the key components are shown in Fig. 6.21, including an outer stator with armature windings, an inner stator having alternately placed PMs and FWs, as well as a cup-rotor made of laminations. As shown in Fig. 6.21(a), the outer stator of the PS machine is identical to the stator of classic fractional-slot PM

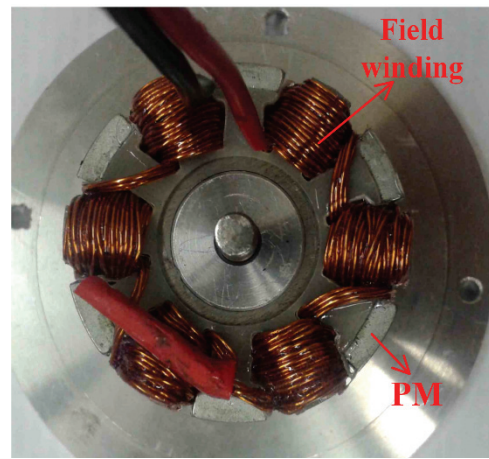
machines, which is easy to fabricate. The inner stator, having six pieces of surface-mounted PMs and six series-connected field coils, is shown in Fig. 6.21(b). It is assembled into an end plate, which is coupled to the frame. The sandwiched rotor shown in Fig. 6.21(c) is the most challenging component and its manufacturing process is illustrated in Fig. 6.22. Firstly, in order to facilitate the manufacture and improve mechanical strength, the iron rib is employed to connect individual iron pieces, as shown in Fig. 6.22(a). Then they are coupled to the non-magnetic plate as shown in Fig. 6.22(b), with which the shaft is linked. Afterwards, the epoxy resin is used to encapsulate the laminated rotor, supported by the non-magnetic tie bars. Finally, this assembled rotor is connected to the machine frame via the bearing.

Table 6.5 Key design parameters of the 12/11 prototype machine.

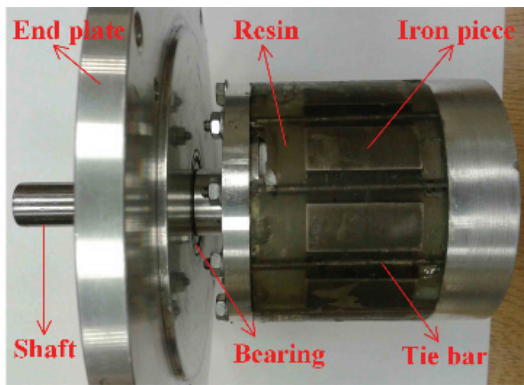
Parameter	Value	Parameter	Value
N_s	12	β_{ri}	24°
N_r	11	R_{iso}	25.75
l_a	25	R_{isy}	13.4
R_{oso}	45	R_{isi}	10.4
R_{osy}	42	β_{ist}	9.5°
R_{osi}	31.75	h_{pm}	4
β_{ost}	18°	β_{pm}	25.5°
g	0.5	N_{ac}	18
h_r	5	N_{dc}	16
β_{ro}	18°		



(a) Outer stator



(b) Inner stator



(c) Rotor

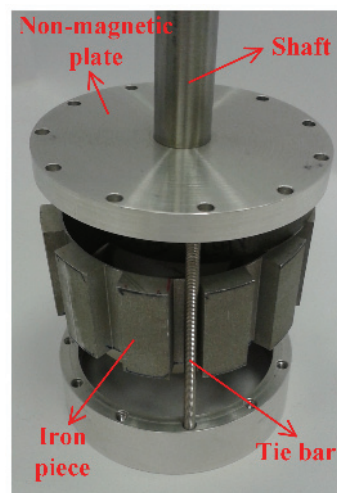


(d) Assembled stators

Fig. 6.21 Prototype of 12/11 consequent-pole PSHE machine.



(a) Rotor iron pieces



(b) Illustration of rotor assembly

Fig. 6.22 Illustration of rotor fabrication.

The phase back-EMFs at 400 r/min without FW excitation are measured and compared with FE predictions in Fig. 6.23. As the end effect is relatively significant in the consequent-pole

machine [WU16a], the 3-D FE calculations are carried out to eliminate the error caused by end effect. An approximate 7.5% difference can be observed between the measured and 3-D FE predicted back-EMFs, and errors should be attributed to the manufacturing tolerances that are discussed in section 2.6, including cutting tolerance on laminations, unaligned inner stator and etc. Moreover, Fig. 6.24 illustrates the flux regulation capability, in which the back-EMFs against different field currents are presented. The variation of the back-EMFs versus field currents can be observed, which implies the flux regulation capability of the proposed machine.

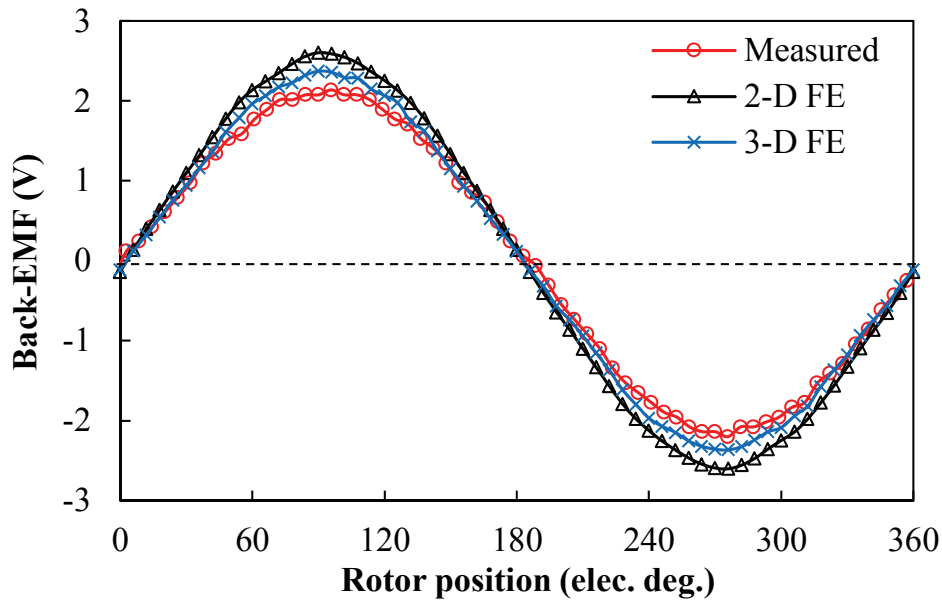


Fig. 6.23 Measured and FE predicted back-EMF waveforms at 400 r/min.

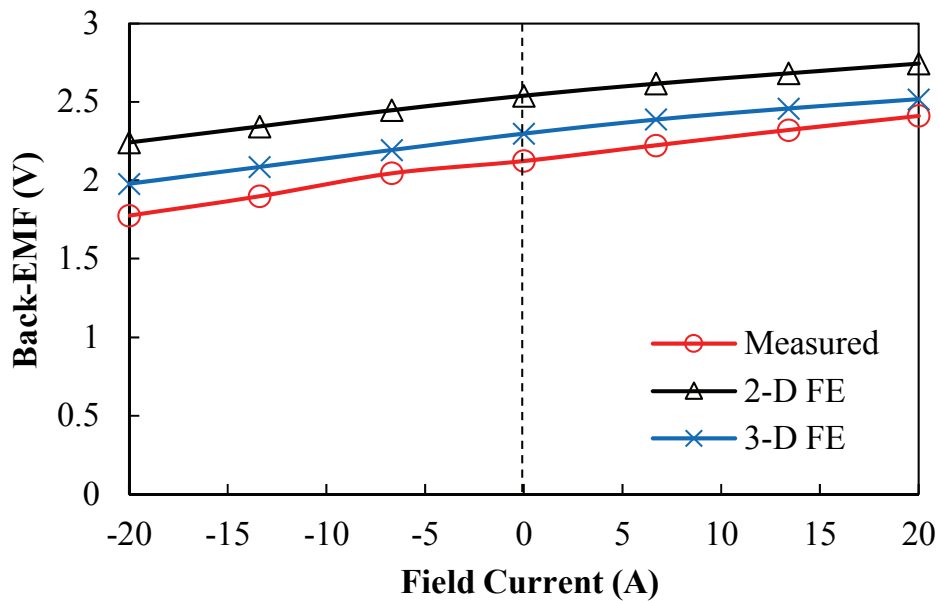
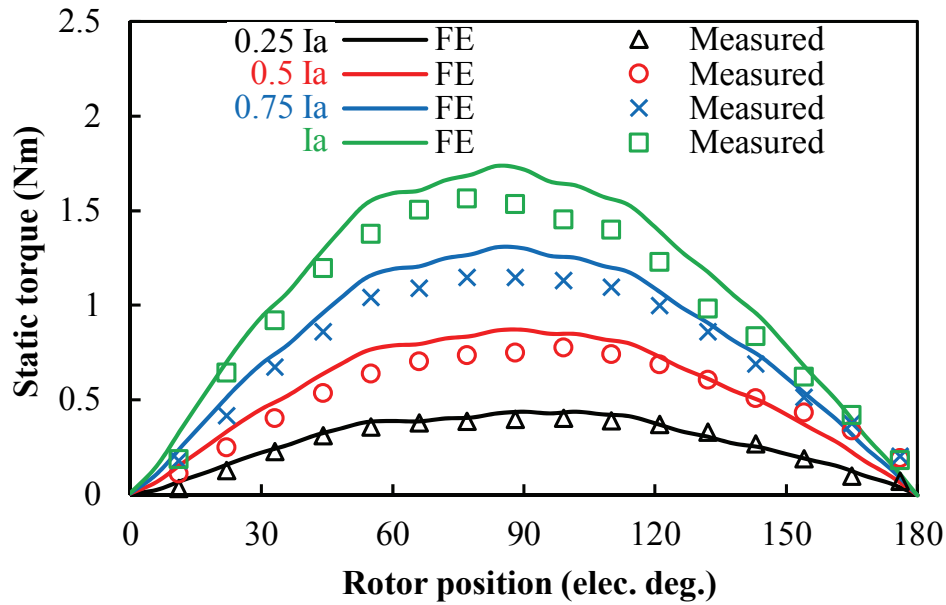
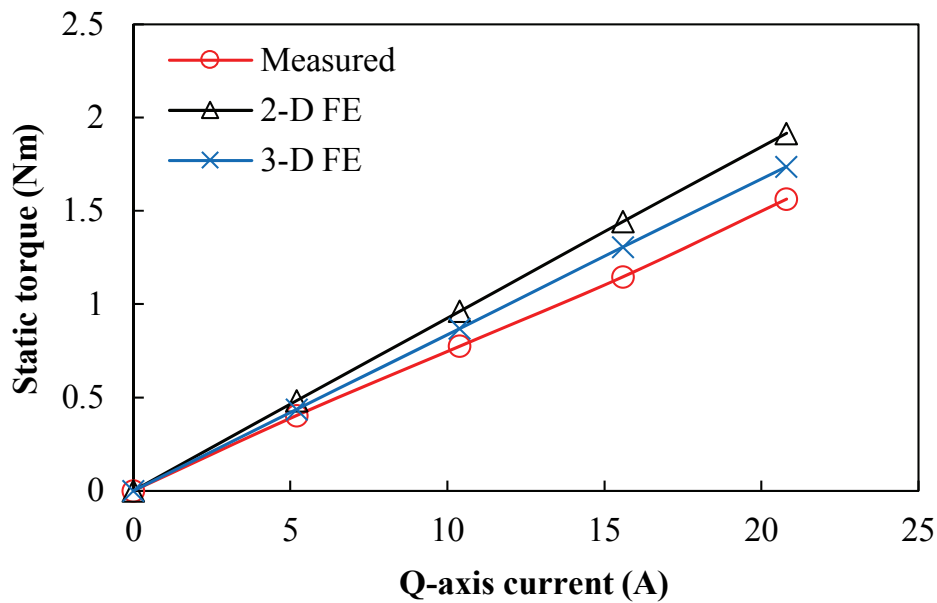


Fig. 6.24 Measured and FE-predicted peak fundamental back-EMFs versus different field currents.

Further, the static torque without FW excitation is measured by locking the rotor at different positions. As shown in Fig. 6.25, good agreement between the measured and 3-D FE predicted torques with different excitations in armature windings can be seen, albeit with the possible manufacturing and measuring tolerances which are introduced in section 2.6.



(a) Torque against rotor position with 3-D FE predictions.



(b) Torque versus q -axis current.

Fig. 6.25 Measured and FE-predicted static torques.

The test platform as shown in Fig. 6.26 is set up to measure the torque-speed curves. The prototype machine is coupled to a brushed DC generator as the load. The operating point of the prototype can be flexibly adjusted by changing the field current of the DC generator as well as

the resistance of the load bank linked to the generator armature windings. An encoder is employed to detect the rotor position of prototype, and a torque transducer is used to measure the torque output. The DC power supply is employed to feed the three-phase inverter. Meanwhile, the FW of the prototype machine is connected to an individual adjustable current source and hence the field current can be continuously adjusted.

The torque-speed curves are measured with the limit of 7.5A peak phase current, which is due to the constraint of inverter capacity. Under three typical field excitations (no field current, flux-enhancing with positive 6.7A field current and flux-weakening with negative 6.7A field current), the torque-speed curves are measured and presented in Fig. 6.27. Although the extremely low torque in the high speed region cannot be achieved due to the inherent friction torque of the load machine, the trends of the three curves can be observed. It can be found that the flux-weakening operation contributes to a higher base speed, and its torque output in the high speed region is higher. Meanwhile, in the low speed region, the flux-enhancing operation has a higher torque than the operation without field current. The difference between the 3-D FE predicted and measured curves should be attributed to the machine tolerances and the error in the drive system, which have been discussed in section 5.5.

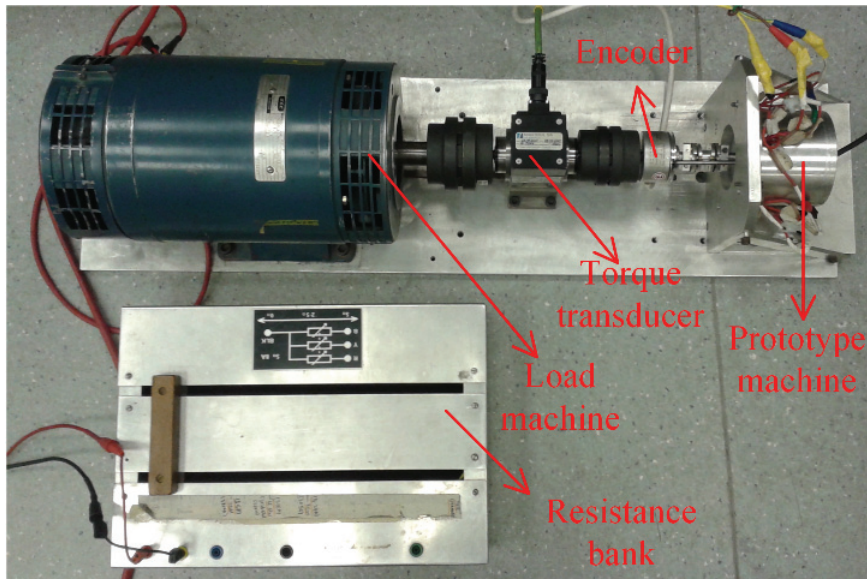


Fig. 6.26 Test platform for torque-speed measurement.

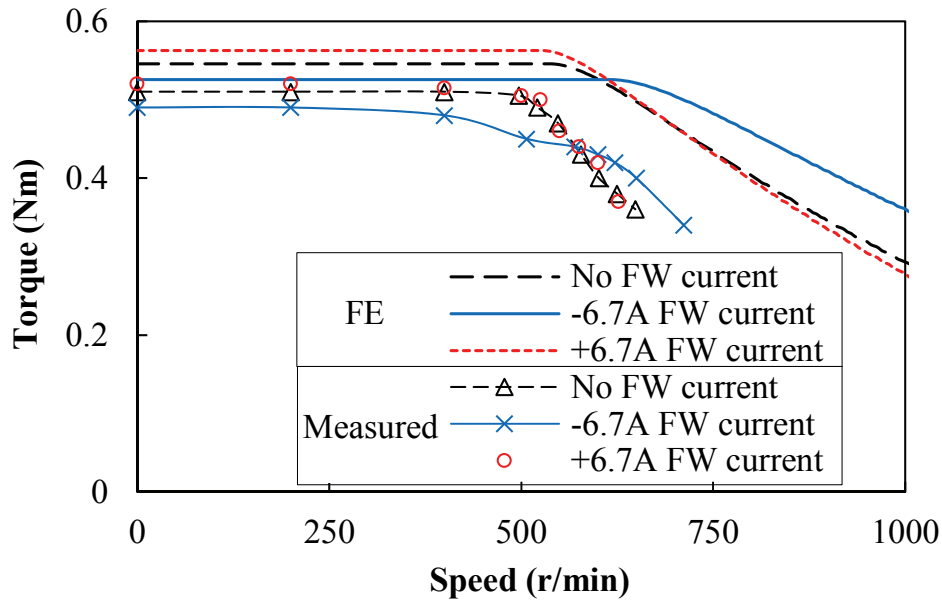


Fig. 6.27 Measured and FE-predicted torque-speed curves under three typical field excitations.

6.6 Conclusion

In this chapter, a novel series PSHE machine with a secondary stator to accommodate PMs as well as FWs, is introduced. The consequent-pole inner stator topology not only saves the PM usage volume but also enhances the flux regulation potential. The proposed machine benefits from good space utilization and elimination of slip rings. The investigations on the slot/pole combinations reveal that the 10- and 14-rotor machines suffer from high flux-linkage harmonics and torque ripples, which are inferior to the 11- and 13-rotor counterparts. Furthermore, the results based on FE predictions and experimental verifications show that the consequent-pole PSHE machines can exhibit outstanding flux regulation capability with good torque density.

Chapter 7. Parallel Hybrid Excited Machine with Separate Excitation Stator

In the previous Chapter 6, the novel PS-FRPM-based HE machines are introduced and evaluated, which feature the series connection between PMs and FWs. In this chapter, the HE machines with parallel connection are obtained by adjusting the relative locations of the PM and FW poles. Based on the PS-FRPM machine, the PM pole-pairs and the FW pole-pairs are alternately placed in the inner stator to realize the parallel magnetic paths, while the outer stator, armature windings and rotor remain unchanged. Compared with the machines in Chapter 6, the only difference is that every two pieces of PMs are with intervals of two FW poles. The proposed machine inherits the advantages of PS machines and further benefits from attractive flux regulation capability due to the parallel topology. The operating principle and the slot/pole number combination rule that are different from the conventional PS machines are illustrated. Moreover, the 2-D FE technique is used to evaluate the electromagnetic performance of the proposed machines with different slot/pole number combinations, confirming the mentioned advantages, together with experiments on a prototype machine.

This part has been published in IEEE Transactions on Energy Conversion.

7.1 Introduction

The concept of HE machines, in which PM and FW excitations coexist, is proposed to combine the advantages of PM machines and electrical-excited (EE) machines [McC87], [SPO89], [CAP15]. The topologies of HE machines are diverse, as two excitation sources can be arranged flexibly. A multitude of novel structures have been proposed and investigated in the past two decades. According to the connection between PM field and FW field, the HE machines are divided into two groups, i.e. series HE and parallel HE topologies.

For series HE machines, the flux created by the FWs would go through PMs. Thus PM flux and FW flux have the same flux path. A typical series HE topology is proposed in [HEN94], in which the FWs are wound around each pole of the surface-mounted PM (SPM) synchronous machine. Design consideration and experimental validation are presented in [FOD07]. Since FWs are allocated on the rotor, this machine requires slip rings and brushes for field current, reducing the reliability of the system. To remove sliding contacts, the stator-PM machine is an

attractive candidate to transform to a HE machine as FWs can be directly located on the stator. Based on the DSPM machines and the SFPM machines, a variety of series HE machines are presented [LEO96], [ZHU07a], [LIU10], [HUA09], [CHE11b], [GAU14].

However, the shortcoming of series HE machines can be easily identified. Since the FW flux has to pass the PMs, which have a permeability close to air, the reluctance of the FW flux loop is quite high, degrading the flux regulation effect. Meanwhile, the PMs have to suffer a high risk of irreversible demagnetization. Consequently, the parallel HE topologies possessing different paths for PM flux and FW flux, are attracting attention. The classic parallel HE structure based on a conventional SPM machine is proposed in [LUO00], where FW poles and PM poles are alternately placed on the rotor, and further analyses are included in [FIN08], [ZHA10]. This topology possesses separated magnetic paths, although the drawbacks are the same as the corresponding series HE machines due to the presence of sliding contacts. The parallel HE structure can also be obtained based on DSPM machines, in which several stator pole units exist, excited by either PMs or FWs [CHE11a], [ZHA12]. These machines feature a relatively simple structure and independent excitations. However, the cross-coupling between the FW unit and the PM unit is inevitable, whilst the power density is low and it also exhibits high torque ripple. The parallel HE SFPM machine which is proposed in [HOA07] employs an outermost iron ring to loop the FW flux. Nevertheless, the flux-leakage is inherently high as the PM flux is partially short-circuited by the iron ring, and the stator is very crowded with FWs, armature coils and PMs, sacrificing the torque density. In addition to the foregoing radial flux machines, the axially divided rotor technique is adopted to achieve parallel HE machines. In [NAO01], with the conventional stator, two rotor parts consisting of the PMs and FWs are axially combined together. In [GEN15], a rotor-PM synchronous machine and an EE-doubly salient machine are axially coupled. Meanwhile, an EE-switched flux machine and a SFPM machine are combined along the axial direction to realize a parallel HE topology [WAN12a]. These axially combined HE machines have two excitation sources to contribute to the air-gap field individually, while the structures are complicated and the space between the two parts is wasted, reducing the compactness and power density. Furthermore, a variety of parallel HE machines with 3-D flux are presented [AMA01], [TAP03], [KOS10], [LIU09], [NED11], [BAR15], which arrange toroid field coils in the central back-iron or at the end-parts of stator. Both radial and axial flux exist in these machines. However, these 3-D flux HE machines are generally very sophisticated and the reluctance for FW flux is high, degrading field control range.

Consequently, a simple parallel HE machine avoiding sliding contacts whilst exhibiting excellent torque density and flux regulation capability is sought for. In this chapter, a parallel partitioned stator (PS) HE (PSHE) machine is presented and investigated, which employs one stator to accommodate armature windings whilst the other stator to accommodate the parallel connected PM and FW poles.

This chapter is organized as follows. In section 7.2, the topology and operating principle of the parallel PSHE machine are presented, followed by the rule of slot/pole number combinations discussed in section 7.3. Then in section 7.4, based on 2-D FE analysis, the electromagnetic performances of the parallel PSHE machines with different slot/pole combinations are comprehensively evaluated. Finally, the prototype is manufactured and the experimental validation is carried out in section 7.5.

7.2 Machine Topology and Operating Principle

The proposed three-phase 12-stator-slot/10-rotor-pole parallel PSHE machine is presented in Fig. 7.1. It has two separated stators and one iron-piece rotor sandwiched between them. The non-overlapping concentrated armature windings are placed on the outer stator whilst the PMs and FWs are allocated on the inner stator (outer stator and inner stator are exchangeable). The FWs consist of non-overlapping concentrated coils, and PMs are surface-mounted on the inner stator. The inner stator pole number is identical to the outer stator slot number, and the central lines of the PMs are aligned with the center of the outer stator slots. It should be emphasized that every PM pole-pair and FW pole-pair are alternately arranged on the inner stator. Therefore the PM flux or FW flux can loop through the adjacent pole individually, resulting in the parallel magnetic paths and thus attractive flux regulation capability. This machine inherits the advantages of stator-PM machine since the rotor is only made of iron, while PMs as well as coils are all located on the stationary component, which improves robustness and temperature management. In fact, the inner stator topology of the parallel PSHE machine is similar to the rotor of the HE machine in [LUO00], but the FWs are moved to the stator to avoid slip rings and brushes. Furthermore, the space utilization of this machine is enhanced thanks to the presence of the double stator, which is beneficial to guarantee the good space utilization and, consequently, improve the torque density.

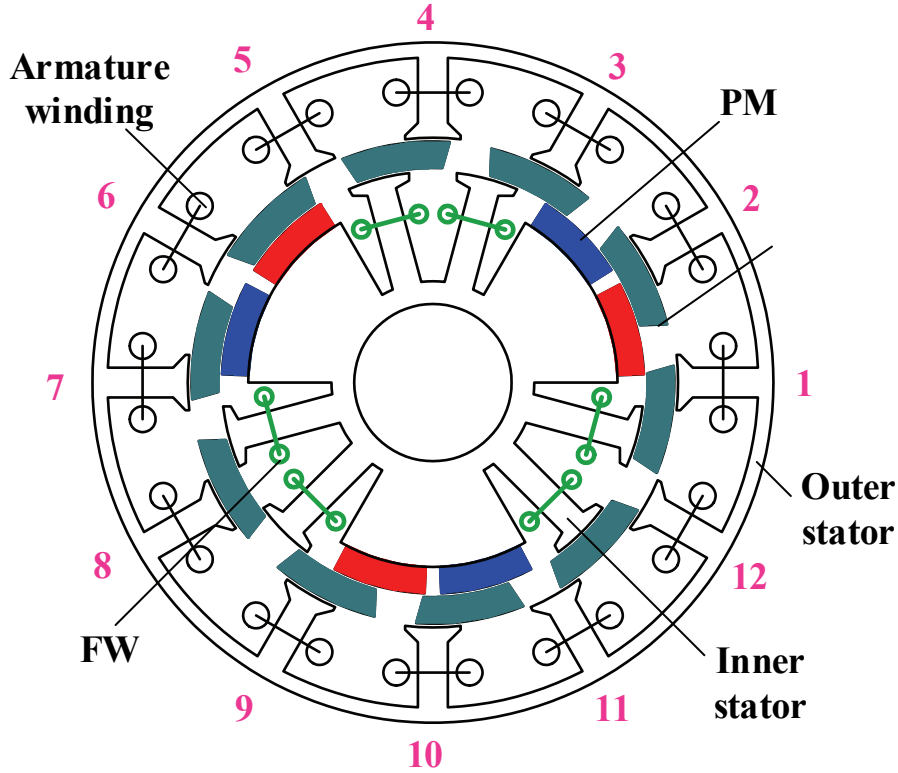


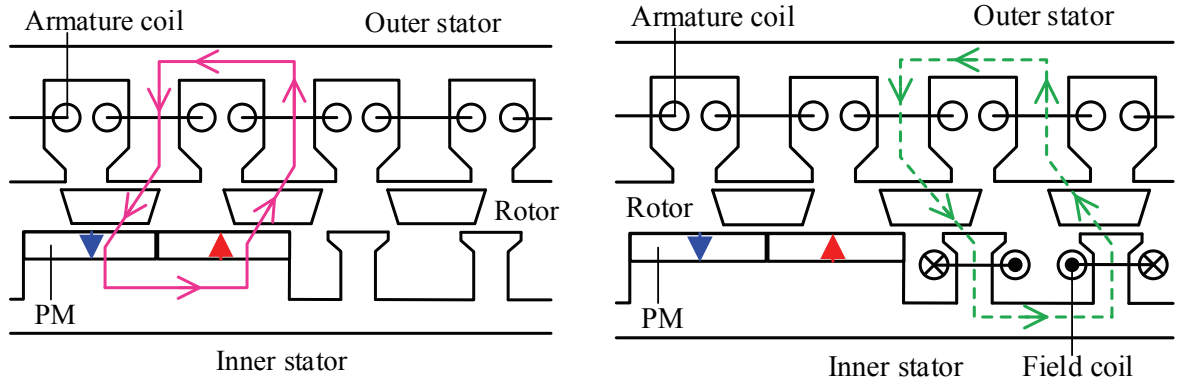
Fig. 7.1 Cross section of three-phase 12-stator-slot/10-rotor-pole parallel PSHE machine.

The parallel paths for PM flux and FW flux are illustrated in Fig. 7.2. The flux generated by PMs as shown in Fig. 7.2(a) and the flux of FWs as shown in Fig. 7.2(b) can contribute to the armature coils individually. As the FW flux is easy to regulate, the accumulative flux linked by the armature coils is adjustable.

The relation between rotor mechanical position θ_m and electric position θ_e is expressed as follows:

$$\theta_e = N_r \cdot \theta_m \quad (7.1)$$

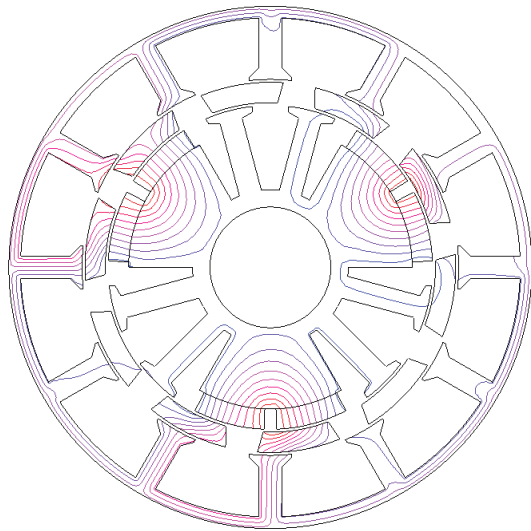
where N_r is the rotor pole number. Fig. 7.3 shows the open-circuit field distributions due solely to PMs at four typical rotor positions, as well as the flux distributions due to only FWs. In the plots with only FW excitations, the PM is set as air. It is clear that the PM excitations and FW excitations have effects on the different armature coils, making each coil have distinctive flux-linkages. But the symmetrical phase flux-linkage can be obtained when the suitable slot/pole number combination is adopted, which will be discussed in the following.



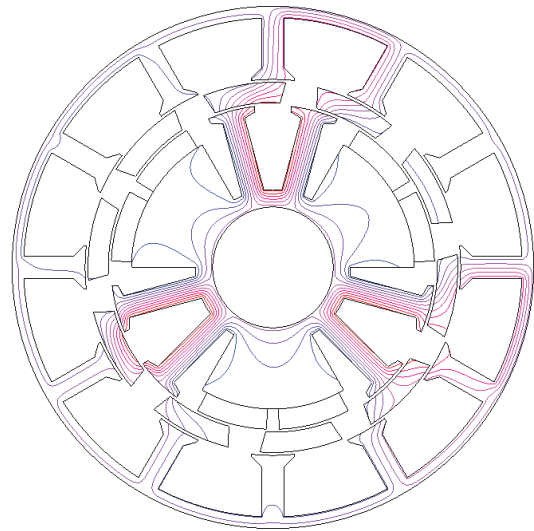
(a) PM flux

(b) FW flux

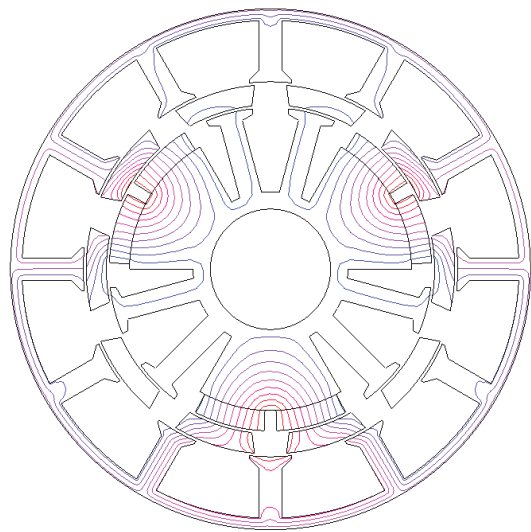
Fig. 7.2 Illustration of the parallel flux paths of PM and FW fluxes.



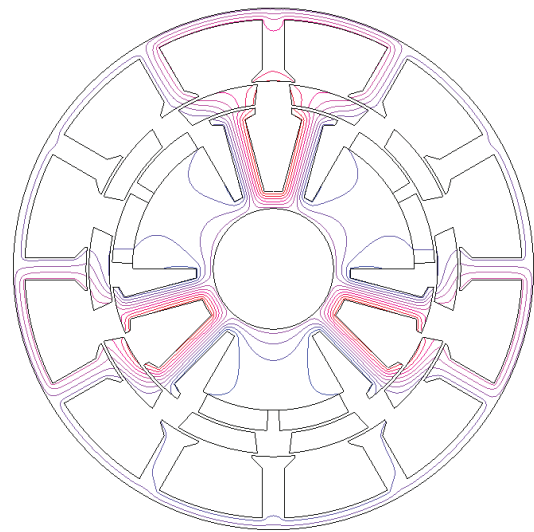
(a) $\theta_e = 0^\circ$, PM excitation



(b) $\theta_e = 0^\circ$, FW excitation



(c) $\theta_e = 90^\circ$, PM excitation



(d) $\theta_e = 90^\circ$, FW excitation

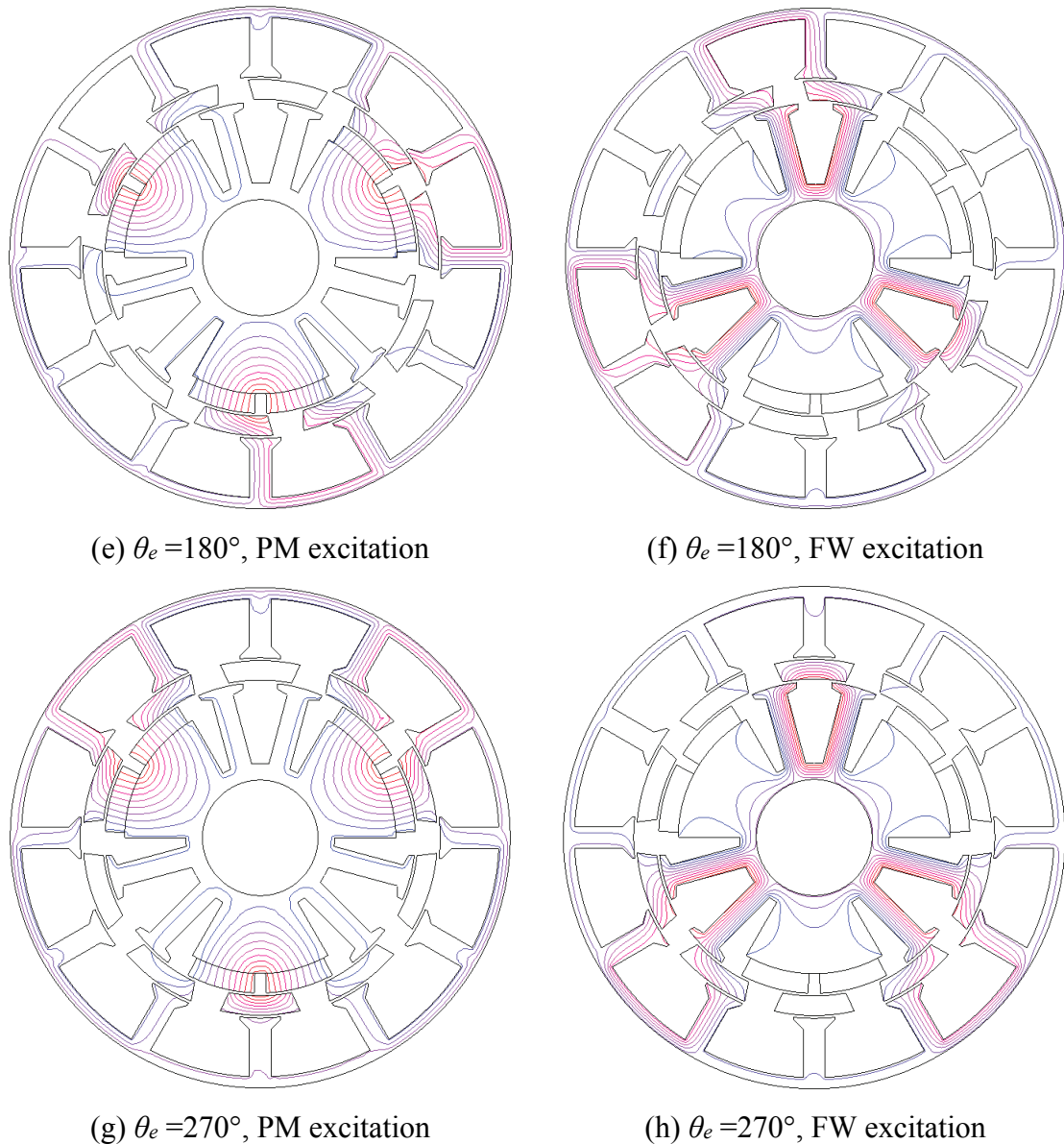


Fig. 7.3 Open-circuit field distributions at typical rotor positions due to PMs or FWs respectively.

For the 12-stator-slot/10-rotor-pole parallel PSHE machine shown in Fig. 7.1, the coil back-EMF phasors are illustrated in Fig. 7.4(a). The armature coils 1, 4, 7, and 10 are forward connected to constitute phase A. Without field current, the open-circuit flux-linkage waveforms of these four coils are shown in Fig. 7.5(a), accompanied with the corresponding phase flux-linkage. It can be seen that each coil exhibits a distinctive waveform, implying that the series connection is necessary. Although the coil flux-linkages are all asymmetric, the resultant phase flux-linkage is characterized with a symmetrical and sinusoidal waveform. This is due to the cancellation of the DC biased components and a large number of harmonics, after connection, as illustrated in Fig. 7.5(b).

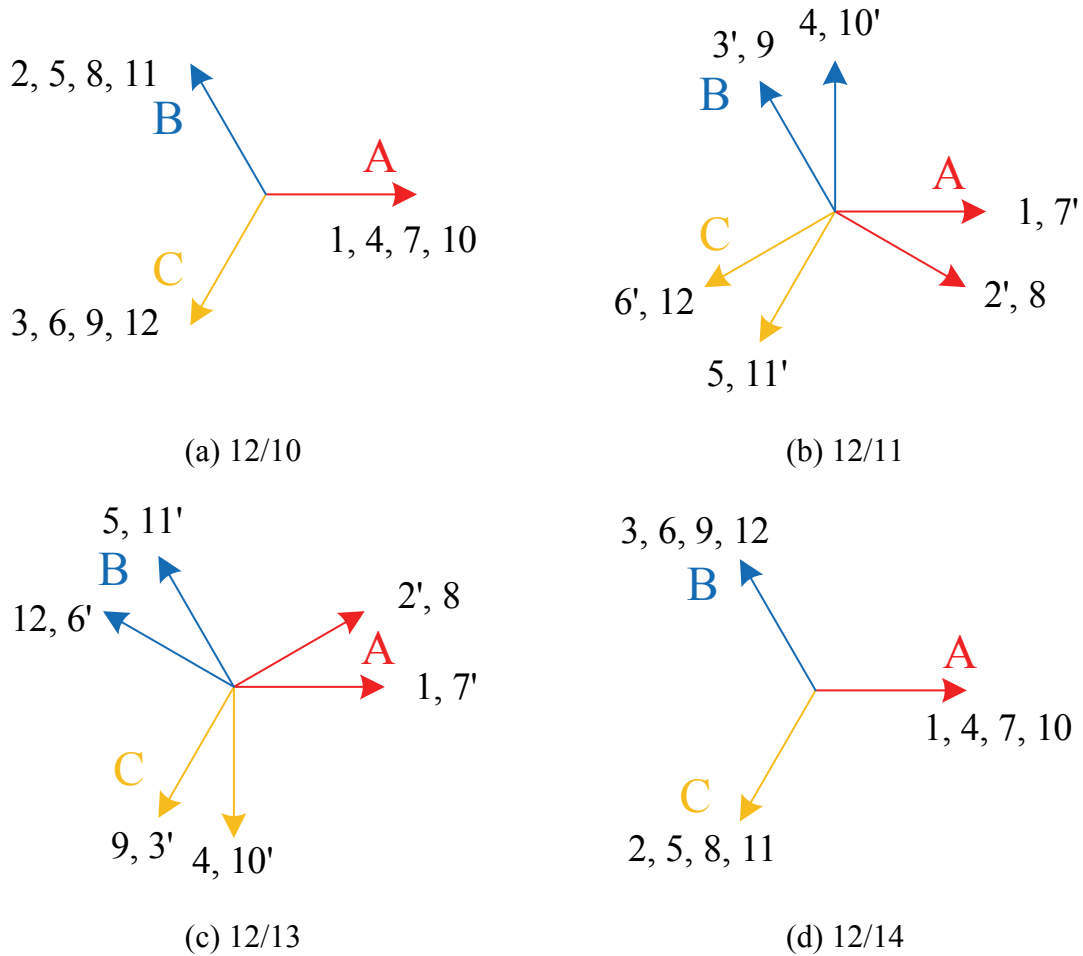
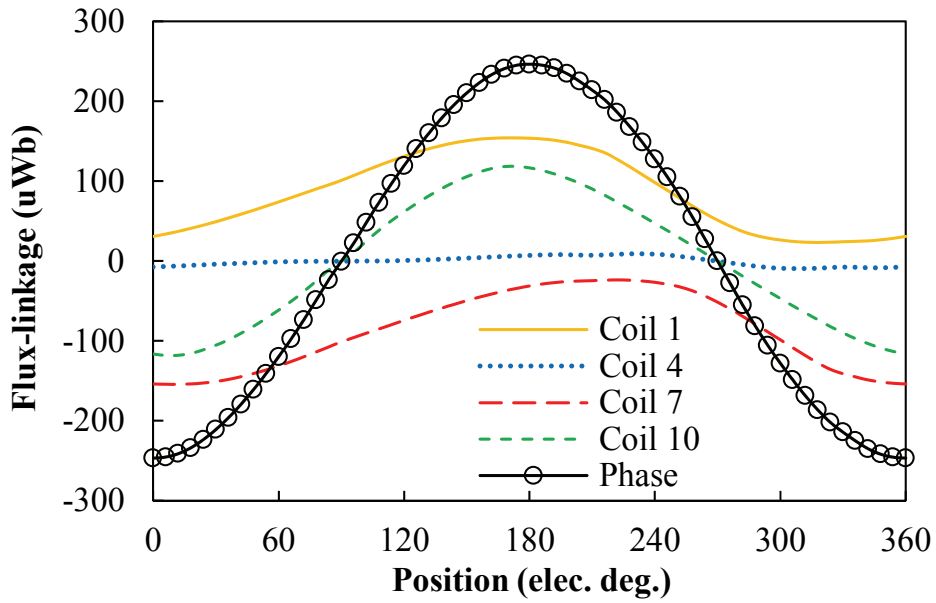
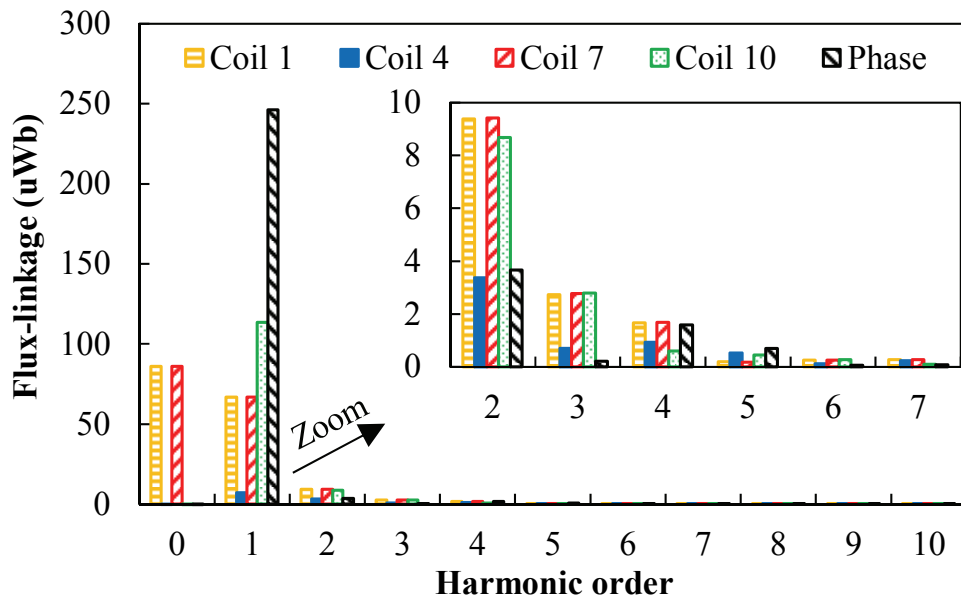


Fig. 7.4 Coil back-EMF phasors for 12-stator-slot parallel PSHE machines with different rotor iron piece numbers.

Furthermore, the flux regulation is easy to realize by injecting different currents into the FWs. Fig. 7.6 shows the open-circuit field distributions under flux-enhancing and flux-weakening conditions. Moreover, the phase flux-linkages under different excitations are compared in Fig. 7.7. The magnitude of flux-linkage under flux-enhancing conditions is almost the sum of flux due to PMs and FWs, while the magnitude under flux-weakening operation is equal to the difference between them, which reveals good flux regulation capability thanks to parallel magnetic paths. In fact, the phase flux linkage is able to be lowered to zero if the reversed FW flux, having identical amplitude to the PM flux, is applied. In addition, the harmonics are always low in the resultant phase flux-linkage.

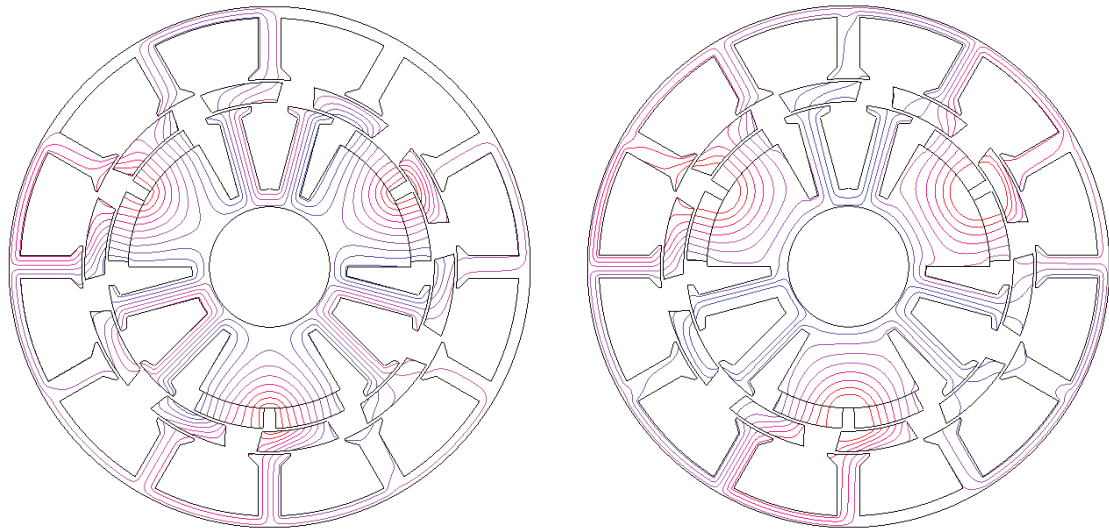


(a) Waveforms



(b) Spectra

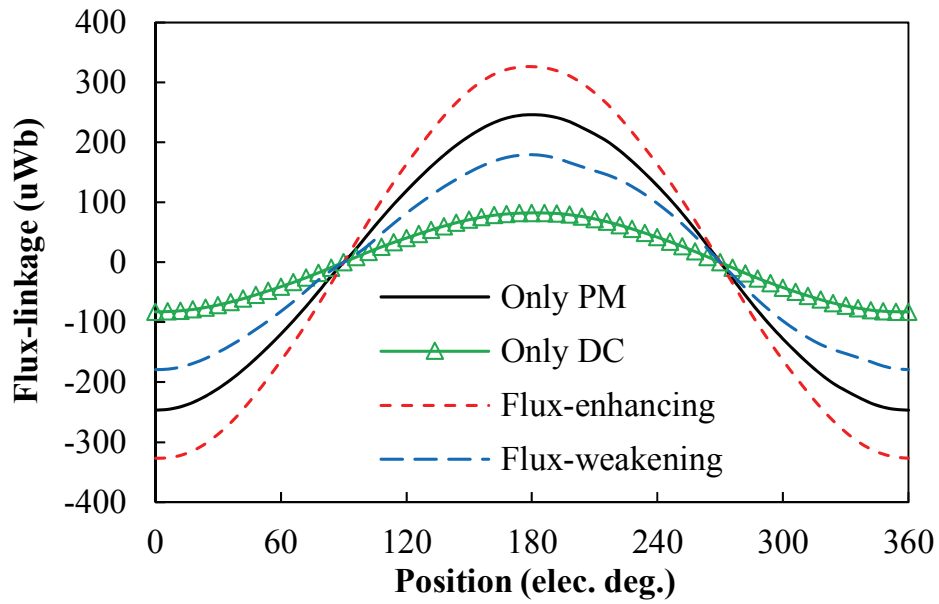
Fig. 7.5 Flux-linkages of coils and corresponding phase of the 12-stator-slot/10-rotor-pole parallel PSHE machine with only PM excitations.



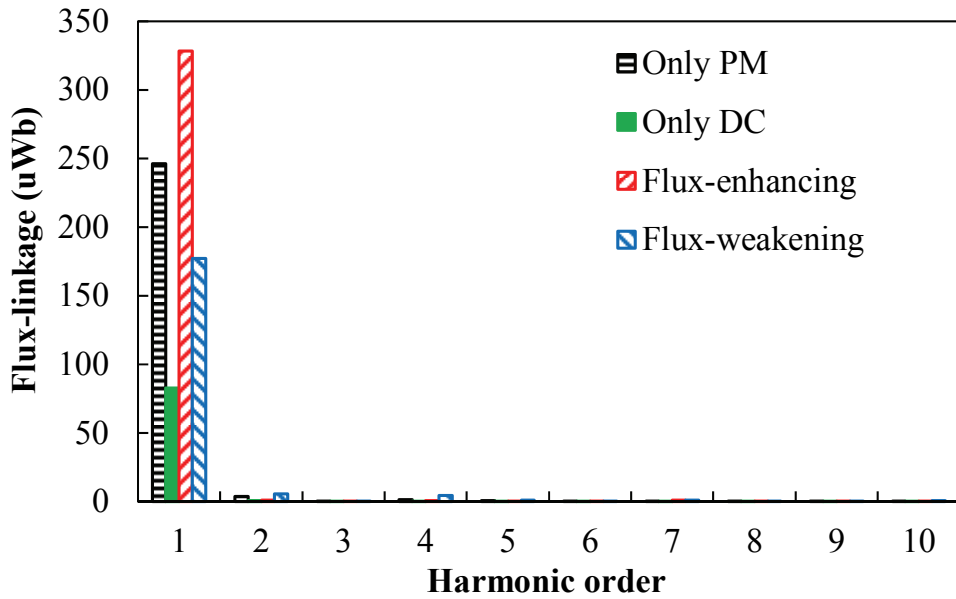
(a) Flux-enhancing

(b) Flux-weakening

Fig. 7.6 Open-circuit field distributions under flux-enhancing and flux-weakening conditions.



(a) Waveform



(b) Spectra

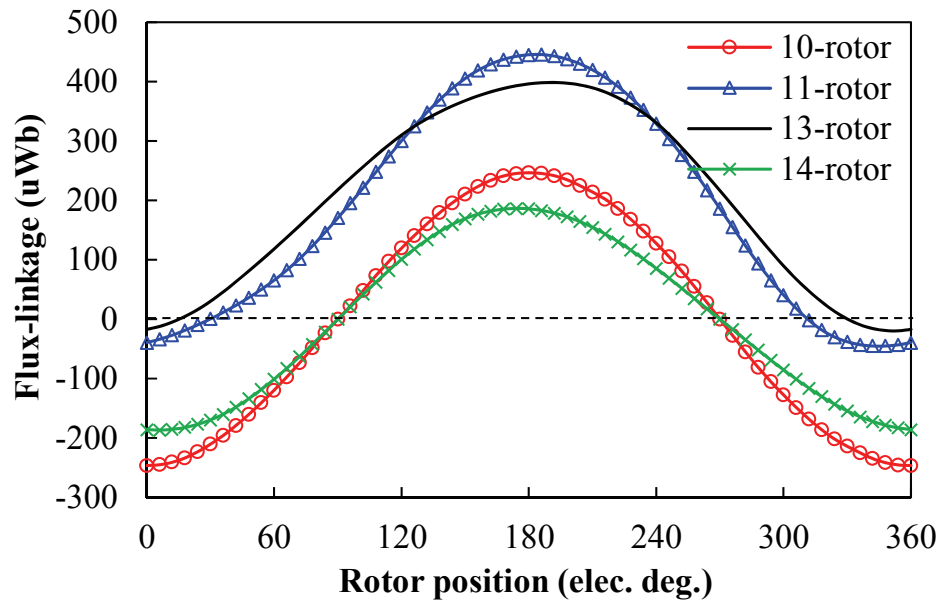
Fig. 7.7 Phase flux-linkages of 12-stator-slot/10-rotor-pole parallel PSHE machine under different excitations.

7.3 Slot/Pole Number Combinations

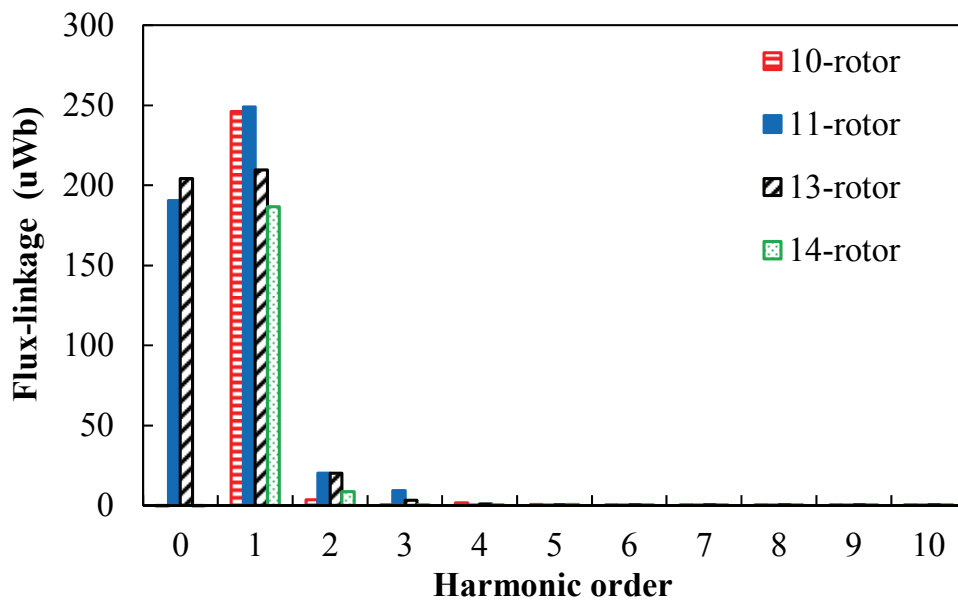
To achieve symmetrical flux-linkage, it is of great importance to choose an appropriate slot/pole number combination. Firstly, the least stator slot number is determined. For the three phase machine, the number of stator slots must be multiples of 3, i.e. $3 \times C_1$ (C_1 is a casual integer). Besides, since the parallel HE topology is applied, two PM poles and two FW poles are the least, requiring the stator slot number as multiples of 4, i.e. $4 \times C_2$ (C_2 is another integer). Therefore, to meet these two conditions, the least number of stator slots is 12. As a machine unit, the 12-stator-slot structure is investigated in detail.

Then, due to the fact that symmetrical coil flux-linkage is difficult to obtain and harmonics cancellation is required in the phase winding, the rotor pole number and hence the winding configuration should be chosen carefully. In general, the rotor pole number should be close to the stator slot number to achieve high winding factor [CHE10b]. For this 12-stator-slot machine unit, the potential rotor pole numbers are 10, 11, 13 and 14. It is expected to obtain the symmetrical flux-linkage even though only PM excitations function as the FW excitation is flexible. Therefore, without FW excitation, the open-circuit phase flux-linkages of the parallel PSHE machines with different rotor pole numbers are compared in Fig. 7.8. It can be found that the 10- and 14-rotor machines have symmetrical waveforms while the 11- and 13-rotor

counterparts suffer remarkable DC biases. Moreover, as the spectra shown in Fig. 7.8(b), the 11- and 13-rotor machines both have more harmonics than the 10- and 14-rotor machines. The reason for this will now be explained.



(a) Waveforms



(b) Spectra

Fig. 7.8 Phase flux-linkages due to only PM excitations of parallel PSHE machines with different rotor pole numbers.

Since the PMs and FWs are both located on the stationary component, the proposed parallel PSHE machine is naturally a stator-PM machine. The relative location of armature coils in the outer stator and the excitation sources in the inner stator is fixed, which is independent to the

rotor pole numbers and winding configurations. To achieve the symmetrical flux-linkage, two kinds of excitation sources should be symmetrically allocated to four coils of the one phase. For the parallel PSHE machine shown in Fig. 7.1, the physical relation between armature coils and PMs is illustrated in Table 7.1, in which the “N” and “S” stand for North pole and South pole respectively. More specifically, the coil labelled with “N” means the flux linked by this coil mainly contributed by the North pole PM. While the “N+S” represents the flux of the corresponding coil, which is dominantly created by one North pole PM and one South pole PM alternately. “0” indicates there is no PM contributing to the coil flux.

Thereafter, with different slot/pole number combinations and thus distinctive winding configurations shown in Fig. 7.4, the characteristics of the four armature coils constituting phase A are summarized in Table 7.2. It should be noted that the reversed winding connections occur in the 11- and 13-rotor machines, while all coils are forward connected in the 10- and 14-rotor structures. As a result, the 10- and 14-rotor parallel PSHE machines can obtain symmetrical PM flux thanks to the forward connection and thus balanced PM function, with which a multitude of harmonics are cancelled out. But there are significant DC biased components in the 11- and 13-rotor machines due to the reversely connected coils, resulting in the asymmetric flux-linkage and a large number of harmonics that are difficult to be cancelled.

Table 7.1 Coils physical relation with the PMs.

Coil	1	2	3	4	5	6	7	8	9	10	11	12
PM	N	N+S	S	0	N	N+S	S	0	N	N+S	S	0

Table 7.2 Characteristics of armature coils for Phase A.

Rotor pole number	A1	A2	A3	A4
10-rotor	N	0	S	N+S
11-rotor	N	N'+S'	S'	0
13-rotor	N	N'+S'	S'	0
14-rotor	N	0	S	N+S

7.4 Electromagnetic Performance

In this section, the electromagnetic characteristics of the four parallel PSHE machines with different rotor pole numbers are all evaluated. Based on the key geometric parameters illustrated in Fig. 7.9, the global optimizations with genetic algorithm for maximizing the average torque under flux-enhancing conditions are carried out for each machine, in which fixed 20W copper losses in armature windings is applied and zero d -axis current control is employed. The armature winding copper loss is defined in (2.1) and the $5A/mm^2$ current density is applied to the FW slots to realize flux-enhancing. The optimization process of the parallel PSHE machines is similar to that discussed in section 4.3. The optimal design parameters are listed in Table 7.3.

Table 7.3 Key design parameters of optimal parallel PSHE machines.

Machine	10-rotor	11-rotor	13-rotor	14-rotor
Stator slot number	12	12	12	12
Rotor pole-pairs number	10	11	13	14
Axial length (mm)	25	25	25	25
Outer stator outer radius (mm), R_{oso}	45	45	45	45
Outer stator yoke radius (mm), R_{osy}	43	43	43	43
Outer stator inner radius (mm), R_{osi}	32.4	34.6	34.6	34.6
Outer stator tooth arc ($^\circ$), β_{ost}	13	13.5	13.5	13.5
Air-gap length (mm), g	0.5	0.5	0.5	0.5
Rotor radial thickness (mm), h_r	3.5	3.5	3	3
Rotor outer pole arc ($^\circ$), β_{ro}	26	25	20	19
Rotor inner pole arc ($^\circ$), β_{ri}	23	20	19	17
Inner stator outer radius (mm), R_{iso}	27.9	30.1	30.6	30.6
Inner stator yoke radius (mm), R_{isy}	13.4	13.4	13.4	13.4
Inner stator inner radius (mm), R_{isi}	10.4	10.4	10.4	10.4
Inner stator tooth arc ($^\circ$), β_{ist}	13	13	13	13
PM height (mm), h_{pm}	3.5	3.5	3.5	3.5
PM pole arc ($^\circ$), β_{pm}	25.5	25.5	25.5	25.5

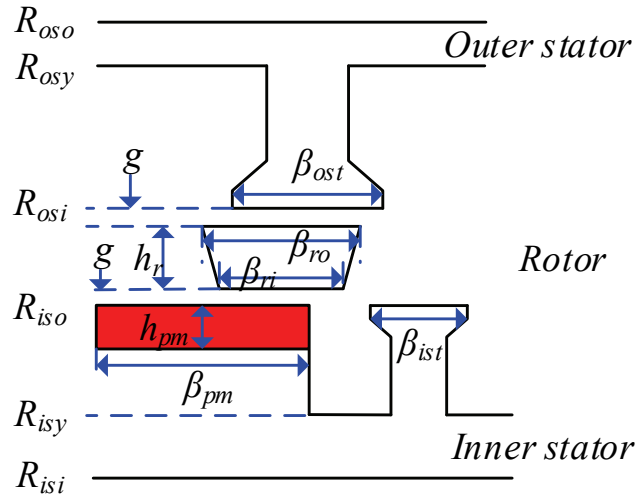
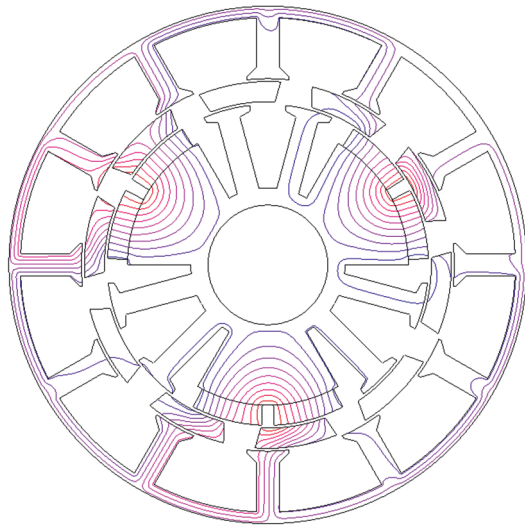


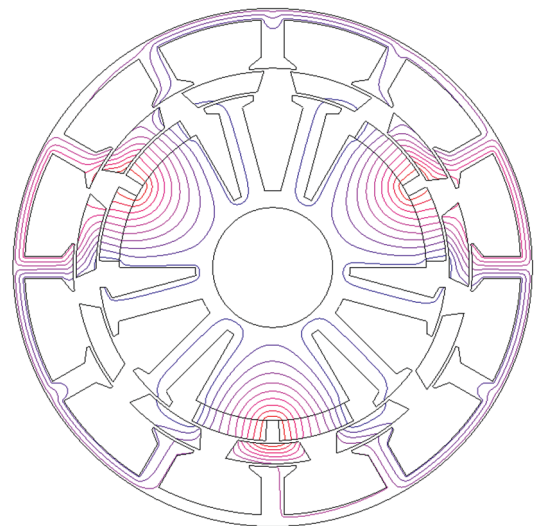
Fig. 7.9 Illustration of key design parameters of parallel PSHE machine.

7.4.1 Open-circuit back-EMF

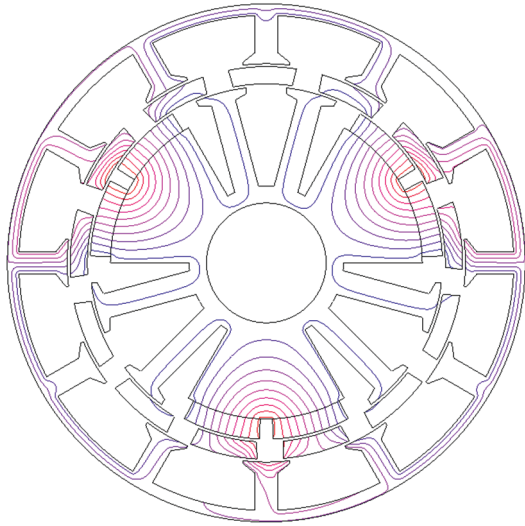
Fig. 7.10 shows the open-circuit field distributions of the parallel PSHE machines with 10-, 11-, 13- and 14-rotor at the d -axis rotor position respectively. Without FW excitation, the open-circuit phase back-EMFs at 400 r/min of the four parallel PSHE machines are shown in Fig. 7.11. It is apparent that the 11- and 13-rotor machines have higher peak fundamental magnitudes than the 10- and 14-rotor counterparts due to their high winding factors. Moreover, it can be seen that the harmonics are remarkably lower in the 10- and 14-rotor machines thanks to the symmetrical flux paths and the cancellation of harmonics. It is worth of noting that although the DC biased flux components are eliminated in the appropriate slot/pole combinations (10- and 14-rotor machines), a small amount of even order harmonics still exist in the phase back-EMFs since the distinctive excitation poles in inner stator act. Hence the even order harmonics cannot be completely cancelled out. This phenomenon will be more significant under flux-weakening conditions in which the difference between PM poles and FW poles intensifies. But negligible harmonics can be achieved under flux-enhancing conditions when FW poles and PM poles are comparable.



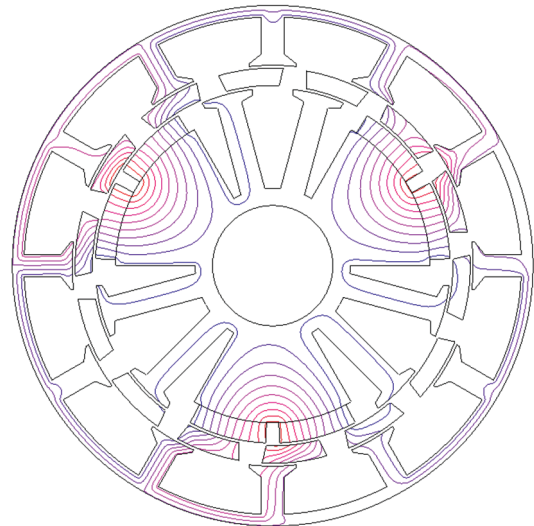
(a) 10-rotor



(b) 11-rotor

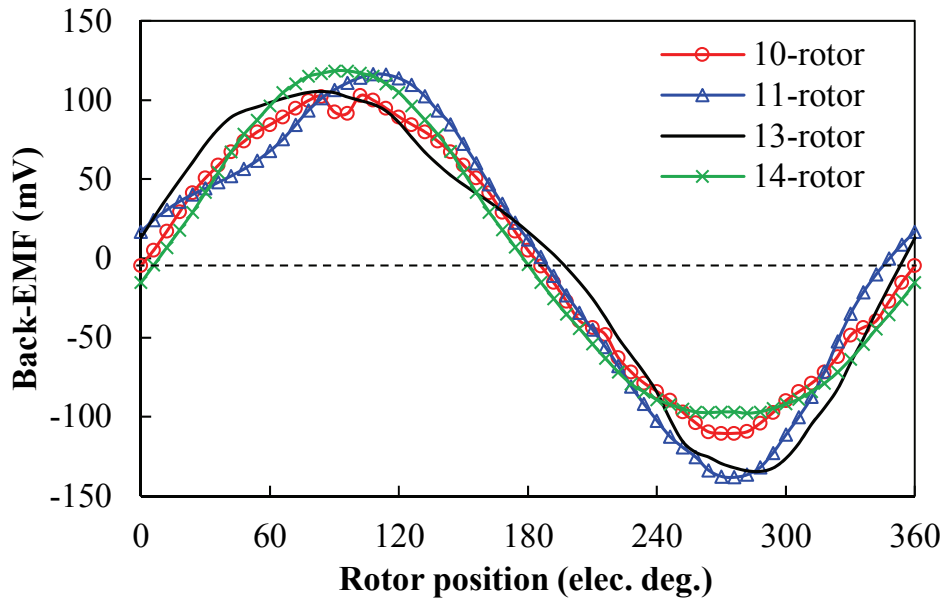


(c) 13-rotor

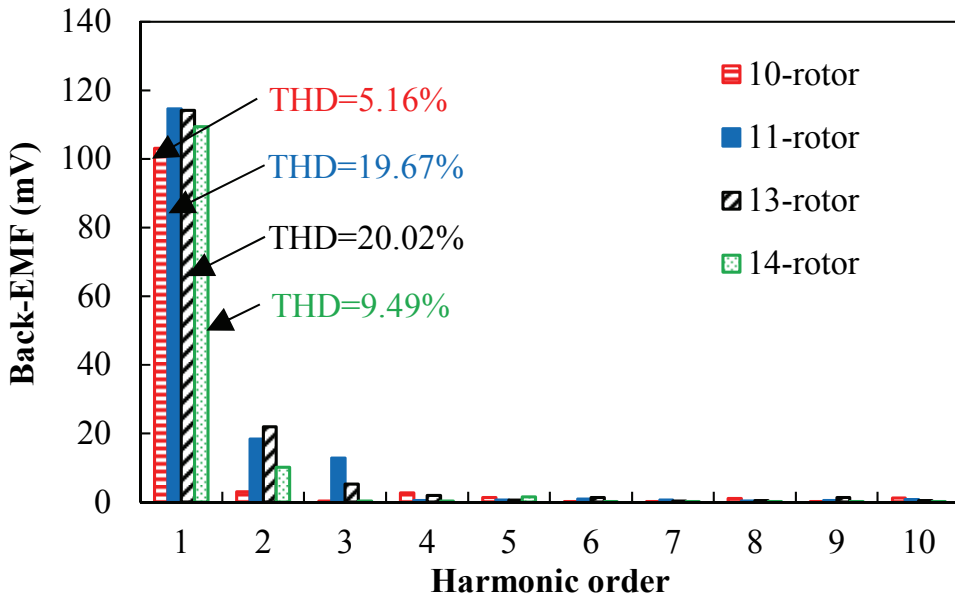


(d) 14-rotor

Fig. 7.10 Open-circuit field distributions of 12-stator-slot parallel PSHE machines with different rotor piece numbers at d -axis position ($\theta_e = 0^\circ$).



(a) Waveforms



(b) Spectra

Fig. 7.11 Open-circuit phase back-EMFs without FW excitation at 400 r/min (1 turn number per coil).

7.4.2 Cogging torque

The cogging torques without field current are compared in Fig. 7.12, in which the peak value of the 10-rotor machine is quite high. It should be mentioned that only the optimization for maximizing torque is carried out, and cogging torque suppression has not been considered. In addition, it can be found that the cogging torque cycle of the four parallel PSHE machines is

different from the corresponding conventional PM machines due to the distinct functions of the PM and FW poles.

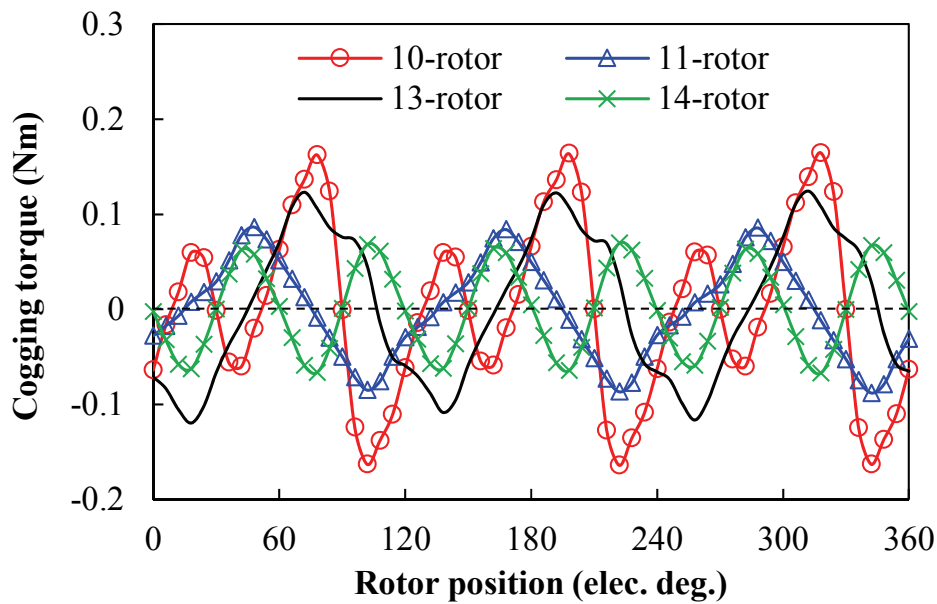
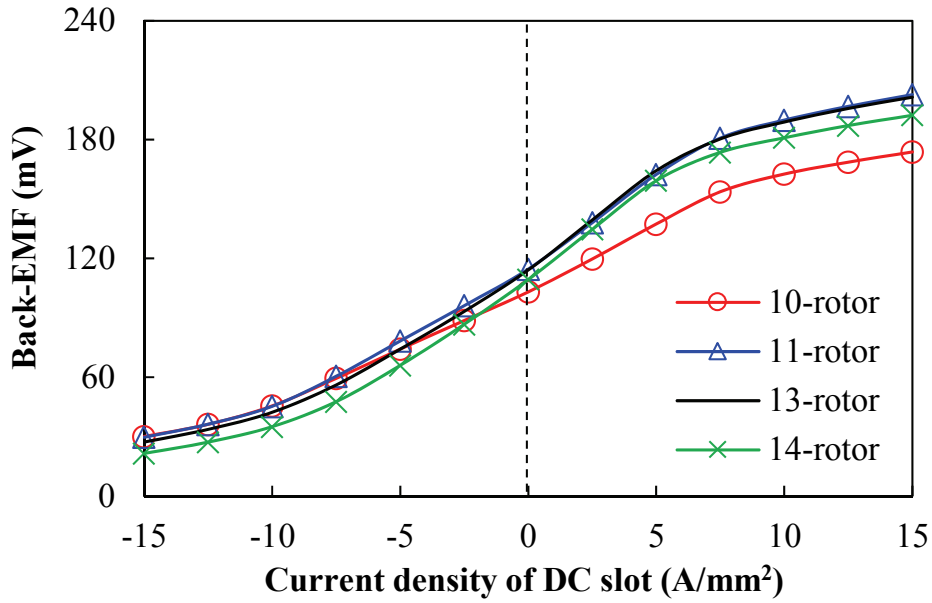


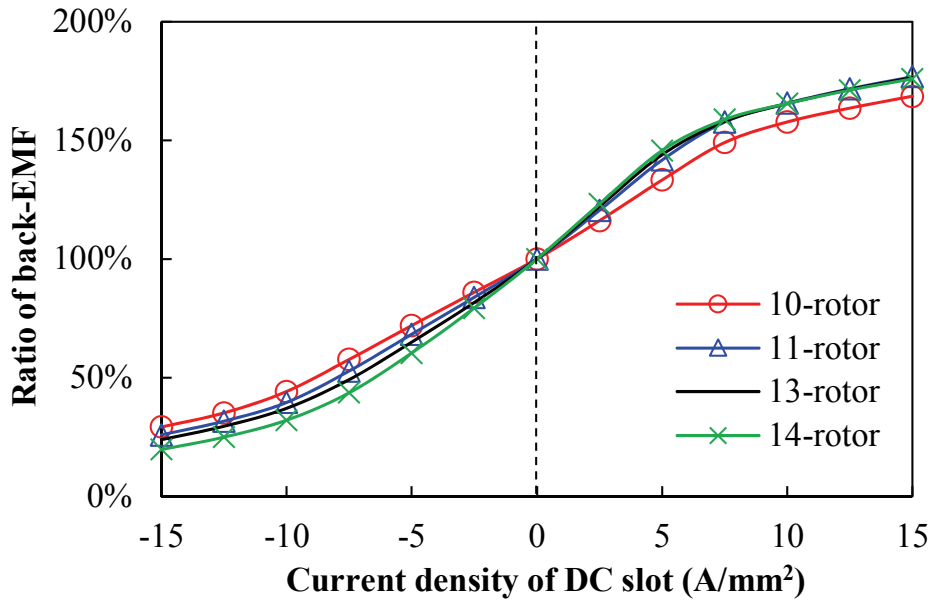
Fig. 7.12 Cogging torques without FW excitation.

7.4.3 Flux regulation capability

The excellent flux regulation capability is a crucial characteristic of the parallel PSHE machine. Fig. 7.13(a) illustrates the peak fundamental back-EMFs at 400 r/min with different field excitations, and the ratios of each back-EMF under different excitations to the back-EMF without field current are presented in Fig. 7.13(b). With 15A/mm^2 current density in the FW slots, the back-EMF can be regulated between approximately 25% and 175%. The 14-rotor machine has a relatively wider flux regulation range than the counterparts. It should be emphasized that the parallel PSHE machine can exhibit almost similar flux-enhancing and flux-weakening capabilities.



(a) Back-EMFs



(b) Ratio of back-EMFs

Fig. 7.13 Variations of peak fundamental phase back-EMFs at 400 r/min versus field excitations.

7.4.4 On-load torque

The high torque density is also essential when flux regulation capability is required. Without FW excitation, the torque waveforms with fixed 20W copper losses in armature windings and zero d -axis current control are presented in Fig. 7.14. The torque ripples are high in all machines due to the inherently high cogging torques and back-EMF harmonics. The torque ripple factor T_{ripple} can be defined as:

$$T_{ripple} = \frac{T_{max} - T_{min}}{T_{ave}} \quad (7.2)$$

where T_{max} , T_{min} , T_{ave} represent the maximum, minimum and average torques during one electrical period respectively. In fact, the torque ripple can be alleviated in the flux-enhancing operation due to the reduced harmonics while it will worsen in the flux-weakening conditions, as shown in Fig. 7.15(b). Meanwhile, the effect of field current on average torque is illustrated as well. With fixed 20W copper losses in armature windings, the average torques versus field excitations are shown in Fig. 7.15(a). The wide torque range is obtained, which corresponds to the back-EMF variations.

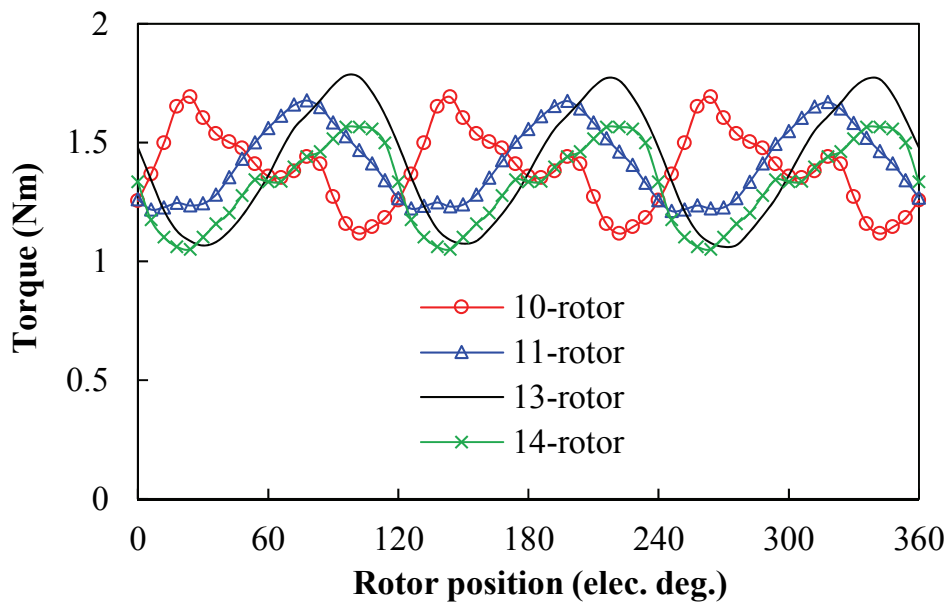
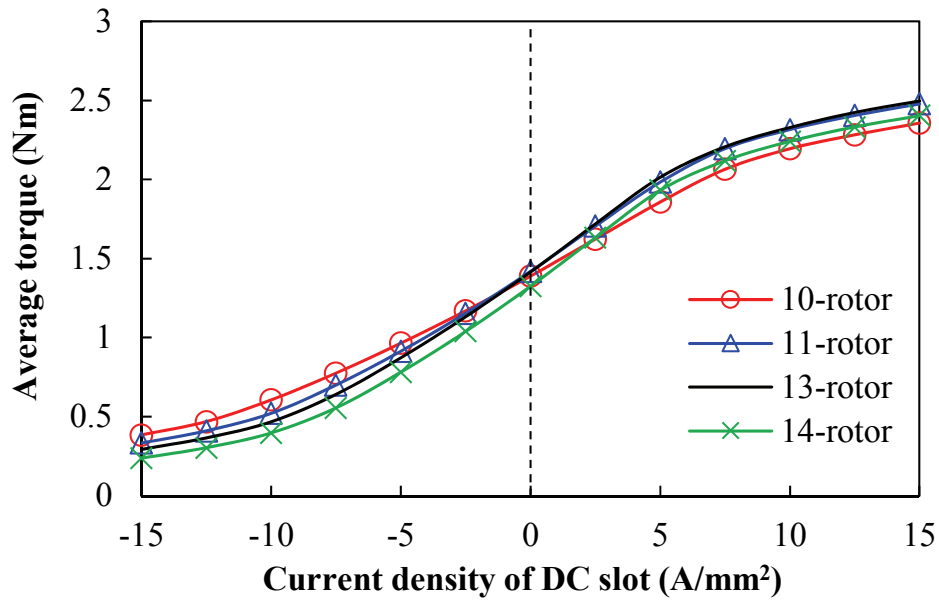
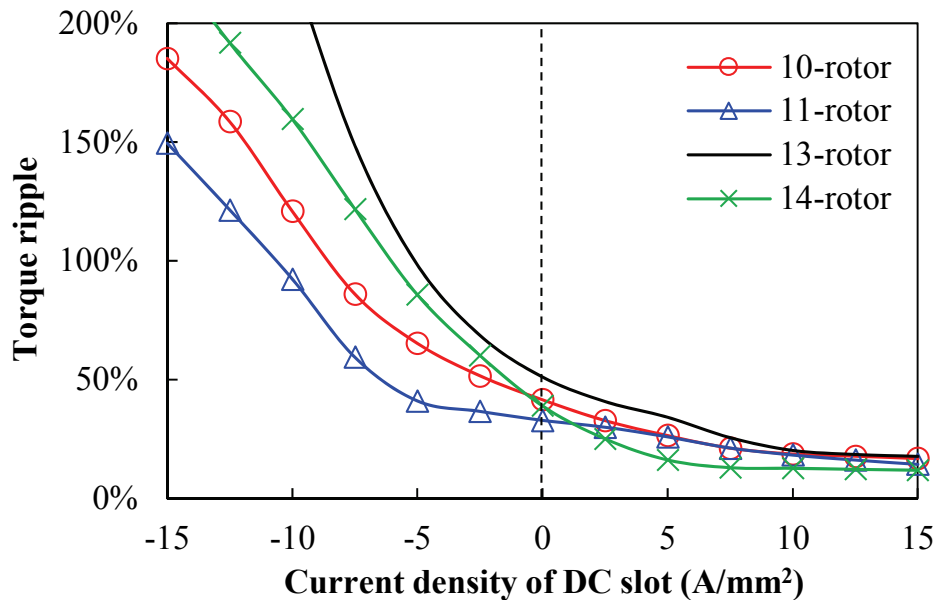


Fig. 7.14 Torque waveforms with 20W copper losses in armature windings and zero d -axis current control.



(a) Average torque



(b) Torque ripple

Fig. 7.15 Average torques and torque ripples versus field excitations under 20W copper losses in armature windings and zero d -axis current control.

Besides, with 20W armature winding copper losses, the variations of average torque against current advance angle (the phase angle between open-circuit back-EMF and armature current) are shown in Fig. 7.16. It is evident that the four parallel PSHE machines always achieve the highest torques when the current advance angle is equal to around 0° , indicating the negligible reluctance torque. Therefore the zero d -axis current control is required to perform high torque. Further, the average torques with different armature winding copper losses are compared in

Fig. 7.17, in which the 13-rotor parallel PSHE machine has the highest torque among the whole range.

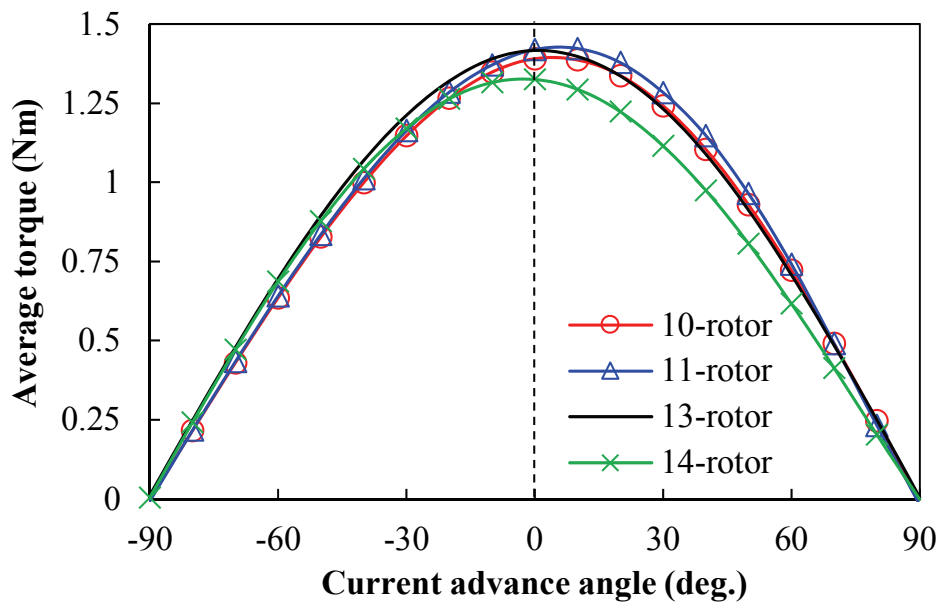


Fig. 7.16 Average torque against current angle (20W copper losses in armature windings).

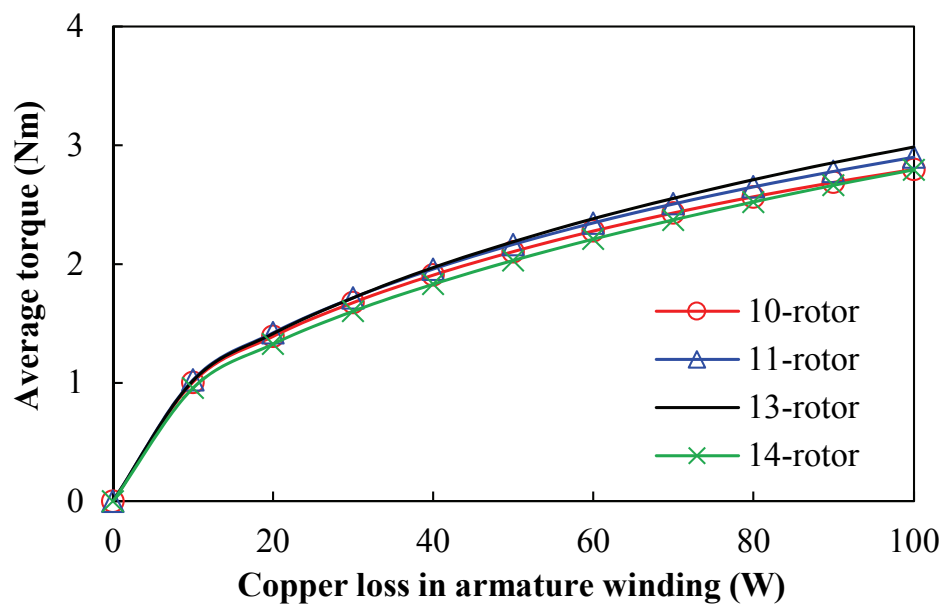
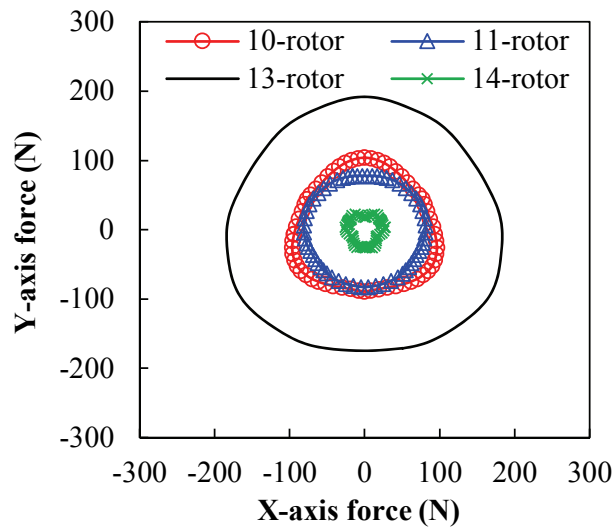


Fig. 7.17 Average torques versus copper losses in armature windings (zero d -axis current control).

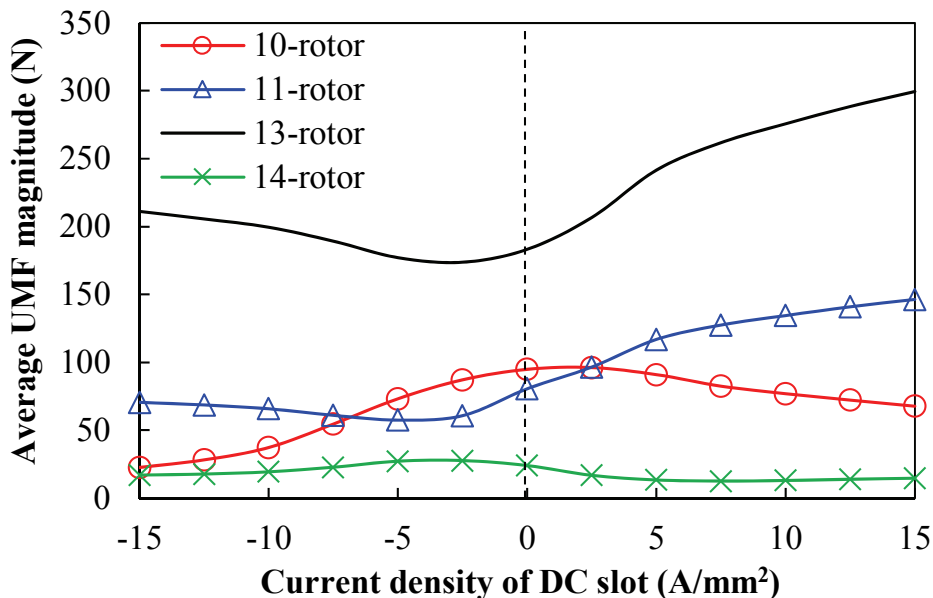
7.4.5 Unbalanced magnetic force

Fig. 7.18(a) and Fig. 7.19(a) illustrate the UMFs of the parallel PS-HESF machines with different rotor piece numbers, under open-circuit and on-load conditions respectively. The 13-rotor machine has the highest UMFs while the 14-rotor one has the lowest. It should be noted

that the UMFs not only occur in the parallel PSHE machines with odd rotor pole numbers (11- and 13-rotor), but also in the machines with even rotor pole numbers (10- and 14-rotor). This is due to the fact that the PM pole-pairs are alternately placed in the inner stator and their resultant force cannot be completely balanced. In addition, the average UMF magnitudes of the machines with different field excitations are illustrated in Fig. 7.18(b) and Fig. 7.19(b), in which 14-rotor machine always has the lowest UMFs. It should be emphasized that the UMFs in the parallel PS-HESF machines would be greatly relieved by multiplying both their stator slot and rotor piece numbers to obtain the balanced force distributions.

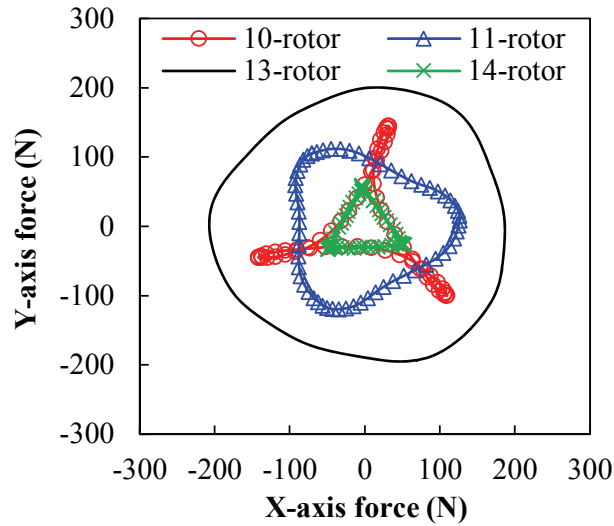


(a) UMF without FW excitation

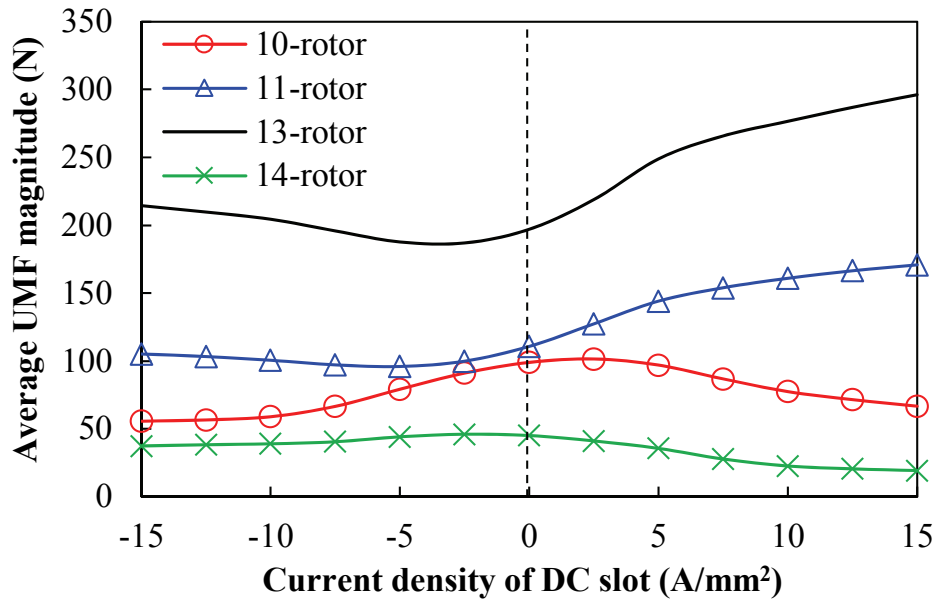


(b) Average UMF magnitudes with different field currents

Fig. 7.18 Open-circuit UMFs of 12-stator-slot parallel PSHE machines with different rotor pole numbers.



(a) UMF without FW excitation



(b) Average UMF magnitudes with different field currents

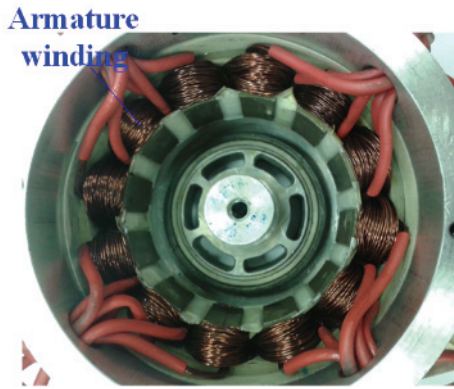
Fig. 7.19 On-load UMFs of 12-stator-slot parallel PSHE machines with different rotor pole numbers (20W copper losses in armature windings, zero d -axis current control).

7.5 Experimental Validation

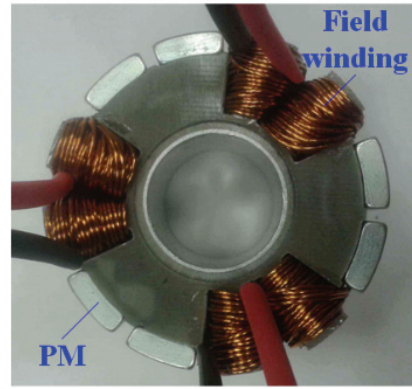
In order to validate the FE predictions, a 12-stator-slot/10-rotor-pole parallel PSHE prototype machine is manufactured. The basic design parameters are listed in Table 7.4. Fig. 7.20 illustrates the key components of the prototype machine, including an outer stator with armature windings, Fig. 7.20(a), an inner stator with PMs as well as FWs, Fig. 7.20(b), and a cup-shaped rotor, Fig. 7.20(c).

Table 7.4 Key design parameters of 12/10 parallel PSHE prototype machine.

Parameter	Value
Axial length	25 mm
R_{oso}	45 mm
R_{osy}	42 mm
R_{osi}	31.75 mm
β_{ost}	18°
g	0.5 mm
h_r	5 mm
β_{ro}	18°
β_{ri}	24°
R_{iso}	25.75 mm
R_{isy}	13.1 mm
R_{isi}	10.8 mm
β_{ist}	17°
h_{pm}	4 mm
β_{pm}	25.5°
Turn number per coil (armature winding)	18
Turn number per coil (field winding)	14



(a) Outer stator



(b) Inner stator



(c) Rotor



(d) Assembled stators

Fig. 7.20 Prototype of proposed 12/10 parallel PSHE machine.

The test is carried out based on this prototype. Fig. 7.21 shows the measured and 2-D FE-predicted phase back-EMFs at 400 r/min without FW excitation, in which the symmetrical waveforms can be observed and the good agreement between measured and FE-predicted results is obtained. There is an around 4.6% difference between the 2-D FE-predicted and test back-EMFs. Furthermore, the fundamental phase back-EMFs against field excitations are shown in Fig. 7.22. The measured results agree well with the FE predictions and the excellent flux regulation capability can be realized. Moreover, based on the test platform in Fig. 2.26, the static torques with different armature currents are tested and presented in Fig. 7.23. The difference between the FE and test results can be attributed to the end effect, the manufacturing tolerances and measuring tolerances discussed in section 2.6.

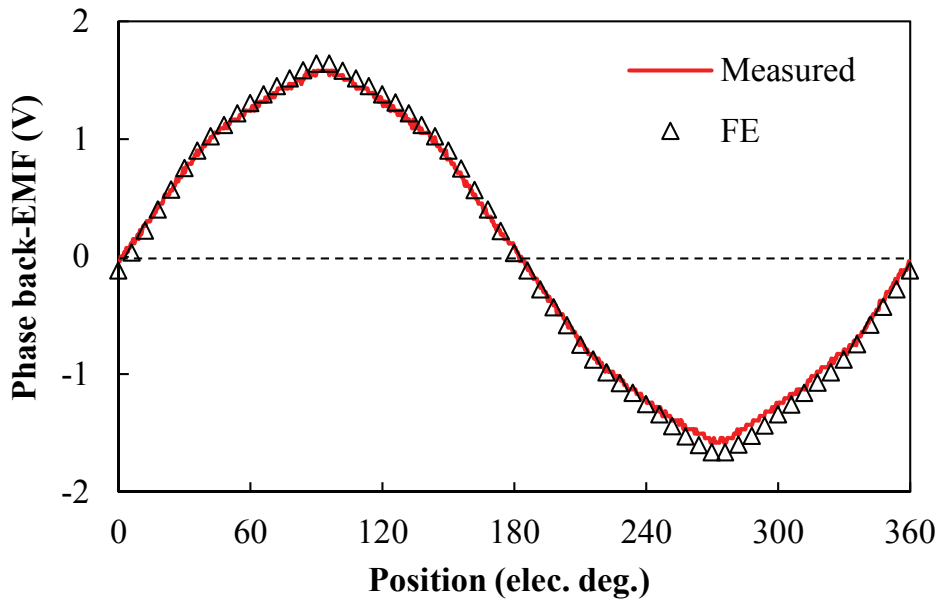


Fig. 7.21 Measured and 2-D FE-predicted phase back-EMF waveforms at 400 r/min without FW excitation.

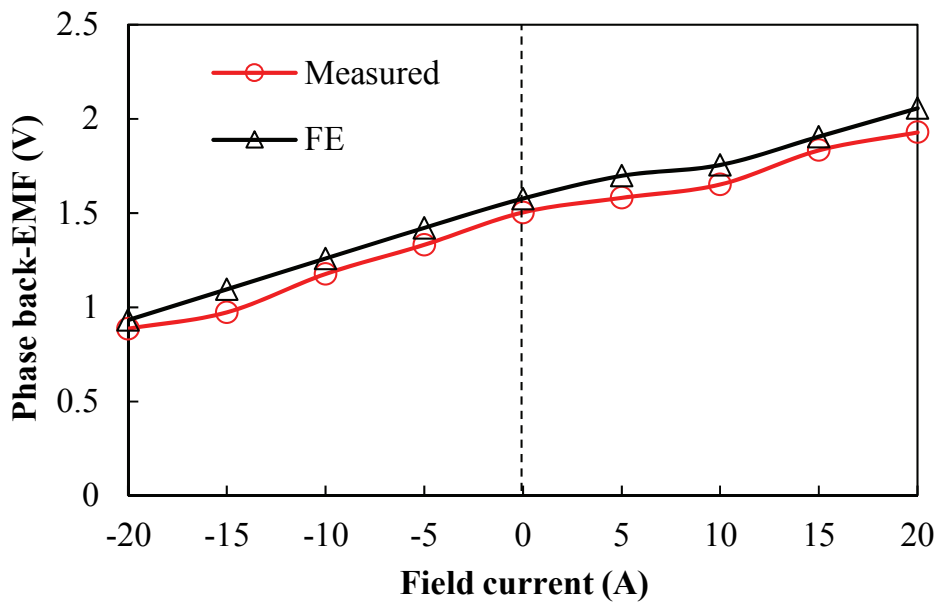


Fig. 7.22 Measured and 2-D FE-predicted fundamental phase back-EMFs at 400 r/min with different field excitations.

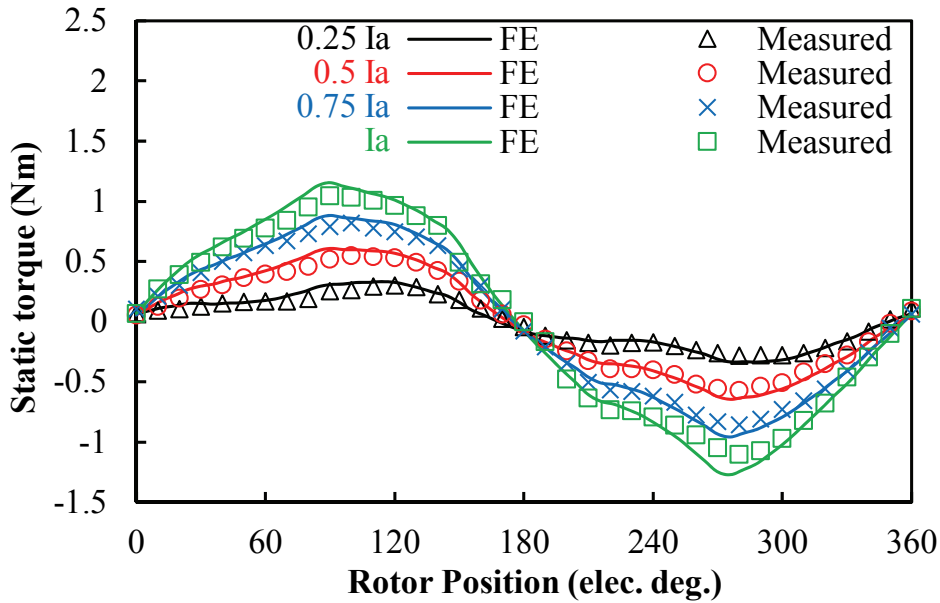


Fig. 7.23 Measured and 2-D FE-predicted static torque waveforms.

7.6 Conclusion

In this chapter, a novel parallel PSHE machine is proposed which features alternately arranged PM pole-pairs and FW pole-pairs on a stator, separated from the original stator having armature windings. The individual paths for PM flux and FW flux are realized, with which the flux regulation capability is enhanced. The operating principle and the rule to obtain symmetrical phase flux-linkage are illustrated, and the results reveal that the 12-stator-slot/10-rotor-pole and the 12-stator-slot/14-rotor-pole machines can inherently exhibit more symmetrical phase flux-linkage thanks to the cancellation of DC bias and harmonics. The parallel PSHE machines have excellent flux controllability due to the parallel magnetic paths, as well as high torque output due to the separated stators and, consequently, better space utilization. However, the back-EMF harmonics are significant in this machine as the excitation poles are not perfectly balanced, and thus the torque ripples are high.

Chapter 8. General Conclusions

8.1 Summary

In this thesis, the existing PS-SFPM and PS-FRPM machines characterised with enlarged available space and improved torque density, are analyzed, and they are proved to share the similar operating principle. Accordingly, the novel inner stators with different PM topologies are proposed to extend the family of PS machines. The comparative study shows that the spoke-shaped IPM inner stator has the highest torque thanks to the largest PM usage volume and flux-focusing, whilst the V-shaped IPM inner stator exhibits the highest torque per PM volume and I-shaped IPM inner stator features with the best flux-weakening potential. Moreover, the ferrite PM is applied to the PS-SFPM machine to take advantage of the enlarged available space and reduce the material cost.

Furthermore, the novel HE machines based on the PS principle are proposed and evaluated. They inherit the benefits of PS machines whilst improve the flux controllability and reduce the PM usage volume. By allocating an inner stator with FWs to the conventional SFPM machine, the DS-HESF machine is obtained, in which the PMs and FWs are placed in the two stators. Moreover, based on the PS-SFPM topology, the PS-HESF machine having both PMs and FWs in the inner stator is presented, in which the excitations and armature windings are separated. The comparison between the proposed machines and the corresponding conventional HESF machines implies that the proposed machines can exhibit not only higher torque output but also better flux controllability than the conventional counterparts.

In addition, a pair of novel PSHE machines originating from the PS-FRPM topology are presented, based on which the series and parallel connections between the PMs and FWs are obtained respectively. The rules of obtaining the symmetrical flux-linkages and back-EMFs in the proposed machines with different slot/pole combinations are identified. It is found that the series PSHE machines can exhibit higher torque output while the parallel PSHE machines benefit from better flux controllability.

8.2 Machine Topologies

A series of novel machine topologies are proposed in this thesis. They can greatly extend the family of PS machines and thus offer more potential candidates for different applications. The details of the proposed machine topologies are summarized in Table 8.1.

8.2.1 Developed sole PM PS machines

The PS-SFPM and PS-FRPM machines employ spoke-shaped IPM and SPM in the inner stators respectively. By replacing their inner stators with I-shaped and V-shaped IPM configurations, two novel PS machines, i.e. the PS-IPM-I and PS-IPM-V machines are obtained. As a result, the features of PS machines including enlarged available space as well as stationary PMs and coils are inherited, whilst more flexible PM arrangements are applicable to meet different requirements. The comparative results reveal that the spoke-shaped IPM inner stator (PS-SFPM machine) can contribute to the highest torque due to the largest PM usage volume, whereas the V-shaped IPM inner stator (PS-IPM-V machine) exhibits the highest torque per PM volume and the I-shaped IPM inner stator (PS-IPM-I machine) has the best flux-weakening potential.

Meanwhile, the ferrite PM can be applied to the PS-SFPM machine, where the material cost is reduced whilst the torque output is high due to the large PM usage volume. It is found that the optimized ferrite PS-SFPM machine can exhibit higher torque than the NdFeB counterpart when the material cost is fixed, which is preferred in the cost-sensitive applications. Moreover, the mechanical stress of the sandwiched rotor is checked, and the risk of irreversible demagnetization of the ferrite PM is evaluated.

8.2.2 DS-HESF machines

Based on the conventional SFPM machine, the DS-HESF machine is obtained by employing an additional inner stator equipped with concentrated non-overlapping FWs. The PMs and armature windings are still in the original outer stator, and the inner stator teeth are aligned with the outer stator slots. Consequently, the two excitation sources, i.e. PMs and FWs, are separated in the two stators. Compared with the conventional machine, the inner space is utilized to improve the machine performance. Meanwhile, since the outer stator of the DS-HESF machine is similar to the conventional SFPM machine, its PM usage volume is relatively high, which is good for torque output but may limit flux regulation.

8.2.3 PS-HESF machines

By reducing the PM length and allocating concentrated non-overlapping FWs to the inner stator of the PS-SFPM machine, the PS-HESF machine is obtained. As a result, the armature windings and excitation sources (both PMs and FWs) are separated in the two partitioned stators. Similar to the PS-SFPM machines, the slot/pole combinations are flexible in the PS-HESF machines. The PS-SFPM machines inherit the benefits of the PS-SFPM machines, and meanwhile, they also have additional flux controllability and reduced PM usage volume. It is found that the PM length factor as well as iron bridge thickness can significantly affect machine performance.

8.2.4 Series and Parallel PSHE machines

Based on the PS-FRPM machine having radially magnetized PMs in the inner stator, a pair of HE machines can be obtained by adding FWs in the inner stator. If one of every two adjacent PMs is removed and the FW is placed around the pole without PM, the series PSHE machine is obtained, in which the PM pole and FW pole are alternately allocated, and therefore, the PM and FW fluxes are connected in series. Alternatively, by removing two successive PMs (one PM pole-pair) in every four adjacent PMs (two PM pole-pairs), and allocating FWs around the poles without PM, the parallel PSHE machine is obtained, in which the PM pole-pair and FW pole-pair are alternately allocated in the inner stator. The parallel connection between the PM and FW fluxes is presented since they can flow independently. Furthermore, the effects of slot/pole combinations are investigated in these machines and the rules of obtaining symmetrical flux-linkages free from even order harmonics are identified.

Table 8.1 Summary of machine topologies.

Machines	Configurations	Features
Developed PS-PM (Chapter 2 Chapter 3)	<ul style="list-style-type: none"> • spoke-shaped IPM, I-shaped IPM, V-shaped IPM, SPM inner stator • NdFeB PM and ferrite PM • sandwiched rotor • armature windings in outer stator 	<ol style="list-style-type: none"> 1. Extended PM configurations 2. Characteristics of each PM topology (spoke-shaped IPM: highest torque V-shaped IPM: highest torque per PM I-shaped IPM: best flux-weakening) 3. Ferrite PM to reduce material cost 4. Mechanical stress check of rotor
DS-HESF (Chapter 4)	<ul style="list-style-type: none"> • additional stator with FWs • sandwiched rotor • conventional stator with tangential PMs and armature windings 	<ol style="list-style-type: none"> 1. Development from SFPM machine 2. Effects of slot/pole number combinations 3. Comparison with the conventional one 4. Hybridization ratio due to iron bridge 5. Relatively high PM volume
PS-HESF (Chapter 5)	<ul style="list-style-type: none"> • tangential PMs and FWs in inner stator • sandwiched rotor • armature windings in outer stator 	<ol style="list-style-type: none"> 1. Development from PS-SFPM machine 2. Effects of slot/pole number combinations 3. Comparison with the conventional one 4. Hybridization ratio due to iron bridge and PM length factor 5. Flexible PM/FW ratio
Series PSHE (Chapter 6)	<ul style="list-style-type: none"> • radial PMs and FWs alternately in inner stator • consequent-pole PMs • sandwiched rotor • armature windings in outer stator 	<ol style="list-style-type: none"> 1. Development from PS-FRPM machine 2. Effects of slot/pole number combinations, rule to obtain symmetrical flux-linkage 3. Consequent-pole to facilitate flux regulation
Parallel PSHE (Chapter 7)	<ul style="list-style-type: none"> • radial PMs and FWs in inner stator • alternately PM and FW pole-pairs • sandwiched rotor • armature windings in outer stator 	<ol style="list-style-type: none"> 1. Development from PS-FRPM machine 2. Effects of slot/pole number combinations, rule to obtain symmetrical flux-linkage 3. Enhanced flux regulation due to parallel connection

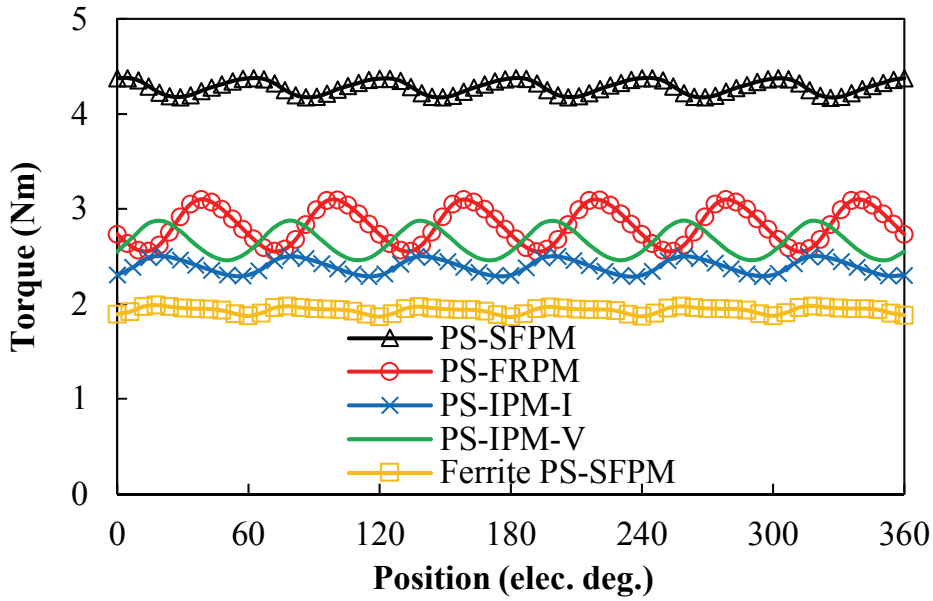
8.3 Performance Evaluation

8.3.1 Comparison of developed sole PM PS machines

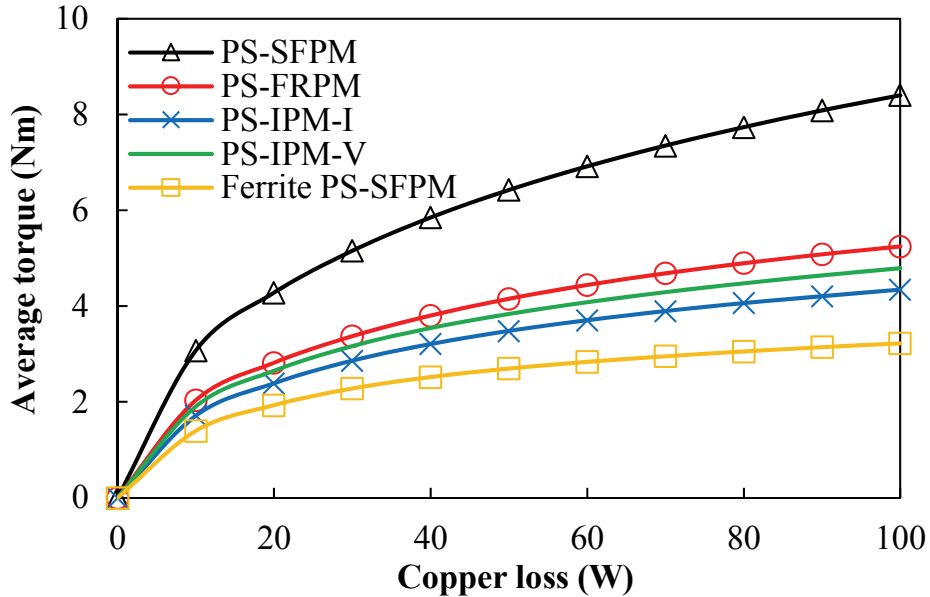
Fig. 8.1 shows the torque characteristics of the optimized PS-SFPM, PS-FRPM, PS-IPM-I, PS-IPM-V machines as well as the ferrite PS-SFPM machine, and the details are listed in Table 8.2. It can be seen that the PS-SFPM machine exhibits the highest average torque and the ferrite PS-SFPM machine has the lowest, while the torques of other three machines are comparable. Considering the PM usage volumes listed in Table 8.2, the PS-IPM-V machine benefits from the highest torque per PM volume. In addition, the flux-weakening potentials of the PS-IPM-I and ferrite PS-SFPM machines are attractive due to their relatively low PM flux. Meanwhile, the ferrite PS-SFPM machine has the lowest material cost since it is free from the expensive NdFeB material.

Table 8.2 Characteristics of developed sole PM PS machines.

	PS-SFPM	PS-FRPM	PS-IPM-I	PS-IPM-V	Ferrite PS-SFPM
PM volume ($\times 10^4$ mm ³)	2.45 (NdFeB)	1.34 (NdFeB)	1.28 (NdFeB)	1.14 (NdFeB)	2.99 (Ferrite)
Average torque (Nm)	4.28	2.82	2.39	2.65	1.93
Torque ripple (%)	4.76	19.43	8.87	15.77	6.44



(a) Torque waveforms with 20W copper losses and $I_d=0$ control



(b) Average torque versus copper loss with $I_d=0$ control

Fig. 8.1 Comparison of developed sole PM PS machines.

8.3.2 DS-HESF machines

The electromagnetic characteristics of the DS-HESF machines with different slot/pole combinations are listed in Table 8.3, accompanied with a corresponding conventional 10-rotor HESF machine as a baseline. It can be found that the DS-HESF machines always have wider flux regulation ranges as well as higher torques than the conventional one. Among the DS-HESF machines, the flux regulation ranges are similar, while the 13- and 14-rotor machines can exhibit higher torques than the counterparts.

Table 8.3 Characteristics of DS-HESF machines.

Rotor pole number	10-	11-	13-	14-	Conventional 10-
Flux range with 15A/mm ² DC	67%-118%	65%-119%	63%-121%	63%-119%	82%-116%
Average torque (Nm)	2.02	2.20	2.36	2.39	1.89
Torque ripple (%)	25.0	3.1	2.3	14.45	35

8.3.3 PS-HESF machines

The comparison details of the four PS-HESF machines and a conventional 10-rotor HESF machine are summarized in Table 8.4, which are based on the models with the fixed PM volume of $5 \times 10^3 \text{ mm}^3$. It can be seen that the PS-HESF machines have much wider flux regulation ranges than the conventional one, and the torque outputs are more than 20% higher. Moreover, the 13- and 14-rotor PS-HESF machines can exhibit wider flux regulation ranges than the 10- and 11-rotor counterpart, whilst the torques of the 11- and 13-rotor machines are higher due to the high winding factor.

Table 8.4 Characteristics of PS-HESF machines.

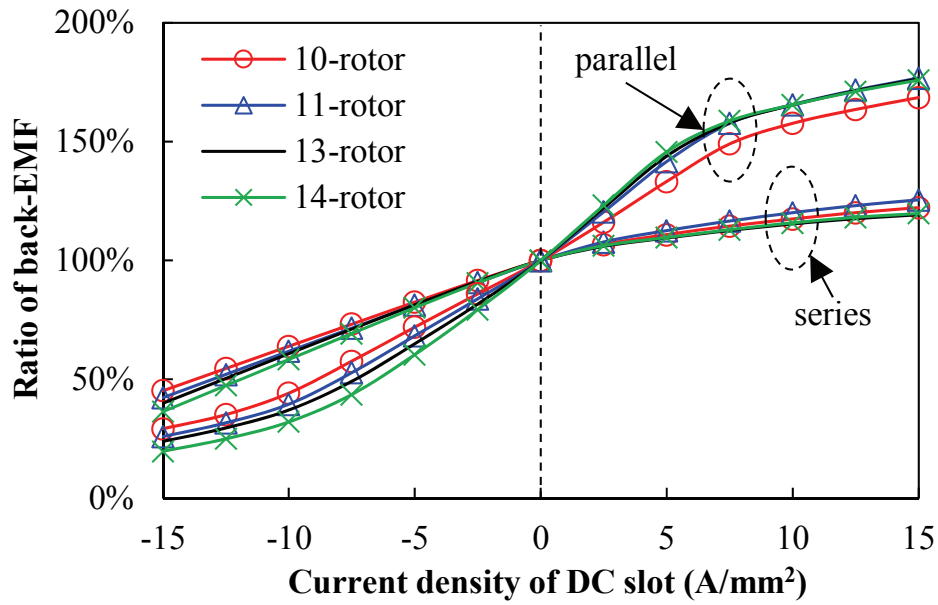
Rotor pole number	10-	11-	13-	14-	Conventional 10-
Flux range with 15A/mm ² DC	2%-175%	0-183%	0-190%	0-192%	72%-128%
Average torque (Nm)	1.37	1.41	1.40	1.33	1.14
Torque ripple (%)	12.5	2.9	2.3	11.0	14.7

8.3.4 Comparison of series and parallel PSHE machines

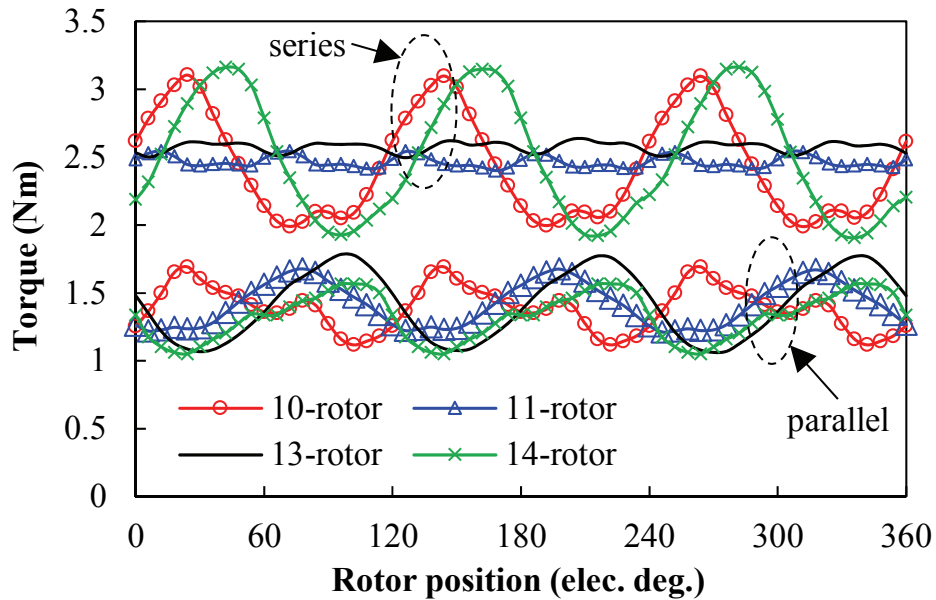
The comparison between the four series PSHE machines with different slot/pole number combinations and the four parallel PSHE machines is presented in Fig. 8.2 and the details are listed in Table 8.5. It can be concluded that the parallel PSHE machines exhibit wider flux regulation ranges than the series machines, which can be attributed to the reduced reluctance of the FW flux loop. The flux-enhancing is more challenging than the flux-weakening in all series HE machines due to the magnetic saturations. However, in the parallel PSHE machines, the capabilities of flux-enhancing and flux-weakening are quite similar thanks to the independent paths for the FW and PM fluxes. On the other hand, the series PSHE machines have higher torques than the parallel counterparts due to the higher open-circuit back-EMFs. Furthermore, the 11- and 13-rotor series PSHE machines can exhibit much lower torque ripples than the 10- and 14-rotor machines, while the torque ripples are always significant in the parallel machines.

Table 8.5 Characteristics of series and parallel PSHE machines.

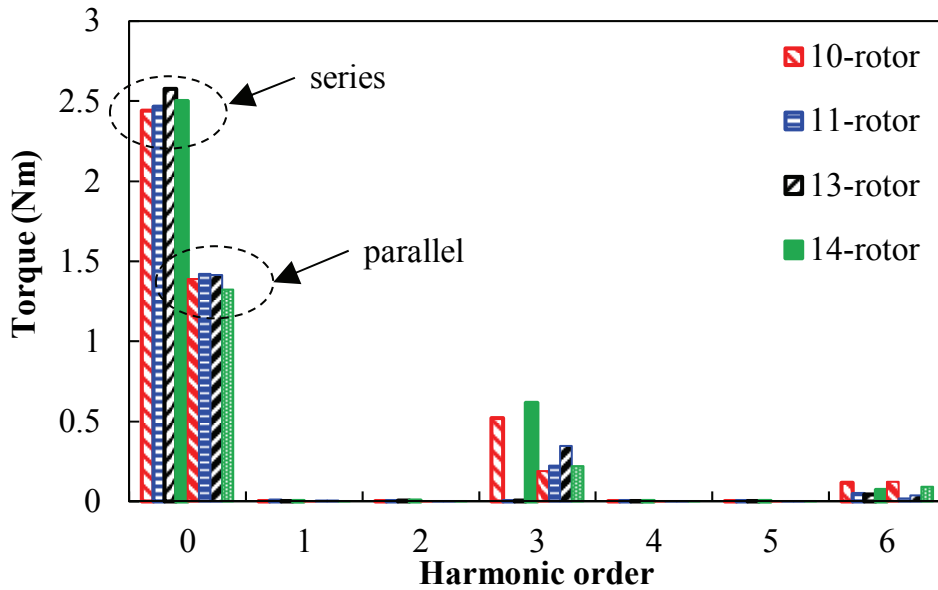
	Series				Parallel			
	10-	11-	13-	14-	10-	11-	13-	14-
Rotor pole number								
Flux range with 15A/mm ² DC	45%- 122%	42%- 126%	40%- 119%	39%- 119%	29%- 169%	26%- 177%	24%- 176%	20%- 176%
Average torque (Nm)	2.44	2.47	2.57	2.49	1.39	1.42	1.42	1.33
Torque ripple (%)	45.7	5.8	5.4	50.4	41.4	32.8	51.0	38.9



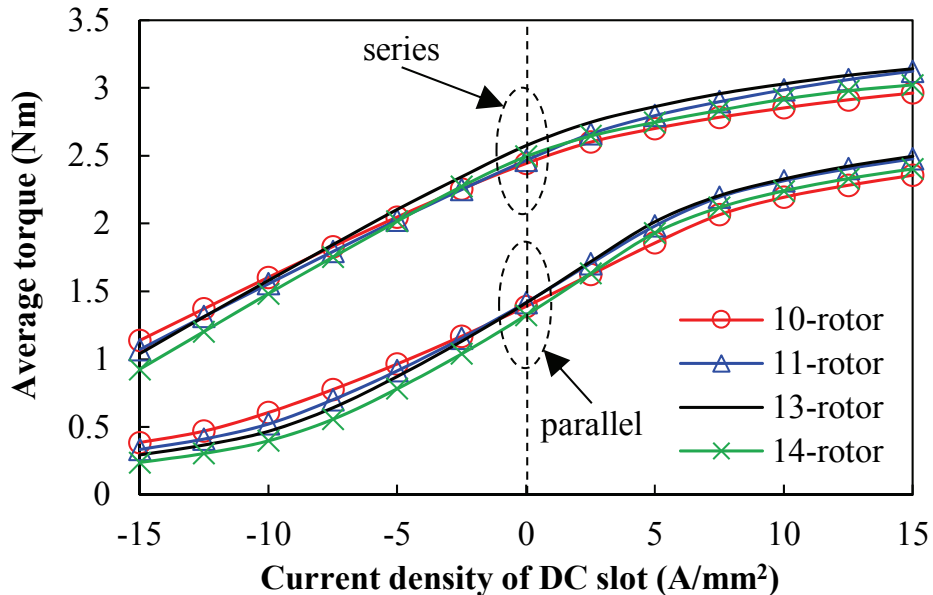
(a) Flux regulation versus field current



(b) Torque waveforms (20W copper loss in armature winding, $I_d=0$ control, no FW current)



(c) Spectra of torque (20W copper loss in armature winding, $I_d=0$ control, no FW current)



(d) Average torque versus field current (20W copper loss in armature windings, $I_d=0$ control)

Fig. 8.2 Comparison of series and parallel PSHE machines with different rotor pole numbers.

Moreover, the on-load UMFs of the series and parallel PSHE machines with different rotor pole numbers are compared in Fig. 8.3, and the characteristics of the DS-HESF and PS-HESF machines are also included. It can be found that the 10- and 14-rotor DS-HESF, PS-HESF, and series PSHE machines are all free from the UMFs, while the 10- and 14-rotor parallel PSHE machines still suffer the UMFs due to the inherent asymmetry. All the 11- and 13-rotor machines have UMFs due to their odd number of rotor pieces, in which 11-rotor DS-HESF machines has the highest UMFs, and the 11- and 13-rotor PS-HESF machines have lower UMFs than the counterparts.

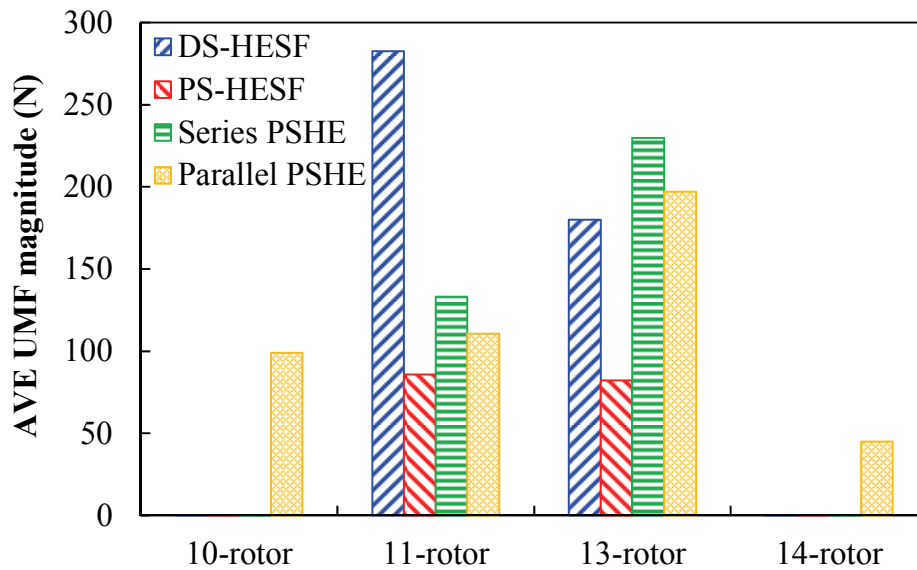


Fig. 8.3 Average on-load UMF magnitudes of the proposed PSHE machines with different rotor pole numbers.

Finally, in order to better illustrate the electromagnetic characteristics of the four PSHE machines investigated in this thesis, the graph shown in Fig. 8.4 is presented. The DS-HESF machine (Chapter 4) features with the relatively high torque output due to the large PM usage volume. The PS-HESF machine (Chapter 5) is characterized with the flexible design, in which the PM and FW usages can be adjusted flexibly, and its harmonics and torque ripples are inherently low. In addition, the series PSHE machine (Chapter 6) is a relatively compromising topology. The parallel PSHE machine (Chapter 7) has the best flux regulation capability, although it suffers significant harmonics and torque ripples.

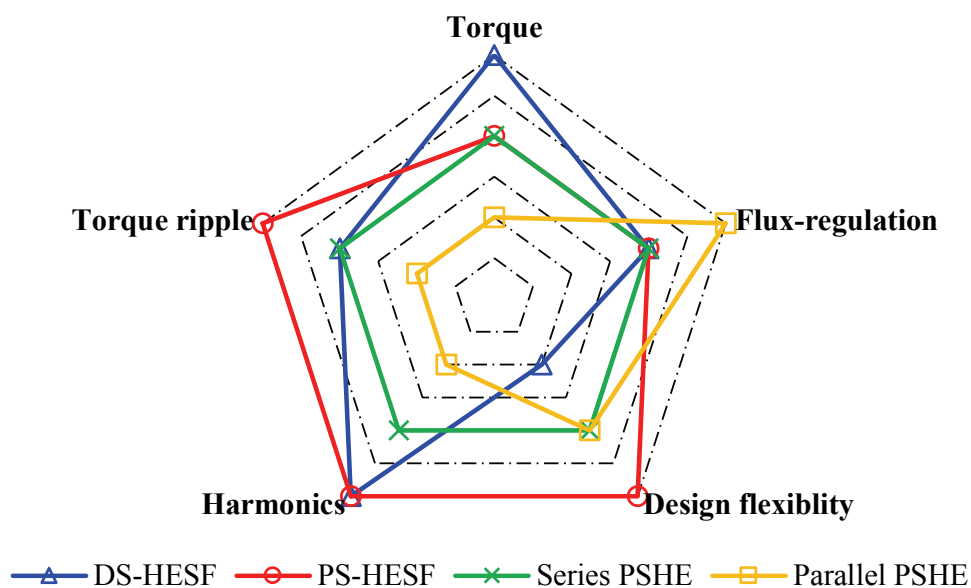


Fig. 8.4 Graph of characteristics of the four proposed PSHE machines.

8.4 Future Work

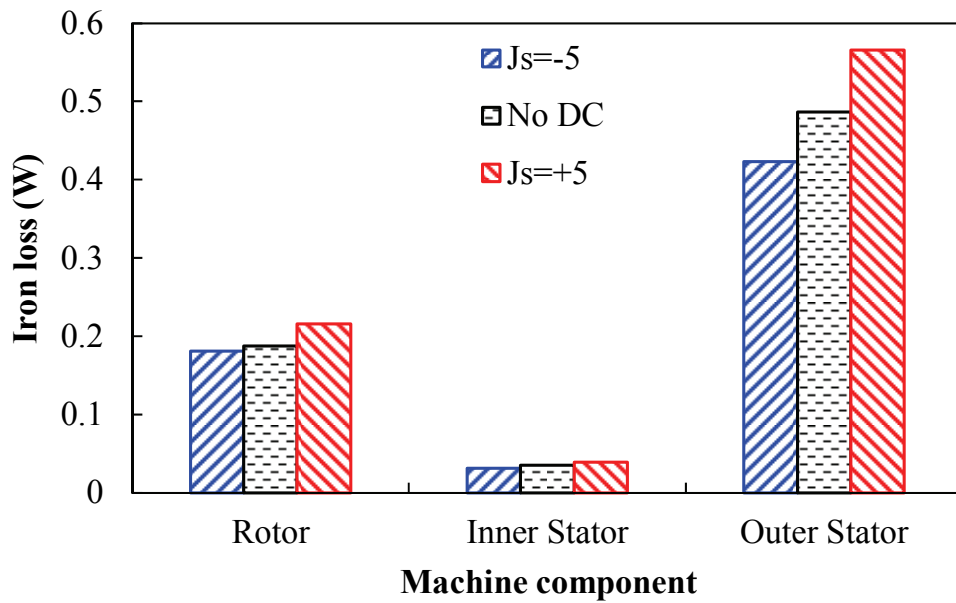
Following the research work in this thesis, the proposed future work, which are being carried out by other PhD students in the Electrical Machines and Drives Research Group at the University of Sheffield, includes:

8.4.1 Iron loss and efficiency

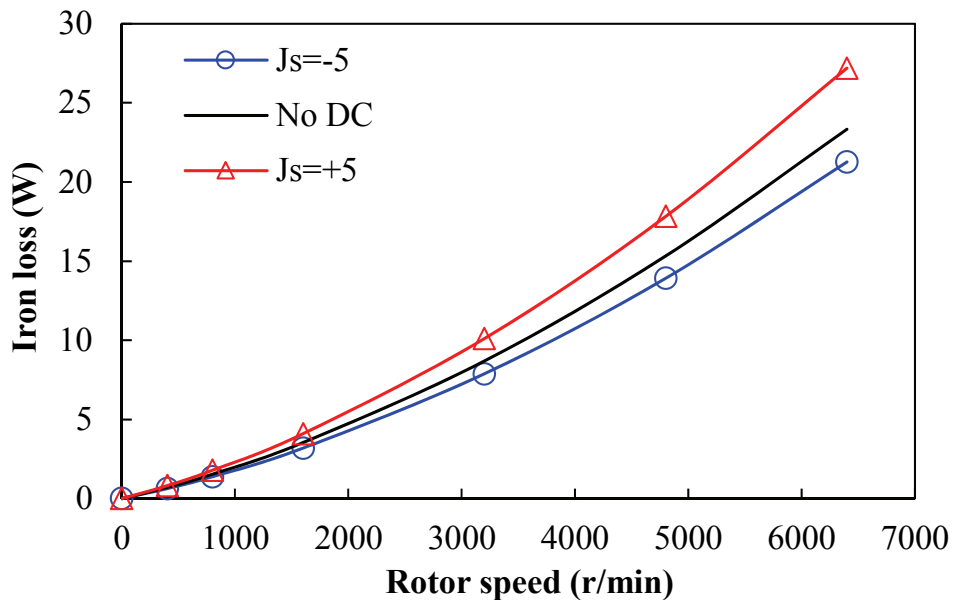
The high-speed system is an important application of the proposed HE machines, with which the benefits of the developed flux-weakening capabilities can be exerted. In addition, the rotor pole-pair number is relatively high in the proposed machines. Therefore, the operating frequency of the HE machines would be high and thus the iron loss would play an essential role in the machine performance.

The iron losses of the Prius-sized sole PM PS-SFPM machines are evaluated in section 3.4.2 and presented in Fig. 3.17. It can be seen that the iron losses of the PS-SFPM machines are higher than the conventional IPM machine due to their high operating frequency and significant flux variation on the rotor.

Moreover, the iron losses of the proposed PSHE machines are predicted as well. The parallel PSHE machines discussed in Chapter 7 are investigated as examples. Fig. 8.5(a) illustrates the on-load iron loss distributions of the 12/10 parallel PSHE machines with three typical FW conditions at speed of 400 r/min, in which 20W copper losses are applied in armature windings and zero d -axis current control is used. Three typical field excitations, viz. $-5\text{A}/\text{mm}^2$, no DC, and $+5\text{A}/\text{mm}^2$ current density on field winding slot are included. It can be found that the rotor and outer stator suffer more iron losses than the inner stator due to the more significant flux variations. Moreover, it is easy to find that the current amplitude in the FWs have an effect on the resultant iron loss, in which the negative currents in FWs can weaken the flux density in the laminations and thus reduce the iron losses. Meanwhile, the overall iron losses increase quickly as the speed increases, as shown in Fig. 8.5(b), and the iron loss would exceed the copper loss when the operation speed is higher than 6000 r/min.



(a) Iron losses on different major components at 400 r/min



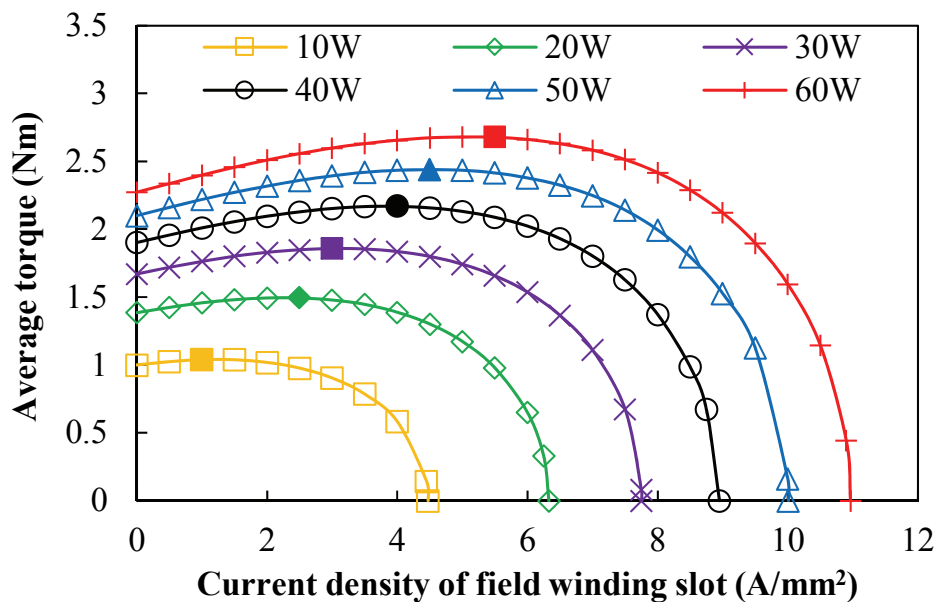
(b) Overall iron losses versus rotor speed

Fig. 8.5 On-load iron losses of the 12/10 parallel PSHE machine (Chapter 7) with different FW currents (fixed zero d -axis current control and 20W copper loss in armature windings).

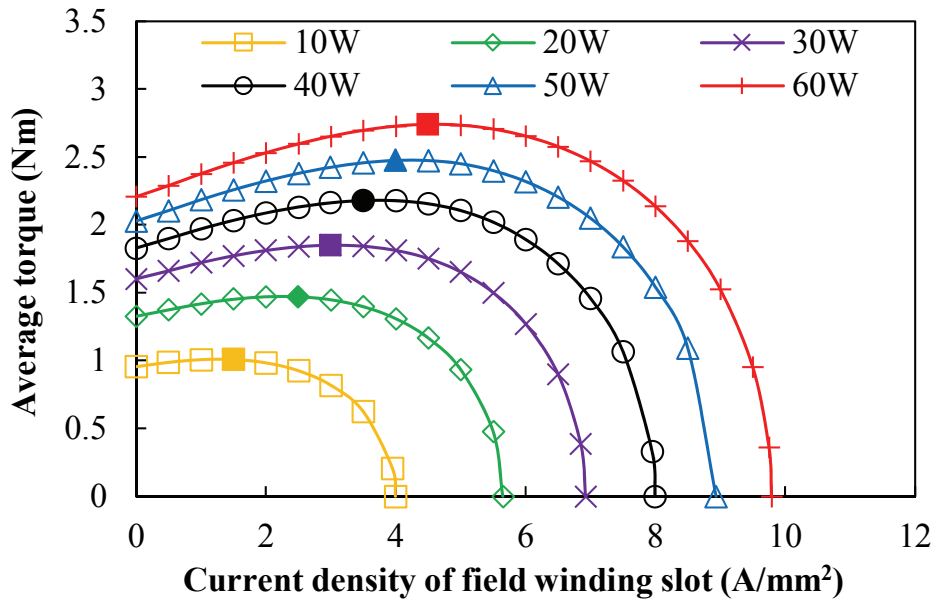
As a result, it can be found that the iron loss evaluation is important in the analysis of the PSHE machines. The possible methods to mitigate the flux variation on the rotor or reduce the operating frequency of the proposed machines should be carried out in the future, including the rotor shaping, halving the rotor pole number and etc..

8.4.2 Control strategies with optimizing field and armature currents

In HE machines, the field current in the FWs and the armature current in the armature windings can be combined flexibly to realize various operations, and thus a multitude of control strategies can be employed to obtain the optimum control [CAP15]. For instance, the parallel PSHE machines in Chapter 7 are investigated. Fig. 8.6 shows the average torque against current density in the FW slots with the constant value of overall copper losses (including copper losses both in FWs and armature windings), in which both the 12/10 and 12/14 structures are presented. The overall copper losses in armature windings and FWs are scanned from 10W to 60W, and it should be noted that the copper loss in the FWs is around 12.5W with the rated 5A/mm² current density on FW slots. The optimum current density in FW slots that contributes to the highest torque is identified in each overall copper loss, and the optimal value varies significantly. This implies that the combinations of field current and armature current should be optimized in the control of HE machines to produce the best performance.



(a) 12/10 parallel PSHE machine



(b) 12/14 parallel PSHE machine

Fig. 8.6 Average torque versus current density in FW slots of the 12/10 and 12/14 parallel PSHE machines (Chapter 7) under the condition that overall copper losses in FWs and armature windings are fixed (fixed zero d -axis current control).

8.4.3 Torque ripple suppression of the parallel PSHE machines

As shown in Fig. 7.12 and Fig. 7.14, the cogging torques and torque ripples are relatively significant in the proposed parallel PSHE machines, which degrade the machine performance. Therefore, the possible methods of alleviating the cogging torque and torque ripple are of importance and interest to be investigated in the future, including rotor shaping, skewing and etc..

8.4.4 Investigations of noise, vibration and stiffness of the PS machines

Due to the presence of the cup-rotor in the proposed PS machines, the mechanical robustness is a focus in the analysis of the PS machines. The fundamental evaluation of the mechanical stress of the rotor is shown in section 3.4.5. In order to comprehensively check the cup-rotor, the noise and vibration predictions should be carried out in the future. The potential techniques to reduce the torsion and radial force on the rotor should also be investigated.

References

- [AKE00] D.A. Akemakou, "Rotary electric machine, especially an alternator for a motor vehicle," U.S. Patent No. 6051904, 18 Apr. 2000.
- [AKE01] D.A. Akemakou, "Brushless polyphase machine in particular motor vehicle alternator," U.S. Patent No. US6242834, 5. Jun. 2001.
- [AMA01] Y. Amara, J. Lucidarme, M. Gabsi, M. Lecrivain, A. Ahmed, and A. Akemakou, "A new topology of hybrid synchronous machine," *IEEE Trans. Ind. Appl.*, vol. 37, no. 5, pp. 1273-1281, Sep./Oct. 2001.
- [AMA09] Y. Amara, L. Vido, M. Gabsi, E. Hoang, A. Ahmed, and M. Lecrivain, "Hybrid excitation synchronous machines: energy-efficient solution for vehicles propulsion," *IEEE Trans. Veh. Tech.*, vol. 58, no. 5, pp. 2137-2149, Jun. 2009.
- [AMA11] Y. Amara, S. Hlioui, R. Belfkira, G. Barakat, and M. Gabsi, "Comparison of open circuit flux control capability of a series double excitation machine and a parallel double excitation machine," *IEEE Trans. Veh. Tech.*, vol. 60, no. 9, pp. 4149-4207, Nov. 2011.
- [AWA16] C. Awah, Z.Q. Zhu, Z. Wu, H. Zhan, J. Shi, D. Wu, and X. Ge, "Comparison of partitioned stator switched flux permanent magnet machines having single- or double-layer windings," *IEEE Trans. Magn.*, vol. 52, no. 1, pp. 9500310, Jan. 2016.
- [BAI16] J. Bai, Y. Liu, C. Tong, Z. Song, and P. Zheng, "Investigation into a magnetic-field-modulated brushless double-rotor machine with the high-strength and low-loss modulating ring rotor," *IEEE Trans. Magn.*, vol. 52, no. 7, pp. 8105504, Jul. 2016.
- [BAR14] M. Barcaro and N. Bianchi, "Interior PM machines using ferrite to replace rare-earth surface PM machines," *IEEE Trans. Ind. Appl.*, vol. 50, no. 2, pp. 979-985, Mar./Apr. 2014.
- [BAR15] P. Barba, M. Bonislawski, R. Palka, P. Paplicki, and M. Wardach, "Design of hybrid excited synchronous machine for electrical vehicles," *IEEE Trans. Magn.*, vol. 51, no. 8, pp. 8107206, Aug. 2015.

- [BIA16] N. Bianchi and H. Mahmoud, "An analytical approach to design the PM in PMAREL motors robust toward the demagnetization," *IEEE Trans. Energy Convers.*, vol. 31, no. 2, pp. 800-809, Jun. 2016.
- [BIN06] A. Binder, T. Schneider, and M. Klohr, "Fixation of buried and surface-mounted magnets in high-speed permanent-magnet synchronous machines," *IEEE Trans. Ind. Appl.*, vol. 42, no. 4, pp. 1031-1037, Jul./Aug. 2006.
- [BOA15] B. Boazzo, A. Vagati, G. Pellegrino, E. Armando, and P. Guglielmi, "Multipolar ferrite-assisted synchronous reluctance machines: a general design approach," *IEEE Trans. Ind. Electron.*, vol. 62, no. 2, pp. 832-845, Feb. 2015.
- [BOL14] I. Boldea, L. Tutelea, L. Parsa, and D. Dorrell, "Automotive electric propulsion systems with reduced or no permanent magnets: an overview," *IEEE Trans. Ind. Electron.*, vol. 61, no. 10, pp. 5696-5711, Oct. 2014.
- [BOL99] I. Boldea, C.X. Wang, and S. Nasar, "Design of a three-phase flux reversal machine," *Elect. Mach. Power Syst.*, vol. 27, pp. 849-863, 1999.
- [BOU12] K. Boughrara, R. Ibtouen, and T. Lubin, "Analytical prediction of magnetic field in parallel double excitation and spoke-type permanent magnet machines accounting for tooth-tips and shape of polar pieces," *IEEE Trans. Magn.*, vol. 48, no. 7, pp. 2121-2137, Jul. 2012.
- [CAI14] H. Cai, B. Guan, and L. Xu, "Low-cost ferrite PM-assisted synchronous reluctance machine for electric vehicles," *IEEE Trans. Ind. Electron.*, vol. 61, no. 10, pp. 5741-5748, Oct. 2014.
- [CAO12] R. Cao, C. Mi, and M. Cheng, "Quantitative comparison of flux-switching permanent-magnet motors with interior permanent magnet motor for EV, HEV and PHEV applications," *IEEE Trans. Magn.*, vol. 48, no. 8, pp. 2374-2384, Aug. 2012.
- [CAP15] F. Capponi, G. Borocci, G. Donato, and F. Caricchi, "Flux regulation strategies for hybrid excitation synchronous machines," *IEEE Trans. Ind. Appl.*, vol. 51, no. 5, pp. 3838-3847, Sep./Oct. 2015.
- [CHA03] K.T. Chau, J. Jiang, and Y. Wang, "A novel stator doubly fed doubly salient permanent magnet brushless machine," *IEEE Trans. Magn.*, vol. 39, no. 5, pp. 3001-3003, Sep. 2003.

- [CHA06a] K.T. Chau, Y. Li, J. Jiang, and S. Niu, "Design and control of a PM brushless hybrid generator for wind power application," *IEEE Trans. Magn.*, vol. 42, no. 10, pp. 3497-3499, Oct. 2006.
- [CHA06b] K.T. Chau, Y. Li, J. Jiang, and C. Liu, "Design and analysis of a stator-doubly-fed doubly-salient permanent-magnet machine for automotive engines," *IEEE Trans. Magn.*, vol. 42, no. 10, pp. 3470-3473, Oct. 2006.
- [CHA08] K.T. Chau, C.C. Chan, and C. Liu, "Overview of permanent-magnet brushless drives for electric and hybrid electric vehicles," *IEEE Trans. Ind. Electron.*, vol. 55, no. 6, pp. 2246-2257, Jun. 2008.
- [CHA96] C.C. Chan, K.T. Chau, J. Jiang, W. Xia, M. Zhu, and R. Zhang, "Novel permanent magnet motor drives for electric vehicles," *IEEE Trans. Ind. Electron.*, vol. 43, no. 2, pp. 331-339, Apr. 1996.
- [CHE00] M. Cheng, K.T. Chau, C.C. Chan, E. Zhou, and X. Huang, "Nonlinear varying-network magnetic circuit analysis for doubly salient permanent-magnet motors," *IEEE Trans. Magn.*, vol. 36, no. 1, pp. 339-348, Jan. 2000.
- [CHE10a] J.T. Chen, and Z.Q. Zhu, "Influence of the rotor pole number on optimal parameters in flux-switching PM brushless AC machines by the lumped-parameter magnetic circuit model," *IEEE Trans. Ind. Appl.*, vol. 46, no. 4, pp. 1381-1388, Jul./Aug. 2010.
- [CHE10b] J.T. Chen, and Z.Q. Zhu, "Winding configurations and optimal stator and rotor pole combination of flux-switching PM brushless AC machines," *IEEE Trans. Energy Convers.*, vol. 25, no. 2, pp. 293-302, Jun. 2010.
- [CHE10c] J.T. Chen, and Z.Q. Zhu, "Comparison of all- and alternate-poles-wound flux-switching PM machines having different stator and rotor pole numbers," *IEEE Trans. Ind. Appl.*, vol. 46, no. 4, pp. 1406-1415, Jul./Aug. 2010.
- [CHE11a] Z. Chen, and N. Zhou, "Flux regulation ability of a hybrid excitation doubly salient machine," *IET Proc. Electr. Power Appl.*, vol. 5, no. 2, pp. 224-229, Feb. 2011.
- [CHE11b] J.T. Chen, Z.Q. Zhu, S. Iwasaki, and R. Deodhar, "A novel hybrid-excited switched-flux brushless AC machine for EV/HEV applications," *IEEE Trans. Veh. Tech.*, vol. 60, no. 4, pp. 1365-1373, May, 2011.

- [CHE11c] M. Cheng, W. Hua, J. Zhang, and W. Zhao, "Overview of stator-permanent magnet brushless machines," *IEEE Trans. Ind. Electron.*, vol. 58, no. 11, pp. 5087-5101, Nov. 2011.
- [CHE11d] J.T. Chen, Z.Q. Zhu, S. Iwasaki, and R. Deodhar, "Influence of slot opening on optimal stator and rotor pole combination and electromagnetic performance of switched-flux PM brushless AC machines," *IEEE Trans. Ind. Appl.*, vol. 47, no. 4, pp. 1681-1691, Jul./Aug. 2011.
- [CHE11e] J.T. Chen, Z.Q. Zhu, S. Iwasaki, and R. Deodhar, "A novel E-core switched-flux PM brushless AC machine," *IEEE Trans. Ind. Appl.*, vol. 47, no. 3, pp. 1273-1282, May/Jun. 2011.
- [CHE14] Z. Chen, B. Wang, Z. Chen, and Y. Yan, "Comparison of flux regulation ability of the hybrid excitation doubly salient machines," *IEEE Trans. Ind. Electron.*, vol. 61, no. 7, pp. 3155-3166, Jul. 2014.
- [DEO97] R. Deodhar, S. Andersson, I. Boldea, and T.J. Miller, "The flux-reversal machine: a new brushless doubly-salient permanent-magnet machine," *IEEE Trans. Ind. Appl.*, vol. 33, no. 4, pp. 925—34, Jul./Au. 1997.
- [DOR12] D. Dorrell, H. Min, and A. Knight, "Alternative rotor designs for high performance brushless permanent magnet machines for hybrid electric vehicles," *IEEE Trans. Magn.*, vol. 48, no. 2, pp. 835-838. Feb. 2012.
- [DUP16] A. Dupas, S. Hlioui, E. Hoang, M. Gabsi, and M. Lecrivain, "Investigation of a new topology of hybrid-excited flux-switching machine with static global winding: experiments and modelling," *IEEE Trans. Ind. Appl.*, vol. 52, no. 2, pp. 1413-1421, Mar./Apr. 2016.
- [EVA10] D. Evans, Z. Azar, L.J. Wu, and Z.Q. Zhu, "Comparison of optimal design and performance of PM machines having non-overlapping windings and different rotor topologies," in *Proc. 5th IET Int. Conf. Power Electronics, Machines and Drives (PEMD)*, Brighton, UK, Apr. 19-21, 2010, pp. 1-7.
- [EVA15] D. Evans and Z.Q. Zhu, "Novel partitioned stator switched flux permanent magnet machines," *IEEE Trans. Magn.*, vol. 51, no. 1, pp. 8100114, Jan. 2015.

- [FAS14] A. Fasolo, L. Alberti, and N. Bianchi, "Performance comparison between switching-flux and IPM machines with rare-earth and ferrite PMs," *IEEE Trans. Ind. Appl.*, vol. 50, no. 6, pp. 3708-3716, Nov./Dec. 2014.
- [FAS14] A. Fasolo, L. Alberti, and N. Bianchi, "Performance comparison between switching-flux and IPM machines with rare-earth and ferrite PMs," *IEEE Trans. Ind. Appl.*, vol. 50, no. 6, pp. 3708-3716, Nov./Dec. 2014.
- [FIN08] T. Finken, and K. Hameyer, "Study of hybrid excited synchronous alternators for automotive applications using coupled FE and circuit simulations," *IEEE Trans. Magn.*, vol. 44, no. 6, pp. 1598-1601, Jun. 2008.
- [FOD07] D. Fodorean, A. Djerdir, I. Vioreal, and A. Miraoui, "A double excited synchronous machine for direct drive application-design and prototype tests," *IEEE Trans. Energy Convers.*, vol. 22, no. 3, pp. 656-665, Sep. 2007.
- [FRE91] W. Freise, "Heteropolar excited synchronous machine," U.S. Patent No. US5051640, Sep. 24, 1991.
- [GAL15] S. Galioto, P. Reddy, A. El-Refaie, and J. Alexander, "Effect of magnet types on performance of high-speed spoke interior-permanent-magnet machines designed for traction applications," *IEEE Trans. Ind. Appl.*, vol. 51, no. 3, pp. 2148-2160, May/Jun. 2015.
- [GAO16a] Y. Gao, R. Qu, D. Li, J. Li, and L. Wu, "Design of three-phase flux reversal machines with fractional-slot windings," *IEEE Trans. Ind. Appl.*, vol. 52, no. 4, pp. 2856-2864, Jul./Aug. 2016.
- [GAO16b] Y. Gao, R. Qu, D. Li, J. Li, and G. Zhou, "Consequent-pole flux-reversal permanent-magnet machine for electric vehicle propulsion," *IEEE Trans. Appl. Supercond.*, vol. 26, no. 4, pp. 5200105, Jun. 2016.
- [GAU14] B. Gaussens, E. Hoang, M. Lecrivain, P. Manfe, and M. Gabsi, "A hybrid-excited flux-switching machine for high-speed DC-alternator applications," *IEEE Trans. Ind. Electron.*, vol. 61, no. 6, pp. 2976-2989, Jun. 2014.
- [GEN15] W. Geng, Z. Zhang, K. Jiang, and Y. Yan, "A new parallel hybrid excitation machine: permanent-magnet /variable-reluctance machine with bidirectional field-regulation capability," *IEEE Trans. Ind. Electron.*, vol. 62, no. 3, pp. 1372-1381, Mar. 2015.

- [HEN94] G. Henneberger, J.R. Hadji-Minaglou, and R.C. Ciorba, "Design and test of permanent magnet synchronous motor with auxiliary excitation winding for electric vehicle application," in *Proc. Euro. Power Electron. Chap. Symp.*, Lausanne, Switzerland, pp. 645-649, Oct. 1994.
- [HOA07] E. Hoang, M. Lecrivain, and M. Gabsi, "A new structure of a switching flux synchronous polyphased machine with hybrid excitation," in *Proc. Euro. Conf. Power Electron. Applicat.*, 2-5 Sep. 2007, pp. 1-8.
- [HOA17] K. Hoang, L. Vido, M. Gabsi, and F. Gillon, "Flux control range broadening and torque ripple minimization of a double excitation synchronous motor," *IEEE Trans. Magn.*, vol. 53, no. 1, pp. 8100510, Jan. 2017.
- [HOA97] E. Hoang, H. Ahmed, and J. Lucidarme, "Switching flux permanent magnet polyphased synchronous machines," in *Proc. Eur. Conf. Power Electron. Applicat. (EPE)*, Trondheim, Norway, 1997, vol. 3, pp. 903-908.
- [HUA05] W. Hua, Z.Q. Zhu, M. Cheng, Y. Pang, and D. Howe, "Comparison of flux-switching and doubly-salient permanent magnet brushless machines," in *Proc. Inter. Conf. Electr. Mach. Sys. (ICEMS)*, vol. 1, pp. 165-170, Sep. 27-29, 2005.
- [HUA08] W. Hua, M. Cheng, Z.Q. Zhu, and D. Howe, "Analysis and optimization of back EMF waveform of a flux-switching permanent magnet motor," *IEEE Trans. Energy Convers.*, vol. 23, no. 3, pp. 727-733, Sep. 2008.
- [HUA09] W. Hua, M. Cheng, and G. Zhang, "A novel hybrid excitation flux-switching motor for hybrid vehicles," *IEEE Trans. Magn.*, vol. 45, no. 10, pp. 4728-4731, Oct. 2009.
- [HUA14] W. Hua, X. Yin, G. Zhang, and M. Cheng, "Analysis of two novel five-phase hybrid-excitation flux-switching machines for electric vehicles," *IEEE Trans. Magn.*, vol. 50, no. 1, pp. 8700305, Nov. 2014.
- [HUA15] W. Hua, G. Zhang, and M. Cheng, "Flux-regulation theories and principles of hybrid-excited flux-switching machines," *IEEE Trans. Ind. Electron.*, vol. 62, no. 9, pp. 5359-5369, Sep. 2015.
- [JAH86] T.M. Jahns, G. Kliman, and T. Neumann, "Interior permanent-magnet synchronous motors for adjustable-speed drives," *IEEE Trans. Ind. Appl.*, vol. IA-22, no. 4, pp. 738-747, Jul./Aug. 1986.

- [KAM12] K. Kamiev, J. Nerg, J. Pyrhonen, V. Zaboin, V. Hrabovcova, and P. Rafajdus, "Hybrid excitation synchronous generators for island operation," *IET Proc. Electr. Power Appl.*, vol. 6, no. 1, pp. 1-11, Jan. 2012.
- [KAM13] K. Kamiev, J. Pryhonen, J. Nerg, V. Zaboin, and J. Tapia, "Modeling and testing of an armature-reaction compensated (PM) synchronous generator," *IEEE Trans. Energy Convers.*, vol. 28, no. 4, pp. 849-859, Dec. 2013.
- [KAM14] K. Kamiev, J. Nerg, J. Pyrhonen, V. Zaboin, and J. Tapia, "Feasibility of an armature-reaction-compensated permanent magnet synchronous generator in island operation," *IEEE Trans. Ind. Electron.*, vol. 61, no. 9, pp. 5075-5085, Sep. 2014.
- [KAM14] K. Kamiev, J. Nerg, J. Pyrhonen, V. Zaboin, and J. Tapia, "Feasibility of an armature-reaction-compensated permanent magnet synchronous generator in island operation," *IEEE Trans. Ind. Electron.*, vol. 61, no. 9, pp. 5075-5085, Sep. 2014.
- [KIM04] T. Kim, and J. Lee, "A study of the design for the flux reversal machine," *IEEE Trans. Magn.*, vol. 40, no. 4, pp. 2053-2055, Jul. 2004.
- [KIM05a] T. Kim, S. Won, K. Bong, and J. Lee, "Reduction of cogging torque in flux-reversal machine by rotor teeth pairing," *IEEE Trans. Magn.*, vol. 41, no. 10, pp. 3964-3966, Oct. 2005.
- [KIM05b] Y. Kim, T. Kim, Y. Kim, W. O, and J. Lee, "Various design techniques to reduce cogging torque in flux-reversal machines," in *Proc. Inter. Conf. Electr. Mach. Sys. (ICEMS)*, Sep. 27-29, 2005, pp. 261-263.
- [KIM16a] D. Kim, H. Hwang, S. Bae, and C. Lee, "Analysis and design of a double-stator flux-switching permanent magnet machine using ferrite magnet in hybrid electric vehicles," *IEEE Trans. Magn.*, vol. 52, no. 7, pp. 8106604, Jul. 2016.
- [KIM16b] M. Kimiabeigi, J. Widmer, R. Long, Y. Gao, J. Goss, R. Martin, T. Lisle, J. Vizan, A. Michaelides, and B. Mecrow, "High-performance low-cost electric motor for electric vehicles using ferrite magnets," *IEEE Trans. Ind. Electron.*, vol. 63, no. 1, pp. 113-122, Jan. 2016.

- [KOS10] T. Kosaka, M. Sridharbabu, M. Yamamoto, and N. Matsui, "Design studies on hybrid excitation motor for spindle drive in machine tools," *IEEE Trans. Ind. Electron.*, vol. 57, no. 11, pp. 3807-3013, Nov. 2010.
- [LAL15] O. Laldin, S. Sudhoff, and S. Pekarek, "Analysis and design of hybrid machines for DC generation," *IEEE Trans. Energy Convers.*, vol. 30, no. 3, pp. 1192-1199, Sep. 2015.
- [LAW52] A.E. Laws, "An electromechanical transducer with permanent magnet polarization," Technical note No. GW.202, royal aircraft establishment, Farnborough, UK, 1952.
- [LEO96] F. Leonardi, T. Matsuo, Y. Li, T.A. Lipo, and P. McCleer, "Design considerations and test results for a doubly salient PM motor with flux control," in *Proc. 31th Ind. Appl. Conf. IAS Annual Meeting*, 6-10 Oct. 1996. vol. 1, pp. 458-463.
- [LI14] D. Li, R. Qu, and T.A. Lipo, "High-power-factor vernier permanent-magnet machines," *IEEE Trans. Ind. Appl.*, vol. 50, no. 6, pp. 3664-3674, Nov./Dec. 2014.
- [LI15] S. Li, Y. Li, and B. Sarlioglu, "Partial irreversible demagnetization assessment of flux-switching permanent magnet machine using ferrite permanent magnet material," *IEEE Trans. Magn.*, vol. 51, no. 7, pp. 8106209, Jul. 2015.
- [LI95] Y. Li and T.A. Lipo, "A doubly salient permanent magnet motor capable of field weakening," in *Proc. Ann. Power Electr. Spec. Conf. (PESC)*, 18-22, Jun. 1995, vol. 1, pp. 565-571.
- [LIA95] Y. Liao, F. Liang, and T.A. Lipo, "A novel permanent magnet motor with doubly salient structure," *IEEE Trans. Ind. Appl.*, vol. 31, pp. 1069-1078, Sep./Oct. 1995.
- [LIU09] X. Liu, H. Lin, Z.Q. Zhu, C. Yang, S. Fang, and J. Guo, "A novel dual-stator hybrid excited synchronous wind generator," *IEEE Trans. Ind. Appl.*, vol. 45, no. 3, pp. 947-953, May/Jun. 2009.
- [LIU10] C. Liu, K.T. Chau, J.Z. Jiang, "A permanent-magnet hybrid brushless integrated starter-generator for hybrid electric vehicles," *IEEE Trans. Ind. Electron.*, vol. 57, no. 12, pp. 4055-4065, Dec. 2010.

- [LIU12] C. Liu, K.T. Chau, and Z. Zhang, "Novel design of double-stator single-rotor magnetic-gear machines," *IEEE Trans. Magn.*, vol. 48, no. 11, pp. 4180-4183, Nov. 2012.
- [LUO00] X. Luo, and T.A. Lipo, "A synchronous/permanent magnet hybrid AC machine," *IEEE Trans. Energy Convers.*, vol. 15, no. 2, pp. 203-210, Jun. 2000.
- [MAI87] A. Mailfert, H. Kubler, and J. Zhou, "Hybrid stepping motors comparative experimental results," in *Proc. Int. Conf. on Electrical Machines (ICEM)*, pp. 781-783, 1987
- [McC87] F.B. McCarty, "Hybrid excited generator with flux control of consequent-pole rotor," U.S. Patent No. 4656379, Apr. 04, 1987.
- [McF14] J. McFarland, T.M. Jahns, and A. El-Refaie, "Demagnetization performance characteristics of flux switching permanent magnet machines," in *Proc. of Int. Conf. on Electrical Machines (ICEM)*, Berlin, Germany, pp. 2001-2007, 2014.
- [McF14] J. Mcfarland, T.M. Jahns, A. El-Refaie, and P. Reddy, "Effect of magnet properties on power density and flux-weakening performance of high-speed interior permanent magnet synchronous machines," in *Proc. Energy Conversion Congress and Exposition (ECCE)*, 14-18 Sep. 2014, pp. 4218-4225.
- [MEL11] L. Melcescu, M. Cistelecan, M. Popescu, and O. Craiu, "Design and development of a hybrid excited claw pole synchronous machine," in *Proc. Aegean Conf. Elec. Mach. Power Electron. (ACEMP)*, Sep. 2011, pp. 799-804
- [MET15] MetalPrices.com, [Online], Available: <http://www.metalprices.com/metal/dysprosium>. 2015.
- [MOR14] S. Morimoto, S. Ooi, Y. Inoue, and M. Sanada, "Experimental evaluation of a rare-earth-free PMASynRM with ferrite magnets for automotive applications," *IEEE Trans. Ind. Electron.*, vol. 61, no. 10, pp. 5794-5756, Oct. 2014.
- [NAO01] N. Naoe and T. Fukami, "Trial production of a hybrid excitation type synchronous machine," in *Proc. Electr. Machines and Drives Conf. (IEMDC)*, 17 Jun. 2001, pp. 545-547.

- [NED11] B. Nedjar, S. Hlioui, Y. Amara, L. Vido, M. Gabsi, and M. Lecrivain, "A new parallel double excitation synchronous machine," *IEEE Trans. Magn.*, vol. 47, no. 9, pp. 2252-2260, Sep. 2011.
- [NER14] J. Nerg, M. Rilla, V. Ruuskanen, J. Pyrhonen, and S. Ruotsalainen, "Direct-driven interior magnet permanent-magnet synchronous motors for a full electric sports car," *IEEE Trans. Ind. Electron.*, vol. 61, no. 8, pp. 4286-4294, Aug. 2014.
- [NIU07] S. Niu, K.T. Chau, J. Jiang, and C. Liu, "Design and control of a new double-stator cup-rotor permanent-magnet machine for wind power generation," *IEEE Trans. Magn.*, vol. 43, no. 6, pp. 2501-2503, Jun. 2007.
- [OAK11] T. Burrell, S. Campbell, C. Coomer, C. Ayers, A. Wereszczak, J. Cunningham, L. Marlino, L. Seiber, and H. Lin, "Evaluation of the 2010 toyota prius hybrid synergy drive system," Oak Ridge National Laboratory, U.S. Department of Energy, Washington D.C. 2011.
- [OLS11] M. Olszewski, "Evaluation of the 2010 Toyota Prius hybrid synergy drive system," Oak Ridge National Laboratory, U.S. Department of Energy, USA, 2011, Available online: <https://info.ornl.gov/sites/publications/files>
- [OOI13] S. Ooi, S. Morimoto, M. Sanada, and Y. Inoue, "Performance evaluation of a high-power-density PMASynRM with ferrite magnets," *IEEE Trans. Ind. Appl.*, vo. 49, no. 3, pp. 1308-1315, May/Jun. 2013.
- [OWE09] R. Owen, Z.Q. Zhu, and G. Jewell, "Hybrid excited flux-switching permanent magnet machines, in *Proc. Euro. Conf. Power Electron. Applicat.*, 8-10 Sep. 2009, pp. 1-10.
- [OWE10a] R. Owen, Z.Q. Zhu, and G. Jewell, "Hybrid-excited flux-switching permanent-magnet machines with iron flux bridges," *IEEE Trans. Magn.*, vol. 46, no. 6, pp. 1726-1729, Jun. 2010.
- [OWE10b] R. Owen, Z.Q. Zhu, A. Thomas, G. Jewell, and D. Howe, "Alternate poles wound flux-switching permanent-magnet brushless AC machines," *IEEE Trans. Ind. Appl.*, vol. 46, no. 2, pp. 790-797, Mar./Apr. 2010.

- [OWE11] R. Owen, Z.Q. Zhu, J. Wang, D. Stone, and I. Urquhart, "Review of variable-flux permanent magnet machines," in *Proc. Int. Conf. on Elec. Mach. and Sys. (ICEMS)*, 20-23 August, 2011, Beijing, China, pp. 1-6.
- [OZA11] I. Ozawa, T. Kosaka, and N. Matsui, "Less rare-earth magnet-high power density hybrid excitation motor designed for Hybrid Electric Vehicle drives," in *Proc. Europ. Conf. Power Electr. Applicat. (EPE)*, Sep. 2009, pp. 1-10.
- [PAT08] N. Patin, L. Vido, E. Monmasson, J. Louis, M. Gabsi, and M. Lecrivain, "Control of a hybrid excitation synchronous generator for aircraft applications," *IEEE Trans. Ind. Electron.*, vol. 55, no. 10, pp. 3772-3783, Oct. 2008.
- [QI09] G. Qi, J. Chen, Z.Q. Zhu, D. Howe, L. Zhou, and C. Gu, "Influence of skew and cross-coupling on flux-weakening performance of permanent-magnet brushless AC machines," *IEEE Trans. Magn.*, vol. 45, no. 5, pp. 2110-2117, May. 2009.
- [RAM15] T. Raminosoa, A. El-Refaie, D. Pan, K. Huh, J. Alexander, K. Grace, S. Grubic, S. Galioto, P. Reddy, and X. Shen, "Reduced rare-earth flux switching machines for traction applications," *IEEE Trans. Ind. Appl.*, vol. 51, no. 4, pp. 2959-2971, Jul./Aug. 2015.
- [RAU55] S.E. Rauch, and L.J. Johnson, "Design principles of the flux-switch alternators," *AIEE Trans.*, vol. 74, no. 3, pp. 1261-1268, Jan. 1955.
- [REB15] R. Rebhi, A. Ibalá, and A. Masmoudi, "MEC-based sizing of a hybrid-excited claw pole alternator," *IEEE Trans. Ind. Appl.*, vol. 51, no. 1, pp. 211-223, Jan./Feb. 2015.
- [REF10] A. El-Refaie, "Fractional-slot concentrated-windings synchronous permanent magnet machines: opportunities and challenges," *IEEE Trans. Ind. Electron.*, vol. 57, no. 1, pp. 107-121, Jan. 2010.
- [SHA15] Shanghai metals market, [Online], Available: <http://www.metal.com/steel>. 2015.
- [SHI11] M. Shi, B. Zhou, J. Wei, Z. Zhang, Y. Mao, and C. Han, "Design and practical implementation of a novel variable-speed generation system," *IEEE Trans. Ind. Electron.*, vol. 58, no. 11, pp. 5032-5040, Nov. 2011.

- [SHI17] J. Shi, A. Wang, and Z.Q. Zhu, "Influence of PM- and armature winding-stator positions on electromagnetic performance of novel partitioned stator permanent magnet machines," *IEEE Trans. Magn.*, vol. 53, no. 1, pp. 8100212, Jan. 2017.
- [SIK15] C. Sikder, I. Husain, and W. Ouyang, "Cogging torque reduction in flux-switching permanent-magnet machines by rotor pole shaping," *IEEE Trans. Ind. Appl.*, vol. 51, no. 5, pp. 3609-3619, Sep./Oct. 2015.
- [SOO94] W.L. Soong, and T.J. Miller, "Field-weakening performance of brushless synchronous AC motor drives," *IEE Proc. Elec. Power Appl.*, vol. 141, no. 6, pp. 331-340, Nov. 1994.
- [SPO89] E. Spooner, and S. Khatab, and N. Nicolaou, "Hybrid excitation of AC and DC machines," in *Proc. Inter. Electr. Machines and Drives, Conf. (IEMDC)*, 13-15 Sep. 1989, pp. 48-52.
- [SUN12] X. Sun, M. Cheng, S. Zhu, and J. Zhang, "Coupled electromagnetic-thermal-mechanical analysis for accurate prediction of dual-mechanical-port machine performance," *IEEE Trans. Ind. Appl.*, vol. 48, no. 6, pp. 2240-2248, Nov./Dec. 2012.
- [SUN15] L. Sun, M. Cheng, and H. Jia, "Analysis of a novel magnetic-g geared dual-rotor motor with complementary structure," *IEEE Trans. Ind. Electron.*, vol. 62, no. 11, pp. 6737-6747, Nov. 2015.
- [SYV95] C. Syverson, "Hybrid alternator," U.S. Patent No. US005397975A, Mar. 14, 1995.
- [TAP02] J. Tapia, L. Leonardi, and T.A. Lipo, "A design procedure for a PM machine with extended field weakening capability," in *Proc. Ind. Appl. Conf. (IAS2002)*, Oct. 2002, vol. 3, pp. 1928-1935.
- [TAP03] J. Tapia, F. Leonardi, and T.A. Lipo, "Consequent-pole permanent-magnet machine with extended field-weakening capability," *IEEE Trans. Ind. Applicat.*, vol. 39, no. 6, pp. 1704-1709, Nov./Dec. 2003.
- [TAR16] P. Taras, G. Li, and Z.Q. Zhu, "Comparative study of fault tolerant switched flux permanent magnet machines," *IEEE Trans. Ind. Electron.*, in press.

- [TER16] M. Terzic, D. Mihic, and S. Vukosavic, "Impact of rotor material on the optimal geometry of high-speed drag-cup induction motor," *IEEE Trans. Energy Convers.*, vol. 31, no. 2, pp. 455-465, Jun. 2016.
- [VAG14] A. Vagati, B. Boazzo, P. Guglielmi, and G. Pellegrino, "Design of ferrite-assisted synchronous reluctance machines robust toward demagnetization," *IEEE Trans. Ind. Appl.*, vol. 50, no. 3, pp. 1768-1779, May/Jun. 2014.
- [VAR13] R. Vartanian, Y. Deshpande, H. Toliyat, "Performance analysis of a ferrite based fractional horsepower permanent magnet assisted SynRM for fan and pump applications," in *Proc. Int. Elec. Mach. Drives Conf. (IEMDC)*, 12-15 May 2013, pp. 1405-1410.
- [WAN01] C.X. Wang, I. Boldea, and S. Nasar, "Characterization of three phase flux reversal machine as an automotive generator," *IEEE Trans. Energy Convers.*, vol. 16, no. 1, pp. 74-80, Mar. 2001.
- [WAN12a] Y. Wang, Z. Deng, and X. Wang, "A parallel hybrid excitation flux-switching generator DC power system based on direct torque linear control," *IEEE Trans. Energy Convers.*, vol. 27, no. 2, pp. 308-317, Jun. 2012.
- [WAN12b] Y. Wang, and Z. Deng, "Comparison of hybrid excitation topologies for flux-switching machines," *IEEE Trans. Magn.*, vol. 48, no. 9, pp. 2518-2527, Sep. 2012.
- [WAN12c] Y. Wang and Z. Deng, "Hybrid excitation topologies and control strategies of stator permanent magnet machines for DC power system," *IEEE Trans. Ind. Electron.*, vol. 59, no. 12, pp. 4601-4616, Dec. 2012.
- [WAN15] S. Wang, S. Ni, Y. Xia, X. Wang, P. Su, and S. Huang, "Hybrid excitation permanent magnet synchronous machines and their structures," in *Proc. Inter. Conf. Electri. Mach. (ICEM)*, Sep. 2014, pp. 2618-2624.
- [WAN16] Y. Wang, and Z. Deng, "A controllable power distribution strategy for open winding hybrid excitation generator system," *IEEE Trans. Energy Convers.*, in press.
- [WAN99] C.X. Wang, S. Nasar, and I. Boldea, "Three-phase flux reversal machine (FRM)," *IEE Proc. Elec. Power Appl.*, vol. 146, no. 2, pp. 139-146, Mar. 1999.

- [WEL03] B. Welchko, T.M. Jahns, W. Soong, and J. Nagashima, "IPM synchronous machine drive response to symmetrical and asymmetrical short circuit faults" *IEEE Trans. Energy Convers.*, vol. 18, no. 2, pp. 291-298, Jun. 2003.
- [WU10] L.J. Wu, Z.Q. Zhu, J.T. Chen, Z.P. Xia, and G. Jewell, "Optimal split ratio in fractional-slot interior permanent-magnet machines with non-overlapping windings," *IEEE Trans. Magn.*, vol. 46, no. 5, pp. 1235-1242, May 2010.
- [WU15a] Z. Wu, Z.Q. Zhu, and J. Shi, "Novel doubly salient permanent magnet machines with partitioned stator and iron pieces rotor," *IEEE Trans. Magn.*, vol. 51, no. 5, pp. 8105212, May 2015.
- [WU15b] Z. Wu and Z.Q. Zhu, "Partitioned stator flux reversal machine with consequent-pole PM stator," *IEEE Trans. Energy Convers.*, vol. 30, no. 4, pp. 1472-1482, Dec. 2015.
- [WU16a] Z. Wu and Z.Q. Zhu, "Comparative analysis of end effect in partitioned stator flux reversal machines having surface-mounted and consequent pole permanent magnets," *IEEE Trans. Magn.*, vol. 52, no. 7, pp. 8103904, Jul. 2016.
- [YOO16] K. Yoon and B. Kwon, "Optimal design of a new interior permanent magnet motor using a flared-shape arrangement of ferrite magnets," *IEEE Trans. Magn.*, vol. 52, no. 7, pp. 8106504, Jul. 2016.
- [ZHA08] Z. Zhang, Y. Yan, S. Yang, and Z. Bo, "Principle of operating and feature investigation of a new topology of hybrid excitation synchronous machine," *IEEE Trans. Magn.*, vol. 44, no. 9, pp. 2174-2180, Sep. 2008.
- [ZHA09] J. Zhang, M. Cheng, Z. Chen, and W. Hua, "Comparison of stator-mounted permanent magnet machines based on a general power equation," *IEEE Trans. Energy Convers.*, vol. 24, no. 4, pp. 826-834, Dec. 2009.
- [ZHA10] Q. Zhang, S. Huang, and G. Xie, "Design and experimental verification of hybrid excitation machine with isolated magnetic paths," *IEEE Trans. Energy Convers.*, vol. 25, no. 4, pp. 993-1000, Dec. 2010.
- [ZHA11] G. Zhang, M. Cheng, W. Hua, and J. Dong, "Analysis of the oversaturated effect in hybrid excited flux-switching machines," *IEEE Trans. Magn.*, vol. 47, no. 10, pp. 2827-2830, Oct. 2011.

- [ZHA12] Z. Zhang, Y. Tao, and Y. Yan, "Investigation of a new topology of hybrid excitation doubly salient brushless DC generator," *IEEE Trans. Ind. Electron.*, vol. 59, no. 6, pp. 2550-2556, Jun. 2012.
- [ZHA13] Z. Zhang, J. Dai, C. Dai, and Y. Yan, "Design consideration of a hybrid excitation synchronous machine with magnetic shunt rotor," *IEEE Trans. Magn.*, vol. 49, no. 11, pp. 5566-5573, Nov. 2013.
- [ZHA14] Z. Zhang, S. Ma, J. Dai, and Y. Yan, "Investigation of hybrid excitation synchronous machines with axial auxiliary air-gaps and non-uniform air-gaps," *IEEE Trans. Ind. Appl.*, vol. 50, no. 3 pp. 1729-1737, May/June. 2014.
- [ZHA15a] P. Zhang, G. Sizov, D. Ionel, and N. Demerdash, "Establishing the relative merits of interior and spoke-type permanent magnet machines with ferrite or NdFeB through systematic design optimization," *IEEE Trans. Ind. Appl.*, vol. 51, no. 4, pp. 2940-2948, Jul./Aug. 2015.
- [ZHA15b] G. Zhang, W. Hua, M. Cheng, J. Liao, K. Wang, and J. Zhang, "Investigation of an improved hybrid-excitation flux-switching brushless machine for HEV/EV applications," *IEEE Trans. Ind. Appl.*, vol. 51, no. 5, pp. 3791-3799, Sep./Oct. 2015.
- [ZHA16] G. Zhang, W. Hua, M. Cheng, and J. Liao, "Design and comparison of two six-phase hybrid-excited flux-switching machines for EV/HEV applications," *IEEE Trans. Ind. Electron.*, vol. 63, no. 1, pp. 481-493, Jan. 2016.
- [ZHU00] Z.Q. Zhu and D. Howe, "Influence of design parameters on cogging torque in permanent magnet machines," *IEEE Trans. Energy Convers.*, vol. 15, no. 4, pp. 407-412, Dec. 2000.
- [ZHU05] Z.Q. Zhu, Y. Pang, D. Howe, S. Iwasaki, R. Deodhar, and A. Pride, "Analysis of electromagnetic performance of flux-switching permanent-magnet machines by nonlinear adaptive lumped parameter magnetic circuit model," *IEEE Trans. Magn.*, vol. 41, no. 11, pp. 4277-4287, Nov. 2005.
- [ZHU07a] X. Zhu, M. Cheng, W. Zhao, C. Liu, and K.T. Chau, "Transient cosimulation approach to performance analysis of hybrid excited doubly salient machine consideration indirect field-circuit coupling," *IEEE Trans. Magn.*, vol. 43, no. 6, pp. 2558-2560, Jun. 2007.

- [ZHU07b] Z.Q. Zhu and D. Howe, "Electrical machines and drives for electric, hybrid, and fuel cell vehicles," *Proc. IEEE*, vol. 95, no. 4, pp. 746-765, Apr. 2007.
- [ZHU09] Z.Q. Zhu, "A simple method for measuring cogging torque in permanent magnet machines," in *Proc. IEEE Power Energy Soc. Gen. Meet.*, Jul. 2009, pp. 1-4.
- [ZHU10] Z.Q. Zhu, and J.T. Chen, "Advanced flux-switching permanent magnet brushless machines," *IEEE Trans. Magn.*, vol. 46, no. 6, pp. 1447-1453, Jun. 2010.
- [ZHU11a] Z. Q. Zhu, "Switched flux permanent magnet machines – innovation continues", in *Proc. Int. Conf. Electr. Mach. Sys. (ICEMS)*, 2011, Beijing, chapter Keynote Speech-06, pp. 1-10.
- [ZHU14a] Z. Q. Zhu, and D. J. Evans, "Overview of recent advances in innovative electrical machines-with particular reference to magnetically geared switched flux machines," in *Proc. Int. Conf. Electr. Mach. Sys. (ICEMS)*, keynote speech Hangzhou, China, Oct. 22-25, 2014, pp. 1-10.
- [ZHU15a] S. Zhu, M. Cheng, W. Hua, X. Cai, and M. Tong, "Finite element analysis of flux-switching PM machine considering oversaturation and irreversible demagnetization", *IEEE Trans. Magn.*, vol. 51, no. 11, pp. 7403404, Nov. 2015.
- [ZHU15b] Z.Q. Zhu, Z. Wu, D. Evans, and W. Chu, "Novel electrical machines having separate PM excitation stator," *IEEE Trans. Magn.*, vol. 51, no. 4, pp. 8104109, Apr. 2015.
- [ZHU15c] Z.Q. Zhu, Z. Wu, D. Evans, and W. Chu, "A wound field switched flux machine with field and armature windings separately wound in double stators," *IEEE Trans. Energy Convers.*, vol. 30, no. 2, pp. 772-783, Jun. 2015.
- [ZON14] Z. Zong, L. Quan, and Z. Xiang, "Comparison of double-stator flux-switching permanent magnet machine and double-stator permanent magnet synchronous machine for electric vehicle applications," in *Proc. Int. Conf. on Electrical Machines and Systems (ICEMS)*, 22-25 Oct. 2014, pp. 234-239.

Publications

Journal papers:

- [J1] Chapter 2 Z.Q. Zhu, **H. Hua**, D. Wu, J.T. Shi, and Z.Z. Wu, “Comparative study of partitioned stator machines with different PM excitation stators,” *IEEE Trans. Ind. Appl.*, vol. 52, no. 1, pp. 199-208, Jan./Feb. 2016.
- [J2] Chapter 3 **H. Hua**, Z.Q. Zhu, M. Zheng, Z.Z. Wu, D. Wu, X. Ge, and C. Wang, “Partitioned stator machines with NdFeB and ferrite magnets,” *IEEE Trans. Ind. Appl.*, in press.
- [J3] Chapter 4 **H. Hua** and Z.Q. Zhu, “Novel hybrid-excited switched-flux machine having separate field winding stator,” *IEEE Trans. Magn.*, vol. 52, no. 7, pp. 8104004, Jul. 2016.
- [J4] Chapter 5 **H. Hua** and Z.Q. Zhu, “Novel partitioned stator hybrid excited switched flux machines,” *IEEE Trans. Energy Convers.*, in press.
- [J5] Chapter 6 **H. Hua**, Z.Q. Zhu, and H. Zhan, “Novel consequent-pole hybrid excited machine with separated excitation stator,” *IEEE Trans. Ind. Electron.*, vol. 63, no. 8, pp. 4718-4728, Aug. 2016.
- [J6] Chapter 7 **H. Hua** and Z.Q. Zhu, “Novel parallel hybrid excited machines with separate stators,” *IEEE Trans. Energy Convers.*, vol. 31, no. 3, pp. 1212-1220, Sep. 2016.
- [J7] **H. Hua**, Z.Q. Zhu, A. Pride, R. Deodhar, and T. Sasaki, “A novel variable flux memory machine with series hybrid magnets,” *IEEE Trans. Ind. Appl.*, in press.
- [J8] Z.Q. Zhu, **H. Hua**, A. Pride, R. Deodhar, and T. Sasaki, “Analysis and reduction of unipolar leakage flux in series hybrid permanent magnet variable flux memory machines,” submitted to *IEEE Trans. Magn.*, in 2017.

International Conference papers:

- [C1] Z.Q. Zhu, **H. Hua**, D. Wu, J.T. Shi, and Z.Z. Wu, "Comparison of partitioned stator machines with different PM excitation stator topologies," in *Proc. Inter. Conf. Ecological Vehicles and Renewable Energies (EVER)*, Monaco, Mar. 31-Apr. 3, 2015, pp. 1-7.
- [C2] **H. Hua**, Z.Q. Zhu, M. Zheng, D. Wu, and Z.Z. Wu "Performance comparison of partitioned stator machines with different PM materials," in *Proc. Inter. Electric Machines and Drives Conf. (IEMDC)*, Idaho, USA, May 10-13, 2015, pp. DF-003751.
- [C3] Z.Q. Zhu and **H. Hua**, "A partitioned stator permanent magnet machine for HEV/EV applications," in *Proc. Sustainable Mobility Appl., Renewables and Tech. (SMART)*, Nov. 23-25, 2015, pp. 1-7.
- [C4] **H. Hua** and Z.Q. Zhu, "Novel switched flux hybrid excited machine having separate field winding stator," in *Proc. Joint MMM/Intermag Conf.*, San Diego, USA, Jan. 11-15, 2016, pp. CJ-06.
- [C5] **H. Hua**, Z.Q. Zhu, A. Pride, R. Deodhar, and T. Sasaki, "A novel variable flux memory machine with series hybrid magnets," in *Proc. Energy Conversion Congress Expo (ECCE)*, Milwaukee, USA, Sep. 18-22, 2016, pp. EC-0239.
- [C6] Z.Q. Zhu, **H. Hua**, A. Pride, R. Deodhar, and T. Sasaki, "Analysis of unipolar leakage flux in series-hybrid permanent magnet machines," in *Proc. IEEE Inter. Magnetics Conf. (Intermag)*, Dublin, Ireland, Apr. 24-28, 2017.
- [C7] **H. Hua**, Z.Q. Zhu, A. Pride, R. Deodhar, and T. Sasaki, "Comparative study of variable flux memory machines with parallel and series hybrid magnets," in *Proc. Energy Conversion Congress Expo (ECCE)*, Cincinnati, USA, Oct. 1-5, 2017.
- [C8] **H. Hua**, Z.Q. Zhu, A. Pride, R. Deodhar, and T. Sasaki, "Comparison of end effect in series and parallel hybrid permanent magnet variable flux memory machines," in *Proc. Inter. Conf. Elec. Mach. Sys. (ICEMS)*, Sydney, Australia, Aug. 11-14, 2017.